

**PREPARATION, CHARACTERIZATION AND TESTING  
OF CATALYSTS CONTAINING PLATINUM AND  
COBALT ON FAUJASITE ZEOLITES**

**PONGTANAWAT KHEMTHONG**

**A Thesis Submitted in Partial Fulfillment of the Requirements for the**

**Degree of Doctor of Philosophy in Chemistry**

**Suranaree University of Technology**

**Academic Year 2008**

การเตรียม การวิเคราะห์ลักษณะ และการทดสอบตัวเร่งปฏิกิริยาที่ประกอบด้วย  
โลหะแพลทินัมและโคบอลต์บนตัวรองรับซีโอไลต์แบบฟูจาไซต์

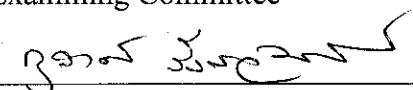
นายพงษ์ชนวัฒน์ เข้มทอง

วิทยานิพนธ์นี้เป็นส่วนหนึ่งของการศึกษาตามหลักสูตรปริญญาวิทยาศาสตรดุษฎีบัณฑิต  
สาขาวิชาเคมี  
มหาวิทยาลัยเทคโนโลยีสุรนารี  
ปีการศึกษา 2551

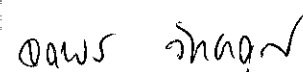
**PREPARATION, CHARACTERIZATION AND TESTING OF  
CATALYSTS CONTAINING PLATINUM AND COBALT ON  
FAUJASITE ZEOLITES**

Suranaree University of Technology has approved this thesis submitted in partial fulfillment of the requirements for the Degree of Doctor of Philosophy.

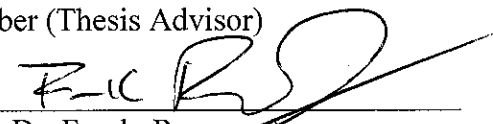
Thesis Examining Committee

  
\_\_\_\_\_  
(Asst. Prof. Dr. Kunwadee Rangriwatananon)

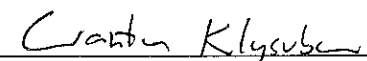
Chairperson

  
\_\_\_\_\_  
(Assoc. Prof. Dr. Jatuporn Wittayakun)

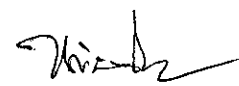
Member (Thesis Advisor)

  
\_\_\_\_\_  
(Prof. Dr. Frank Roessler)

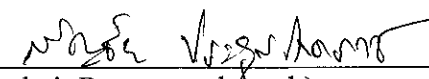
Member

  
\_\_\_\_\_  
(Dr. Wantana Klysubun)

Member


  
\_\_\_\_\_  
(Assoc. Prof. Dr. Nurak Gridanurak)

Member

  
\_\_\_\_\_  
(Dr. Sanchai Prayoonpokarach)

Member

  
\_\_\_\_\_  
(Prof. Dr. Pairote Sattayatham)

  
\_\_\_\_\_  
(Assoc. Prof. Dr. Prapan Manyum)

Vice Rector for Academic Affairs

Dean of Institute of Science

พงษ์ชนวัฒน์ เข้มทอง : การเตรียม การวิเคราะห์ลักษณะ และการทดสอบตัวเร่งปฏิกิริยา  
ที่ประกอบด้วยโลหะแพลทินัมและโคบอลต์บนซีโอไลต์แบบฟูจาไซต์ (PREPARATION,  
CHARACTERIZATION AND CATALYTIC TESTING OF CATALYSTS  
CONTAINING PLATINUM AND COBALT ON FAUJASITE ZEOLITES)  
อาจารย์ที่ปรึกษา : รองศาสตราจารย์ ดร.จตุพร วิทยาคุณ, 171 หน้า.

งานนี้เริ่มจากการสกัดซิลิกาออกจากแคลบข้าวที่มีความบริสุทธิ์ 98 เปอร์เซ็นต์ แล้ว  
เปลี่ยนให้เป็นสารละลายโซเดียมซิลิเกตเพื่อใช้สังเคราะห์ซีโอไลต์โซเดียมโพแตสเซียมเอกซ์ที่มี  
ปริมาณซิลิกาต่ำ (NaK-LSX) และซีโอไลต์โซเดียมวาย (NaY) พบว่าสังเคราะห์ได้สำเร็จโดยยืนยัน  
ได้จากเทคนิคการเลี้ยวเบนของรังสีเอกซ์ นอกจากนี้ได้ศึกษาลักษณะทางกายภาพ การกระจายตัว  
ของขนาดอนุภาค และหาพื้นที่ผิวของซีโอไลต์ทั้งสองชนิด โครงสร้างของซีโอไลต์ NaK-LSX ไม่  
เปลี่ยนหลังจากแลกเปลี่ยนไอออนกับแอมโมเนียมแต่โครงสร้างถูกทำลายหลังจากการแคลไซน์  
ส่วน NaY สังเคราะห์ได้เฟสบริสุทธิ์โดยวิธีสองขั้นตอน โดยบ่มที่อุณหภูมิห้อง 24 ชั่วโมงแล้วตก  
ผลึกที่อุณหภูมิ 90 องศาเซลเซียสนาน 24 ชั่วโมง ผลึกที่ได้มีโครงสร้างแข็งแรงหลังจากทำการ  
แลกเปลี่ยนไอออนและเผาแคลไซน์ จากนั้นนำซีโอไลต์ว้ายไปใช้เป็นตัวรองรับของตัวเร่งปฏิกิริยา

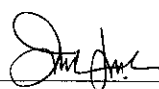
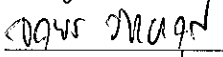
ความสามารถในการรีดิวซ์ของโคบอลต์บนซีโอไลต์ว้ายในรูปของโซเดียมและโปรตอน  
(Co/NaY และ Co/HY ตามลำดับ) ศึกษาได้ด้วยเทคนิคการดูดกลืนรังสีเอกซ์ ก่อนนำไปทดสอบ  
การเร่งปฏิกิริยาไฮโดรจิโนไลซิสของบิวเทน ผลจากการทดลองพบว่าคุณสมบัติทางกายภาพและ  
ทางเคมีโคบอลต์ขึ้นอยู่กับฟอร์มของตัวรองรับ หลังจากรีดิวซ์ด้วยแก๊สไฮโดรเจนที่อุณหภูมิ 420  
องศาเซลเซียส 5 ชั่วโมง โคบอลต์บน NaY เกิดการรีดิวซ์บางส่วนเป็นโลหะโคบอลต์ในขณะที่  
โคบอลต์บนตัวรองรับ HY ไม่มีการเปลี่ยนแปลงหลังจากรีดิวซ์ที่สภาวะเดียวกัน บ่งชี้ว่าโคบอลต์  
ออกไซด์บน HY รีดิวซ์ได้ยาก และพบว่าฟอร์มที่มีความว่องไวต่อปฏิกิริยาไฮโดรจิโนไลซิสของ  
บิวเทนคือ Co/NaY

การเพิ่มประสิทธิภาพของโคบอลต์ด้วยแพลทินัมบนตัวรองรับโซเดียมวายโดยใช้ปริมาณ  
แพลทินัมคงที่ 1 เปอร์เซ็นต์โดยน้ำหนัก พบว่าเมื่อปริมาณโคบอลต์ 1 เปอร์เซ็นต์โดยน้ำหนัก  
รีดิวซ์ได้ยากแม้จะทำการรีดิวซ์ที่ 400 องศาเซลเซียส นาน 5 ชั่วโมง ในขณะที่โคบอลต์ปริมาณ 6  
และ 10 เปอร์เซ็นต์โดยน้ำหนักแสดงผลการรีดิวซ์เกือบสมบูรณ์ บ่งชี้ว่าแพลทินัมช่วยในการรีดิวซ์  
ของโคบอลต์ ความสามารถในการเร่งปฏิกิริยาของตัวเร่งปฏิกิริยาโลหะคู่ผสมกว่าตัวเร่งปฏิกิริยา  
โลหะเดี่ยว หลังจากการเร่งปฏิกิริยา 30 นาที ค่าการแปรผันของโคบอลต์บนตัวรองรับโซเดียมวาย  
มีค่า 40 เปอร์เซ็นต์ โดยเกิดเฉพาะมีเทน ในขณะที่ค่าการแปรผันของตัวเร่งปฏิกิริยาโลหะคู่ผสม  
เกิดขึ้นเกือบสมบูรณ์ ผลิตภัณฑ์ที่เกิดขึ้นคือ มีเทน อีเทน ส่วนโพรเพนเกิดหลังจากเกิดปฏิกิริยา 60

นาที่ ดังนั้นการเพิ่มโลหะแพลทินัมลงไปช่วยเพิ่มการรีดิวซ์และช่วยในการเร่งปฏิกิริยาไฮโดรจีโนไลซิสบิวเทนของโคบอลต์บนตัวรองรับโซเดียมวอย

ศึกษาการเร่งปฏิกิริยาไอโซเมอร์ไรเซชันของนอร์มัลเฮกเซนด้วยตัวเร่งปฏิกิริยาโลหะแพลทินัมบนตัวรองรับโปรตอนซีโอไลต์วอยและตัวเร่งปฏิกิริยาผสมระหว่างแพลทินัมบนตัวรองรับโซเดียมวอยและตัวเร่งปฏิกิริยาโลหะแพลทินัมบนตัวรองรับซีโอไลต์โปรตอนวอย (อัตราส่วนโดยน้ำหนัก 1:3) พบว่าที่อุณหภูมิ 300 องศาเซลเซียส ความเจาะจงต่อปฏิกิริยามีค่าเหมือนกันทั้งสองตัวเร่งปฏิกิริยา ผลผลิตกัณฑ์ไอโซเมอร์หลักที่ได้คือเมทิลเพนเทนและไดเมทิลบิวเทน ผลผลิตกัณฑ์ไอโซเมอร์ประกอบไปด้วย 2 เมทิลเพนเทน 3 เมทิลเพนเทน 2,2 ไดเมทิลบิวเทน 2,3 ไดเมทิลบิวเทน ส่วนที่อุณหภูมิ 450 องศาเซลเซียส ตัวเร่งปฏิกิริยาโลหะแพลทินัมบนตัวรองรับโปรตอนซีโอไลต์วอยเกิดผลผลิตกัณฑ์การแตกตัวในปริมาณที่สูงซึ่งประกอบไปด้วย โพรเพน บิวเทน และเพนเทน ส่วนผลผลิตกัณฑ์ไอโซเมอร์ที่ได้คล้ายคลึงกับการเร่งปฏิกิริยาที่อุณหภูมิ 300 องศาเซลเซียสแต่ให้ผลผลิตสูงกว่า ตัวเร่งปฏิกิริยาผสมระหว่างแพลทินัมบนตัวรองรับโซเดียมวอยและตัวเร่งปฏิกิริยาโลหะแพลทินัมบนตัวรองรับซีโอไลต์โปรตอนวอยมีความจำเพาะเจาะจงต่อการเกิดปฏิกิริยาไอโซเมอร์ไรเซชันของนอร์มัลเฮกเซนที่อุณหภูมิสูงมากกว่าตัวเร่งปฏิกิริยาโลหะแพลทินัมบนตัวรองรับโปรตอนซีโอไลต์วอยแสดงให้เห็นว่าการเพิ่มโซเดียมวอยจำเป็นต่อปฏิกิริยาไอโซเมอร์ไรเซชัน

สาขาวิชาเคมี  
ปีการศึกษา 2551

ลายมือชื่อนักศึกษา   
ลายมือชื่ออาจารย์ที่ปรึกษา 

PONGTANAWAT KHEMTHONG : PREPARATION, CHARACTERIZATION  
AND CATALYTIC TESTING OF CATALYSTS CONTAINING PLATINUM  
AND COBALT ON FAUJASITE ZEOLITES. THESIS ADVISOR : ASSOC.  
PROF. JATUPORN WITTAYAKUN, Ph.D. 171 PP.

#### ZEOLITES/CATALYSTS/ HYDROGENOLYSIS/ISOMERIZATION

Amorphous silica powder with 98% purity was extracted from rice husk, converted to a sodium silicate solution, and used as a silica source for the synthesis of sodium-potassium low silica type X (NaK-LSX) and sodium Linde type Y (NaY). The syntheses were successful as confirmed by XRD. The structure of NaK-LSX did not change after ion-exchange to ammonium form but collapsed after subsequent calcination. The zeolite NaY in pure phase was obtained from two-step synthetic route in which aged for 24 h at room temperature and crystallized for 24 h at 90°C. The structure of NaY was retained after the ion-exchange and calcination. The NaY was used as a catalyst support for cobalt and platinum in the form of monometallic and bimetallic.

Reducibility of monometallic cobalt on zeolite Y in sodium and proton forms (Co/NaY and Co/HY respectively) was studied by XAS before testing on butane hydrogenolysis. The physicochemical properties of cobalt strongly depend on the form of support. After reduction in H<sub>2</sub> at 400°C for 3 h, the Co in Co/NaY was partially reduced to metallic Co while Co in Co/HY was not changed after reduction with similar conditions indicating that the cobalt oxides on HY are difficult to reduce. The active form of Co catalysts for butane hydrogenolysis is metallic cobalt.

The enhancement of platinum (Pt) on Co supported on zeolite NaY as a second metal with fixed Pt loading at 1 wt% for butane hydrogenolysis was also studied. The catalyst with Co loading of 1 wt% was difficult to reduce to active form at 400°C in H<sub>2</sub> for 3 h. The bimetallic catalyst with Co loadings of 6 wt% and 10 wt% were almost fully reduced indicating that the addition of Pt assisted Co reduction. The catalytic activities of the bimetallic catalysts were higher than monometallic catalysts. After 30 minutes, the conversion on Co/NaY was 40% with methane as a product while the conversions on the bimetallic catalysts were almost 100%. The products on the bimetallic catalysts after 30 minutes were methane and ethane while propane was observed after 60 minutes. Thus, the presence of Pt enhanced reducibility and performance of butane hydrogenolysis on Co/NaY.


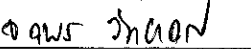
Isomerization of *n*-hexane on Pt/HY and a mixture between Pt/NaY and Pt/HY (weight ratio 1:3) was studied. At 300°C the selectivity were similar on both catalysts, with the methylpentanes (MP) and dimethylbutane (DMB) as main and primary isomerization products whose distribution included 2-MP, 3-MP, 2,2-DMB and 2,3-DMB. At 450°C, the 1Pt/HY gave higher cracking products including ethane, propane and butane. The isomerization products were similar to those at 300°C but with higher yields. The mixture Pt/NaY: Pt/HY gave a higher selectivity for *n*-hexane isomerization at high temperature than Pt/HY indicating that an addition of NaY is necessary for isomerization.

School of Chemistry

Academic Year 2008

Student's Signature

Advisor's Signature

## **ACKNOWLEDGEMENT**

I would like to express my fullness to all those who have helped me throughout my study. First of all, I would like to thank my thesis advisor, Assoc. Prof. Dr Jatuporn Wittayakun for his patience invaluable supervision, advice and giving thoughtful guidance with knowledge towards the completion of this research. His encouragement, understanding and supervision are very much appreciated. I am also very thankful to the thesis examining committee including Asst. Prof. Dr. Kunwadee Rangriwatananon, Dr. Wantana Klysubun, Prof. Dr. Frank Roessner, Assoc. Prof. Dr. Nurak Grisdanurak, and Dr. Sanchai Prayoonpokarach for their helpful suggestions.

I would also to thanks all of my good friends at Suranaree University of Technology, Synchrotron Light Research Institute (Public Organization) and Technische Chemie II, Carl von Ossietzky Universität, whom I have shared working experience with and made it a good time. Our friendship is a wonderful gift.

In addition, I would like to acknowledge the financial support from Suranaree University of Technology, Carl von Ossietzky Universität Oldenburg and Synchrotron Light Research Institute (Public Organization) Grant 2-2548/PS01.

Finally, I would like thank my parents and my brother for their love, support and continual encouragement during my education.

Pongtanawat Khemthong



# CONTENTS

	<b>Page</b>
ABSTRACT IN THAI.....	I
ABSTRACT IN ENGLISH.....	III
ACKNOWLEDGEMENT.....	VI
CONTENTS.....	VII
LIST OF FIGURES.....	XII
LIST OF TABLES.....	XIX
LIST OF ABBREVIATION.....	XXI
<b>CHAPTER</b>	
<b>I INTRODUCTION.....</b>	<b>1</b>
1.1 Research objectives.....	2
1.2 Scope and limitations of the study.....	2
<b>II LITERATURE REVIEW.....</b>	<b>4</b>
2.1 Background for rice husk silica (RHS).....	4
2.2 Zeolite properties.....	5
2.3 Heterogeneous catalyst background.....	6
2.3.1 Supported Co, Pt and Pt-Co catalysts.....	7
2.3.2 Characterization of bimetallic catalyst.....	8

## CONTENTS (Continued)

	<b>Page</b>
2.3.3 Catalytic performance of Pt bimetallic catalysts on hydrogenolysis reaction.....	11
2.4 References.....	12
 <b>III SYNTHESIS AND CHARACTERIZATION OF ZEOLITE LSX FROM RICE HUSK SILICA.....</b>	 <b>16</b>
3.1 Introduction.....	17
3.2 Experimental.....	18
3.2.1 Materials for RHS extraction and zeolite synthesis.....	18
3.2.2 Silica extraction from rice husk.....	19
3.2.3 Synthesis of zeolite LSX.....	19
3.2.4 Characterization of RHS and NaK-LSX.....	20
3.3 Results and Discussion.....	21
3.3.1 RHS characterization.....	21
3.3.2 Characterization of NaK-LSX by XRD.....	23
3.3.3 Characterization of NaK-LSX by FTIR.....	25
3.3.4 Surface area analysis of NaK-LSX by BET.....	26
3.3.5 Morphology of NaK-LSX studied by SEM.....	29
3.3.6 Particle size distribution of NaK-LSX by DPSA.....	31
3.3.7 Characterization and thermal stability of NH <sub>4</sub> -LSX from ion exchange of NaK-LSX.....	33

## CONTENTS (Continued)

	<b>Page</b>
3.4 Conclusions.....	36
3.5 Referneces.....	36
<b>IV SYNTHESIS OF ZEOLITE NaY FROM RICE HUSK SILICA..</b>	<b>40</b>
4.1 Introduction.....	41
4.2 Experimental.....	42
4.2.1 Synthesis of zeolite NaY.....	42
4.2.2 Characterization of NaY zeolite.....	43
4.3 Results and discussion.....	44
4.3.1 Textural properties.....	44
4.3.2 Comparison between one-step and two-step routes.....	44
4.3.3 Crystallization time in two-step route.....	46
4.3.4 Morphology of NaY by SEM.....	47
4.3.5 Particle size distribution of NaY by DPSA.....	49
4.4 Conclusions.....	50
4.5 References.....	51
<b>V REDUCIBILITY OF COBALT CATALYSTS SUPPORTED ON NaY AND HY INVESTIGATED BY XAS AND THEIR PERFORMANCE ON BUTANE HYDROGENOLYSIS.....</b>	<b>53</b>
5.1 Introduction.....	54
5.2 Experimental.....	56

## CONTENTS (Continued)

	<b>Page</b>
5.2.1 Catalyst preparation.....	56
5.2.2 Catalyst characterization.....	56
5.2.3 Catalytic testing on butane hydrogenolysis.....	58
5.3 Results and discussion.....	60
5.3.1 Characterization by N <sub>2</sub> adsorption-desorption.....	60
5.3.2 Characterization by XRD and TEM.....	61
5.3.3 Characterization by XANES.....	64
5.3.4 Characterization by EXAFS.....	74
5.3.5 Catalytic testing for butane hydrogenolysis.....	78
5.4 Conclusions.....	79
5.5 References.....	80
<b>VI REDUCIBILITY OF Co AND Co-Pt SUPPORTED ON ZEOLITE NaY INVESTIGATED BY X-RAY ABSORPTION AND THE CATALYTIC PERFORMANCE FOR BUTANE HYDROGENOLYSIS.....</b>	<b>85</b>
6.1 Introduction.....	86
6.2 Experimental.....	87
6.2.1 Catalyst preparation.....	87
6.2.2 Catalysts characterization.....	88
6.2.3 Catalytic testing on butane hydrogenolysis.....	89

## CONTENTS (Continued)

	<b>Page</b>
6.3 Results and discussion.....	90
6.3.1 N <sub>2</sub> adsorption-desorption analysis on surface of Co catalysts.....	90
6.3.2 NH <sub>3</sub> -TPD on their acidity of Co catalysts.....	91
6.3.3 Nature of Co in monometallic catalysts investigated by XANES.....	95
6.3.4 Nature of Co in bimetallic catalysts investigated by XANES.....	102
6.3.5 Structure of reduced mono- and bimetallic Co catalysts from EXAFS study.....	108
6.3.6 Catalytic testing of <i>n</i> -butane hydrogenolysis.....	113
6.3.7 XANES study on reducibility of Co catalysts after spent in the reaction.....	121
6.4 Conclusions.....	122
6.5 References.....	123
<b>VII ISOMERIZATION OF <i>n</i>-HEXANE OVER Pt SUPPORTED ON ZEOLITE Y SYNTHESIZED FROM RICE HUSK SILICA.....</b>	<b>127</b>
7.1 Introduction.....	128
7.2 Experimental.....	131
7.2.1 Catalyst preparation.....	131
7.2.2 Catalysts characterization.....	132

**CONTENTS (Continued)**

	<b>Page</b>
7.2.3 Catalytic activity testing.....	132
7.3 Results and discussion.....	136
7.3.1 XRD result.....	136
7.3.2 NH <sub>3</sub> -TPD result.....	137
7.3.3 Catalytic studies.....	137
7.4 Conclusions.....	145
7.5 References.....	145
<b>VIII CONCLUSIONS</b> .....	<b>148</b>
<b>APPENDICES</b> .....	<b>150</b>
APPENDIX A CHARACTERIZATION OUTPUT.....	151
APPENDIX B REACTION OUTPUT.....	159
APPENDIX C XAS DATA OUTPUT.....	164
<b>CURRICULUM VITAE</b> .....	<b>174</b>

## LIST OF FIGURES

<b>Figure</b>	<b>Page</b>
3.1 Powder XRD pattern of RHS.....	22
3.2 XRD spectrum of (a) NaK-LSX synthesized from RHS and (b) standard NaX.....	23
3.3 IR analysis of NaK-LSX zeolite from RHS .....	25
3.4 N <sub>2</sub> adsorption-desorption isotherm at N <sub>2</sub> temperature on the synthesized NaK-LSX .....	27
3.5 HK cumulative pore volume (a) and BJH pore size distribution (b) of NaK-LSX zeolite, where V is the cumulative pore volume (cm <sup>3</sup> /g).....	29
3.6 SEM images of synthesized Na-LSX with magnification of (a) 1500 and (b) 25000, respectively, and (c) particle size distribution measured from all particles in (a).....	30
3.7 Particle size distribution of NaK-LSX synthesized from RHS; (a) percentage of sample below a certain size of particle, (b) percentage of sample above a certain size of particle and (c) histogram plot and frequency curve of particle.....	32
3.8 XRD patterns of (a) Na-LSX (b) NH <sub>4</sub> -LSX, and (c) NH <sub>4</sub> -LSX after calcination .....	33
3.9 SEM images of NH <sub>4</sub> -LSX with magnification of 1500.....	34

## LIST OF FIGURES (Continued)

<b>Figure</b>	<b>Page</b>
3.10 Thermogram of zeolite NH <sub>4</sub> LSX (solid line is weight and dash line is first derivative of weight with respect to temperature).....	35
4.1 XRD spectrum of NaY from one-step and two-step synthesis (A) standard Y zeolite, (B) two-step, (C) one-step; (Y = NaY and P = NaP).....	45
4.2 XRD spectrum of NaY from two-step synthesis crystallized at (A) 22 h, (B) 24 h, (C) 48 h, and (D) 72 h ; (Y = NaY and P = NaP).	46
4.4 SEM images of zeolite Y synthesized from RHS with magnification of (A) ×7000, (B) ×20000 and (C) ×40000.....	48
4.5 SEM images of zeolite NaP with magnification of (A) ×1500 and (B) ×8000.....	49
4.6 Particle size distribution of zeolite Y synthesized from RHS analyzed by DPSA.....	50
5.1 Schematic diagram of reactor setup for butane hydrogenolys.....	59
5.2 N <sub>2</sub> adsorption-desorption isotherm of NaY, 6Co/NaY and 6Co/HY..	60
5.3 XRD patterns of reduced 6Co/NaY and 6Co/HY compared with the parent NaY.....	62



## LIST OF FIGURES (Continued)

<b>Figure</b>	<b>Page</b>	
5.4	TEM images of reduced 6Co/NaY (A) and reduced 6Co/HY (B)....	63
5.5	The XANES spectrum of Co K-edge of reference standard materials.....	65
5.6	The XANES spectrum of 6Co/NaY after being calcined (•••••), reduced (— — —), and tested on butane hydrogenolysis (——).....	68
5.7	The XANES spectrum of 6Co/HY after being calcined (•••••), reduced (— — —), and tested on butane hydrogenolysis (——).....	69
5.8	Linear combination fit of reduced (A) and spent 6Co/HY (B) compare with standard of CoO, Co <sub>3</sub> O <sub>4</sub> and Co foil.....	70
5.9	Linear combination fit of reduced (A) and spent 6Co/NaY (B) compare with standard of CoO, Co <sub>3</sub> O <sub>4</sub> and CoCl <sub>2</sub> ·6H <sub>2</sub> O.....	73
5.10	Modules of Fourier transform of standard materials (A); Co foil (a), CoO (b), Co <sub>3</sub> O <sub>4</sub> (c), CoCl <sub>2</sub> (d) and samples (B); calcined 6Co/NaY (b), reduced 6Co/NaY(a), reduced 6Co/HY(c), calcined 6Co/HY (d).....	75
5.11	Fourier transforms from experiment (——) and curved fitting results (-----) for catalyst samples.....	76

## LIST OF FIGURES (Continued)

<b>Figure</b>	<b>Page</b>
5.12 Conversion in butane hydrogenolysis on supported Co catalysts at 300°C.....	79
6.1 NH <sub>3</sub> -TPD profile of monometallic xCo/NaY catalysts.....	92
6.2 NH <sub>3</sub> -TPD profile of bimetallic xCo-Pt/NaY catalysts.....	93
6.3 Total acid sites as function of cobalt content of xCo/NaY and xCo-1Pt/NaY .....	95
6.4 The XANES spectrum of Co K-edge of reference standard Materials.....	96
6.5 XANES spectra of reduced xCo/NaY (x = 10 %wt, 6 %wt, and 1 %wt, respectively).....	97
6.6 Linear combination fit of freshly reduced 1Co/NaY compared with reference materials. Note that only observed components were included in the plot.....	99
6.7 Linear combination fit of freshly reduced 6Co/NaY compared with standard reference materials. Note that only observed components were included in the plot.....	100
6.8 Linear combination fit of freshly reduced 10Co/NaY compared with standard reference materials. Note that only observed components were included in the plot.....	101

## LIST OF FIGURES (Continued)

<b>Figure</b>	<b>Page</b>	
6.9	The XANES spectrum of reduced $\text{Co}_x\text{-1Pt/NaY}$ supported on NaY ( $x = 10\ \text{wt}\%$ , $6\ \text{wt}\%$ , and $1\ \text{wt}\%$ , respectively).....	103
6.10	Linear combination fit of freshly reduced $1\text{Co-1Pt/NaY}$ compare with standard reference material. Note that only observed components were included in the plot.....	104
6.11	Linear combination fit of freshly reduced $6\text{Co-1Pt/NaY}$ compare with standard reference material. Note that only observed components were included in the plot.....	105
6.12	Linear combination fit of freshly reduced $10\text{Co-1Pt/NaY}$ compare with standard reference material. Note that only observed components were included in the plot.....	106
6.13	Fourier transforms (top) and $k^3$ -weighted Co K-edge EXAFS function ( $k^3 \cdot \chi(k)$ ) (bottom) of reduced $6\text{Co/NaY}$ : experiment (—) and curved fitting results (-----).....	109
6.14	Fourier transforms (top) and $k^3$ -weighted Co K-edge EXAFS function ( $k^3 \cdot \chi(k)$ ) (bottom) of reduced $10\text{Co/NaY}$ : experiment (—) and curved fitting results (-----).....	110
6.15	Fourier transforms (top) and $k^3$ -weighted Co K-edge EXAFS function ( $k^3 \cdot \chi(k)$ ) (bottom) of reduced $6\text{Co-1Pt/NaY}$ : experiment (—) and curved fitting results (-----).....	111

## LIST OF FIGURES (Continued)

<b>Figure</b>	<b>Page</b>
6.16 Fourier transforms (top) and $k^3$ -weighted Co K-edge EXAFS function ( $k^3 \cdot \chi(k)$ ) (bottom) of reduced 10Co-1Pt/NaY: experiment (—) and curved fitting results (-----).....	112
6.17 The conversion in butane hydrogenolysis of xCo/NaY catalysts at 300°C.....	114
6.18 Schematic of multiple hydrogenolysis reaction from <i>n</i> -butane.....	115
6.19 Conversion in butane hydrogenolysis on 6Co/NaY catalysts at 300°C – 500°C.....	115
6.20 Conversion in butane hydrogenolysis on supported xCo-1Pt/NaY catalysts at 300°C.....	116
6.21 The selectivity in butane hydrogenolysis of 6Co-1Pt/NaY catalysts at 300°C.....	117
6.22 Schematic of single <i>n</i> -butane hydrogenolysis reaction.....	118
6.23 Conversion in butane hydrogenolysis on supported 6Co-1Pt/NaY catalysts at various temperatures from 300°C – 380°C.....	119
6.24 Selectivity in butane hydrogenolysis on supported 6Co-1Pt/NaY catalysts at various temperatures from 300°C – 380°C.....	119
6.25 XANES spectra of spent xCo/NaY (x = 10 %wt, 6 %wt, and 1 %wt, respectively).....	121

## LIST OF FIGURES (Continued)

<b>Figure</b>	<b>Page</b>
6.26	The XANES spectrum of spent xCo-1Pt/NaY supported on NaY (x = 10 %wt, 6 %wt, and 1 %wt, respectively).....
	122
7.1	Reaction pathway of <i>n</i> -hexane isomerization diagram.....
	128
7.2	Schematic diagram for <i>n</i> -hexane isomerization via hydrogen spillover.....
	131
7.3	Diagram of temperature program and condition of catalysts during treatment.....
	133
7.4	Schematic diagram of <i>n</i> -hexane isomerization reactor.....
	135
7.5	XRD spectra of calcined catalysts.....
	136
7.6	(a) Conversions of <i>n</i> -hexane and (b) Selectivities for isomerization over 1Pt/HY and mixed Pt/HY:1Pt/NaY (1:3) at 300°C .....
	139
7.7	Product selectivity on isomer of <i>n</i> -hexane isomerization over 1Pt/HY and mixed 1Pt/HY:1Pt/NaY (1:3) at 300°C and 450°C.....
	140
7.8	Conversions (a) of <i>n</i> -hexane and Selectivities (b) for isomerization over 1Pt/HY and mixed Pt/HY:1Pt/NaY (1:3) at 450 °C .....
	142
7.9	Product selectivity on isomer of <i>n</i> -hexane isomerization over 1Pt/HY and mixed 1Pt/HY:1Pt/NaY at 300°C and 450°C.....
	143
7.10	Propose mechanism pathway of <i>n</i> -hexane isomerization.....
	144

## LIST OF TABLES

<b>Table</b>	<b>Page</b>
2.1 Examples of supported Pt-Co bimetallic catalysts on various supports.....	8
3.1 RHS components determined by XRF.....	22
3.2 Peak positions, d-spacing and relative intensity of NaK-LSX and standard NaX.....	24
3.3 Textural properties of synthesized NaK-LSX zeolite.....	27
3.4 Percentile of NaK-LSX particle size distribution analyzed by DPSA.....	32
4.1 Textural properties of synthesized zeolite Y.....	44
5.1 Surface area of NaY and Co supported on NaY and HY.....	61
5.2 Co K-edge energy position for Co/Y samples with respect to Co Metal Foil (7709 Ev).....	67
5.3 Linear combination fitting of XANES spectra for reduced and spent of Co/NaY and Co/HY catalyst with contributes to standard material.....	71
5.4 Results from the analysis of EXAFS Data of Co/NaY and Co/HY .....	78
6.1 Textural physical properties of samples Co/NaY and Co <sub>x</sub> -1Pt/NaY.....	90
6.2 Maximum desorption temperature and total acid sites from	

## LIST OF TABLES (Continued)

<b>Table</b>	<b>Page</b>
NH <sub>3</sub> -TPD results.....	94
6.3 Percent reduction of cobalt in reduced Co <sub>x</sub> /NaY catalysts from Linear Combination Fitting of XANES spectra and fitting parameters.....	102
6.4 Percent reduction of cobalt in reduced Co <sub>x</sub> -1Pt/NaY catalysts from Linear Combination Fitting of XANES spectra and fitting parameters.....	107
6.4 Results from the analysis of EXAFS data of reduced Co/NaY and Co-Pt/NaY.....	113
7.1 Examples of supported Pt catalysts on various supports.....	129
7.2 The overview of the separation conditions of GC-MS (HP 5890).....	134
7.3 The overview of the separation conditions of GC-FID (HP 6890).....	134
7.4 Experimental result on acidity of noble metal promoted Pt samples.....	137

## LIST OF ABBREVIATIONS

<i>n</i>	=	Normal
wt%	=	Percentage of weight
°C	=	Degree of Celcius
d	=	d spacing
cm <sup>-1</sup>	=	wave number
HK	=	Howath-Kawazoe
BJH	=	Barrett–Joyner–Halenda
LSX	=	Low Silica Type X
FAU	=	Faujasite Zeolite
HY	=	Proton Y
NaY	=	Sodium Y
ICP	=	Inductive Couple Plasma Spectroscopy
XRF	=	X-ray Fluorescence Spectroscopy
XRD	=	X-ray Diffraction
IR	=	Infrared Spectroscopy
BET	=	Brunauer-Emmette-Teller
NH <sub>3</sub> -TPD	=	Ammonia Temperature Programmed Adsorption
EXAFS	=	Extended X-ray Absorption Fine Structure
XAS	=	X-ray Adsorption Spectroscopy
XANES	=	X-ray Absorption Near Edge Structure
RH	=	Rice Husk



**LIST OF ABBREVIATIONS (Continued)**

RHS	=	Rice Husk Silica
Pt	=	Platinum
Co	=	Cobalt
SEM	=	Scanning Electron Microscopy
TEM	=	Transmission Electron Microscopy
DPSA	=	Distribution Particle Size Analyzer
2-MP	=	2-Methylpentanes
3-MP	=	3-Methylpentanes
2,2-DMB	=	2,2-Dimethylbutane
2,3-DMB	=	2,3-Dimethylbutane

# CHAPTER I

## INTRODUCTION

This thesis includes synthesis and characterization of faujasite zeolites (FAU) which are porous material with well-ordered structure and good thermal stability, using rice husk silica (RHS). The FAU zeolites in this work are Linde type Y (Y) and low silica type X (LSX). Details of syntheses and characterization of Y and LSX are in Chapter III and IV, respectively. Because LSX was not stable in an exchange process with ammonium ion to convert to proton form, only Y was used as a catalyst support for catalyst containing cobalt and platinum. In Chapter V, cobalt catalysts supported on Y in both sodium and proton form (Co/NaY and Co/HY respectively) were prepared by impregnation and characterized by various techniques. Their properties before and after reduction by hydrogen were investigated by X-ray absorption (XAS) techniques. Their reducibility and catalytic conversion for butane hydrogenolysis were compared. The Co/NaY was found to be more superior in the catalytic performance and it was modified further by adding platinum to produce a bimetallic catalyst Pt-Co/NaY. The changes in the reducibility of Co/NaY and Pt-Co/NaY catalysts were also investigated by XAS and their catalytic performances for butane hydrogenolysis were compared. In addition, Pt/HY and a mixture of Pt/HY and Pt/NaY were also prepared and tested for n-hexane isomerization. Conditions for each reaction were investigated to determine an optimum condition for each catalyst.

## **1.1 Research objectives**

- 1.1.1 To synthesize and characterize zeolites LSX and Y using rice husk silica.
- 1.1.2 To study the properties of synthesized LSX and Y before utilization as support.
- 1.1.3 To prepare and characterize Co/HY, Co/NaY, Pt-Co/NaY, Pt/NaY, and Pt/HY catalysts by impregnation methods.
- 1.1.4 To study the catalytic performance of supported Co/HY, Co/NaY and Pt-Co/NaY for *n*-butane hydrogenolysis.
- 1.1.5 To understand the effect of parameters such as reducibility of metal catalyst, metal loading and temperature on the hydrogenolysis reaction.
- 1.1.6 To study the catalytic performance of Pt/HY and mixed Pt/HY:PtNaY for *n*-hexane isomerization reaction.
- 1.1.7 To understand the effect of parameters such as acid strength and temperature on the isomerization reaction.

## **1.2 Scope and limitations of the Study**

- 1.2.1 The silica was extracted from rice husk by leaching with 3 M HCl for 6 h and calcinations at 550°C for 6 h.
- 1.2.2 The rice husk silica was used as a silica source for the synthesis of zeolites LSX and Y.
- 1.2.3 Zeolites LSX and Y were characterized by techniques and instruments available mainly at Suranaree University of Technology.

- 1.2.4 Pt, Co and Pt-Co catalysts were prepared by impregnation methods. Precursors were  $\text{H}_2\text{PtCl}_6 \cdot x\text{H}_2\text{O}$  and  $\text{CoCl}_2 \cdot 6\text{H}_2\text{O}$ .
- 1.2.5 The catalysts were characterized by techniques and instruments available at Suranaree University of Technology, Synchrotron Light Research Institute (Public Organization) and University of Oldenburg, Germany.
- 1.2.6 Only cobalt containing catalysts were characterized by XAS because the energy required for platinum edges was not available.
- 1.2.7 The Co/NaY and Pt-Co/NaY catalysts were tested for butane hydrogenolysis in a plug flow reactor at Suranaree University of Technology.
- 1.2.8 The catalytic testing of Pt/HY and Pt/NaY catalysts was studied for *n*-hexane isomerization in a plug flow reactor at University of Oldenburg, Germany.

## **CHAPTER II**

### **LITERATURE REVIEW**

#### **2.1 Background for rice husk silica (RHS)**

Rice husk (RH) is by-product of the rice milling process. The main compositions are lignin, cellulose, and hydrated silica (10 wt% – 20 wt%). Reports have been published on the composition, properties, and intended uses of RH (Williams et al., 2000; Park et al., 2003). One of the potential applications of rice husk is as filler for manufacturing lignocellosic fiber-thermoplastic composites (Park et al., 2003). Such efforts have resulted in minor usage, mostly in low-value applications in agricultural areas or as fuel. Little advantage is taken of the RH and pollution is caused in such disposal processes. However, because of the high silica content in RH, the utilization of RH has been significantly widened in the past few decades. At present, RH are the raw materials for the production of a series of silicon-based materials, including silicon carbide, silica, silicon nitride, silicon tetrachloride, pure silicon, and zeolites (Sun, et al., 2001; Huang et al., 2001).

RH can be directly combusted to produce silica without any pretreatment including vapor-phase reaction, sol-gel and thermal decomposition technique (Kapur, 1985; Huang et al., 2001; Williams et al., 2000). However, there are high impurities such as alkali metal oxides. To improve the silica purity, acids such as HCl, H<sub>2</sub>SO<sub>4</sub>, HNO<sub>3</sub>, and HF have been used as leaching agent in pre-treatment before combustion.

HCl is the most often used because it is effective in substantially removing most of the metallic impurities producing silica with purity 96% – 99% (Chorkendorff et al., 2003; Sun et al., 2001; Prasetyoko et al., 2005; Williams et al., 2000; Liou et al., 2004). In general, acid treatment of RH prior to combustion does not affect the structural nature (amorphicity) of the produced silica. After acid leaching, the silica produced is completely white in color and has high purity suitable to use as a starting material in material synthesis. In this work RHA is raw material for the synthesis of FAU zeolites which are used further as support materials for Pt-Co catalysts.

## 2.2 Zeolite properties

Zeolites are microporous crystalline materials which are attractive to researchers due to their solid acidity, ion-exchange capability, adsorption/release capability, and molecular-level pores. They are usually synthesized under hydrothermal condition from solutions of sodium aluminate, sodium silicate, or sodium hydroxide (Roberie et al., 2001; Cundy et al., 2005). The zeolite structures are based on a three-dimensional arrangement of  $\text{SiO}_4$  or  $\text{AlO}_4^-$  connected through their oxygen atoms to form sub-units and finally large lattices by repeating identical building blocks. Zeolites can be classified into three categories:

- Small pore size with eight membered-ring pore aperture having free diameters of 0.30 nm – 0.45 nm.
- Medium pore zeolites with ten membered-ring pore aperture, 0.45 nm – 0.60 nm in free diameters.
- Large pore zeolites with 12 membered-ring aperture, 0.6 nm – 0.8 nm.

This work focuses on zeolites X and Y of which faujasite framework and the composite building units (CBUs) are double 6-ring consisting of a very large cavity with four 12-ring windows. This cavity is of tetrahedral symmetry known as the supercage. The connectivity of this cage allows molecules to diffuse in three dimensions in the crystal interior (IZA. www, 2000).

Although zeolites X and Y are in the same framework structural type (FAU), they are markedly different in their framework composition and properties. Zeolite X has a Si/Al  $\sim 1.25$  (AlSiO<sub>4</sub>) and belongs to the space group F<sub>d3</sub> while zeolite Y has Si/Al  $\sim 2.3$  and belongs to the space group F<sub>d3m</sub>. Thus, all reactions are confined to the supercages.

Zeolites in this thesis will be synthesized by using RHS and utilized as support materials for Co, Pt and Pt-Co catalysts. Several types of zeolites including MOR, NaX, Beta, ZSM-5, ZSM-48, and FSM-16 have been successfully synthesized from this silica source (Wang et al., 1998; Katsuki et al., 2005; Prasetyoko et al., 2005).

### **2.3 Heterogeneous catalyst background**

Catalyst is a substance that increases the rate of a reaction but is not consumed permanently. They are classified as homogeneous if they are present in the same phase as the reagent and heterogeneous if they are present in a different phase from that of reactant.

Heterogeneous catalysts, mainly solid, compose of metal or metal oxides and a promoter that dispersed on supports materials such as oxides and creates metal particles with high surface area. Metal particles are contacted with oxide support to create small metal particles with large surface area and it must be compatible with the

corresponding metal. Modern catalyst formulations often include “active” metal (e.g. Pt) combined with other less active metals (e.g. Ru, Au) because the incorporation of two different metals might therefore create new materials with different or new redox and acid properties. The second metal can enhance catalyst performance in several ways, such as promote desired reactions, prevent undesirable side reactions, or enhance catalyst longevity (Parvulescu et al., 2004).

### **2.3.1 Supported Co, Pt and Pt-Co catalysts**

Platinum (Pt) is a noble metal that widely used not only in homogeneous but also in heterogeneous catalysis. Supported platinum particles containing a few atoms of Pt can catalyze a wide variety of hydrocarbon conversion reactions involving C-C and C-H activation and are ubiquitous in the petrochemical industries (oil refinery, catalytic cracking, reforming processes fine and chemicals and oxo process), catalytic converters (incorporated in gasoline-fueled automobile exhaust systems) as well as tips of spark plugs for controlling vehicle emissions (three-way and deNO<sub>x</sub>) and in proton exchange membrane in solid-polymer-electrolyte fuel cells (PEM/SPE) (Ichikawa et al., 2000; Kua et al., 1998). In addition, Pt can form bimetallic catalysts by incorporation with other metals such as Co to improve catalytic performances.

Cobalt (Co) is also the effective catalyst in hydrocarbon synthesis especially for the petroleum and chemical industries. Cobalt-modified noble metal catalysts such as the addition Pt to Co greatly improved the activity of CO oxidation and selectivity to alcohol. Therefore, more effective for car exhaust purification (Kwak et al., 2005).

Supported platinum catalysts modified by incorporation of second metal or other dopants have been reported in many applications. More examples of supported



Pt-Co bimetallic catalysts on various supports preparation method and catalyzed reactions are shown in Table 2.1.

**Table 2.1** Examples of supported Pt-Co bimetallic catalysts on various supports

Metals/Support	Methods	Catalyzed reactions	Reference
Pt-Co/NaY	Impregnation	Cyclohexane dehydrogenation	Tetenyi et al., 2002
Pt-Co/Al <sub>2</sub> O <sub>3</sub>		Benzene hydrogenation	
Pt-Co/Kenyaite*	Impregnation	Hydrocarbon combustion	Kalvachev et al., 2006
Pt-Co/NaY	Ion exchange	NO <sub>x</sub> Reduction	Gutierrez et al., 1998

\*Kenyaite = Na<sub>2</sub>Si<sub>22</sub>O<sub>41</sub>(OH)<sub>8</sub> · 6H<sub>2</sub>O

### 2.3.2 Characterization of bimetallic catalyst

Structural characterization of metal catalyst is important in catalysis. Spectroscopy, microscopy, and methods based on adsorption and desorption or bulk reaction are tools to investigate the nature of an active catalyst.

X-ray diffraction (XRD) technique is used to identify the crystalline phases of metal particle and support materials and determine average particles size by using Scherrer formula.

Brunauer-Emmett-Teller (BET) technique is introduced for the characterization of catalysts by measurement the amount of gas adsorbed and desorbed, from BET equation. This instrument can be utilized for making measurements of both surface and the porosity of materials.

Temperature programmed desorption of ammonia ( $\text{NH}_3$ -TPD) technique has proved for investigating adsorption on the solid surface, especially Bronsted-acid. Ammonia is using probe molecule are useful in determining the number and strength of binding sites on a catalyst.

Electron microscopy such as scanning electron microscopy (SEM) and transmission electron microscopy (TEM) is employed in this work to determine the size and shape of supported particles. It can also reveal information on the composition and internal structure of the particles by detecting the characteristic X-rays that are produced by the interaction of electrons with matter.

Infrared spectroscopy (IR) is applied to identify adsorbed species, in which chemisorbed on the catalyst surface. Sometime IR spectra of adsorbed probe molecules such as CO and NO give valuable information on adsorption sites on a catalyst.

However, all techniques above can not determine the nature of metal-metal interaction, coordination number, metal-metal distance and oxidation state. Although information from techniques such as temperature-programmed reduction (TPR) imply whether the two metals are intact or not, it is not quantitative. X-ray crystallography is the method for definitive determination of the structure of new coordination complex but crystalline materials are not easy to obtain (Penner-Hahn, 1999). Techniques that can provide those information are X-ray absorption spectroscopy (XAS), extended X-ray absorption fine structure (EXAFS) and X-ray absorption near edge structure (XANES). The measurement of XAS is relatively straightforward using modern synchrotron X-ray as a light source.

XAS measures the absorption of X-ray as a function of X-ray energy, in which an electron is excited from one energy level to another and finally ejected via the photoelectric effect. The ejected electron is scattered from atoms surrounding the absorbing atom and XAS signal dominantly result from the other two or three closest shells of atomic neighbors surrounding the absorbing atom (Rehr et al., 2000; Verberckmoes et al., 1998). Each core electron has a well-defined binding energy, and when the energy of the incident X-ray is scanned across one of these energies, there is an abrupt increase in the absorption coefficient, so-called absorption edge. XAS is determined pre-, near- and extended-edge, and is therefore commonly subdivided into pre-edge X-ray absorption (PEXA), XANES and EXAFS (Penner-Hahn, 1999). However, the importance of XAS is fine structure superimposed on the adsorption edge which has been applied extensively to the characterization of solid catalysts, particularly highly dispersed metals, metal oxides, and metal sulfides (Odzak et al., 2001). XAS spectrum provides a local structure probe both long-range order and non-crystalline samples or compare solution structure with solid state structure.

EXAFS refers to the oscillatory structure in the X-ray absorption coefficient above the absorption edge or beyond about 50 eV to 1000 eV of threshold. The EXAFS phenomenon is due to the creation of a photoelectron by photon absorption above the ionization threshold and interference effects in the electronic wavefunction, between the outgoing wave from the central atom and the scattered waves from its neighbors. EXAFS data can be analyzed to determine the absorber-scatter distance with accuracy 0.02 Å. This distance are generally characteristic of certain kinds of binds and can often be used to identify the neighboring atoms and provides the

structure surrounding the element of interest. Coordination number can also be determined with accuracy of 25% (Penner-Hahn et al., 1999).

XANES refers to the structure in the spectra within about 30 eV of threshold where scattering is strong and inelastic losses are relatively weak. It can provide formal oxidation state, coordination chemistry (Rehr et al., 2005; Newville, 2004).

### **2.3.3 Catalytic performance of Pt bimetallic catalysts on hydrogenolysis reaction**

As mentioned in section 2.3.1 that Pt particles are active for the reaction of hydrogenolysis, which involves the breaking of a chemical bond in an organic molecule with the simultaneous addition of a hydrogen atom to each of the resulting molecular fragments. Hydrogenolysis reaction has been observed that the nature of support influence the rate of the reactions on catalytically active metal particles. The rate of hydrogenolysis is several orders of magnitude higher when Pt particles are supported on an acidic support compared with on basic support. In addition, inhibition of the hydrogenolysis of alkanes by hydrogen is much stronger for basic supports. Because it involves the formation of metal-proton adducts on Bronsted acidic supports, electron transfer between support and particle (Ji et al., 2005).

The catalytic performances of supported bimetallic catalysts also depend on the state of metal dispersion, structure with shape and morphology of the metal, particle compositions, size and distribution as well as the metal-support interactions (Ichikawa, 2000). The modification of the catalytic behaviors of a noble metal through the addition of a second metal able to form alloy phases or intermetallic compounds with former is an interesting field in heterogeneous catalysis. The bimetallic catalysts showed enhanced selectivity as compared to the monometallic platinum catalyst

(Silvestre-Albero et al., 2005). This thesis proposal is interested in cobalt to incorporate as second metal and focused on butane hydrogenolysis which is catalyzed by Pt bimetallic catalyst. The reaction products are propane, ethane and methane.

## 2.4 References

- Cundy, S. C. and Cox, A. P. (2005). The hydrothermal synthesis of zeolites: Precursors, intermediates and reaction mechanism. **Micropor. Mesopor. Mat.** 82: 1-78.
- Gutierrez, L., Boix, A., and Petunchi, J. O. (1998). Promoting effect of Pt on Co-zeolites upon the SCR of NO<sub>x</sub>. **J. Catal.** 179: 179-191.
- Huang, S., Jing, S., Wang, J., Wang, Z. and Jin, Y. (2001). White silica obtained from rice husk in fluidized propellant bed. **Powder Technol.** 117: 232-238.
- Ichikawa, M. (2000). Ship-in-Bottle catalyst technology novel templating fabrication of platinum group metals nanoparticles and wires in micro/mesopores. **Platinum Metal. Rev.** 44: 3-14.
- IZA. (2000). Database of Zeolite Structures [On-line] Available: <http://www.iza-structure.org/databases>
- Ji, Y., Eerden, A. M-J., Koot, V., Kooyman, P. J., Meeldijk, J. D., Weckhuysen, B. M. Koningsberger, D. C. (2005). Influence of support ionicity on the hydrogen chemisorption of Pt particles dispersed in Y zeolite: consequences for Pt particle size determination using the H/M method. **J. Catal.** 234: 376-384.
- Kalvachev, Y., Kostov-Kytin, V., Todorova, S., Tenchev, K., and Kadinov, G. (2006). Synthetic kenyaite as catalyst support for hydrocarbon combustion. **Appl. Catal. B-Environ.** 66: 192-197.

- Kapur, P. C. (1985). Production of reactive bio-silica from the combustion of rice husk in a tube-in-basket (TiB) burner. **Powder Technol.** 44: 63-67.
- Katsuki, H., Furuta, S., Watari, T., and Komarneni, S. (2005). ZSM-5 zeolites/porous carbon composite: Conventional-and microwave-hydrothermal synthesis from carbonized rice husk. **Micropor. Mesopor. Mat.** 86: 145-151.
- Kua, J., and Goddard, W. A. (1998). Chemisorption of Organics on Platinum 2. Chemisorption of  $C_2H_x$  and  $CH_x$  on Pt (111). **J. Phys. Chem. B.** (102): 9492-9500.
- Kwak C., Park, T.-J., and Suh, D. J. (2005). Effects of sodium addition on the performance of PtCo/ $Al_2O_3$  catalysts for preferential oxidation of carbon monoxide from hydrogen-rich fuels. **Appl. Catal. A- Gen.** 278: 181-186.
- Liou, T.-H. (2004). Preparation and characterization of nano-structured silica from rice husk. **Mater. Sci. Eng.** 364: 313-323.
- Newville, M. (2004). Fundamentals of XAFS. (1.6 rev. ed.).
- Odzak, J. F., Argo, A. M., Lai, F. S., Gates, B. C., Pandya, K., and Feraria, L. (2001). A flow-through X-ray absorption spectroscopy cell for characterization of powder catalysts in the working state. **Rev. Sci. Instrum.** 72: 20-30.
- Park, B. D. (2003). Characterization of anatomical features and silica distribution in rice husk using microscopic and micro-analytical techniques. **Biomass Bioenerg.** 25: 319-327.
- Prasetyoko, D., Ramli, Z., Endud, S., Hamdan, H., and Sulikowski, B. (2006). Conversion of rice husk ash to zeolite beta. **Waste Manage.** 26: 1,173-1,179.

- Parvulescu, V., Anastasescu C., and Su, B. L. (2004). Bimetallic Ru-(Cr, Ni, or Cu) and La-(Co or Mn) incorporated MCM-41 molecular sieves as catalysts for oxidation of aromatic hydrocarbons. **J. Mol. Catal. A-Chem.** 211: 142-148.
- Penner-Hahn, J. E. (1999). X-ray adsorption spectroscopy in coordination chemistry. **Coordin. Chem. Rev.** 190-192: 1101-1123.
- Rehr, J. J., and Albers, R. C. (2000). Theoretical approaches to x-ray absorption fine structure. **Rev. Mod. Phy.** 72: 621-654.
- Rehr, J. J., Aankudinov A. (2005). Progress in theory and interpretation of XANES. **Coordin. Chem. Rev.** 249: 131-140.
- Roberie, T. G., Hildebrandt, D., Creighton, J., and Gilson, J.-P. (2001). Preparation of Zeolite Catalysts. In M. Guisnet, J.-P. Golson (eds.). **Zeolites for Clean Technology**. Catalytic science series (Vol. 3, p 57-63). London: Imperial College Press.
- Silvestre-Albero, J., Serrano-Ruiz, J.C., Sepulveda-Escribano, A., and Guez-Reinoso, F. R. (2005) Modification of the catalytic behaviour of platinum by zinc in crotonaldehyde hydrogenation and iso-butane dehydrogenation. **Appl. Catal. A-Gen.** 292: 244–251.
- Sun, L., and Gong, K. (2001). Silicon-Based Material from rice husks and their applications, **Ind. Eng. Chem. Res.** 40: 5861-5877.
- Telenyi, P., and Galsan, V. (2002). Hydro-dehydrogenation of six-member hydrocarbon cycles on supported platinum-cobalt bimetallic catalysts, **Appl. Catal. A- Gen.** 229: 181-192.

- Verberckmoes, A. A., Weckhuysen, B. M., and Schoonheydt, R. A. (1998). Spectroscopy and coordination chemistry of cobalt in molecular sieves. **Micropor. Mesopor. Mat.** 22: 165-178.
- Wang, H., Lin, P. K. S., Huang, Y. J., Li, M. C., and Tsaur, L. K. (1998). Synthesis of zeolite ZSM-48 from rice husk ash. **J. Hazard. Mater.** 58: 147-152.
- Williams, P. T., and Nugranad N. (2000). **Energy.** 25: 493 -513.



# CHAPTER III

## SYNTHESIS AND CHARACTERIZATION OF ZEOLITE LSX FROM RICE HUSK SILICA

### **Abstract**

Silica powder with approximately 98% purity was extracted from rice husk (RH), converted to a sodium silicate solution, and used as a silica source for the synthesis of low silica type X (LSX) by hydrothermal process. The synthesized zeolite in the form of Na and K cations, referred to as NaK-LSX, was characterized by X-ray diffraction (XRD) and Fourier transform infrared spectroscopy (FT-IR), which confirmed the success of the synthesis. Images from scanning electron microscopy (SEM) of NaK-LSX displayed multi-faceted spherulite particles composed of polycrystal particles with different sizes along with small amorphous particles. The particle size distribution of NaK-LSX from a laser diffraction particle size analyzer (DPSA) was in the range of 0.2  $\mu\text{m}$  – 50  $\mu\text{m}$  and nitrogen adsorption indicated a surface area around 400  $\text{m}^2/\text{g}$ . The structure of LSX did not change after the ion-exchange to produce an ammonium form but collapsed after subsequent calcination.

### 3.1 Introduction

The composition of rice husks varies with geological location. Mainly it contains organic substance and approximately 20 wt% of silica ( $\text{SiO}_2$ ) and after combustion the white ash contains approximately over 90 wt% of  $\text{SiO}_2$  (Williams and Nugranad, 2000; Park, 2003; Hamdan et al., 1997; Kapur, 1985; Huang et al., 2001). There are impurities in rice husk ash such as oxides of alkali metal which could be removed by leaching rice husk with acids before calcination; such a method could improve the purity of rice husk silica (RHS) to 96 wt% – 99 wt%. (Williams and Nugranad, 2000; Sun and Gong, 2001; Chorkendorff et al., 2003; Liou, 2004; Prasetyoko et al., 2006). With high purity, RHS has potential as a silica source for the production of silicon-based inorganic materials such as silicon carbide ( $\text{SiC}$ ); silicon nitride ( $\text{SiN}$ ); mesoporous silica including MCM-41 and MCM-48; and zeolites (Wang et al., 1998; Huang et al., 2001; Sun and Gong, 2001; Grisdanurak et al., 2003, Mohamed, 2004; Katsuki et al, 2005; Prasetyoko et al., 2005). This study focuses on using RHS as a silica source for the synthesis of low silica zeolite type X (LSX).

Zeolites are microporous crystalline aluminosilicates in which the structural framework contains tetrahedral  $\text{TO}_4$  units ( $\text{T} = \text{Si}$  or  $\text{Al}$ ) linked together by oxygen sharing (Corma, 2001). The general formula of zeolite is  $\text{M}_a^{n+}[\text{Si}_x\text{Al}_y\text{O}_z] \cdot m\text{H}_2\text{O}$  where  $\text{M}_a^{n+}$  are extra-framework cations;  $[\text{Si}_x\text{Al}_y\text{O}_z]$  is the zeolite framework; and  $m\text{H}_2\text{O}$  are sorbed water molecules (Roberie et al., 2001). Zeolites are related to several industrial applications, for example they are catalysts in fluid cracking, sorbents in volatile organic removal (Cundy et al., 2005), a solid-state hydrogen storage medium (Langmi et al., 2005; Li and Yang, 2006), and an internal side space for synthesis of transition-metal encapsulation (Salavati-Niasari et al., 2006).

Zeolite LSX is in the faujasite (FAU) family with a framework containing double 6 rings linked through sodalite cages that generate supercages with pore diameters of 7.4 Å. The typical Si/Al ratio of LSX is in the range of 1 – 1.5. It belongs to the space group  $F_{3m}$  (Auerbach et al., 2003) and has a large number of extra-framework cations. LSX can be synthesized from a variety of silica sources including natural clay such as kaolinite, oil shale ash, and commercial silicates (Chandrasekhar and Pramada, 2001a, 2002b; Machado and Miotto, 2005). There are no reports on the synthesis of LSX with a silica source from rice husk.

Here we report the synthesis of zeolite LSX with the formula  $Na_{73}K_{22}[Si_{97}Al_{95}O_{384}] \cdot 212H_2O$  (Esposito et al., 2004) by using RHS as a silica source and characterization by X-ray diffraction (XRD), Fourier transform infrared spectroscopy (FTIR), surface area analysis, scanning electron microscopy (SEM), and laser diffraction particle size analyzer (DPSA). Its stability after ion exchange to ammonium and proton forms (NH<sub>4</sub>-LSX and H-LSX, respectively) was studied by thermogravimetric analysis (TGA).

## 3.2 Experimental

### 3.2.1 Materials for RHS extraction and zeolite synthesis

Hydrochloric acid (37.0% HCl, Carlo-Erba), sodium silicate solution (Na<sub>2</sub>SiO<sub>3</sub>; 28.7% SiO<sub>2</sub>, 8.9% Na<sub>2</sub>O, Panreac, N Brand clarified), sodium aluminate (~ 55.0% – 56.0% of NaAlO<sub>2</sub>, Riedel-de Haën), sodium hydroxide (97.0% NaOH, Carlo-Erba), potassium hydroxide (85.0% KOH; Ajax Fine Chem), ammonium nitrate (99.0% NH<sub>4</sub>NO<sub>3</sub>, J. T. Baker), and rice husk for RHS (local rice mill in Lampang, Thailand).

### 3.2.2 Silica extraction from rice husk

Rice husk was washed thoroughly with water to remove the adhering soil and dust and dried at 100°C overnight. The dried rice husk then was refluxed in 3 M HCl solution for 6 h, filtered and washed repeatedly with water until the filtrate was neutral and dried in an oven at 100°C overnight. Finally, the refluxed rice husk was pyrolyzed in a hot air furnace muffle (Carbolite, CWF1200) at 550°C for 3 h to remove the organic contents to obtain the white RHS.

### 3.2.3 Synthesis of zeolite LSX

The LSX synthesis was synthesized by hydrothermal method with an initial batch composition of  $5.5\text{Na}_2\text{O} : 1.65\text{K}_2\text{O} : 1\text{Al}_2\text{O}_3 : 2.2\text{SiO}_2 : 122\text{H}_2\text{O}$  prepared from sodium silicate and sodium aluminate solution with a method modified from that described by Kühl (2001). The sodium silicate solution was prepared by slowly adding RHS into 100 mL of 14 wt% NaOH solution under stirring until a homogeneous solution was obtained. In the LSX synthetic procedure, sodium aluminate was dissolved in deionized water and slowly added into a solution containing KOH and NaOH. The new solution was mixed with diluted sodium silicate solution. The resulting mixture was transferred into a polypropylene bottle, capped and sealed with paraffin film. Aging and crystallization were carried out at 70°C for 3 h without stirring, then adjusted to 100°C for 2 h to complete crystallization; the sample was cooled down to room temperature and washed with water and 0.01 N NaOH solution, and dried at 110°C – 125°C overnight. The obtained product was zeolite LSX in the form of Na and K cations and was designated as NaK-LSX throughout this article.

### 3.2.4 Characterization of RHS and NaK-LSX

The chemical compositions of RHS in the form of oxides were analyzed by energy dispersive XRF (EDS Oxford Instrument ED 2000) with an array of 16 anodes analyzing crystals and Rh X-ray tube as a target with a vacuum medium.

Phase and crystallinity of RHS and NaK-LSX were confirmed by powder XRD (Bruker AXS diffractometer D5005) with nickel filter Cu K<sub>α</sub> radiation scanning from 4° – 50° at a rate of 0.05 °/s with current 35 kV and 35 mA.

Functional groups within the NaK-LSX structure were identified by FT-IR (Spectrum GX, Perkin-Elmer) using KBr as a medium. IR spectra were scanned in the range of 400 cm<sup>-1</sup> – 4,000 cm<sup>-1</sup> with a resolution of 4 cm<sup>-1</sup>.

The specific surface area, pore volumes, and pore sizes of NaK-LSX were determined from a nitrogen adsorption isotherm by a Quantachrome (NOVA 1200e) gas adsorption analyzer at liquid nitrogen temperature. The sample was degassed at 300°C for 3 h before the measurement.

Crystallite size and morphology of NaK-LSX were studied by SEM (JEOL JSM-6400) with applied potential 10 kV – 20 kV.

Particle size distribution of NaK-LSX was determined by DPSA (Malvern Instruments, Mastersizer 2000) with the sample dispersed in distilled water and analyzed by He-Ne laser. The standard volume percentiles at 10, 50, and 90, or denoted as d(0.1), d(0.5), and d(0.9), respectively, were recorded from the analysis and used to calculate the width of the distribution. The width was calculated from the equation below:

$$\frac{d(0.9) - d(0.1)}{d(0.5)} \quad (1)$$

Finally, NaK-LSX was exchanged to NH<sub>4</sub>-LSX by stirring in 1.2M NH<sub>4</sub>NO<sub>3</sub> for 18 h. After filtration and drying, the obtained NH<sub>4</sub>-LSX product was calcined at 400°C to convert to H-LSX. Thermal stabilities of NH<sub>4</sub>-LSX were investigated by TGA on a Simultaneous Differential Thermal Analysis (SDT 2690) by heating from room temperature to 1000°C with a heating rate of 10°C/min in nitrogen flow (100 ml/min). The phases of both materials were also analyzed by XRD.

### **3.3 Results and discussion**

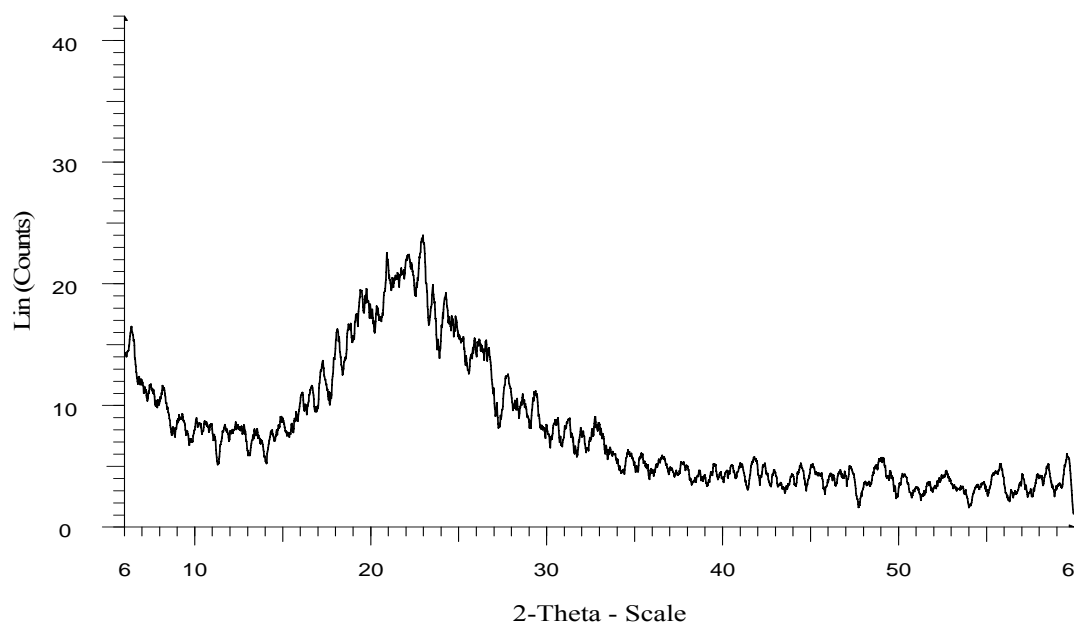
#### **3.3.1 RHS characterization**

The chemical compositions of RHS in the form of oxides are shown in Table 3.1. The major component was SiO<sub>2</sub> along with small amounts of Al<sub>2</sub>O<sub>3</sub>, K<sub>2</sub>O, CaO and Fe<sub>2</sub>O<sub>3</sub>. The purity of RHS was sufficient to use as a silica source for the synthesis of NaK-LSX. The purity from this study was higher than that of rice husk ash (RHA) obtained from combustion without leaching which was less than 95% (Kapur, 1985; Williams and Nugranad, 2000; Huang et al., 2001; Liou, 2004). However, that silica from RHA was still suitable for the synthesis of several porous materials such as MCM-41, zeolite beta, zeolite ZSM-5 and zeolite Y (Sun and Gong, 2001; Gridanurak et al., 2003; Khemthong and Wittayakun, 2006a, 2006b; Prasetyoko et al., 2006).

**Table 3.1** Chemical component of RHS determined by XRF

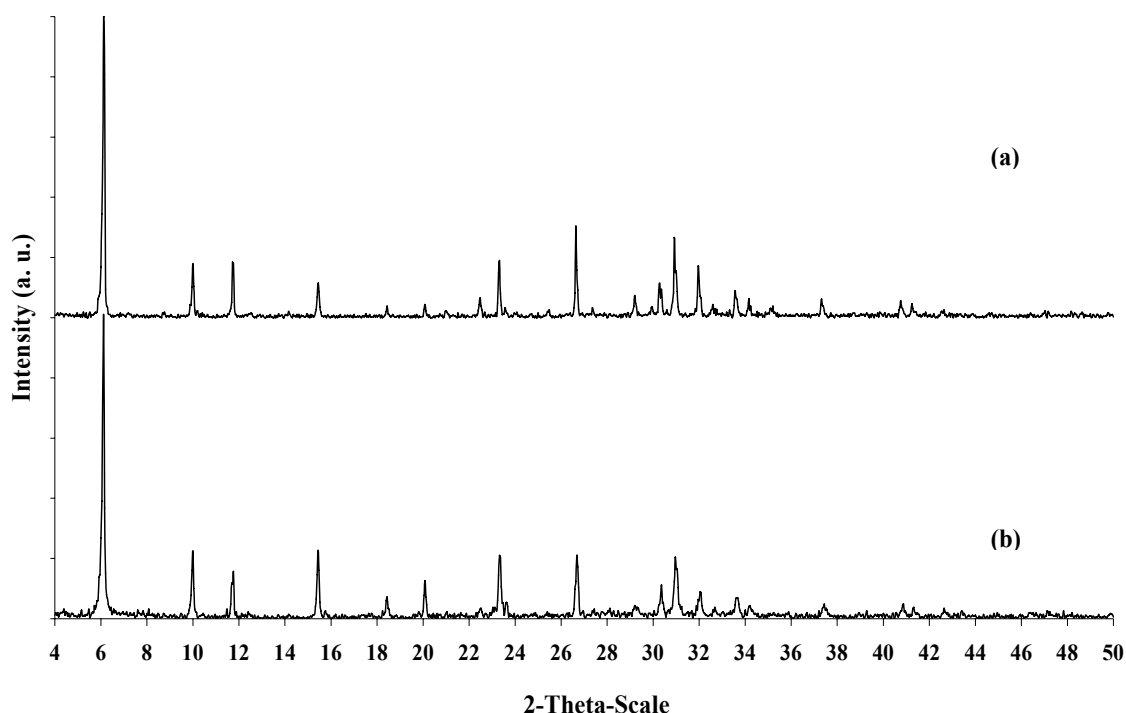
Components	(%wt.)
SiO <sub>2</sub>	97.96
Al <sub>2</sub> O <sub>3</sub>	00.56
K <sub>2</sub> O	00.06
CaO	00.98
Fe <sub>2</sub> O <sub>3</sub>	00.02

The powder XRD pattern of RHS is shown in Figure 3.1. Only a broad peak at approximately 22 degrees which was a characteristic of amorphous silica was observed. This phase was more suitable for the NaK-LSX synthesis than the crystalline form because it could be dissolved to form sodium silicate more easily. A longer time would be needed in the synthesis with crystalline silica (Hamdan et al., 1997).

**Figure 3.1** Powder XRD patterns of RHS

### 3.3.2 Characterization of NaK-LSX by XRD

The formation of the NaK-LSX framework synthesized from RHS was confirmed by XRD comparing with standard NaX (Figure 3.2).



**Figure 3.2** XRD spectrum of (a) NaK-LSX synthesized from RHS and (b) standard NaX

The sample gave peaks at positions similar to that of the standard NaX, indicating the formation of a faujasite structure, and the sharp peaks indicated high crystallinity. The relative crystallinity to the standard NaX was calculated in the equation below (Gosh et al., 1994; Tangkawanit and Rangsriwatananon, 2004) and the obtained value was approximately 100%.

$$\% \text{ Crystallinity} = \left( \frac{\sum^{12} \text{intensity of XRD peak of product}}{\sum^{12} \text{intensity of XRD peak of standard zeolite NaX}} \right) \times 100$$



The details of peak positions, d-spacing and relative intensity of NaK-LSX and standard NaX are presented in Table 3.2.

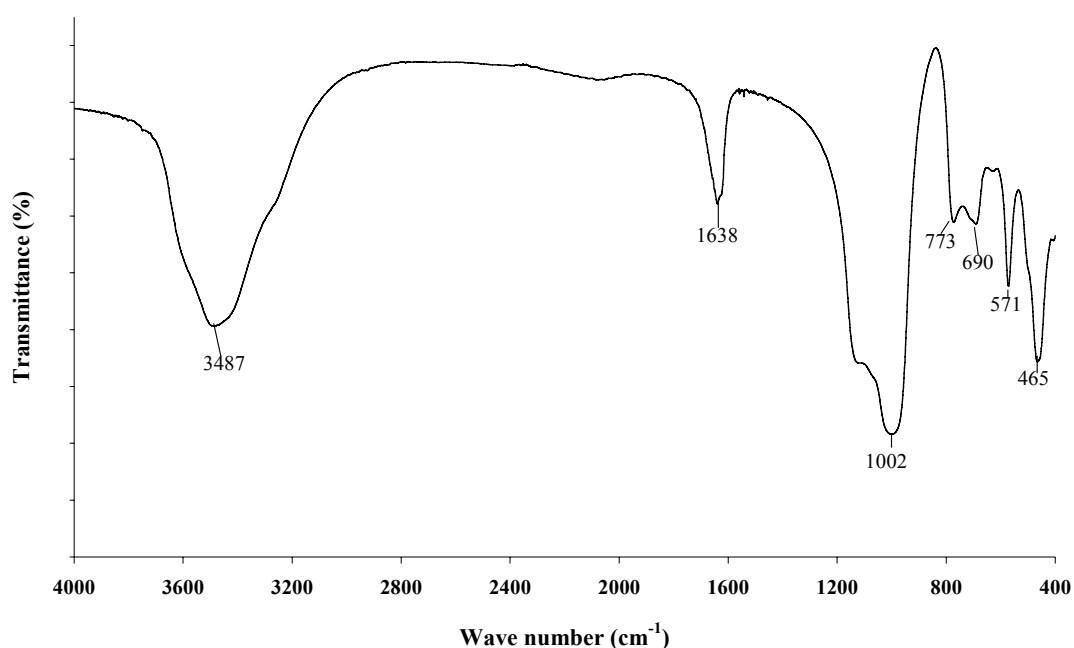
**Table 3.2** Peak positions, d-spacing and relative intensity of NaK-LSX and standard NaX

$2\theta$	d	Relative intensities	
		Standard NaX	Synthesized LSX
6.10	14.48	100.00	100.00
15.43	5.74	22.70	13.10
9.99	8.85	22.40	17.30
26.70	3.34	22.10	29.40
23.32	3.81	21.00	20.00
30.10	2.88	20.40	26.20
11.73	7.54	16.40	17.80
20.09	4.42	12.60	6.90
30.36	2.94	11.21	13.10
32.03	2.79	8.62	17.30
18.43	4.81	7.18	4.20
34.24	2.62	4.89	6.20

Although all the XRD peaks of NaK-LSX were similar to those of the standard NaX, the sequence of intensities were different. This was not surprising because our sample contains both Na and K cations, while the standard only has the Na cation. It was previously reported that the sequence of peak intensities depended strongly on type of cations (Joshi et al., 2002; Esposito et al., 2004) and the presence of  $K^+$  attenuates them. Moreover, the lower Si/Al ratio enhances the line intensities (Kühl, 1987).

### 3.3.3 Characterization of NaK-LSX by FTIR

The synthesized NaK-LSX was characterized by FTIR to identify functional groups in the structure. Figure 3.3 shows a strong peak at  $1002\text{ cm}^{-1}$  which was assigned to an asymmetric T–O stretching.



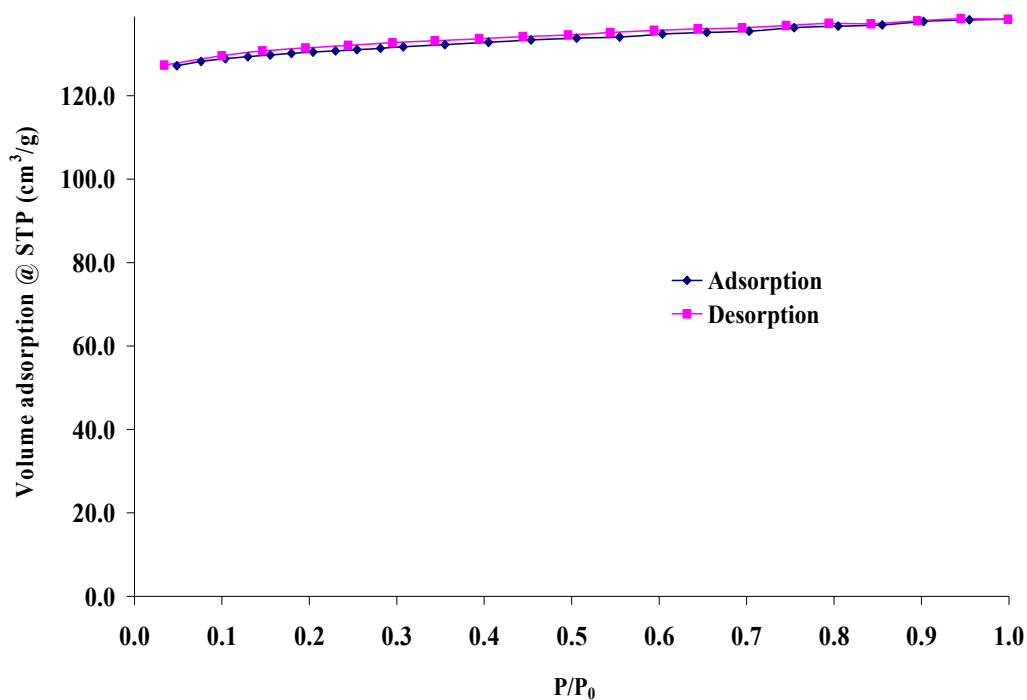
**Figure 3.3** Spectrum of IR analysis of NaK-LSX zeolite from RHS

In general, T–O is a tetrahedral atom referred to the framework of Si, Al composition and may shift to a lower frequency with an increase of the number of tetrahedral Al atoms (Lee et al., 2006). Bands in the region  $773\text{ cm}^{-1}$ ,  $690\text{ cm}^{-1}$  and  $571\text{ cm}^{-1} - 460\text{ cm}^{-1}$  were attributed mainly to the symmetric stretching, double ring and T–O bending vibrations, respectively. Lee (2006) and Sang et al. (2006) reported that a band at  $600\text{ cm}^{-1} - 500\text{ cm}^{-1}$  is related to the topological arrangement of secondary units of structure in zeolites that contain the double 4 and 6 rings external linkage peak

associated with the FAU structure and also observed in all the zeolite structures. The band with a peak at  $3,487\text{ cm}^{-1}$  was assigned to OH stretching and the vibration at  $1,638\text{ cm}^{-1}$  was referred to bending vibration of adsorbed water molecule (Dyer et al., 2004).

### **3.3.4 Surface area analysis of NaK-LSX by N<sub>2</sub> adsorption-desorption isotherm**

The N<sub>2</sub> adsorption isotherm of NaK-LSX is shown in Figure 3.4. It was type I based on IUPAC's classification with a large nitrogen uptake at low pressure and the desorption isotherm almost overlapping with the adsorption isotherm. The step increased in N<sub>2</sub> adsorption with an increased relative pressure,  $P/P_0$  and N<sub>2</sub> adsorbed amount reaching  $127\text{ cm}^3/\text{g}$  at  $P/P_0 = 0.048$  suggesting the presence of an appreciable amount of micropore on the NaK-LSX surface. This result was common for the zeolite structure as explained by Langmi (2005) that zeolite X has a very open framework and the entries to internal pores are not restricted by a large cation. Moreover, the effect of a cation on the surface area and pore structure show that the ion-exchange processes could induce enormous changes in surface and pore structure and these ions inhibited the movement of nitrogen molecule into pores or the so-called pore blocking effect, resulting in the decrease in surface area (Langmi et al., 2003; Rakoczy and Traa, 2003; Huang et al., 2004). Table 3.3 shows results from a nitrogen adsorption study including the BET surface areas, and average pore diameters of NaK-LSX.



**Figure 3.4** N<sub>2</sub> adsorption-desorption isotherm at N<sub>2</sub> temperature on the synthesized NaK-LSX

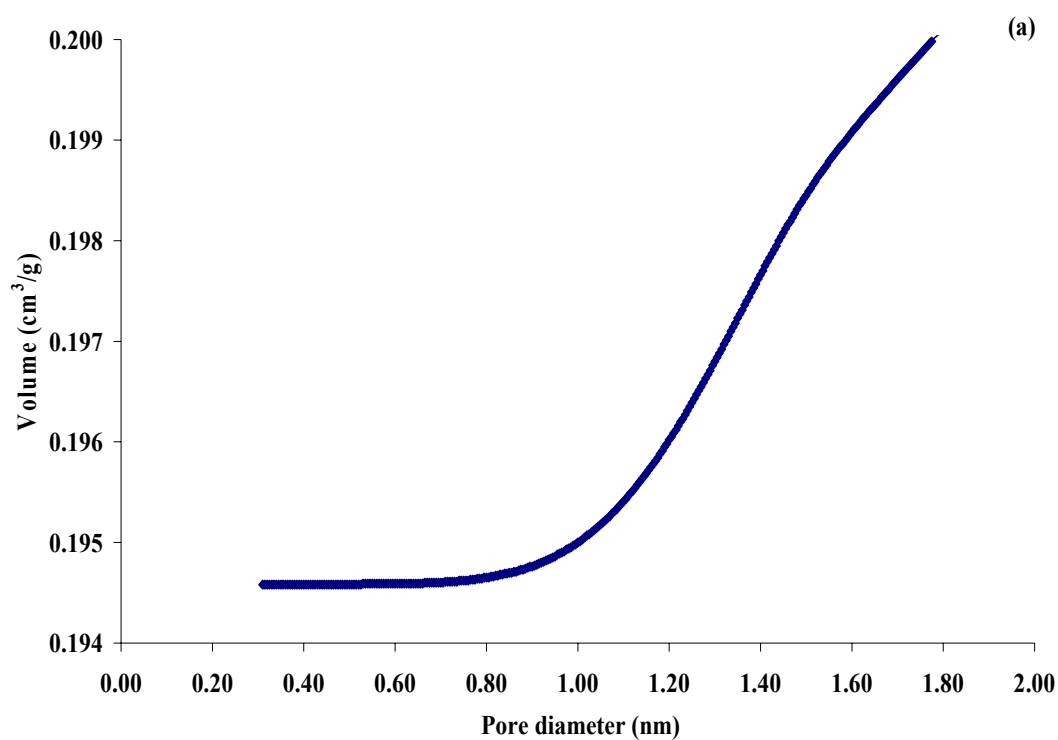
**Table 3.3** Textural properties of synthesized NaK-LSX zeolite

Textual Properties	Value	Unit
BET surface area <sup>a</sup>	391.4	(m <sup>2</sup> /g)
Micropore diameter <sup>b</sup>	13.58	(nm)

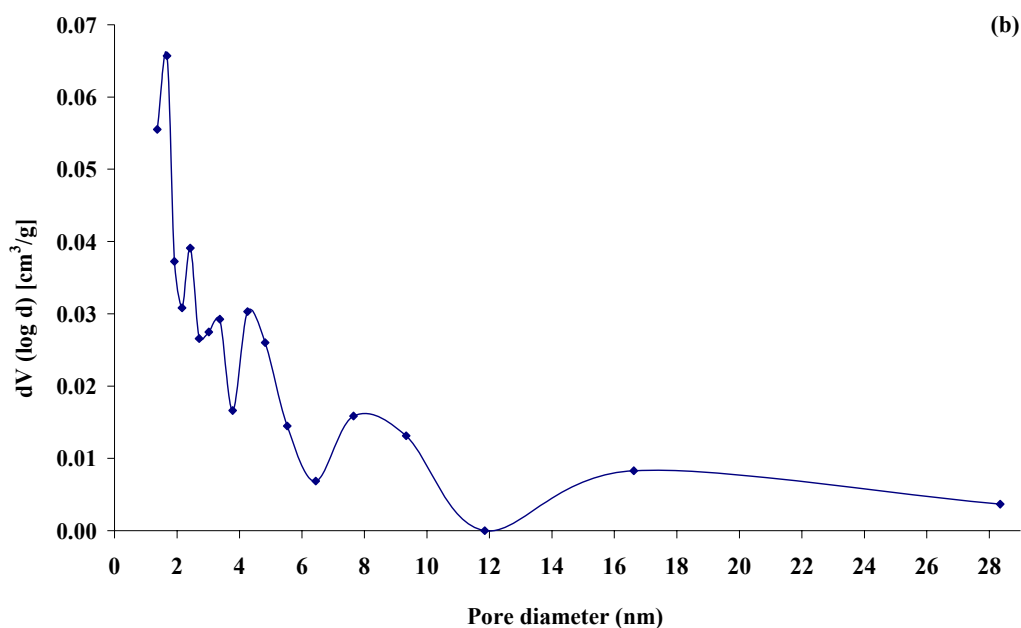
<sup>a</sup>Multipoint BET analysis, <sup>b</sup>DA method

The BET surface area and pore volume of NaK-LSX form RHS was interesting as it supported material for catalysis preparation or other application. (Langmi et al., 2005). Figure 3.5 shows cumulative pore volume and pore size distributions of NaK-LSX from N<sub>2</sub> adsorption. The pore diameter of NaK-LSX, shown in Figure 3.5(a), was calculated by the HK method and showed a narrow pore width between 0.3 nm – 1.9

nm with pore volume of  $0.195 \text{ cm}^3/\text{g} - 0.201 \text{ cm}^3/\text{g}$  (Chang, 2006 and Lee, 2006). Nevertheless, the curves of pore size distribution evaluated from desorption data by utilizing the BJH model shown in Figure 3.5(b) exhibited a narrow pore size distribution ranging from 1.3 nm – 30.0 nm with the highest pore size at 1.7 nm. However, a shoulder peak distribution is dominant. Chang (2006) and Lee (2006) discussed that cause from the more interconnected surface pore of LSX.



**Figure 3.5** HK cumulative pore volume (a) and BJH pore size distribution (b) of NaK-LSX zeolite, where  $V$  is the cumulative pore volume ( $\text{cm}^3/\text{g}$ )

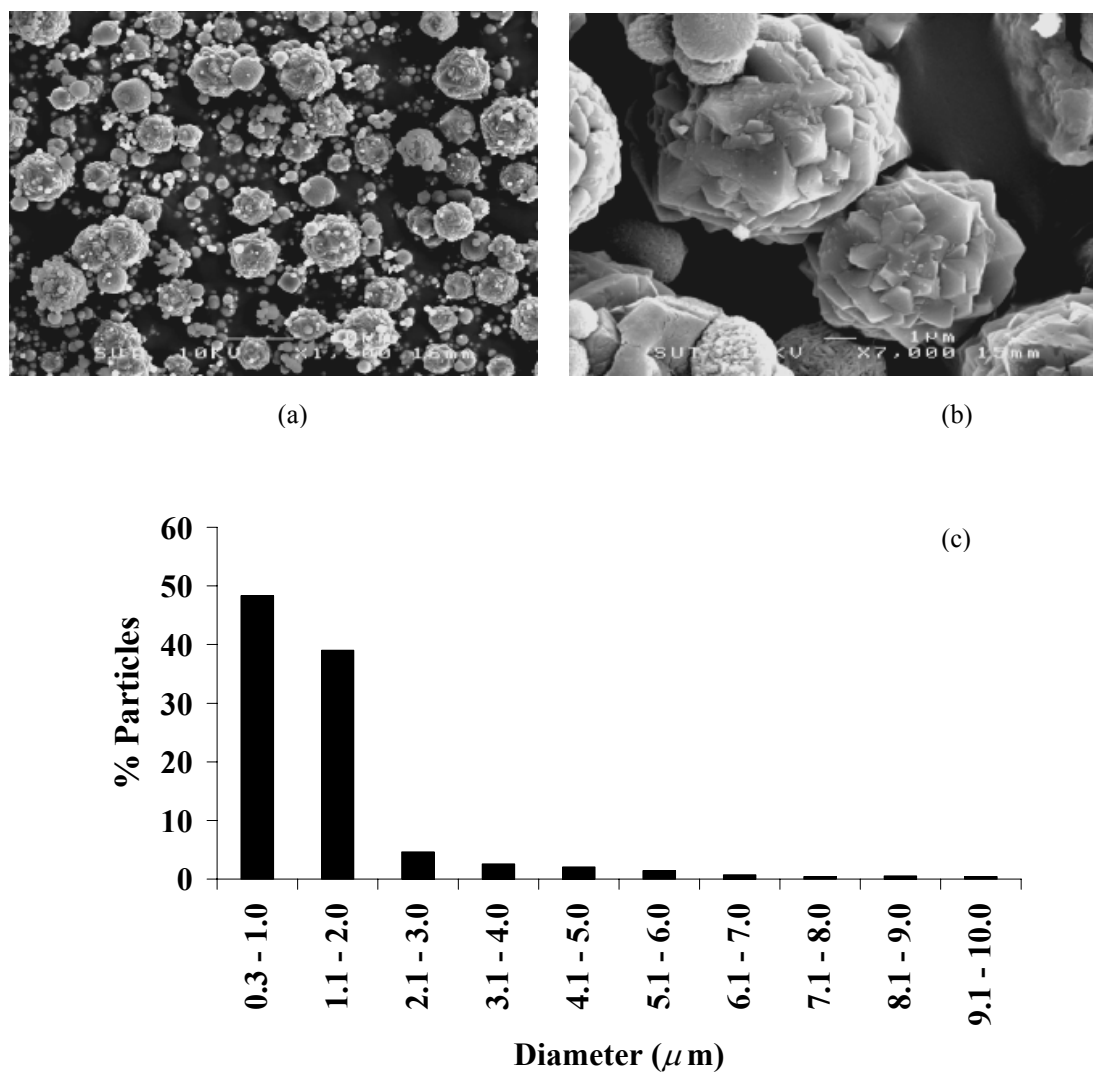


**Figure 3.5** (continued) HK cumulative pore volume (a) and BJH pore size distribution (b) of NaK-LSX zeolite, where  $V$  is the cumulative pore volume ( $\text{cm}^3/\text{g}$ )

### 3.3.5 Morphology of NaK-LSX studied by SEM

Shape and size of NaK-LSX particles synthesized from RHS were studied by SEM and images are displayed in Figure 3.6 with magnification of 1,500 (a) and 25,000 (b). In the image with the smaller magnification, the solid product contained a mixture of multi-faceted spherulite crystals with a particle diameter approximately  $6 \mu\text{m} - 10 \mu\text{m}$  along with round amorphous particles with a particle diameter approximately  $0.2 \mu\text{m} - 5.0 \mu\text{m}$ . The multi-faceted spherulite particles were composed of polycrystal particles with different sizes along with small particles. Because some particles apparently connected with other particles, (Figure 3.5a), the particle size distribution was expected to be large as it was confirmed by DPSA. The particles in

Figure 3.6(a) were distributed in the range of  $0.3\ \mu\text{m} - 10\ \mu\text{m}$  with the largest contribution in the  $0.3\ \mu\text{m} - 2.0\ \mu\text{m}$  range.



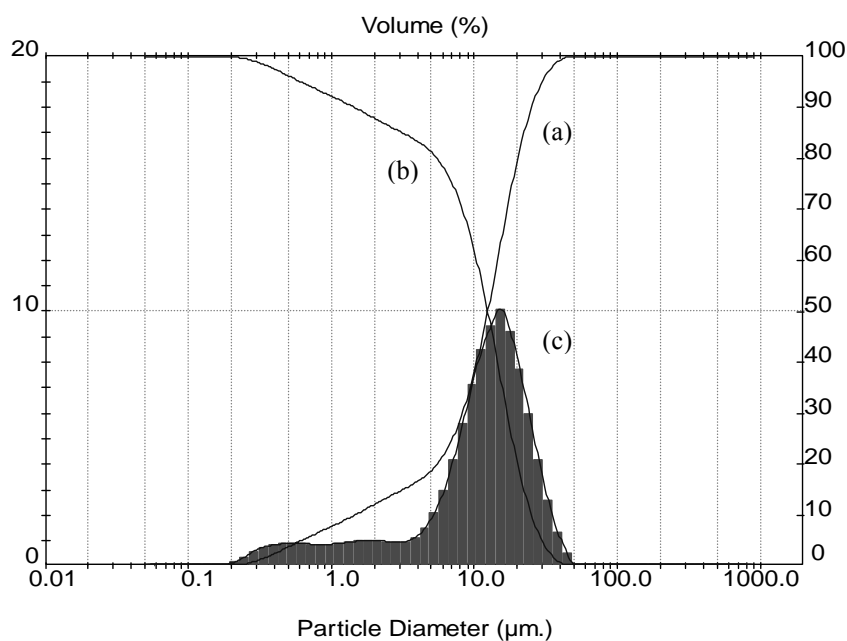
**Figure 3.6** SEM images of synthesized Na-LSX with magnification of (a) 1,500 and (b) 25,000, respectively, and (c) particle size distribution measured from all particles in (a)

### 3.3.6 Particle size distribution of NaK-LSX by DPSA

The particle size distribution of Na-LSX was also investigated with DPSA and the results are presented as a histogram in Figure 3.7. The sizes were classified as oversize (area a), undersize (area b), and the histogram plot and frequency curves (c). The histogram plot shows the percentage of volume of particles, and the height of the histogram bars (left hand scale) was at  $15.0\ \mu\text{m} - 17.5\ \mu\text{m}$  as for the majority of particles. The peak frequency curve provided the apparent tail in particle size analysis and shows the dominantly single modal distributions at  $5\ \mu\text{m} - 50\ \mu\text{m}$ . Note that the results from DPSA were the size and distribution of bulk particles which might be composed of several small particles clustered together, and thus were different from the results from SEM which displayed images of isolate particles. Because the shape of samples as seen in SEM varied from a spherical shape to multi-faceted spherulite, that caused a different light scattering or diffraction effect based on the angularity of the crystals and their hydrodynamic behavior suspension (Cundy and Cox, 2005).

Only the important part of the DPSA data was summarized in Table 3.4 because there were too many numbers in the full data. The particle size distribution of NaK-LSX at volume percentiles of 10 was above  $1.43\ \mu\text{m}$ , while that of 50 was  $12.35\ \mu\text{m}$  and that of 90 was below  $24\ \mu\text{m}$ . The large particle size distribution of zeolite X was common as Lee et al. (2006) reported that uniformly sized NaX was difficult to synthesize in a large single phase crystal because crystal nuclei grew rapidly during the crystallization period and might transfer into zeolite NaP which was a more stable phase.





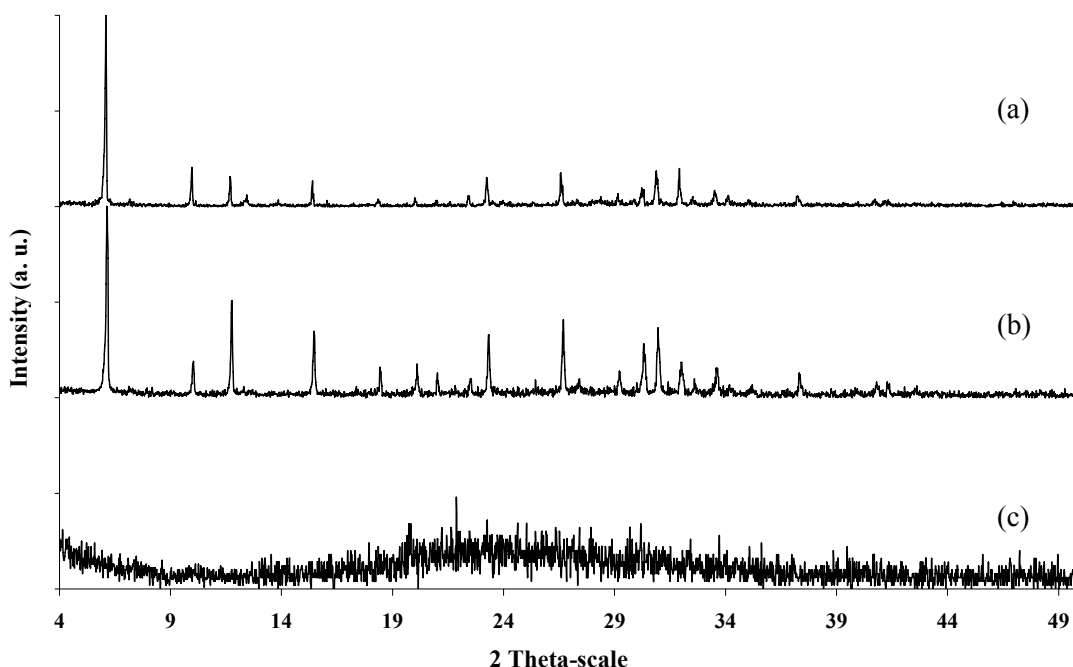
**Figure 3.7** Particle size distribution of NaK-LSX synthesized from RHS; (a) percentage of sample below a certain size of particle, (b) percentage of sample above a certain size of particle and (c) histogram plot and frequency curve of particle

**Table 3.4** Percentile of NaK-LSX particle size distribution analyzed by DPSA

Statistic distribution of particle	Result (% volume)	Unit
d(0.1)	1.43	( $\mu\text{m}$ )
d(0.5)	12.35	( $\mu\text{m}$ )
d(0.9)	25.05	( $\mu\text{m}$ )
Average diameter	13.23	( $\mu\text{m}$ )
Span (width of distribution)	1.91	( $\mu\text{m}$ )

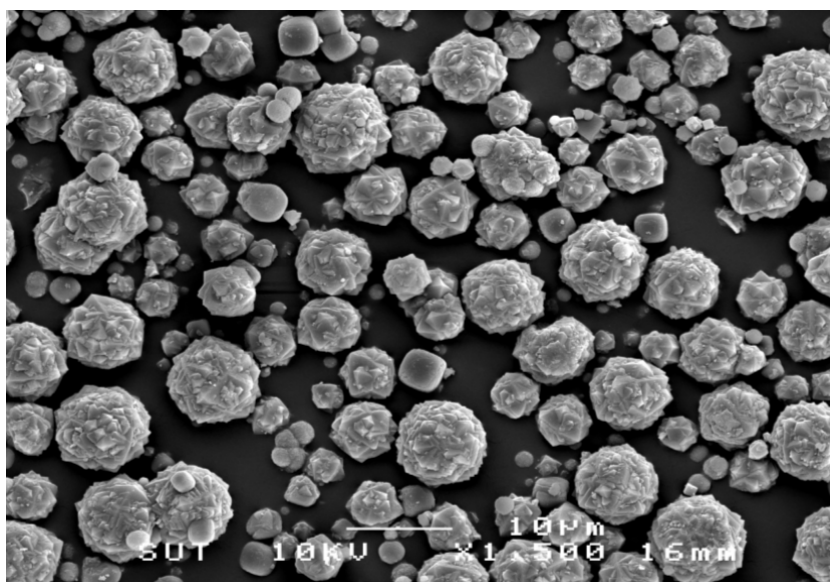
### 3.3.7 Characterization and thermal stability of $\text{NH}_4\text{-LSX}$ from ion exchange of NaK-LSX

LSX in ammonium form ( $\text{NH}_4\text{-LSX}$ ) was prepared by ion exchange of NaK-LSX with a  $\text{NH}_4\text{NO}_3$  solution and characterized by powder XRD. As shown in Figure 3.8(b), the resulting material still had all peaks positioned similarly to that of the standard NaX. The sequence of intensities was different from the standard NaX because of the difference in cation type as discussed earlier. The  $\text{NH}_4\text{-LSX}$  was also studied by SEM and the micrograph is displayed in Figure 3.9. Compared with the NaK-LSX in Figure 3.6(a), the exchanged zeolite contained more crystalline particles and the amorphous particles might be removed with a basic solution during the exchange and wash process.



**Figure 3.8** XRD patterns of (a) Na-LSX (b)  $\text{NH}_4\text{-LSX}$ , and (c) calcined  $\text{NH}_4\text{-LSX}$

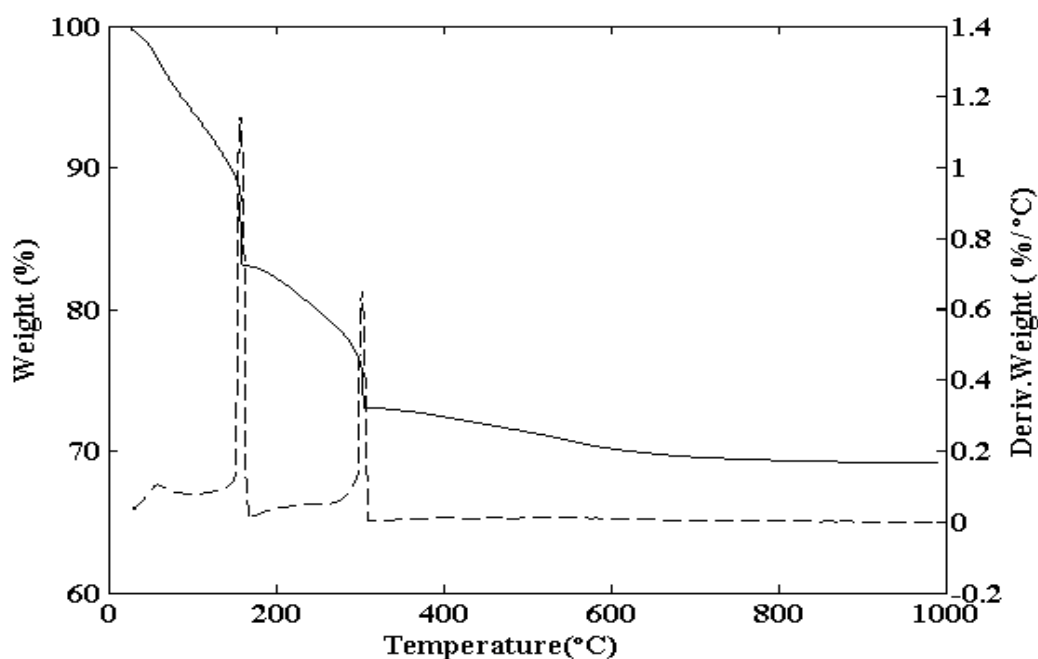
In general, zeolite in proton form can be obtained by calcination of ammonium form which releases ammonia. Thus,  $\text{NH}_4\text{-LSX}$  was calcined at  $400^\circ\text{C}$  for 3 h and the resulting material was characterized by XRD. As shown in Figure 3.8 (spectrum c), the characteristic peaks of zeolite X were no longer observed indicating the collapse of the  $\text{NH}_4\text{-LSX}$  structure to an amorphous form upon calcination. From this result, we investigated the thermal stability of  $\text{NH}_4\text{-LSX}$  by thermal analysis.



**Figure 3.9** SEM micrographs of  $\text{NH}_4\text{-LSX}$  with magnification of 1500

The thermal stability of  $\text{NH}_4\text{-LSX}$  was studied by thermal analysis. The results in Figure 3.10 demonstrated weight loss of  $\text{NH}_4\text{-LSX}$  when the temperature was raised from room temperature to  $1000^\circ\text{C}$ , along with the first derivative of weight loss. When  $\text{NH}_4\text{LSX}$  was heated, there were three ranges of weight loss. The first range, with approximately 17 wt% loss below  $200^\circ\text{C}$ , was attributed to removal of adsorbed water (Chandrasekhar and Pramada, 2001; Joshi et al., 2002; Huang et al., 2004). The second

region with approximately 10 wt% loss between 200°C and 300°C, was caused by the decomposition of  $\text{NH}_4^+$  ion to ammonia and proton (Chandrasekhar and Pramada, 2001). The last region was a relatively small loss compared with the other two regions from 300°C – 650°C, possibly caused by loss of the structural hydroxyl group. No further weight loss was observed at a higher temperature. In general at the temperature range of 900°C – 1018°C, zeolite will be converted to mullite and glass phases (Chandrasekhar and Pramada, 2001; Esposito et al., 2004).



**Figure 3.10** Thermogram of zeolite  $\text{NH}_4\text{LSX}$  (solid line is weight and dash line is first derivative of weight with respect to temperature)

### 3.4 Conclusions

RHS in amorphous phase with 98% purity was prepared by leaching rice husk with HCl acid and calcination, and used as a silica source for the synthesis of zeolite NaK-LSX. The formation of the zeolite structure was confirmed by XRD and FTIR. The NaK-LSX crystal morphology was multi-faceted spherulite particles as shown by SEM micrographs. The particle size distribution from DPSA shows a large scale in crystal size and size distribution. The BET surface area of the NaK-LSX was approximately 400 m<sup>2</sup>/g. The ion-exchange with ammonium ions gives NH<sub>4</sub>-LSX and the zeolite structure was still maintained after ion exchange. However, the structure collapsed after convert to proton form.

### 3.5 References

- Auerbach, M. S., Carrado, A. K. and Dutta, P. K. (2003). **Handbook of Zeolite Science and Technology**. 1<sup>st</sup> ed. Marcel Dekker Inc., NY, (1p.)
- Chandrasekhar, S. and Pramada, N. P. (2001). Sintering behavior of ammonium exchanged low silica zeolites synthesized by two different routes. **Ceram. Int.** 27: 351-361.
- Chandrasekhar, S. and Pramada, N. P. (2002). Thermal study of low silica zeolites and their magnesium exchanged forms. **Ceram. Int.** 28: 177-186 .
- Corma A. (2001). Zeolites as catalysts. In: **Fine Chemicals Through Heterogeneous Catalysis**. Sheldon R. A., and Bekkum, H. (eds.). Wiley-VCH, Weinheim (80p.)

- Cundy, S. C. and Cox, A. P. (2005). The hydrothermal synthesis of zeolites: Precursors, intermediates and reaction mechanism. **Micropor. Mesopor. Mat.** 82(1-2): 1-78.
- Dyer, A., Tangkawanit, S. and Rangsiwatananon, K. (2004). Exchange diffusion of  $\text{Cu}^{2+}$ ,  $\text{Ni}^{2+}$ ,  $\text{Pb}^{2+}$ , and  $\text{Zn}^{2+}$  into analcime synthesized from perlite. **Micropor. Mesopor. Mat.** 75: 273–279.
- Esposito, S., Ferone, C., Pansini, M., Bonaccorsi, L. and Proverbio, E. (2004). A comparative study of the thermal transformations of Ba-exchanged zeolites A, X and LSX. **J. Eur. Ceram. Soc.** 24: 2,689-2,697.
- Grisdanurak, N., Chiarakorn, S. and Wittayakun, J. (2003). Utilization of mesoporous molecular sieves synthesized from natural source rice husk silica to chlorinated volatile organic compounds (CVOCs) adsorption. **Korean J. Chem. Eng.** 20: 950-955.
- Huang, C. F., Lee, F. J., Lee, K. C. and Chao, P. H. (2004). Effects of cation exchange on the pore and surface structure and adsorption characteristics of montmorillonite. **Colloid. Surface. A.** 239: 41-47.
- Huang, S., Jing, S., Wang, J., Wang, Z. and Jin, Y. (2001). White silica obtained from rice husk in fluidized propellant bed. **Powder Technol.** 117: 232-238.
- Joshi, U.D., Joshi, P. N., Tamhankar, S. S., Joshi, V. P., Idagec, B. B. Joshid, V. V. and Shiralkar, P. V. (2002). Influence of the size of extraframework monovalent cations in X-type zeolite on their thermal behavior. **Thermochim. Acta.** 387: 121-130.
- Kapur, C. P. (1985). Production of reactive bio-silica from the combustion of rice husk in a tube-in-basket (TiB) burner. **Powder Technol.** 44: 63-67.

- Katsuki, H., Furuta, S., Watari, T. and Komarneni, S. (2005). ZSM-5 zeolites/porous carbon composite: Conventional-and microwave-hydrothermal synthesis from carbonized rice husk. **Micropor. Mesopor. Mat.** 86: 145-151.
- Khemthong, P., and Wittayakun, J., (2006a). Synthesis and characterization of Na-LSX and NaY zeolites from rice husk silica. In **The Regional Symposium on Chemical Engineering, Proceeding and Abstracts** (p32). Singapore.
- Khemthong, P., and Wittayakun, J., (2006b). Synthesis and characterization of Zeolites Y from rice husk silica. In **The 32<sup>nd</sup> Congress on Science and Technology of Thailand, Proceeding and Abstracts** (p163). Thailand.
- Kühl, G. (2001). Low Silica Type X. In: **Verified Syntheses of Zeolitic Materials**. 2<sup>nd</sup> ed. Robson, H. (ed.). Elsevier Science B. V., Amsterdam, p. 153-154.
- Li, Y., and Yang, T. R. (2006). Hydrogen storage in low silica type X zeolites. **J. Phys. Chem. B.** 110: 17,175-17,181.
- Liou, H. T. (2004). Preparation and Characterization of nano-structured silica from rice husk. **Mat. Sci. Eng. A.** 364: 313-323.
- Park, B. D. (2003). Characterization of anatomical features and silica distribution in rice husk using microscopic and micro-analytical techniques. **Biomass Bioenerg.** 25: 319-327.
- Prasetyoko, D., Ramli, Z., Endud, S., Hamdan, H., and Sulikowski, B. (2006). Conversion of rice husk ash to zeolite beta. **Waste Manage.** 26: 1,173-1,179.
- Rakoczy, A. R., and Traa, Y. (2003). Nanocrystalline zeolite A: synthesis, ion exchange and dealumination. **Micropor. Mesopor. Mat.** 60: 69-78.
- Roberie, G. T., Hildebrandt, D., Creighton, J., and Gilson, J.-P. (2001). Preparation of Zeolite Catalysts. In: **Zeolites for Cleaner Technologies**. Guisnet, M., and

- Golson, J.-P. (eds). Catalytic Science Series. Imperial College Press, London.  
(3): 57-63.
- Sang, S., Liu, Z., Tian, P., Liu, Z., Qu, L., and Zhang, Y. (2006). Synthesis of small crystals zeolite NaY. **Mater. Lett.** 60: 1,131-1,133.
- Sun, L., and Gong, K. (2001). Silicon-based material from rice husks and their applications. **Ind. Eng. Chem. Res.** 40: 5,861-5,877.
- Tangkawanit, S., and Rangsiwatananon, K. (2004). Synthesis and kinetic study of zeolite from Lopburi perlite. **Suranaree J. Sci. Technol.** 12: 61-68
- Wang, H., Lin, K. S. P., Huang, J. Y., Li, C. M., and Tsaun, K. L. (1998). Synthesis of zeolite ZSM-48 from rice husk ash. **J. Hazard. Mater.** 58: 147-152.
- Williams, T. P., and Nugranad N. (2000). Comparison of products from the pyrolysis and catalytic pyrolysis of rice husks. **Energy.** 25: 493-513.



# CHAPTER IV

## SYNTHESIS AND CHARACTERIZATION OF ZEOLITE

### NaY FROM RICE HUSK SILICA

#### **Abstract**

Rice husk silica (RHS) in amorphous phase with 98% purity was prepared from rice husk, solid waste from rice milling, by leaching with hydrochloric acid and calcination. The RHS was used effectively as silica source for the synthesis of zeolite Y in sodium form (NaY). The zeolite in pure phase was obtained from two-step synthetic route in which starting gels were mixed, aged for 24 h at room temperature and crystallized for 24 h at 90°C. The NaY crystals were octahedral with twinned and overgrowth polycrystals. The diameter of single crystal particle from scanning electron microscope was approximately 0.6  $\mu\text{m}$  – 1.0  $\mu\text{m}$  whereas the average diameter from laser diffraction particle size analyzer were approximately 10  $\mu\text{m}$  as small crystals apparently agglomerated to form larger particles. When the crystallization time was longer than 24 h, NaY slowly transformed to zeolite NaP.

## 4.1 Introduction

Rice husk which is often considered as solid waste from rice milling contains approximately 70% of organic compounds and 30% of hydrate silica (Park, 2003; Williams, and Nugranad, 2000). In general, rice husk can be used as cheap source for energy by combustion or other purposes as low value materials. However, its value could be improved by extracting the silica content and use in the production of silicon-based inorganic materials. When rice husk is leached with mineral acid and calcined in air, white powder containing silica in high purity referred to as rice husk silica (RHS) is obtained. The RHS is a silica source for the production of inorganic materials containing silicon such as silicon carbide and silicon nitride (Huang, 2000; Auerbach, 2003). In a research field related to catalysis, RHS is used as silica source for the synthesis of mesoporous silica such as MCM-41 and MCM-48; and microporous materials such as zeolites (Katsuki, 2005; Prasetyoko, 2006; Sun, 2001; Wang, 1998). In this work, RHS was successfully used as silica source for the synthesis of zeolite Linde type Y in sodium form (NaY).

Zeolites are microporous crystalline aluminosilicates composed of tetrahedral  $\text{TO}_4$  units ( $T = \text{Si}$  or  $\text{Al}$ ) linked together by sharing oxygen atoms. General formula of zeolites is  $\text{M}_a^{n+}[\text{Si}_x\text{Al}_y\text{O}_z] \cdot m\text{H}_2\text{O}$  where  $\text{M}^{n+}$  is extra-framework cation;  $[\text{Si}_x\text{Al}_y\text{O}_z]$  is zeolite framework; and  $m\text{H}_2\text{O}$  is water molecules in sorbed phase (Roberie, 2001). Zeolites are interested by several researchers because they have properties that can be related to various applications such as solid acidity, ion-exchange capability, adsorption/release capability, and molecular-level pores. Zeolite NaY, the main focus in this work, is in faujasite (FAU) family with a framework containing double 6 rings linked through sodalite-cages generating supercages with average pore diameter of 7.4

Á. There are several applications of FAU zeolites such as fluid cracking catalysts and sorbents in volatile organic removal (Cundy, 2005).

The goal of this research was to use RHS as silica source in the synthesis of NaY with the formula  $\text{Na}_{56}[\text{Al}_{56}\text{Si}_{136}\text{O}_{384}]\cdot 250\text{H}_2\text{O}$ . Two different synthetic routes, one-step and two-step, and crystallization time were investigated. The NaY products were characterized by X-ray diffraction (XRD), scanning electron microscopy (SEM), laser diffraction particle size analyzer (DPSA) and surface area analysis (BET).

## 4.2 Experimental

### 4.2.1 Synthesis of zeolite NaY

Rice husk was refluxed as described in chapter 3. The zeolite NaY was synthesized from a seed gel and feedstock gel with a procedure modified from that described elsewhere (Ginter, 2001). The major difference between seed gel and feedstock gel is that the feedstock gel is used immediately after preparation without aging. Briefly, the seed gel was prepared with an initial batch with molar ratio  $10.67\text{Na}_2\text{O}:\text{Al}_2\text{O}_3:10\text{SiO}_2:180\text{H}_2\text{O}$ . NaOH was dissolved in deionized water followed by an addition of  $\text{NaAlO}_2$  with continuous stirring. Then  $\text{Na}_2\text{SiO}_3$  solution was added to the previous solution and stirred until homogeneous. The mixture was transferred into a polypropylene (PP) bottle, capped, and aged at room temperature for 24 h.

The feedstock gel with molar ratio  $4.30\text{Na}_2\text{O}:\text{Al}_2\text{O}_3:10\text{SiO}_2:180\text{H}_2\text{O}$  was freshly prepared before the synthesis of NaY. Briefly, NaOH was dissolved in deionized water followed by an addition of  $\text{NaAlO}_2$  with continuous stirring. The  $\text{Na}_2\text{SiO}_3$  solution was added and the mixture was stirred until homogeneous.

The NaY synthesis was carried out by slow addition of the seed gel into the feedstock gel under stirring. The mixture was transferred into a PP bottle, capped, and crystallized at 90°C. This study compared two synthetic routes for NaY. The first route was “one-step” synthesis in which the mixture of seed gel and feedstock gel was mixed and taken directly to crystallization at 90°C for 24 h. The second route was a “two-step” synthesis in which the seed gel and the feedstock gel were mixed and aged at room temperature for 24 h and crystallized at 90°C at various time (22 h – 72 h). After the crystallization was complete, the sample was cooled down to room temperature and NaY was separated by filtration and washed with distilled water thoroughly and dried at 110°C.

#### **4.2.2 Characterization of NaY zeolite**

The specific surface areas of NaY were determined by Quantachrome (NOVA 1200e) gas adsorption analyzer and nitrogen adsorption isotherms were obtained at liquid nitrogen temperature. The sample was degassed at 300°C for 3 h before the measurement.

Phase and crystallinity of NaY were confirmed by powder XRD (Bruker AXS diffractometer D5005) with nickel filter Cu K<sub>α</sub> radiation scanning from 4° – 50° at a rate of 0.05 °/s with current 35 kV and 35 mA. The intensity of peak at 22.5° was chosen for the crystallinity comparison. Morphology of NaY was studied by SEM (JEOL JSM-6400) with applied potential 10 kV. Particle size distribution was determined by DPSA (Malvern Instruments, Mastersizer 2000) with sample dispersed in distilled water and analyzed by He-Ne laser. The standard volume percentiles at 10, 50, and 90% or denoted as d(0.1), d(0.5), and d(0.9), respectively, were recorded from

the analysis and used to calculate the width of the distribution. The width was calculated from the equation 1 in chapter III.

## 4.3 Results and discussion

### 4.3.1 Textural properties

Table 4.1 lists the BET surface areas, pore volumes ( $V_p$ ), and average pore diameters ( $D_p$ ) of zeolite Y with different synthesis routes and crystallization times. The BET surface areas and pore volumes of two-step route show higher surface area than one-step route. However, in case of two-step route; the higher surface area was found at crystallization time 24 h and then was dramatically reduced with increasing crystallization time.

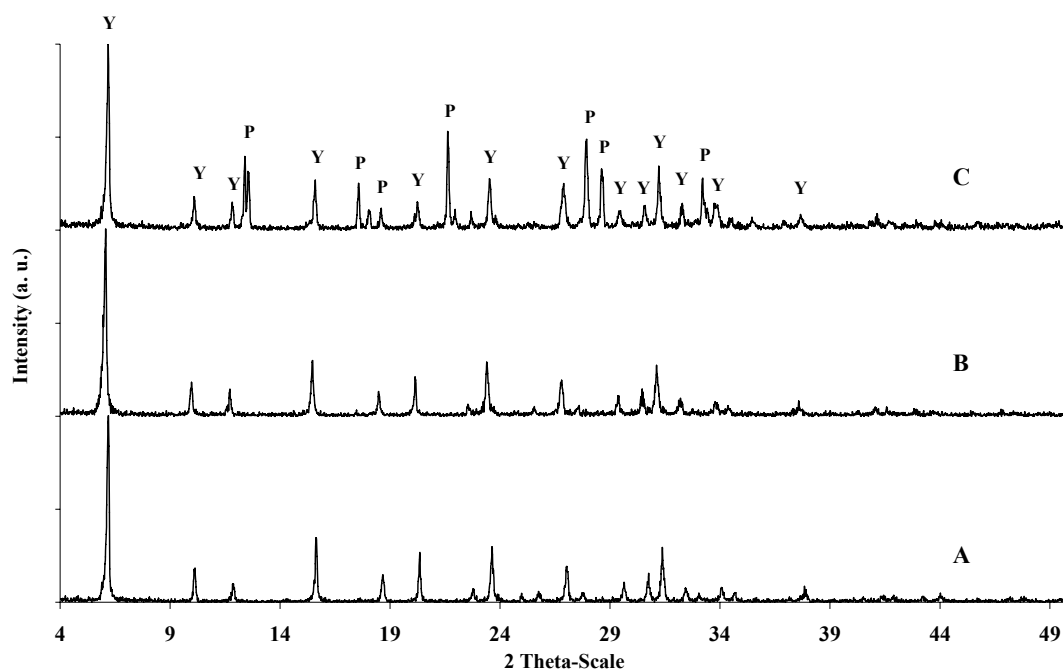
**Table 4.1** Textural properties of synthesized zeolite Y

Sample	BET area ( $m^2/g$ )	$V_p$ ( $cm^3/g$ )	$D_p$ (nm)
One-step	382.10	0.194	2.693
Two-step			
22 h	440.10	0.220	2.565
24 h	625.10	0.320	2.547
48 h	12.71	0.002	2.593
76 h	31.13	0.006	3.820

### 4.3.2 Comparison between one-step and two-step routes

In this work, two synthetic routes for NaY synthesis were compared, namely, one-step and two-step. The products from both routes were characterized by XRD

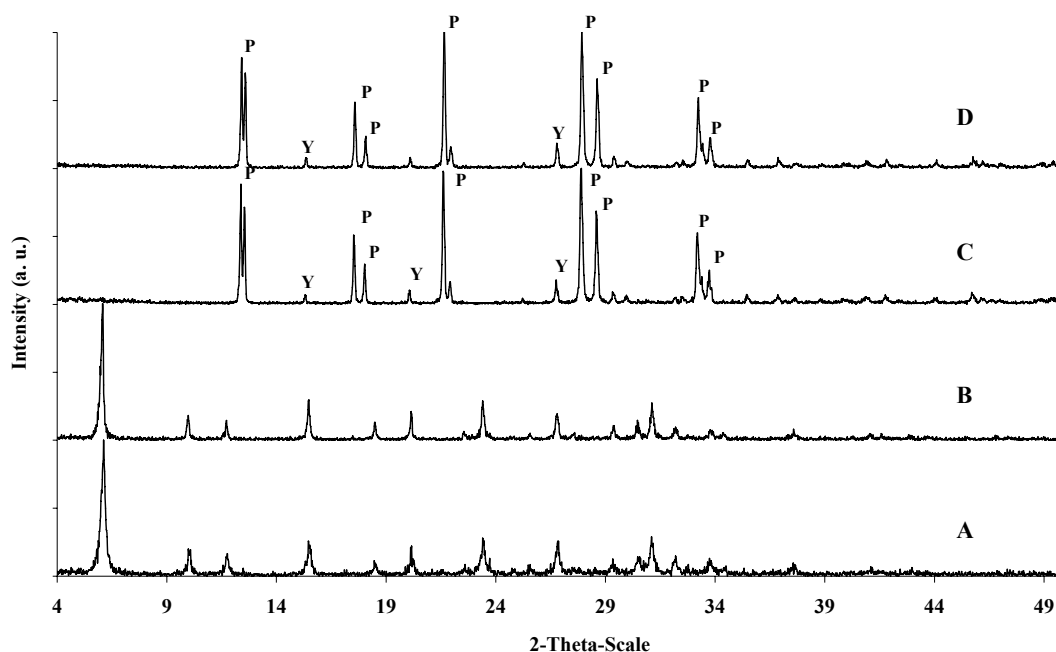
comparing with the pattern of standard NaY. As shown in Figure 4.1, two-step route gave XRD pattern which is characteristic of NaY and all peaks were similar to the standard NaY. Thus, the product from two-step route contained NaY in pure phase. In contrast, the product from one-step route gave XRD peaks which were characteristic of both NaY and NaP. From this observation, aging time was required for NaY synthesis from RHS and the suitable way for the synthesis was two-step route. It was also reported that aging time is essential for synthesis of NaY (with Si/Al ratio 1.8) from kaolin (Chandrasekhar and Pramada, 2004). The less aging time resulted in the formation of NaP.



**Figure 4.1** XRD spectra of NaY from one-step and two-step synthesis (A) standard Y zeolite, (B) two-step, (C) one-step; (Y = NaY and P = NaP)

### 4.3.3 Crystallization time in two-step route

In the synthesis of NaY by two-step route, the crystallization time was varied from 22 h – 72 h and the results were displayed in Figure 4.2. In standard method (Ginter, 2001), the crystallization time was recommended to be 22 h with no more than 2 additional hours. Thus, we carried out crystallization at both 22 h and 24 h. Product obtained from crystallization from both periods displayed only spectrum characterizing NaY. XRD peaks from 22 h (Figure 4.2, spectrum A) had lower intensities and broader than that from 24 h (Figure 4.2, spectrum B). The conclusion drawn from this study was that the optimum crystallization time for the synthesis of zeolite NaY with RHS was 24 h.



**Figure 4.2** XRD spectra of NaY from two-step synthesis crystallized at (A) 22 h, (B) 24 h, (C) 48 h, and (D) 72 h ; (Y = NaY and P = NaP)

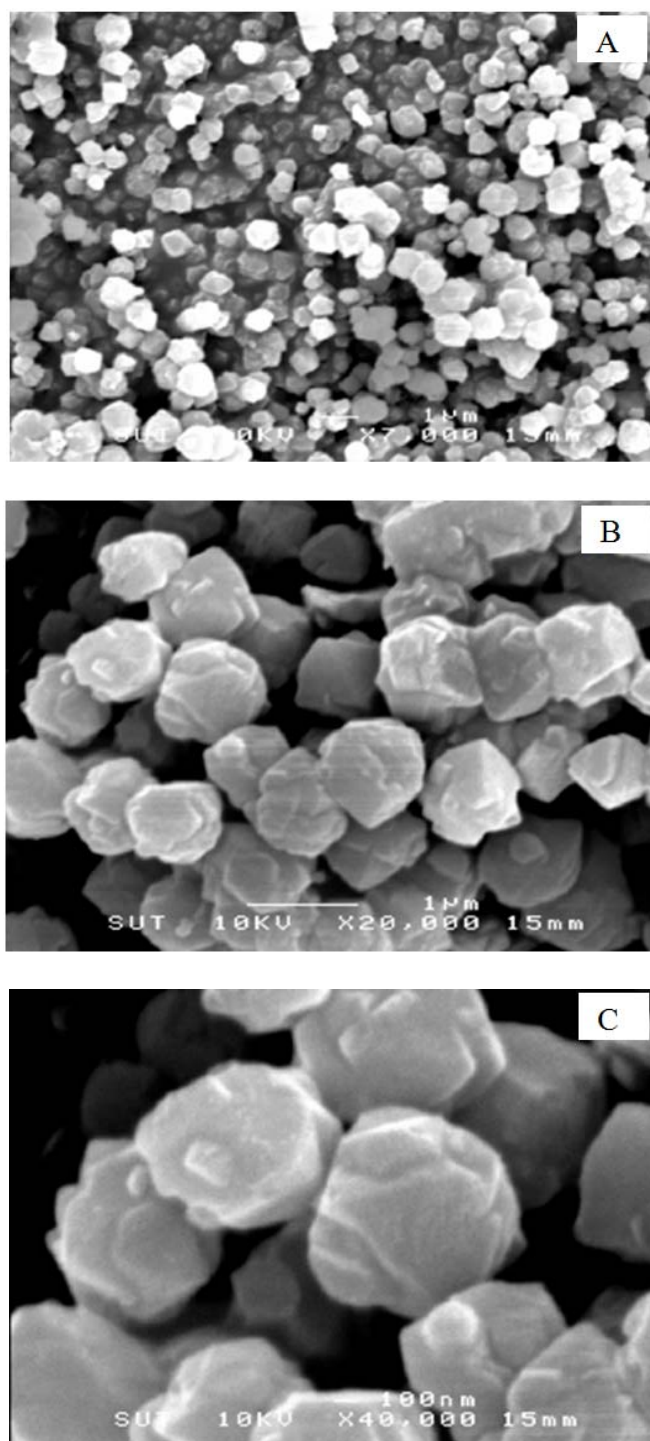
After 24 h, extra peaks in XRD spectrum which are characteristic of zeolite NaP started to appear. The intensity of NaP peaks increased with crystallization time while that of the peaks of NaY decreased. The peaks of NaP were dominant at 48 h and 72 h, the peaks of NaY were still observed with low intensity (Figure 4.2, spectrum C and D). Longer time is required to transform NaY to NaP completely which reported by Albert (1998) that was synthesis of NaP in pure phase from commercial silica suspension with crystallization time of 5 days.

#### **4.3.4 Morphology of NaY by SEM**

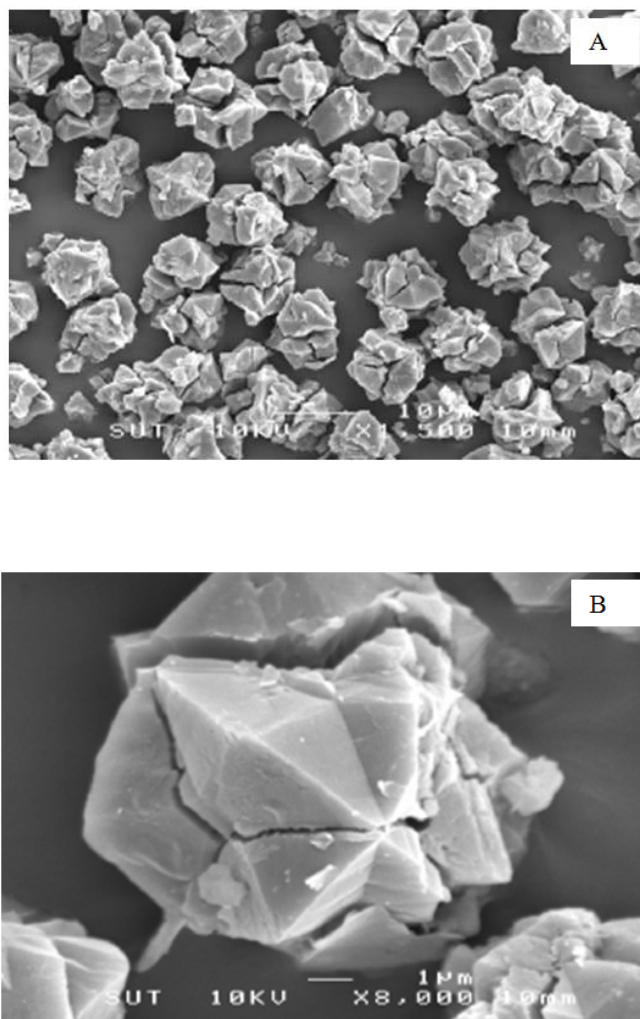
The SEM micrograph of NaY synthesized from RHS at optimum conditions, two-step route and 24 h crystallization time, with magnification of  $\times 7000$ ,  $\times 20000$  and  $\times 40000$  are displayed in Figure 4.4. The particles were mixture of octahedral and twinned and overgrown zeolite Y crystals. Several crystals were apparently fused together to form agglomerate particles. The particle size of isolate crystal from SEM micrograph was approximately 1  $\mu\text{m}$ .

As mentioned earlier that NaY underwent transformation to NaP completely after crystallization for 72 h. The morphology of NaP was also studied by SEM. As exhibited in Figure 4.5, the crystal shape of NaP was apparently different from that of NaY (Figure 4.3). The shape of crystals was spherulitic particles of approximately 6  $\mu\text{m}$  – 8  $\mu\text{m}$ . Most crystals had cracks through the center and virtually similar, but much larger than that of zeolite P prepared from commercial silicate (Albert, 1998).





**Figure 4.4** SEM images of zeolite Y synthesized from RHS with magnification of (A)  $\times 7000$ , (B)  $\times 20000$  and (C)  $\times 40000$

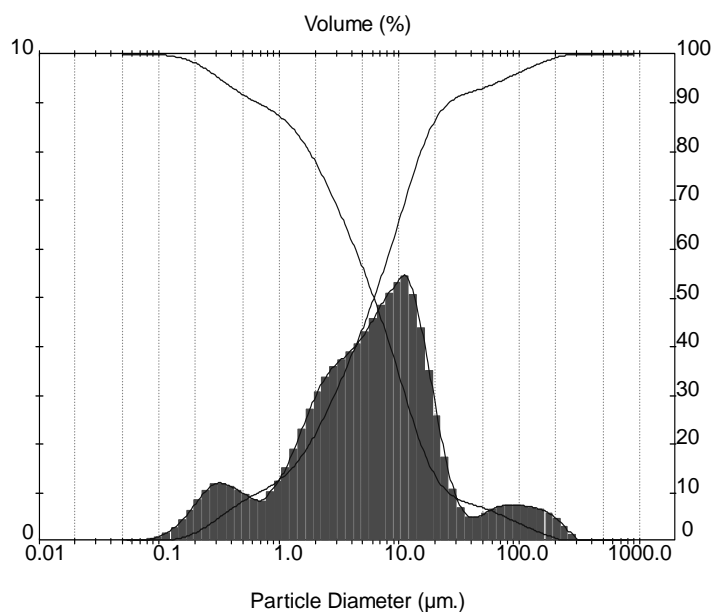


**Figure 4.5** SEM images of zeolite NaP with magnification of (A)  $\times 1500$  and (B)  $\times 8000$

#### 4.3.5 Particle size distribution of NaY by DPSA

The result from DPSA analysis was the particle size distribution and the statistics of distribution calculated from the results using the derived diameters, an internationally agreed method of defining the mean and other moments of particles size British standards; BS2955:1993. The standard percentile of zeolite samples from the analysis at 10%, 50%, and 90% were 0.66  $\mu\text{m}$ , 6.18  $\mu\text{m}$ , and 25.93  $\mu\text{m}$ , respectively. The width of distribution was 4.09  $\mu\text{m}$ . The particle size distribution by

DPSA could also be displayed in histogram (Figure 4.6) revealing that the obtained products were not homogeneous in size. The average particle size from DPSA was approximately 15  $\mu\text{m}$ . This average was different from the size of isolate crystals from SEM because several crystals fused together to form large particles.



**Figure 4.6** Particle size distribution of zeolite Y synthesized from RHS analyzed by DPSA

## 4.5 Conclusions

RHS in amorphous phase with 98% purity was prepared by leaching rice husk with HCl acid and calcination; and used as silica source for the synthesis of zeolite NaY. The NaY in pure phase was obtained from two-step synthetic route in which starting gels were mixed, aged for 24 h at room temperature and crystallized for 24 h at 90°C. The NaY crystals were octahedral with twinned and overgrowth polycrystals. The diameter of single crystal from scanning electron microscope was approximately 0.6  $\mu\text{m}$  – 1.0  $\mu\text{m}$  whereas the average diameters of zeolite particles from laser

diffraction particle size analyzer were approximately 10  $\mu\text{m}$ . When the crystallization time was longer than 24 h, NaY slowly transformed to zeolite NaP.

#### 4.5 References

- Albert, B. R., Cheetham, A. K., Stuart, J. A. and Adams, C. J. (1998). Investigations on P zeolites: synthesis, characterization, and structure of highly crystalline low-silica NaP. **Micropor. Mesopor. Mat.** 21: 133-142.
- Auerbach S. M., Carrado K. A. and Dutta P. K. (2003). **Handbook of zeolite science and technology**. Marcel Dekker, New York
- Chandrasekhar, S. and Pramada, P. N. 2004. Kaolin-based zeolite Y, a precursor for cordierite ceramics. **Appl. Clay Sci.** 27: 187– 198.
- Cundy, C. S. and Cox, P. A. (2005). The hydrothermal synthesis of zeolites: Precursors, intermediates and reaction mechanism. **Micropor. Mesopor. Mat.** 82: 1-78.
- Ginter, D. (2001). Zeolite Y synthesis. In Robson H., (Ed.), *Verified Syntheses of Zeolitic Materials*, 2<sup>nd</sup>, Naterland, Amsterdam.
- Huang, S., Jing, S., Wang, J., Wang, Z. and Jin, Y. (2000). Silica white obtained from rice husk in fluidized bed. **Powder Technol.** 117: 232-238.
- Katsuki, H., Furuta, S., Watari, T. and Komarneni, S. (2005). ZSM-5 zeolites/porous carbon composite: Conventional-and microwave-hydrothermal synthesis from carbonized rice husk. **Micropor. Mesopor. Mat.** 86: 145-151.
- Park, B-D. (2003). Characterization of anatomical features and silica distribution in rice husk using microscopic and micro-analytical techniques. **Biomass Bioenerg.** 25: 319-327.

- Prasetyoko, D., Ramli, Z., Endud S., Hamdan H. and Sulikowski B. (2006). Conversion of rice husk ash to zeolite beta. **Waste Manage.** 26: 1173–1179.
- Sun, L. and Gong, K. (2001). Silicon-Based Material from rice husks and their applications. **Ind. Eng. Chem. Res.** 40: 5861-5877.
- Roberie, T. G., Hildebrandt, D., Creighton, J. and Gilson, J.-P. (2001). Preparation of Zeolite Catalysts, In M. Guisnet, J.-P. Golson (Eds.), **Zeolites for Clean Technology**. Catalytic science series, 3, 57-63, Imperial College Press, London.
- Wang, H., Lin, P. K. S., Huang, Y. J., Li, M. C. and Tsaor, L. K. (1998). Synthesis of zeolite ZSM-48 from rice husk ash. **J. Hazard. Mater.** 58: 147-152.
- Williams, P. T. and Nugranad N. (2000). Comparison of products from the pyrolysis and catalytic pyrolysis of rice husks. **Energy.** 25: 493-513.

# CHAPTER V

## REDUCIBILITY OF COBALT SPECIES IMPREGNATED ON NaY AND HY ZEOLITES

### Abstract

Reducibility of 6 wt.% cobalt impregnated on zeolite Y in sodium and proton form (6Co/NaY and 6Co/HY, respectively) was studied mainly by X-ray absorption spectroscopy including X-ray absorption near edge spectroscopy (XANES) and extended X-ray absorption fine structure (EXAFS) along with other techniques such as X-ray diffraction. The results indicated that the physicochemical properties of Co strongly depended on the form of support. After calcination in air,  $\text{Co}^{2+}$  species were observed on both NaY and HY. After reduction in  $\text{H}_2$  at 420 °C for 5 h, the XANES spectra of Co species in 6Co/NaY were partially reduced to metallic form. Linear combination fit of XANES spectra of freshly reduced and spent 6Co/NaY shows weight of reduced Co to be 50% and 42%, respectively. On the other hand, Co species in 6Co/HY was not reducible with similar conditions and remained as  $\text{Co}^{2+}$  and  $\text{Co}^{3+}$ . EXAFS analysis confirmed metallic Co in the freshly reduced 6Co/NaY with first-shell Co-Co coordination number of 6. EXAFS also confirmed that Co in 6Co/HY was surrounded by four oxygen atoms. Because the metallic cobalt is the active form, 6Co/NaY was significantly more active than 6Co/HY in butane hydrogenolysis at 400 °C (average conversion of 32 vs. 2%, respectively).

## 5.1 Introduction

Cobalt is an effective catalyst for hydrocarbon reactions and has been widely used in petroleum and chemical industries (Kwak et al., 2005). Its catalytic properties depend on the size of metal particles which is controlled by the interaction between metal and support (Wang et al., 2005). It is also known that the type of support can affect the physicochemical properties of metal catalyst such as reducibility of the metal catalysts which is an extent of transformation of metal oxides to metallic form. Various studies have been performed on the reducibility of cobalt-based catalyst supported on  $\text{Al}_2\text{O}_3$ ,  $\text{SiO}_2$  and  $\text{TiO}_2$  at  $350^\circ\text{C}$  for 10 h. The orders of reduction temperature of Co oxides on these supports are in this order:  $\text{Al}_2\text{O}_3 > \text{TiO}_2 > \text{SiO}_2$  (Menicol et al., 1982). All supports have a strong interaction with cobalt as indicated by two-step reduction process that occurred at high temperature. The first step is a reduction of  $\text{Co}_3\text{O}_4$  to  $\text{CoO}$  in the temperature range of  $200^\circ\text{C} - 400^\circ\text{C}$  and the second step is from  $\text{CoO}$  to  $\text{Co}^0$  above  $700^\circ\text{C}$  (Kwak et al., 2005; Jacobs et al., 2002; Jacobs et al., 2007; Arnoldy and Moulijn, 1985; Lapidus et al., 1991; Girardon et al., 2007). However, high temperature during the reduction process causes agglomeration of cobalt particles which results in poor metal dispersion on the support and decreases the reducibility (Menicol et al., 1982). To improve metal dispersion, cobalt can be deposited on zeolites which can presumably confine the metal particle size and limit particle growth because their structure composed of uniform cages with a certain diameter. Zeolites are also known for shape and size selectivity and often used in bifunctional catalysts.

The reduction of metal ion in zeolite to metallic form is generally carried out in hydrogen atmosphere. However, Co has a negative electrochemical potential ( $-0.28$

eV) which makes it difficult to reduce (Emsley, 1991). The extent of reduction of cobalt on zeolites depends on several parameters such as calcination temperature (Lu et al., 1992) and the employed form of zeolite (Tang et al., 2004). The reducibility of Co ions in zeolite is dependent on their location and chemical states, for example, they are more easily reduced when they are in supercage than in sodalite cages of zeolite NaY. Thus, the shift of reduction temperature to higher temperature could be observed when the ions migrated from supercage to the hidden sites of small cages (Uytterhoeven, 1978). Bronsted acids sites are generated in Co on zeolite NaY prepared by impregnation leading to agglomeration of Co particle and made it difficult to reduce with hydrogen at temperature below 527°C (Wang et al., 2005; Uytterhoeven, 1978; Guzzi, 2005). However, high reduction temperature may lead to migration of Co from the zeolite pore or collapse of the zeolite framework. When cobalt oxides are not fully reduced, they will give low catalytic activity. The cobalt reduction at low temperature as 300°C can be enhanced by treating the zeolite with sodium hydroxide or sodium acetate because the CoO<sub>x</sub> particles are encapsulated in supercages and could be partially reduced to metallic cobalt at temperature as low as 300°C (Tang et al., 2004).

In our work, it is necessary to understand the catalytic reduction conditions of cobalt supported on zeolite Y before further application in butane hydrogenolysis. Because there are not many reports on the effect of the zeolite form on the reduction of cobalt (Tang et al., 2004), we have investigated the reducibility of cobalt oxides supported on zeolite Y in sodium and proton form, denoted Co/NaY and Co/HY, respectively by X-ray absorption spectroscopy (XAS) including X-ray absorption near edge spectroscopy (XANES) and extended X-ray absorption fine structure (EXAFS).



The information from XAS can lead to understanding about the relationship between forms of metal, support types and the catalytic activity. The catalysts are prepared by impregnation and also characterized by X-ray diffraction (XRD) before testing for butane hydrogenolysis.

## **5.2 Experimental**

### **5.2.1 Catalyst preparation**

Zeolite Y in sodium form (NaY) was synthesized from a seed gel and feedstock gel with a “two-step” procedure (Wittayakun, 2008). The ammonium form (NH<sub>4</sub>Y) was obtained by further exchange with NH<sub>4</sub><sup>+</sup> ions for 24 h using conventional method (Chandrasekhar, 2001). After the separation by centrifugation, the process was repeated five times to ensure the maximum ion exchange. The obtained NH<sub>4</sub>Y was dried overnight at 100°C and used for impregnation.

Co/NaY and Co/HY were prepared by impregnation NaY and NH<sub>4</sub>Y, respectively, with aqueous solutions of CoCl<sub>2</sub>·H<sub>2</sub>O. Each mixture was kept at room temperature for 24 h, dried at 120°C for 3 h and calcined at 300°C for 3 h in a muffle furnace. Upon calcination, the NH<sub>4</sub>Y would decompose to produce HY and the cobalt supported on HY was obtained. The cobalt content in both Co/NaY and Co/HY determined by ICP-OES spectrometer (Perkin Elmer, Optima 7000DV) was 5.8 wt% and 5.5 %wt, respectively.

### **5.2.2 Catalyst characterization**

Nitrogen adsorption-desorption isotherm of the parent NaY, Co/NaY and Co/HY were obtained at liquid nitrogen temperature with a Quantachrome (NOVA 1200e) gas adsorption analyzer. Each sample was degassed at 300°C for 3 h before

the measurement. The specific BET surface areas was determined at the relative pressure range of 0.05 – 0.35.

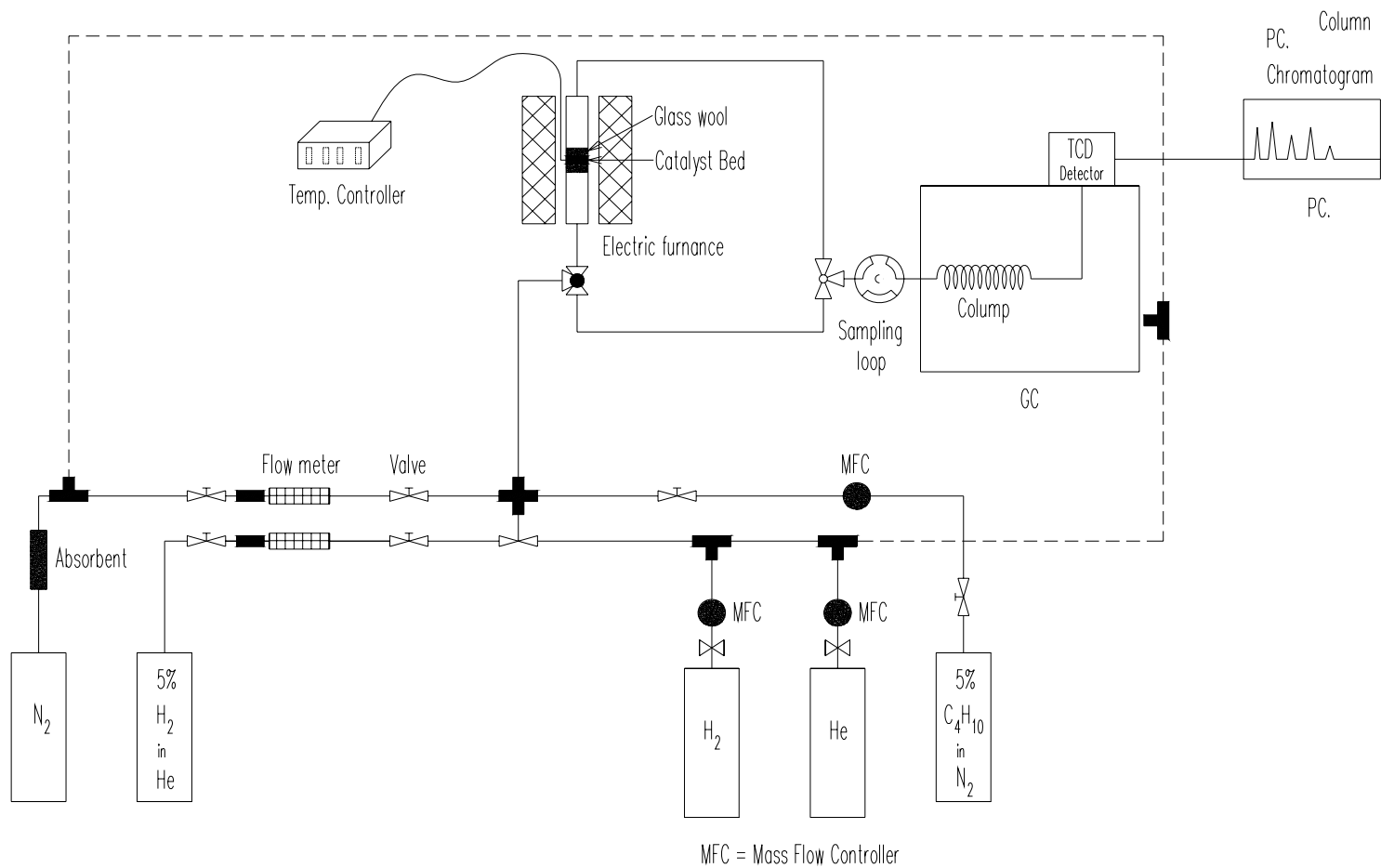
Phase and crystallinity of reduced Co catalysts were confirmed by powder XRD (Bruker AXS D5005) with nickel filtered Cu K $\alpha$  radiation scanning from 4° – 50° at a rate of 0.05°/s. The parent NaY zeolite was used as a reference for peak assignment. To prepared reduced samples, each catalyst powder was pressed, crushed, and sieved to 200  $\mu$ m – 350  $\mu$ m and dried at 120°C for 5 h. Approximately 0.1 g of catalyst was packed into a quartz tube, pretreated at 100°C in He flow (50 ml/min) for 1 h and reduced under H $_2$  (50 ml/min) at 420°C for 5 h.

The local environment of cobalt on both Co/NaY and Co/HY was studied by XANES and EXAFS at beamline-8 of the Synchrotron Light Research Institute (Public Organization), Thailand with a procedure similar to the literature (Klysubun, 2007). A double Ge (220) crystal monochromator was employed for selection of photon energy. X-ray absorption experiments were performed on calcined and reduced catalysts. Each sample was pressed into a frame covered by polyimide tape and mounted onto a sample holder. The XANES and EXAFS spectra of Co K-edge were obtained at room temperature in fluorescent mode using a 13-element Ge detector. Incident photon intensity was monitored by an ion chamber filled with 29 mbar Ar. The photon energy was calibrated by a Co foil at 7709 eV. Linear combination fit of XANES spectra and data reduction of EXAFS spectra were processed with Athena (Ravel, 2005) and analyzed with EXAFSPAK programs (George and Pickering, 2006). Linear combination fit was performed on normalized spectra with energy ranging from -20.00 eV – 30.00 eV relative to the edge energy. The curve fitting of

EXAFS data was carried out on the first coordination shell using single-scattering with Mackale equation. For Fourier transform (FT), the  $k^3$  weighting was selected.

### **5.2.3 Catalytic testing on butane hydrogenolysis**

The catalytic performance on butane hydrogenolysis was determined in a tubular flow reactor (Figure 5.1). Each catalyst was reduced under  $H_2$  (50 ml/min) at 400°C for 3 h. A gas reaction mixture containing  $C_4H_{10}$ ,  $H_2$  and He with flow rate ratio of 0.5 : 30 : 69.5 ml/min was flown into the reactor at 400°C and the products were analyzed by an on-line gas chromatography (SRI-GC-310C) equipped with a thermal conductivity detector (TCD).



**Figure 5.1** Schematic diagram of reactor setup for butane hydrogenolysis

## 5.3 Results and discussion

### 5.3.1 Characterization by N<sub>2</sub> adsorption-desorption

The adsorption isotherms surface area of parent NaY, reduced 6Co/NaY and reduced 6Co/HY are shown in Fig. 2. All samples possess a type I isotherm which is a characteristic of microporous material. The volume of nitrogen uptake increased quickly at low relative pressure as the micropores were filled. Among these samples the adsorption volume at low relative pressure decreased after Co was loaded indicating decrease of surface area (see Table 1). The amount adsorbed increased slightly and a hysteresis loop at high relative pressure indicating that some wide mesopores or narrow macropores were also formed [Rouquerol and Rouquerol, 1999]. This behavior was previously reported in other zeolites [Tang et al., 2004, 21].

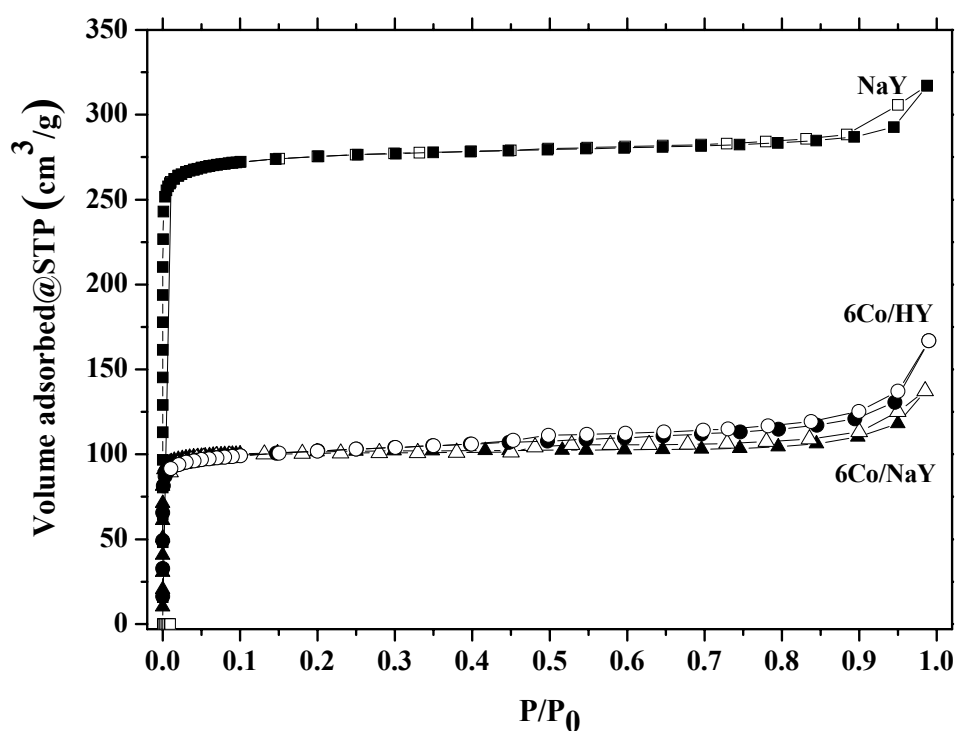


Figure 5.2 N<sub>2</sub> adsorption-desorption isotherm of NaY, 6Co/NaY and 6Co/HY

The surface area of 6Co/NaY and 6Co/HY are about half of that of the parent NaY, possibly from blockages of the zeolite pores by the metal species.

Table 5.1 Surface area of NaY and Co supported on NaY and HY

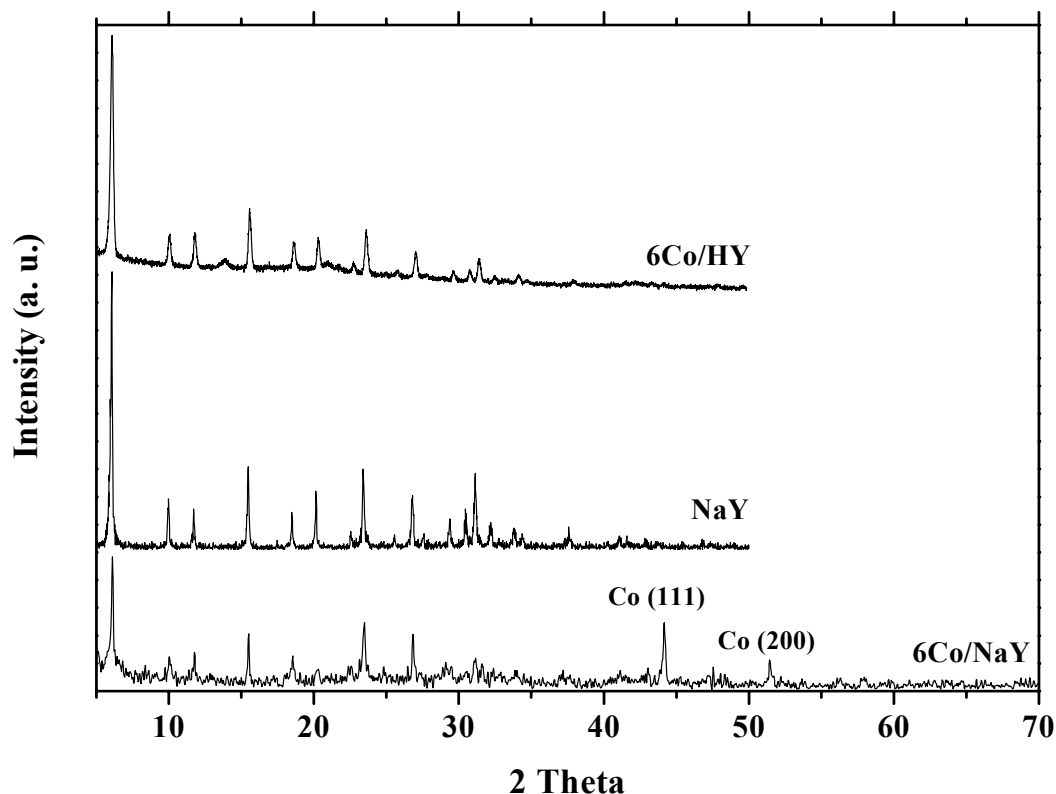
Sample	BET surface area (m <sup>2</sup> /g)
NaY	700
6Co/NaY	334
6Co/HY	334

### 5.3.2 Characterization by XRD and TEM

The XRD spectra of 6Co/NaY and 6Co/HY after reduced at 420°C in H<sub>2</sub> flow are shown in Fig. 5.3. Both samples show the characteristic of zeolite Y [Guzci et al., 2002, Ginter, 2001] indicating that the zeolite structure is retained.

However, the peak intensities were lower than that of the parent NaY indicating decrease in zeolite crystallinity after the catalyst preparation. This change could be related to the hysteresis in the nitrogen adsorption-desorption isotherms. In addition, characteristic XRD peaks of metallic Co at 44.31 and 51.65 degree were observed on the reduced 6Co/NaY sample. This result was similar to that in the literature [Glaspell et al., 2004]. It was evidence that Co species on NaY could be reduced to metallic form and the presence of these peaks indicated that the metallic cobalt on NaY had large crystal size. This was confirmed by TEM images (Fig. 5.4A) showing Co particles as dark spots dispersed on the NaY support. In contrast, the metallic peaks were not observed in the XRD spectrum of reduced 6Co/HY samples. Moreover, the peaks corresponding to Co<sub>3</sub>O<sub>4</sub> and CoO [O-Shea et al., 2007] were not

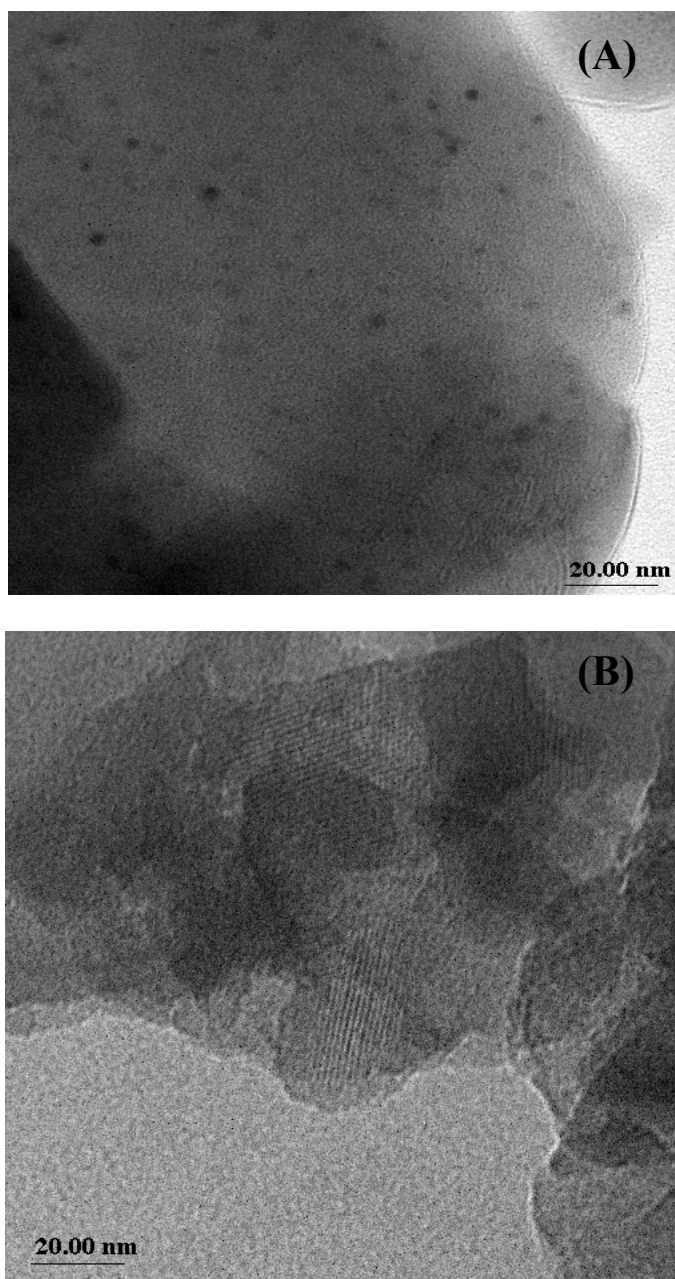
observed either. These results indicated that cobalt was well dispersed on the HY support. The cobalt species probably dispersed on zeolite surface and confined inside the zeolite cages. Their forms or locations could not be determined by XRD.



**Figure 5.3** XRD patterns of reduced 6Co/NaY and 6Co/HY compared with the parent NaY

Lu et al. (1992) reported that Co species prepared by ion exchange, with metal loading of 5.6% located inside the pore cavity of zeolite and could not be detected by XRD because the particle sizes were less than 2.5 – 3.0 nm. Rosynek and Polansky (1991) reported that most of metal ions in the supercages migrated into sodalite cage at high reduction temperature (550°C). In addition, the absence of the peaks of  $\text{Co}_3\text{O}_4$

at  $2\theta = 36.88, 38.58$  and  $44.70$  and of CoO at  $2\theta = 36.53$  and  $42.41$  from the XRD pattern of 6Co/HY may indicate that metal particles are inside the zeolite cages.



**Figure 5.4** TEM images of reduced 6Co/NaY (A) and reduced 6Co/HY (B)



The well dispersion of cobalt species was also confirmed by the TEM image in Fig. 5.4B that the metal particles were not observed. The TEM image of this sample also displayed scattering mesoporous features which supported the presence of nitrogen adsorption-desorption isotherm.

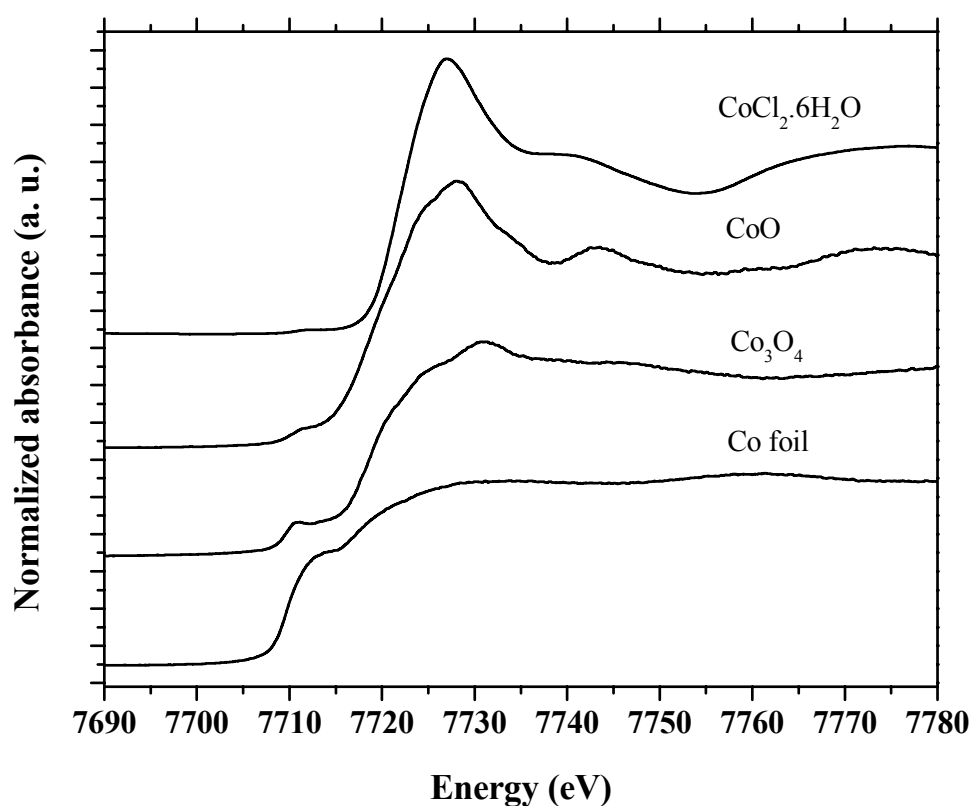
The XRD spectra indicated that only Co species on NaY could be reduced by the studied conditions but the degree of reduction could not be determined by this technique. In addition, it was not plausible to identify the forms of cobalt species on HY by XRD. From the appearance of 6Co/NaY and 6Co/HY, it was visible that the Co forms on NaY and HY after reduction were different because the color of 6Co/NaY was gray while that of 6Co/HY was light blue. Consequently, we employed XAS to investigate the forms and reducibility of cobalt on both catalysts.

### 5.3.3 Characterization by XANES

To investigate the forms and local environment of cobalt, both XANES and EXAFS spectra at Co K edge of both Co/HY and Co/NaY were taken and compared with reference materials. The XANES spectra of reference materials in this work including Co foil,  $\text{Co}_3\text{O}_4$ , CoO and the precursor  $\text{CoCl}_2 \cdot 6\text{H}_2\text{O}$  are plotted in Figure 5.5 and their Co K-edge positions are listed in Table 5.2. Their XANES features are well distinguishable from one another. Except for Co foil, pre-edge peaks are observed at about 7709 eV in agreement with previous reports (Profeti et al., 2008; Choy et al., 2001).

In general, the pre-edge absorption originates from a dipole transition of 1s to hybridized 4p-3d band of a transition metal in tetrahedral site and a quadruple transition of 1s to 3d band in octahedral site (Groot, 2001). It is known that the dipole

transition is much stronger than the quadruple transition, therefore  $\text{Co}_3\text{O}_4$  having a spinel structure shows a higher pre-edge peak because 2/3 of the metals as  $\text{Co}^{2+}$  is in tetrahedral sites (surrounded by four oxygen atoms) and 1/3 as  $\text{Co}^{3+}$  in octahedral sites (surrounded by six oxygen atoms) while the Co metals in  $\text{CoO}$  and  $\text{CoCl}_2 \cdot 6\text{H}_2\text{O}$  are in an octahedral center.



**Figure 5.5** The XANES spectra of Co K-edge of reference standard materials

The XANES spectra of 6Co/NaY and 6Co/HY after being calcined, reduced and tested for butane hydrogenolysis are shown in Figure 5.6 and 5.7, respectively. Their edge energies are presented in Table 5.2. Before reduction, both Co/HY and NaY were calcined in air. The absorption edges of the calcined Co/HY and NaY shifted 10 eV and 11.8 eV respectively from that of the Co foil indicating that cobalt

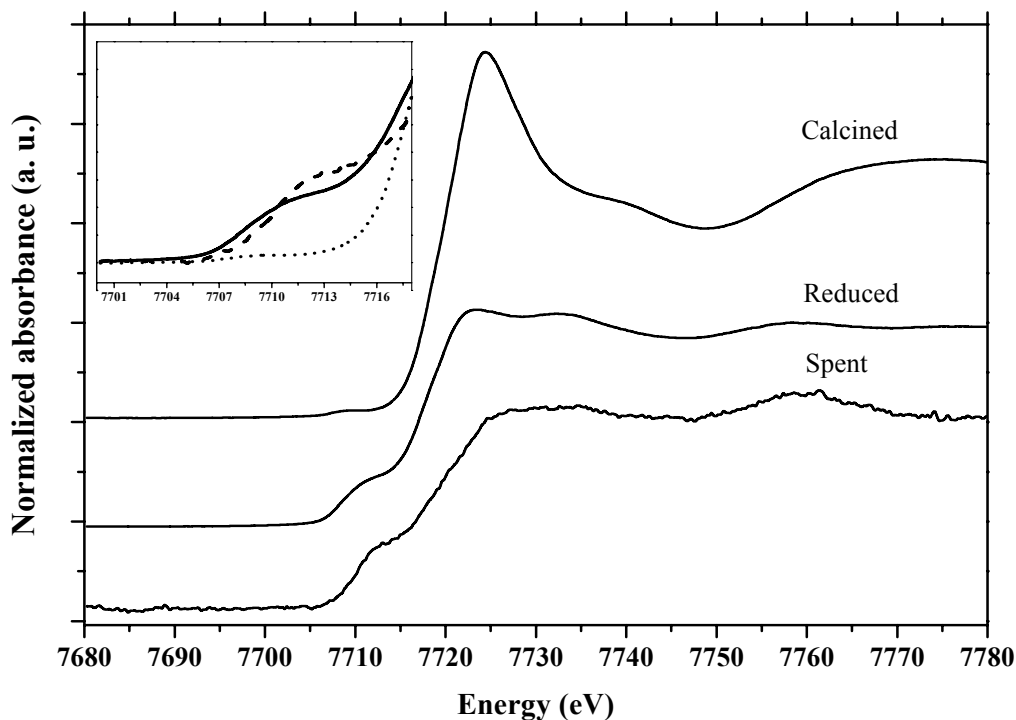
precursors might remain in original form and partially oxidized to cobalt oxide. Beale and Sankar (2006) reported that a strong white line and preservative shape of peak according to consistency with Co(II) in octahedral coordination, most likely as hexa-aqua species  $[\text{Co}(\text{H}_2\text{O})_6]^{2+}$  residing in the supercages of the zeolite structure. The overall spectra show small pre-edge characteristic, strong white line and the main absorption edge similar to that of  $\text{CoCl}_2$ , suggesting that the Co species supported on HY and NaY after calcination were predominantly in the form of  $\text{Co}^{2+}$ . The  $\text{Co}^{2+}$  might reside at the same location and acquired octahedral coordination by adsorbing water molecules as described in the literature (Li et al., 2001).

After reduction and reaction, the edge energy of Co/NaY (Figure 5.6) is shifted to that of Co metal and the white-line intensity is decreased. This implies that Co is partially reduced. On the other hand, the spectrum of Co/HY (Figure 5.7) remains in the same shape with lower white-line intensity indicating changes of cobalt phase possibly due to desorption of water molecules (Lee et al., 2003) and formation of oxide phase as confirmed by linear combination fit (Figure 5.8). It can be concluded that the oxides of cobalt on HY were not reducible with our conditions. This is probably due to the strong interaction between cobalt oxides and HY.

**Table 5.2** Co K-edge energy position for Co/Y samples with respect to Co metal foil (7709 keV)<sup>a</sup>

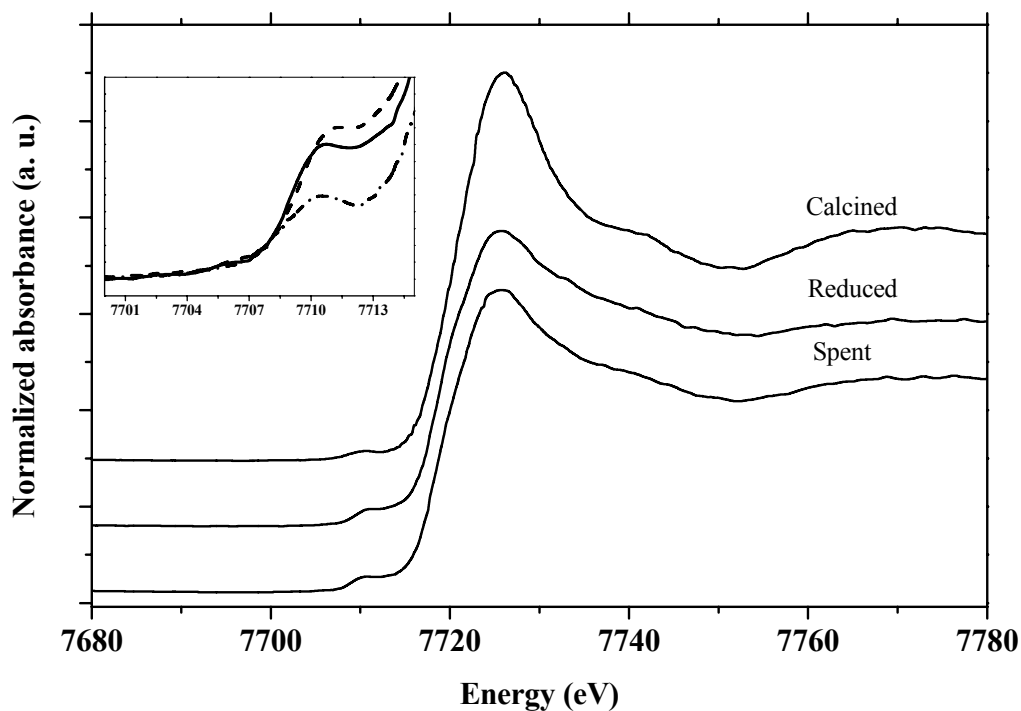
Compounds	Pre-edge position	K-edge position $E$ (eV)	$\Delta E$ (eV)
Standard			
Co foil	-	7709.0	0.0
CoO	7711.58	7717.2	8.2
Co <sub>3</sub> O <sub>4</sub>	7710.91	7719.6	10.6
CoCl <sub>2</sub> ·6H <sub>2</sub> O	7711.76	7720.5	11.5
Co <sub>2</sub> SiO <sub>4</sub>	7711.46	7717.7	8.7
Calcined catalysts			
6Co/HY	7710.06	7720.8	11.8
6Co/NaY	7711.76	7720.6	11.6
Reduced catalysts			
6Co/HY	7710.70	7718.3	9.3
6Co/NaY	-	7709.7	0.7
Spent catalysts			
6Co/HY	7710.70	7718.7	9.7
6Co/NaY	-	7709.7	0.7

<sup>a</sup> The edge position is defined as the first inflection point.



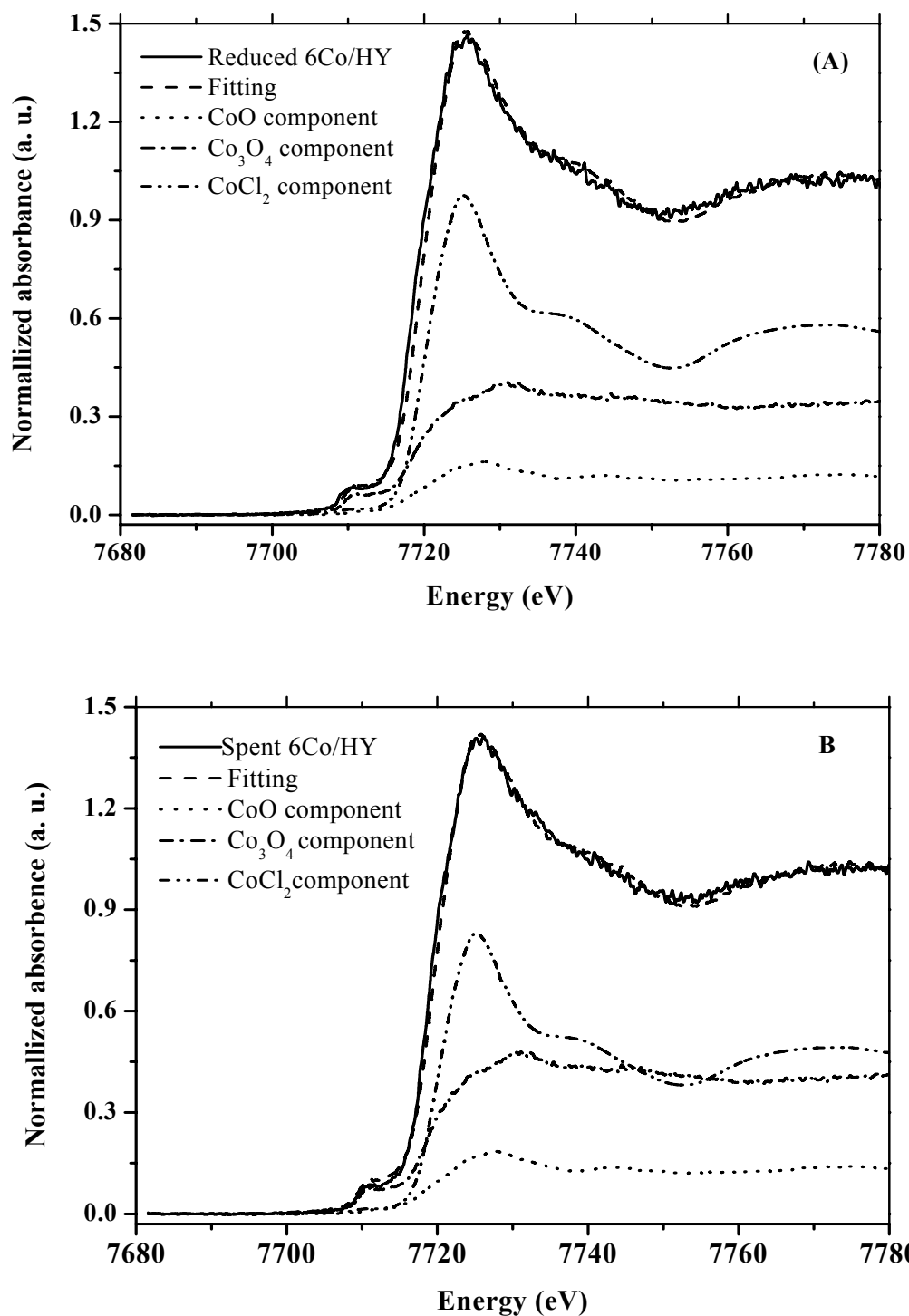
**Figure 5.6** The XANES spectra of 6Co/NaY after being calcined (•••••), reduced (---), and tested on butane hydrogenolysis (—)

In addition, the increases of intensities of the pre-edge feature in the reduced and spent Co/HY confirms that Co migrates to the small cages and generates  $\text{Co}_3\text{O}_4$  which is difficult to reduce at low temperature. A slight increase of pre-edge in the both reduced and spent Co/HY catalysts corresponds to the decrease of octahedral phase of Co. This suggests that some cobalt species is stabilized during reduction in a distorted octahedral or coordinatively unsaturated site (Choy et al., 2001; El-Malki et al., 2000). Distortion of this octahedral symmetry allows p-d mixing dipole transition and enhances intensity of the pre-edge. Thus this cobalt with high oxidation state is difficult to reduce and does not prefer to adsorb hydrogen during the reduction process (Haneda et al., 2003).



**Figure 5.7** The XANES spectra of 6Co/HY after being calcined (•••••), reduced (---), and tested on butane hydrogenolysis (—)

In order to quantify the amount of each form of cobalt in the 6Co/NaY catalyst after being calcined, reduced and tested for butane hydrogenolysis reaction, the linear combination of the XANES spectra of Co/NaY and Co/HY were calculated using XANES data (shown in Figure 5.8 and 5.9) standard compounds (Co foil, CoO, Co<sub>2</sub>SiO<sub>4</sub> and Co<sub>3</sub>O<sub>4</sub>) as bases. The weight percent of metallic Co of the reduced 6Co/NaY sample is 45.20% and oxides phase of CoO and Co<sub>3</sub>O<sub>4</sub> are 30.70% and 24.10%, respectively.



**Figure 5.8** Linear combination fit of reduced (A) and spent 6Co/NaY (B) compare with standard of CoO, Co<sub>3</sub>O<sub>4</sub> and Co foil

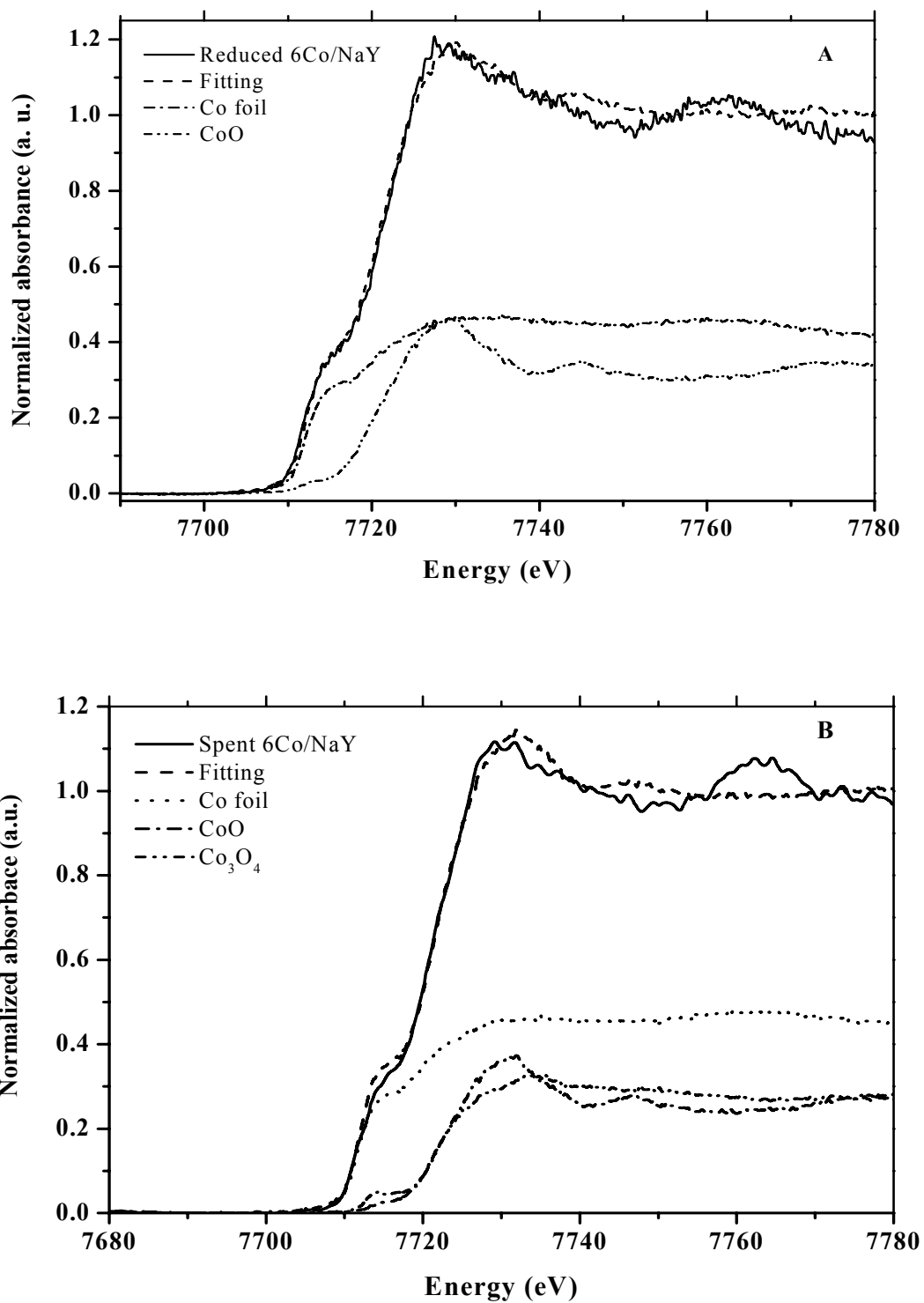
**Table 5.3** Linear combination fitting of XANES spectra for reduced and spent of Co/NaY and Co/HY catalyst with contributes to standard material

Group	Weight (%)	R-factor	Chi-square	Reduced chi-square
Calcined 6Co/NaY		0.0022	0.5752	0.0023
1: CoCl <sub>2</sub>	73.60			
2: CoO	25.40			
3: Co <sub>3</sub> O <sub>4</sub>	0.90			
Reduced 6Co/NaY		0.0057	0.1587	0.0032
1: Co foil	45.20			
2: CoO	30.70			
3: Co <sub>3</sub> O <sub>4</sub>	24.10			
Spent 6Co/NaY		0.0456	7.1333	0.0285
1: Co foil	46.40			
2: CoO	25.60			
3: Co <sub>3</sub> O <sub>4</sub>	28.00			
Calcined 6Co/HY		0.0038	1.0657	0.0043
1: CoCl <sub>2</sub>	81.40			
2: CoO	18.60			
3: Co <sub>3</sub> O <sub>4</sub>	0.00			
Reduced 6Co/HY		0.0019	0.3989	0.0017
1: CoCl <sub>2</sub>	54.40			
2: CoO	11.40			
3: Co <sub>3</sub> O <sub>4</sub>	34.20			
Spent 6Co/HY		0.0008	0.1706	0.0007
1: CoCl <sub>2</sub>	46.30			
2: CoO	13.00			
3: Co <sub>3</sub> O <sub>4</sub>	40.70			



After being tested for butane hydrogenolysis the mixed characteristic phase of Co metal, CoO, and Co<sub>3</sub>O<sub>4</sub> were found to be 46.4%, 25.6%, and 28.0% respectively. On the other hand, the metallic cobalt is absent in the 6Co/HY catalyst after reduction. Only CoCl<sub>2</sub>, CoO, and Co<sub>3</sub>O<sub>4</sub> are detected at 54.4%, 11.4% and 34.2 %, respectively. After being tested in the reaction the Co<sup>2+</sup> content in CoCl<sub>2</sub>, is decreased to 46.3% while phases of CoO, and Co<sub>3</sub>O<sub>4</sub> are increased to 13.0% and 40.7%, respectively, indicating that some Co species migrates to the small cage and generates Co<sub>3</sub>O<sub>4</sub> as evident by an increase of pre-edge of XANES spectrum.

The irreducibility of Co<sup>2+</sup> species in zeolites NaY had been reported before (Lu, 1992; Tang, 2004; Guzzi, 2005). The reasons of this phenomenon were given to low electrochemical reduction potential of cobalt ions and the strong bond to the zeolite-framework oxygens. Haneda et al. (2003) found that the reduction of Co<sub>3</sub>O<sub>4</sub> could occur at lower temperature in the presence of alkali ions such as Li, Na, K, Rb and Cs, because the Co–O bond was weakened. They suggested that sodium formed Na–O–Al, suppressed the formation of surface spinel cobalt species and promotes the reduction of cobalt oxide to metallic state (Kwak et al., 2005). The metal cations may exist in three different locations inside the Y zeolite including supercages, sodalite cages, and hexagonal prisms. The order of reduction of metal precursors in these locations increases in the following order: hexagonal prisms > sodalite cages > supercages (Haneda et al., 2003).

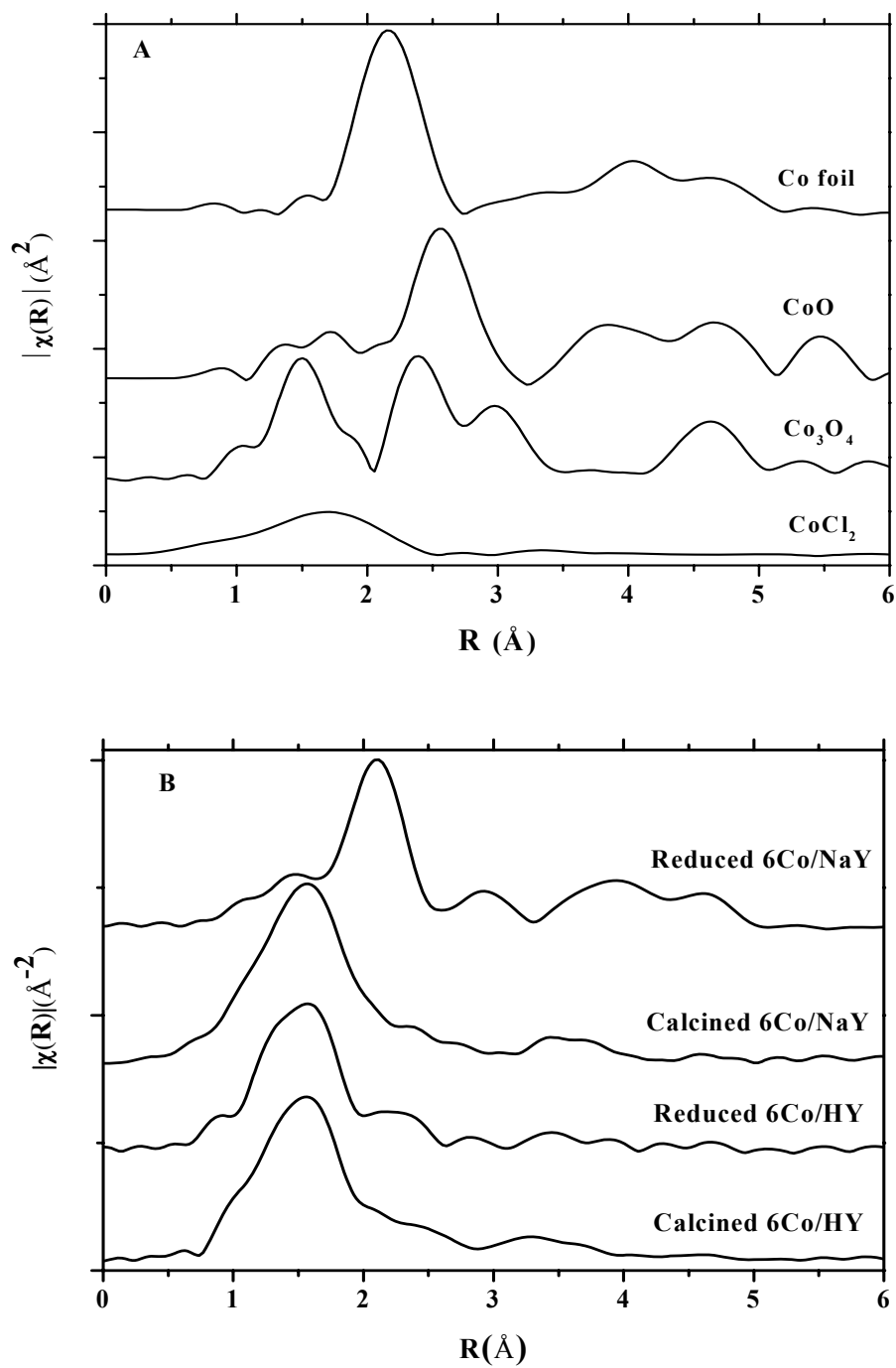


**Figure 5.9** Linear combination fit of reduced (A) and spent 6Co/HY (B) compare with standard of CoO, Co<sub>3</sub>O<sub>4</sub> and CoCl<sub>2</sub>·6H<sub>2</sub>O

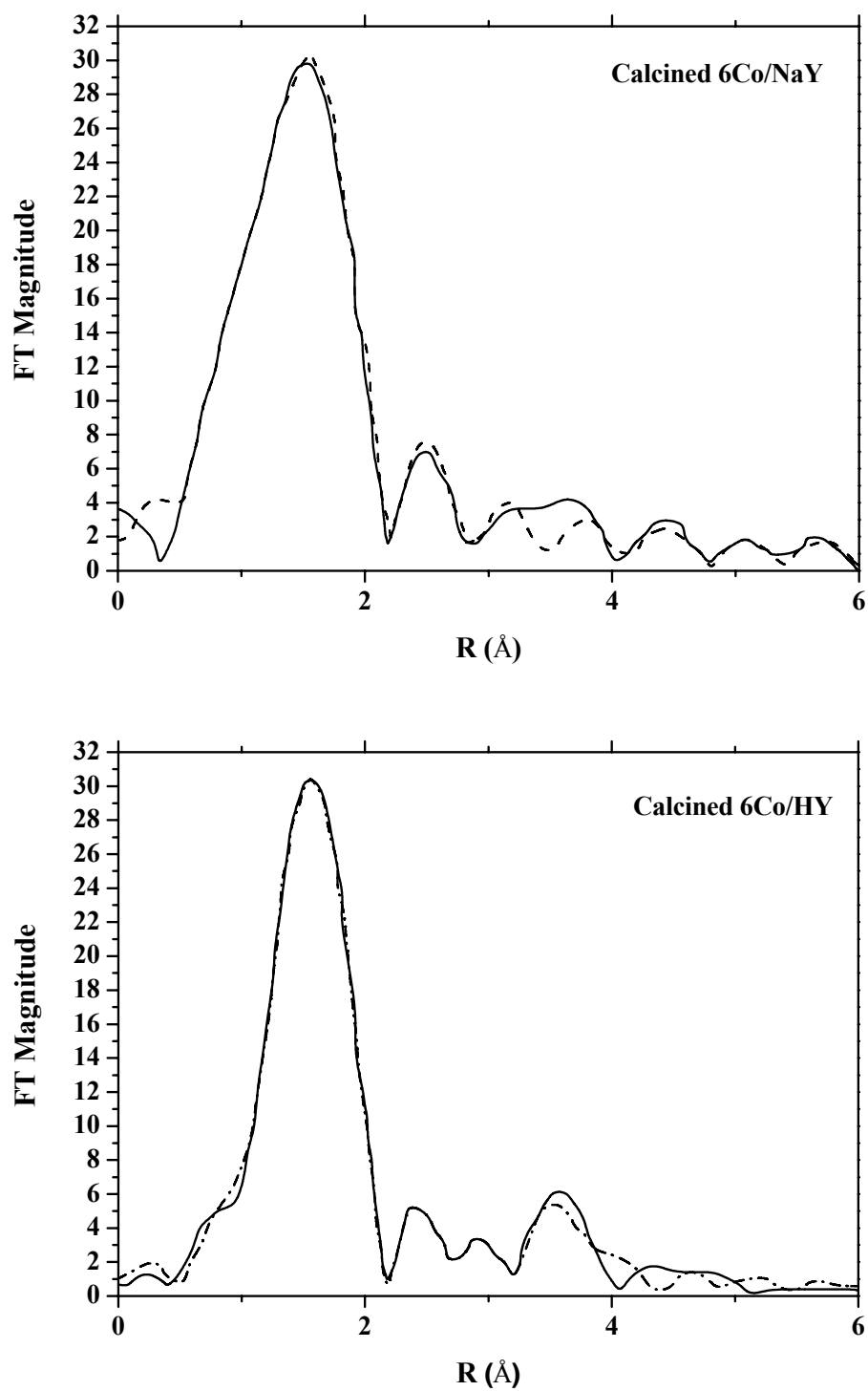
### 5.3.4 Characterization by EXAFS

Figure 5.10 shows the Fourier-transformed data of the XAS spectrum in the EXAFS region. Figure 5.10A shows spectra of standard materials and Figure 5.10B shows spectra of Co/NaY and Co/HY after calcination and reduction. Qualitative information from the EXAFS data well agrees with the XANES results: The first peaks of calcined Co/NaY and Co/HY are nearly similar indicating that they likely contain cobalt in the same form. However, the first peaks of reduced Co/NaY and Co/HY were different: only the FT pattern of the reduced 6Co/NaY resembles that of Co foil reflecting the presence of metallic Co.

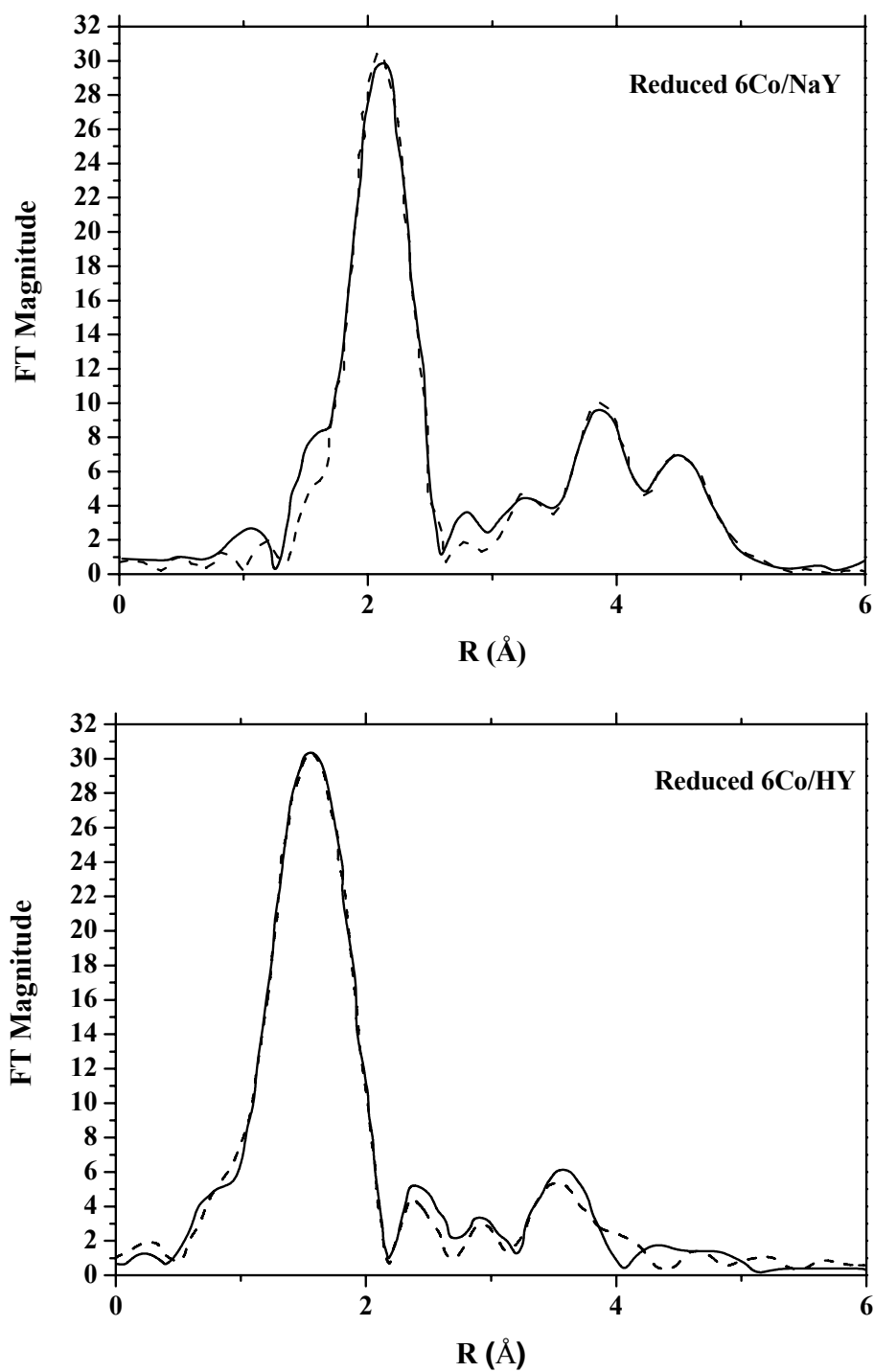
The curve fitting results of Co/NaY and Co/HY are plotted in Figure 5.11 and tabulated in Table 5.4. We report only the results of calcined and reduced Co catalysts. The spectrum of spent catalyst in the reaction could not be analyzed in the EXAFS region because of poor data quality. This may be due to the fact that the sample was diluted with Al<sub>2</sub>O<sub>3</sub> prior to the reaction. Based on the best fit, the first-shell coordination numbers (N) of Co-O for 6Co/NaY and 6Co/HY after calcinations are 7.6 and 6.3, respectively. After being reduced, the first shell becomes Co-Co with N = 8 in Co/NaY while the local structure in Co/HY significantly retains. This result indicated that during reduction under H<sub>2</sub> atmosphere, cobalt oxide was reduced and agglomerated to form cobalt particles leading to higher coordination number, similar to a report by Guzci et al. (2002) that showed the long distances Co-Co bond (2.5 Å) with coordination number 7.7. Using X-ray absorption spectroscopy, we have significantly shown that local structure depends on the support both of which have affected the reducibility of the metal cations.



**Figure 5.10** Modules of Fourier transform of standard materials (A); Co foil, CoO,  $\text{Co}_3\text{O}_4$ ,  $\text{CoCl}_2$  and samples (B); calcined 6Co/NaY, reduced 6Co/NaY, reduced 6Co/HY, calcined 6Co/HY



**Figure 5.11** Fourier transforms from experiment (—) and curved fitting results (-----) for catalyst samples.



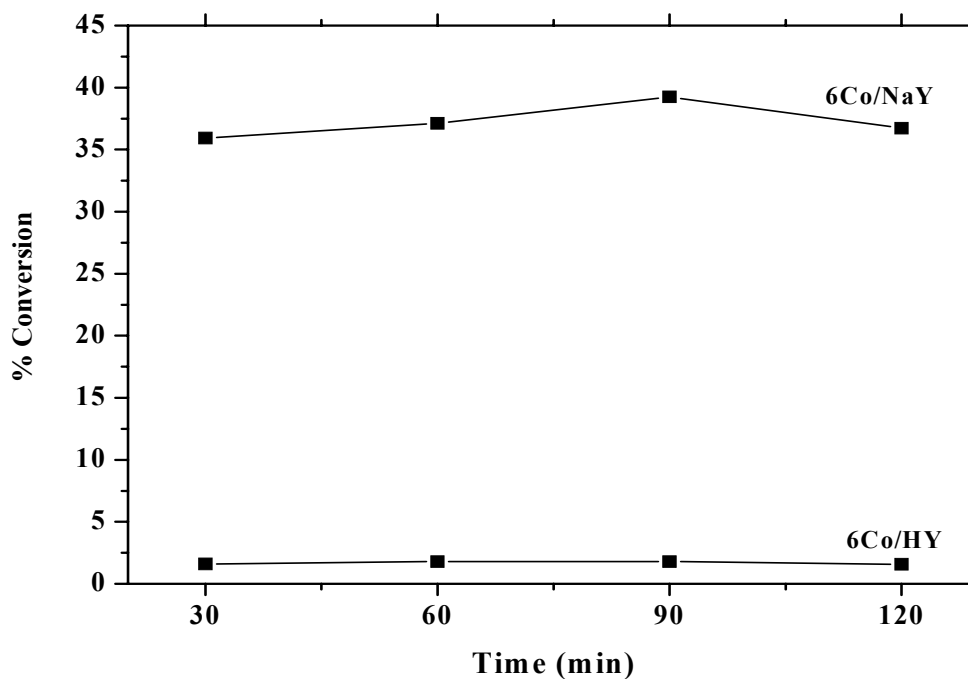
**Figure 5.11** (continued) Fourier transforms from experiment (—) and curved fitting results (-----) for catalyst samples.

**Table 5.4** Results from the analysis of EXAFS data of Co/NaY and Co/HY

Samples	Component (1 <sup>st</sup> shell)	CN	R (Å)	E <sub>0</sub> (eV)	σ <sup>2</sup> (Å <sup>2</sup> )
Calcined 6Co/NaY	Co-O	7.56	2.02	-4.86	0.006
Calcined 6Co/HY	Co-O	6.28	2.06	-5.02	0.008
Reduced 6Co/NaY	Co-Co	8.02	2.49	-12.48	0.008
Reduced 6Co/HY	Co-O	6.28	2.05	3.68	0.008

### 5.3.5 Catalytic testing for butane hydrogenolysis

The result from catalytic testing is shown in Figure 5.12. When the Co/NaY was reduced at 400°C in H<sub>2</sub> atmosphere for 3 h, the conversion in butane hydrogenolysis was 32% with methane as a major product (100%).



**Figure 5.12** Conversion in butane hydrogenolysis on supported Co catalysts at 300°C

On the other hand, the Co/HY reduced at similar condition gave the butane conversion of 2% and the only observed product was methane. These results indicate that cobalt in oxide forms is inactive. The conversions on both catalysts were constant during the test duration.

## 5.4 Conclusions

The reducibility of cobalt species supported on zeolite Y depends on the zeolite form. The cobalt oxides in Co/NaY are reducible at about 45.20% at 400°C for 3 h and become metallic cobalt particles with coordination number of eight after reduction. This form is active for butane hydrogenolysis. In contrast, the cobalt oxides in Co/HY can not be reduced with similar conditions and it is remained as cobalt oxides surrounded by six oxygen atoms, inactive for butane hydrogenolysis



## 5.5 References

- Arnoldy, P. and Mounlijn, J. A. (1985). Temperature-programmed reduction of CoO/Al<sub>2</sub>O<sub>3</sub> catalysts. **J. Catal.** 93: 38-54.
- Beale, A. M. and Sankar, G. (2006). Understanding the crystallization of nanosized cobalt aluminate spinel from ion-exchanged zeolites using combined in situ QEXAFS/XRD. **Chem. Mater.** 18: 263 – 272.
- Chandrasekhar, S. and Pramada, N. P. (2001). Sintering behavior of ammonium exchanged low silica zeolites synthesized by two different routes. **Ceram. Int.** 27: 351-361.
- Choy, J. H., Jung, H. and Yoon, J-B. (2001). Co K-edge XAS study on a new cobalt doped-SiO<sub>2</sub> pillared clay. **Synchrotron Rad.** 8: 599-601.
- Donohue, M. D. and Aranovich, G. L. (1998). Adsorption Hysteresis in Porous Solids. **J. Colloid Interf. Sci.** 205: 121-130.
- El-Malki, E-M., Werst, D., Doan, P. E. and Sachtler, W. M. H. (2000). Coordination of Co<sup>2+</sup> cations inside cavities of zeolite MFI with lattice oxygen and adsorbed ligands. **J. Phys. Chem. B.** 104: 5924-5931.
- Emsley J. (1991). **The elements.** (2<sup>nd</sup> ed). Oxford University Press, London, p. 54.
- Glaspell, G. P., Jagodzinski, P. W. and Manivannan, A. (2004). Formation of cobalt nitrate hydrate, cobalt oxide, and cobalt nanoparticles using laser vaporization controlled condensation. **J. Phys. Chem. B.** 108: 9604-9607.
- George, G. N. and Pickering, I. J. (2006). EXAFSPAK; A suite of computer programs for analysis of X-ray absorption spectra [On-Line]. Available: <http://www-ssrl.slac.stanford.edu/exafspak.html>.

- Ginter, D. (2001). Zeolite Y synthesis. In H. Robson (Ed.), **Verified syntheses of zeolitic materials**, 2<sup>nd</sup>, Amsterdam.
- Girardon, J-S., Quinet, E., Grilboval-Constant, A., Chernavkii, P. A., Genembre, L. and Khodakov, A. Y. (2007). Cobalt dispersion, reducibility, and surface sites in promoted silica-supported Fischer–Tropsch catalysts. **J. Catal.** 248: 143-157.
- Groot, F. D. (2001). High-resolution X-ray emission and X-ray absorption spectroscopy. **Chem. Rev.** 101: 1779-1880.
- Guczi, L. (2005). Bimetallic nano-particles: featuring structure and reactivity. **Catal. Today.** 101: 53-64.
- Guczi, L., Bazin, D., Kovacs, I., Borko, L., Schay, Z, Lynch, J., Parent, P., Lafon, C., Stefler, G., Koppány, Zs. And Sajó, I. (2002). Structure of Pt–Co/Al<sub>2</sub>O<sub>3</sub> and Pt–Co/NaY bimetallic catalysts: Characterization by *In Situ* EXAFS, TPR, XPS and by activity in Co (Carbon Monoxide) hydrogenation. **Topics in Catalysis.** 20: 129-139.
- Haneda, M., Kintaichi, Y. and Hamada, H. (2003). Alkali metal-doped cobalt oxide catalysts for NO decomposition. **Appl. Catal. B-Environ.** 46: 473-482.
- Jacobs, G., Das, T. K., Zhang, Y., Li, Racollet, J. G. and Davis, B. H. (2002). Fischer–Tropsch synthesis: support, loading, and promoter effects on the reducibility of cobalt catalysts. **Appl. Catal. A-Gen.** 233: 263-281.
- Jacobs, G., Ji, Y., Davis, B. H., Cronauer, D., Kropf, A. J. and Marshall, C. L. (2007). Fischer–Tropsch synthesis: Temperature programmed EXAFS/XANES investigation of the influence of support type, cobalt loading, and noble metal

- promoter addition to the reduction behavior of cobalt oxide particles. **Appl. Catal. A- Gen.** 333: 177-191.
- Klysubun, W., Sombunchoo, P., Wongprachanukul, N., Tarawarakarn, P., Klinkhieo, S., Chairapa, J. and Songsiriritthigul P. (2007). Commission and performance of x-ray absorption beamline at the Siam photon Laboratory. **Nucl. Instrum. Meth. A.** 582: 87-89.
- Kwak, C., Park, T.-J. and Suh, D. J. (2005). Effects of sodium addition on the performance of PtCo/Al<sub>2</sub>O<sub>3</sub> catalysts for preferential oxidation of carbon monoxide from hydrogen-rich fuels. **Appl. Catal. A-Gen.** 278: 181-186.
- Lapidus, A., Krylova, A., Borovkov, V. and Zaitsev, A. (1991). Hydrocarbon synthesis from carbon monoxide and hydrogen on impregnated cobalt catalysts Part I. Physico-chemical properties of 10% cobalt/alumina and 10% cobalt/silica. **Appl. Catal.** 73: 65-81.
- Li, W., Yu, S. Y., Meitzner, G. D. and Iglesia, E. (2001). Structure and properties of cobalt-exchanged H-ZSM5 catalysts for dehydrogenation and dehydrocyclization of alkanes. **J. Phys. Chem. B.** 105: 1176-1184.
- Lee, J-F, Wei, A-C. and Chao, K-J. (2003). In situ X-ray absorption spectroscopic study on the reducibility of cobalt-containing aluminophosphate molecular sieves. **J. Mol. Catal. A-Chem.** 203: 165-172.
- Lu, G., Hoffer, T. and Guzzi, L. (1992). Reducibility and CO hydrogenation over Pt and Pt-Co bimetallic catalysts encaged in NaY-zeolite. **Catal. Lett.** 14: 207-220.
- Mcnicol, B.D., Gentry, S.J., Jones, A. and Hurst, N.W. (1982). Temperature programmed reduction., **Catal. Rev.-Sci. Eng.** 24: 233-309.

- O-Shea, V. A. P., Homs, N., Pereira, E. B., Nafria, R. and Piscina, P. R. (2007). X-ray diffraction study of  $\text{Co}_3\text{O}_4$  activation under ethanol steam-reforming. **Catal. Today.** 126: 148-152.
- Profeti, L. P.R., Ticianelli, E. A. and Assaf, E. M. (2008). Production of hydrogen by ethanol steam reforming on  $\text{Co}/\text{Al}_2\text{O}_3$  catalysts: Effect of addition of small quantities of noble metals. **J. Power Sources.** 175: 482-489.
- Ravel, B. and Newville, M. (2005). Athena, Artemis, Hephaestus: data analysis for X-ray absorption spectroscopy using IFEFFIT. **J. Synchrotron Rad.** 12: 537-541.
- Rosynek, M. P. and Polansky, C. A. (1991). Effect of cobalt source on the reduction properties of silica-supported cobalt catalysts. **Appl. Catal.** 73: 97-112.
- Rouquerol, F. and Rouquerol, J. K. S. (1999). **Adsorption by powders and porous solids, principles, methodology and applications**, Academic Press, p.220.
- Tang, Q., Zhang, Q., Wang, P., Wang, Y. And Wan, H. (2004). Characterizations of cobalt oxide nanoparticles within faujasite zeolites and the formation of metallic cobalt. **Chem. Mater.** 16: 1967-1976.
- Uytterhoeven, J. B. (1978). Tailoring texture of amorphous aluminosilicates by using organic additives. **Acta Phys. Chem.** 24: 53-57.
- Wang, W-J., Lin, H-Y. and Chein, Y-W. (2005). Carbon monoxide hydrogenation on cobalt/zeolite catalysts. **J. Porous Mat.** 12: 5-12.
- Wittayakun, J., Khemthong, P. and Prayoonpokarach, S. (2008). Synthesis of zeolite NaY from rice husk silica. **Korean J. Chem. Eng.** 25: 861-864.

Xu, B., Rotunno, F., Bordiga, S., Prins, R. and Bokhoven, J. A. (2006).

Reversibility of structural collapse in zeolite Y: Alkane cracking and characterization. **J. Catal.** 241: 66-73.

**CHAPTER VI**

**REDUCIBILITY OF Co AND Co-Pt SUPPORTED ON**

**ZEOLITE NaY INVESTIGATED BY X-RAY**

**ABSORPTION AND THE CATALYTIC PERFORMANCE**

**FOR BUTANE HYDROGENOLYSIS**

**Abstract**

The hydrogenolysis of alkanes over supported metal catalysts is an interesting hydrocarbon reaction for industrial applications. The aim of this work was to investigate an enhancement of platinum as a second metal for butane hydrogenolysis on cobalt (Co) supported on zeolite NaY. The monometallic xCo/NaY and bimetallic xCo-Pt/NaY catalysts were prepared by impregnation method and characterized by X-ray diffraction, ammonia adsorption-desorption, X-ray absorption (both XANES and EXAFS). Both catalysts were tested for butane hydrogenolysis in a flow reactor at atmospheric pressure. Because both monometallic and bimetallic catalysts with low Co content were difficult to reduce to active form at 400°C in H<sub>2</sub> for 5 h, the focus was on 6 wt% and 10 wt% Co loading, all with fixed Pt loading at 1 wt%. The monometallic with Co loadings 6 wt% and 10 wt% showed percentage of reduction of 71.20% and 93.80%, respectively, while bimetallic catalyst show higher percentages of reduced Co of 95.90% and 98.80%, respectively indicating that the addition of Pt assisted Co reduction. The catalytic activities of the bimetallic catalysts were higher

than monometallic catalysts. After 30 minutes, the conversion on xCo/NaY was 40% with methane as a product while the conversions on the bimetallic catalysts were almost 100%. The products on the bimetallic catalysts after 30 minutes were methane and ethane while propane was observed after 60 minutes. Thus, the presence of Pt enhanced reducibility and performance of butane hydrogenolysis on Co/NaY

## 6.1 Introduction

Hydrogenolysis is structure sensitive reaction interesting for both theoretical aspects as one of the most fundamental hydrocarbon reactions and for industrial applications. Hydrogenolysis of simple alkanes ( $C_1 - C_4$ ) over metal catalysts has been known for many years and has been incorporated into many reviews of hydrocarbon reactions (Mériaudeau et al., 1997; Jackson et al., 1999; Rice and Keptner, 2004)]. *n*-Butane is also useful molecules for studying bond shift isomerisation reactions. In the reforming of light hydrocarbons (in the range  $C_5 - C_{11}$ ) hydrogenolysis has to be minimized to achieve a better selectivity of production of aromatics. Therefore a greater understanding of the hydrogenolysis mechanism, and the identification and removal of the reactive sites responsible for the reaction should lead to more highly selective reforming catalysts. Although the hydrogenolysis of butane has been studied extensively for many years (Jackson et al., 1998; Chotisuwan et al., 2006; Haddad et al., 1995) there is not much study for cobalt on this reaction.

It is well known that cobalt is one of the most active catalyst for industrial chemistry such as Fischer-Tropsch synthesis, steam reforming and hydrogenolysis reaction. Our previous paper reported the reducibility of cobalt supported on zeolite Y in  $Na^+$  and  $H^+$  forms prepared by impregnation method as described elsewhere in

chapter V. The natures of the supported cobalt before and after reduction were investigated by X-ray absorption spectroscopy (XAS), mainly with X-ray absorption near edge spectroscopy (XANES). The reducibility of cobalt with 6 wt% loading depended on the form of zeolite, higher for the oxides on sodium form. Thus, the 6Co/NaY was significantly more active for butane hydrogenolysis than 6Co/HY when pretreated with similar conditions. This work further investigated characteristics of monometallic cobalt and bimetallic cobalt-platinum supported on zeolite NaY before testing on butane hydrogenolysis. The reduced catalysts before the reaction testing were characterized by XAS using both both XANES and extended X-ray absorption fine structure (EXAFS) spectroscopy along with X-ray diffraction (XRD) and ammonia temperature programmed desorption (NH<sub>3</sub>-TPD). We aimed to understand the characteristics of catalysts that had influence on activities and selectivities. The catalysts after the reaction testing (spent catalysts) were also characterized by both XANES and EXAFS.

## **6.2 Experimental**

### **6.2.1 Catalyst preparation**

Zeolite Y in sodium form (NaY) was synthesized with rice husk silica (RHS) with a method in the literature (Wittayakun et al., 2008). The obtained NaY was used as a support for the preparation of monometallic cobalt and bimetallic cobalt-platinum by impregnation.

Monometallic xCo/NaY catalysts were prepared by impregnation with aqueous solutions of CoCl<sub>2</sub>·6H<sub>2</sub>O on NaY to produce cobalt loading of 1 wt%, 6 wt%, and 10 wt%. Bimetallic xCo-1Pt/NaY catalysts were prepared from a solution contains both



$\text{CoCl}_2 \cdot 6\text{H}_2\text{O}$  and  $\text{H}_2\text{PtCl}_6$  precursors on NaY with a fixed Pt loading of 1 wt% and Co loading of 1 %wt, 6 %wt, and 10 %wt. The catalysts were air dried at room temperature for 24 h, dried in a hot air oven at 120°C for 3 h and calcined in a muffle furnace at 300°C for 3 h. The cobalt content in both xCo/NaY and xCo-1Pt/NaY were determined by ICP-OES spectrometer (Perkin Elmer, Optima 7000DV).

### 6.2.2 Catalysts characterization

Nitrogen adsorption-desorption analysis were carried out on a Quantachrome (NOVA 1200e) gas adsorption analyzer and specific surface areas of the catalysts were calculated from BET method. Each sample was pressed (1000 N/m<sup>2</sup>), crushed and sieved to 200 μm – 350 μm and dried for 3 h at 120°C. The sample about 0.2 g was then packed and degassed at 300°C for 3 h before the measurement. Data were collected at the liquid nitrogen temperature.

Ammonia temperature programmed desorption (NH<sub>3</sub>-TPD) was measured by Raczek Analysetechnik equipped with thermal conductivity detector (TCD). The sample about 0.30 g was packed in a tubular U-shaped quartz cell and sandwiched with quartz wool on both sides. The pre-treatment or conditioning was performed from room temperature to 450°C in He flow (50 ml/min) at atmospheric pressure with a heating rate of 10°C/min and held for 1 h before cooling down to room temperature. Then ammonia was flowed over the sample at 70°C for 30 minutes and the excess ammonia was flushed out by heating with a rate of 10°C/min to 130°C by He at a flow rate of 50 ml/min and held for 17 hours. Then the temperature was raised to 500°C with a heating rate of 10°C/min. The amount of desorbed ammonia was detected by a thermal conductivity detector and the peak areas were calculated by origin programs.

The local environment of Co in both monometallic and bimetallic on NaY was studied by XANES and EXAFS at beamline 8 of Synchrotron Light Research Institute (Public Organization), Thailand. A double Ge (220) crystal monochromator was used for selection of photon energy. X-ray absorption experiments were performed on calcined, reduced, and spent catalysts samples. Samples were pressed into a frame covered by polyimide tape and mounted onto the sample holder. The XANES and EXAFS spectra of Co K-edge were obtained at room temperature in transmission mode using gas-filled ionization chamber filled with Ar gas. Intensity of the incident x-ray beam ( $I_0$ ) with 49 mbar of Ar and transmitted x-ray beam ( $I_1$ ) with 269 mbar of Ar were monitored by a 10-cm long ion chamber and a 40-cm long ion chamber, respectively. The photon energy was calibrated by a Co foil at 7709 eV. For the XANES measurement, the photon energy was scanned from -30 eV below the edge to 80 eV above the edge. EXAFS data were measured by three time scans and averaged from -100 eV to 700 eV.

Linear combination fit of XANES spectra and data reduction of EXAFS spectra were extracted by Athena program (Ravel and Newville, 2005) and analyzed with EXAFSPAK (George and Pickering, 2006) programs. Linear combination fit and the curve fitting processes were similar to those in the literature (Khemthong et al., 2009).

### **6.2.3 Catalytic testing on butane hydrogenolysis**

The catalytic performance for butane hydrogenolysis was determined in a tubular flow reactor. Each catalyst powder was pressed with 500 N/m<sup>2</sup> then crushed and sieved to 200  $\mu\text{m}$  – 350  $\mu\text{m}$  and dried at 120°C for 5 h to remove adsorbed water. Approximately 0.1 g of catalyst diluted with 0.9 g of  $\alpha\text{-Al}_2\text{O}_3$  before packing into a

quartz tube with diameters 6 mm, pretreated at 100°C in He flow (50 ml/min) for 1 h and reduced under H<sub>2</sub> (50 ml/min) at 400°C for 5 h. A gas reaction mixture containing C<sub>4</sub>H<sub>10</sub>, H<sub>2</sub> and He with flow rate ratio of 0.5 : 30 : 69.5 ml/min was flowed into the reactor from 300°C – 500°C and the products were analyzed by an on-line GC equipped with TCD.

## 6.3 Results and discussion

### 6.3.1 N<sub>2</sub> adsorption-desorption analysis on surface of Co catalysts

The adsorption isotherms of xCo/NaY and xCo-1Pt/NaY catalysts are in Appendix A. They all had adsorption isotherm type I with hysteresis loop type A that attributed to cylindrical pores of microporous materials. Their physical properties are summarized in Table 6.1. From the result, surface area of the samples decreased when metal content were increased, possibly from partial blockages of the pore channel of zeolite Y by the metal. However, the surface area of mono and bi-metallic were not significant different.

**Table 6.1** Textural physical properties of samples xCo/NaY and xCo-1Pt/NaY

No.	Sample name	BET surface area (m <sup>2</sup> /g)	Pore Volume (cm <sup>3</sup> /g)
Monometallic catalysts			
1	1Co/NaY	572.79	0.4506
2	6Co/NaY	414.59	0.4001
3	10Co/NaY	230.33	0.2738

**Table 6.1** (continued) Textural physical properties of samples xCo/NaY and xCo-1Pt/NaY

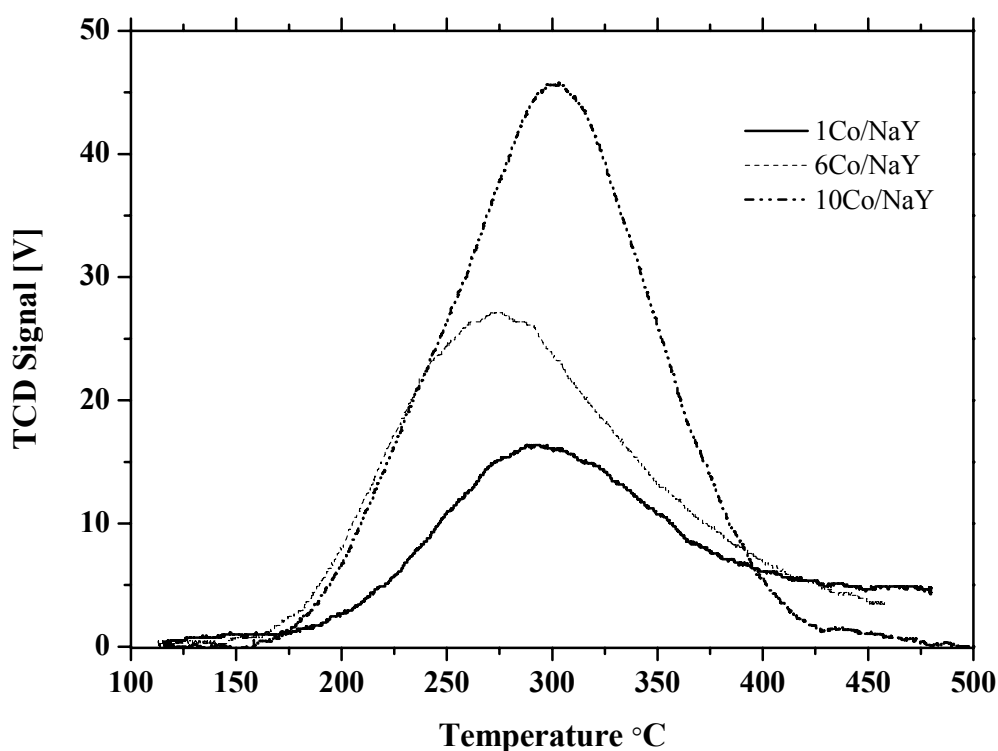
No.	Sample name	BET surface area (m <sup>2</sup> /g)	Pore Volume (cm <sup>3</sup> /g)
Bimetallic catalysts			
1	1Co-1Pt/NaY	580.42	0.4399
2	6Co-1Pt/NaY	439.72	0.3927
3	10Co-1Pt/NaY	209.29	0.2021

### 6.3.2 NH<sub>3</sub>-TPD on their acidity of Co catalysts

Thermal desorption studies using probe molecule are useful in determining the number and strength of binding sites on a catalyst. Ammonia often overestimates the quantity of acid sites by penetrating into all pores of the solid. Also, ammonia is a very basic molecule which is capable of titrating weak acid sites which may not contribute to the activity of catalysts. The strongly polar adsorbed ammonia is also capable of adsorbing additional ammonia from the gas phase. These molecules are protonated to form ammonium ions by the acid sites and decompose to ammonia product. Figure 6.1 shows NH<sub>3</sub>-TPD profiles of monometallic xCo/NaY catalysts.

NH<sub>3</sub>-TPD profiles were obtained by raising the sample temperature with a heating rate 10°C/min. In general, a zeolite in sodium form showed only one broad peak corresponding to Lewis acid sites (Zang et al., 2006). All samples gave one peak and the peak area increased with cobalt loading. From this result indicated that increased in adsorption capacity of NH<sub>3</sub> related to increasing of cobalt content. The amount of acid sites and cobalt loading are plot in Figure 6.3 and the actual values are included in Table 6.2. All of the experimental data presented are consistent with the

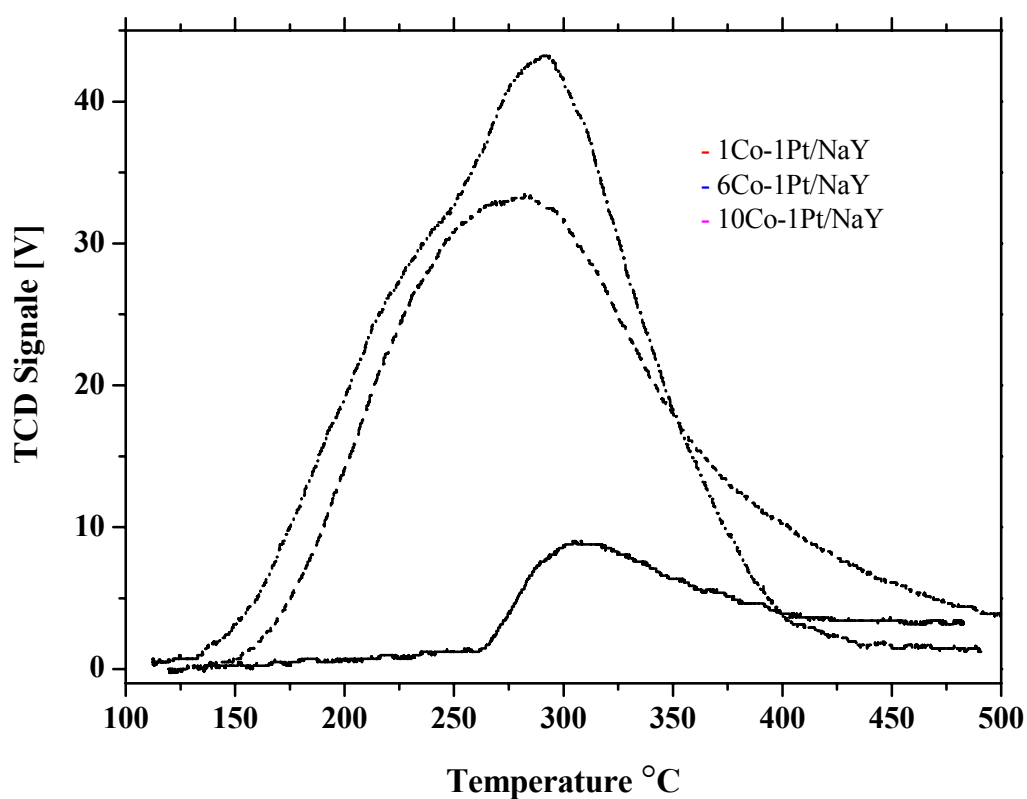
framework Co being present as Co (II) in samples. There by creating  $\text{Co}^{2+}$  ions at cationic position of zeolite Lewis acid sites and almost site for lone pair orbital of  $\text{NH}_3$  reacts with the empty orbitals of  $\text{Co}^{2+}$  (Idariss, 2008) indicate that cobalt oxide was form out side the structure of zeolite.



**Figure 6.1**  $\text{NH}_3$ -TPD profile of monometallic  $x\text{Co}/\text{NaY}$  catalysts

The  $\text{NH}_3$ -TPD profiles of bimetallic  $\text{CoPt}/\text{NaY}$  are shown in Figure 6.2 and the actual values are included in Table 6.2. The ammonia desorption on  $1\text{Co}-1\text{Pt}/\text{NaY}$  was apparently lower than that of  $1\text{Co}/\text{NaY}$  probably because the presence of Pt on the same support. The decrease in desorption temperature was observed when amount of Co loading increased in both mono- and bimetallic catalysts. This influence has been attributed to repulsive adsorbate-adsorbate interactions between adjacent ammonia

molecules at high coverage that weaken the adsorption strength. The incorporation of cation such as  $Zn^{2+}$  into Bronsted acid site of zeolite H-ZSM-5 increased the Lewis acid sites which lead to ion exchange with OH group of zeolite and can caused the decrease of desorption temperature below than 500°C (Haken et al., 2001; Vrålstad et al., 2006).



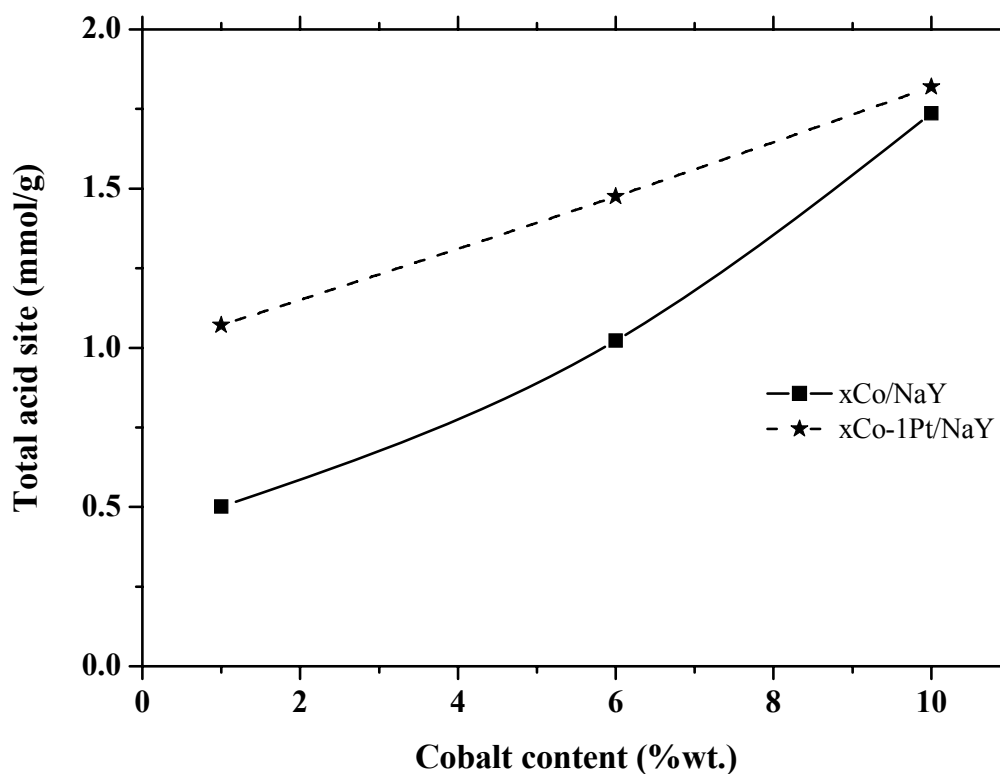
**Figure 6.2**  $NH_3$ -TPD profile of bimetallic xCo-Pt/NaY catalysts

The amounts of ammonia desorbed that increased with cobalt loading are shown in the plot in Figure 6.3. The total acid site was increased as increased Co content indicated that the Lewis acid site was generated and related to the Co loading. Mhamdi et al. (2009) studied Co exchanged with H-ZSM-5 and found that Co inhibits the strong acidity and generates new acids site which are Lewis type. An incorporation

of Pt in the bimetallic catalysts caused an increase of Lewis acidity in the cobalt catalysts.

**Table 6.2** Maximum desorption temperature and total acid sites from NH<sub>3</sub>-TPD results

Catalysts	Max. Temperature (°C)	Total acid site (mmol/g)
<b>Monometallic</b>		
1Co/NaY	298	0.5009
6Co/NaY	275	1.0230
10Co/NaY	303	1.7368
<b>Bimetallic</b>		
1Co-1Pt/NaY	308	0.1663
6Co-1Pt/NaY	283	1.4747
10Co-1Pt/NaY	300	1.8191



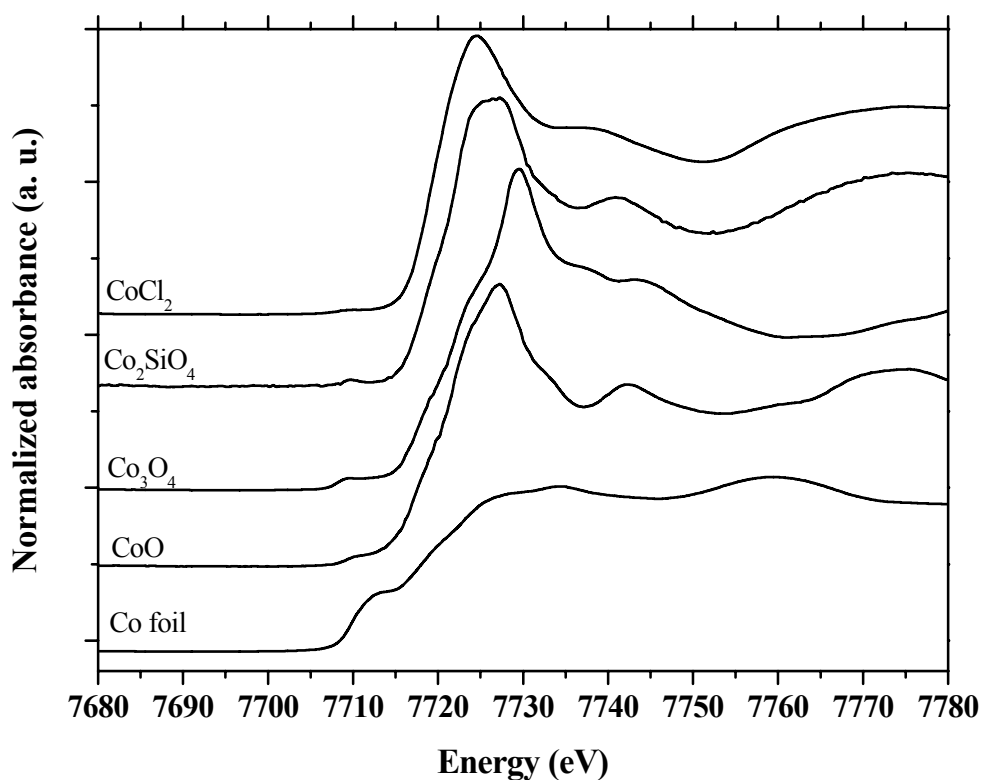
**Figure 6.3** Total acid sites as function of cobalt content of xCo/NaY and xCo-1Pt/NaY

### 6.3.3 Nature of Co in monometallic catalysts investigated by XANES

XANES is a method that allows a determination of oxidation state or valence state of metal in the catalyst samples that can be deduced from energy shift of the X-ray absorption edge. With and increase of oxidation state, the absorption features in the XANES spectrum are shifted to higher energies. An important feature of the XANES profile is a pre-edge which is a small peak before the rise of the edge. The pre-edge can be observed in several Co samples in this work. This peak is attributed to a  $1s \rightarrow 3d$  transition which is normally dipole-forbidden. However, it becomes allowed when the metal has tetrahedral coordination (Vrålstad et al., 2006; Profeti et al., 2008; Choy et al., 2001; Groot 2001; Drozdova et al., 2002). In this part we would



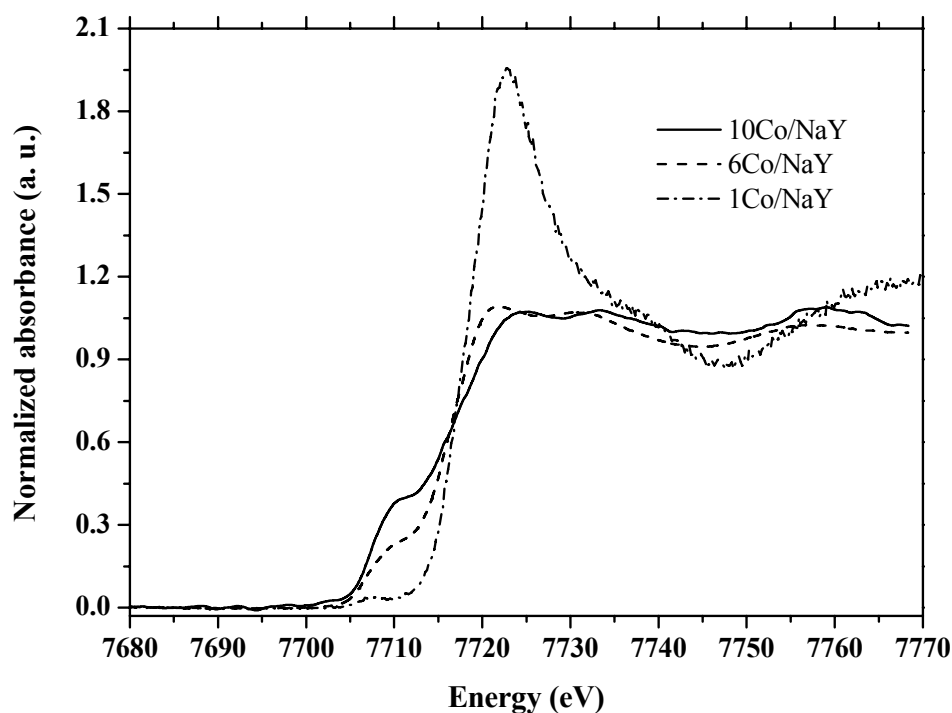
first discuss the XANES results of mono- and bimetallic catalysts before and after reduction. Then the EXAFS results were discussed. The XANES and EXAFS results were would be discussed again after the catalysts were tested for butane hydrogenolysis.



**Figure 6.4** The XANES spectra of Co K-edge of reference standard materials

The normalized XANES spectra of Co K-edge of reference materials are shown in Figure 6.4. These patterns are used as fingerprints to determine oxidation state and site symmetry of cobalt species. Co in  $\text{CoCl}_2$ , and  $\text{CoO}$  has octahedral structure; that in  $\text{Co}_2\text{SiO}_4$  has tetrahedral structure (Wu et al., 2007), and that in  $\text{Co}_3\text{O}_4$  has mixed tetrahedral and octahedral structures (Ramallo-Lopez et al., 2004; Vrålstad

et al., 2006). Figure 6.5 shows XANES spectrum of reduced Co/NaY with Co loading of 1 wt%, 6 wt% and 10 wt%.



**Figure 6.5** XANES spectra of reduced xCo/NaY (x = 10 wt%, 6 wt%, and 1 wt%, respectively)

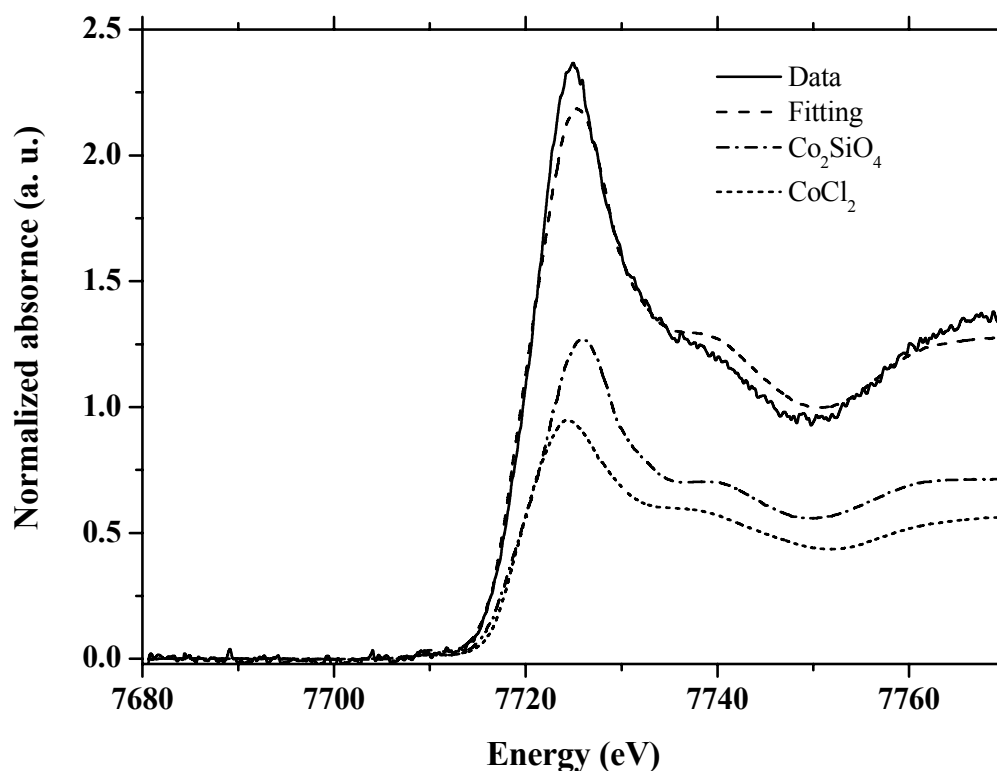
The Co K-edge in the XANES spectrum of reduced 1Co/NaY showed a shape similar to those of  $\text{CoCl}_2$  spectrum suggesting that after reduction cobalt remained in a form of divalent  $\text{Co}^{2+}$  in octahedral structure. The color of reduced 1Co/NaY was dark blue which is characteristic of octahedral  $\text{Co(II)}$ , due to the transition of  ${}^4\text{T}_{1g}(\text{F}) \rightarrow {}^4\text{T}_{1g}(\text{P})$  (Vrålstad et al., 2006). The oxidation state can be determined by the position of the absorption peak, because the photon energy required to excite an electron is dependent on the oxidation state. The main absorption peak as white line is attributed to the allowed transition from 1s to 4p orbital as a main component and absorption

edge found at 7720 eV, with the spectrum of  $\text{CoCl}_2$  reference standard. The percentage of reduction was determined by a linear combination fit as shown in Figure 6.6.

The XANES spectrum of reduced 6Co/NaY and 10Co/NaY were similar to that of the Co metal foil. The absorption edge shifted to lower energy as  $\text{Co}^{2+}$  is reduced to Co metal indicating that cobalt oxides were reduced. The percentages of Co reduction of these catalysts were determined by a linear combination fit as shown in Figure 6.7 and 6.8, respectively. The XANES spectrum of reduced catalysts suggested that a catalyst with a low amount of Co was difficult to reduce because Co was well dispersed on the NaY support. The cobalt species formed small  $\text{CoO}_x$  clusters and had a strong metal-support interaction. It might form Co silicates with silanol groups of NaY leading to the formation of unreducible  $\text{CoO}_x$ . Li et al. (2001) studied the reducibility of Co in H-ZSM5 prepared by ion exchange and found that the Co species remained unreduced even at 1000°C for Co/Al ratio of 0.009 – 0.22 but reduced at in a higher Co loading (Co/Al = 0.22).

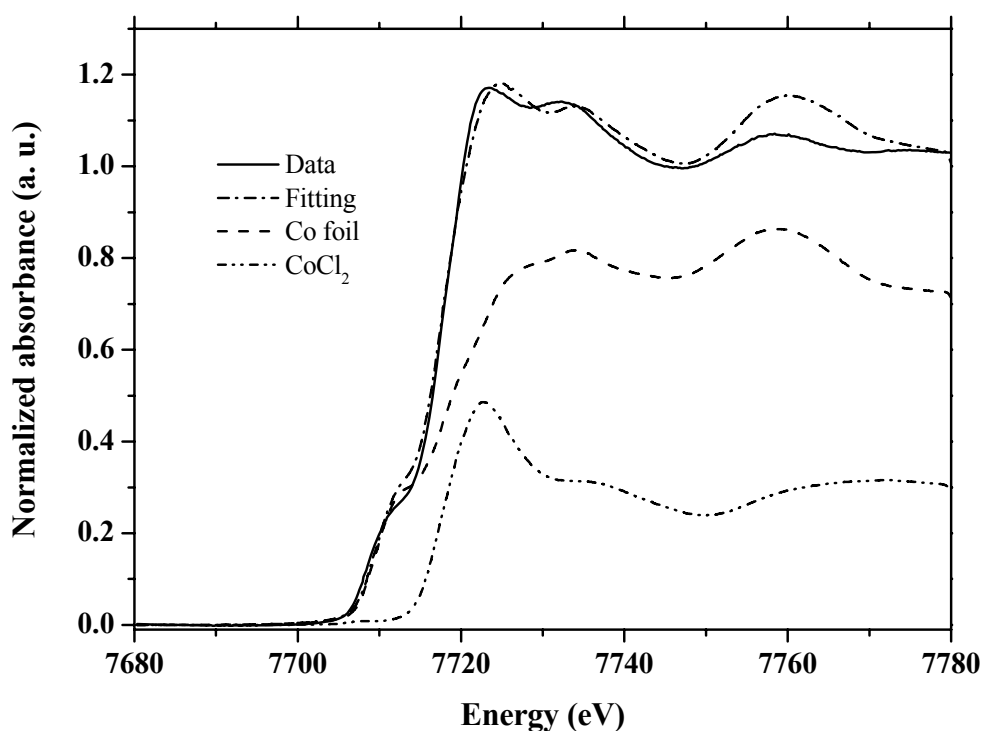
When a sample contains the same cation in two or more sites with different local structure and valence state, its XANES spectrum include the sum of all characters. Vice versa, an amount of the cation at each site can be determined from the XANES spectrum by a linear combination fit (Dominko et al., 2009). This calculation can be performed with the Athena program by simulating a linear combination of reference spectrum with known amount compared with the catalyst sample. The comparison will indicate the reducibility of the metal. In this work linear combination fit of reduced xCo/NaY samples were carried out. The fitting results are shown in Figures 6.6 – 6.8 for the cobalt loading of 1 wt%, 6 wt% and 10 wt%. Figure

6.6 shows result from a linear combination fit of freshly reduced 1Co/NaY compared with all reference materials. However, reduced cobalt as in cobalt foil was not observed and only  $\text{CoCl}_2$  and  $\text{Co}_2\text{SiO}_4$  were deduced from the fitting. The percentages of found components from the calculation are included in Table 6.3. The result indicated that cobalt in monometallic Co/NaY catalyst with low metal loading could not be reduced by this condition. We also conducted a linear combination fit of reduced Co/NaY with 3 wt% loading and found that the cobalt was not reducible as well.



**Figure 6.6** Linear combination fit of reduced 1Co/NaY compared with standard reference materials. Note that only observed components were included in the plot.

Because the metallic cobalt is an active form for hydrogenolysis (Khemthong et al., 2009), we would only used the catalyst with cobalt loading of 6 wt% and 10 wt% for the catalytic testing. Figure 6.7 shows result from a linear combination fit of reduced 6Co/NaY compared with all reference materials.

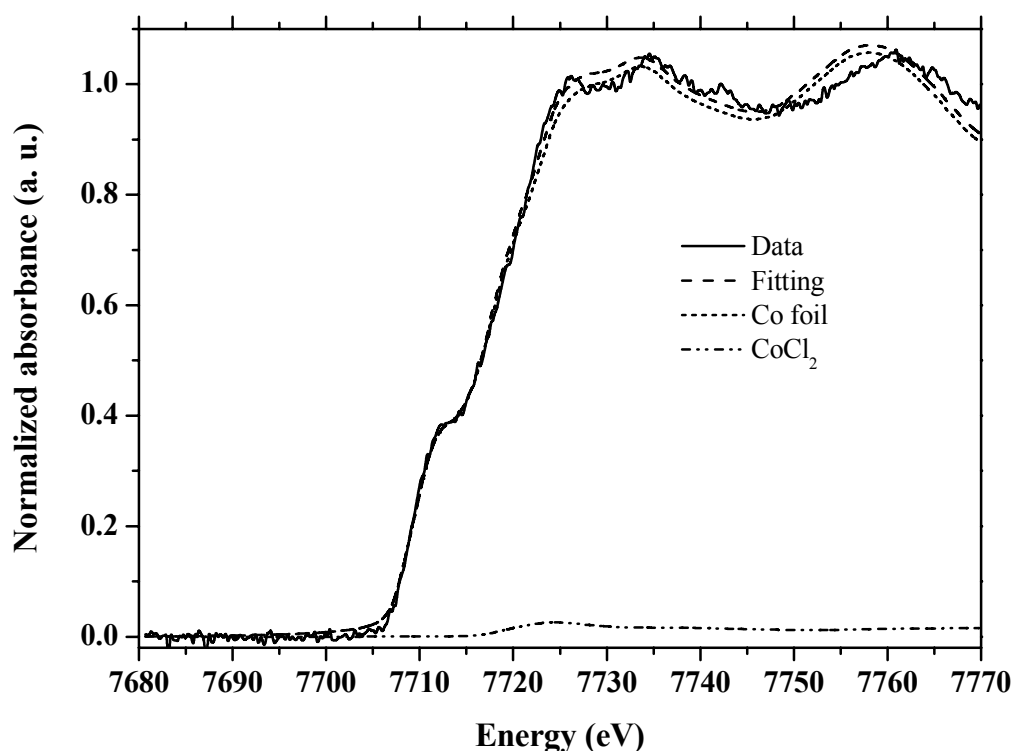


**Figure 6.7** Linear combination fit of reduced 6Co/NaY compared with standard reference materials. Note that only observed components were included in the plot.

However, only cobalt in metallic phase as in cobalt foil and  $\text{Co}^{2+}$  as in  $\text{CoCl}_2$  were deduced from the fitting. The result indicated that cobalt in monometallic 6Co/NaY catalyst could be reduced by this condition but not completely. A longer

reduction time or higher reduction temperature would complete the reduction. The percentages of found components from the calculation are included in Table 6.3.

Figure 6.8 shows result from a linear combination fit of reduced 10Co/NaY compared with all reference materials. The major component of this sample was deduced to be metallic cobalt and traces of  $\text{Co}^{2+}$  as in  $\text{CoCl}_2$  were suggested from the fitting. The result indicated that cobalt in monometallic 10Co/NaY catalyst could be reduced almost completely by this condition. The percentages of found components from the calculation are included in Table 6.3. This catalyst was expected to be more active than the other loadings.



**Figure 6.8** Linear combination fit of reduced 10Co/NaY compared with standard reference materials. Note that only observed components were included in the plot.

In order to quantify the amount of cobalt reduction form in the xCo/NaY catalyst after being reduced, the linear combination of the XANES spectra of Co<sub>x</sub>/NaY were calculated using XANES data and summarized in table 6.3. From the result found that only Co loading 1 wt% of Co was difficult to reduced regarding on at low percentage of loading induce high dispersion of Co and strong interaction which will effect on reducibility.

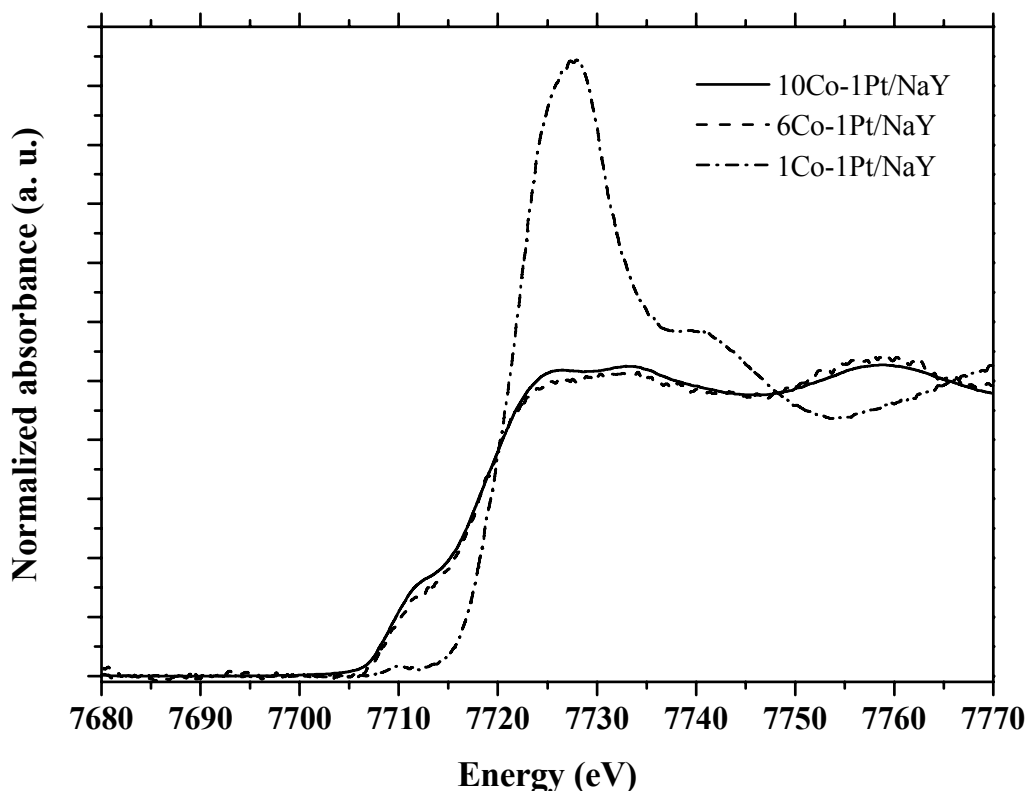
**Table 6.3** Percent reduction of cobalt in reduced xCo/NaY catalysts from linear combination fitting of XANES spectra and fitting parameters.

Group	Weight (%)	R-factor	Chi-square	Reduced chi-square
Reduced 1Co/NaY		0.0035	1.0596	0.0043
1: Co <sub>2</sub> SiO <sub>4</sub>	56.10			
2: CoCl <sub>2</sub>	43.90			
Reduced 6Co/NaY		0.0022	0.3508	0.0014
1: Co foil	75.80			
2: CoCl <sub>2</sub>	24.20			
Reduced 10Co/NaY		0.0005	0.0675	0.0003
1: Co foil	93.80			
2: CoCl <sub>2</sub>	6.20			

#### 6.3.4 Nature of Co in bimetallic catalysts investigated by XANES

Enhancement of Co reducibility by Pt was studied on the catalysts with similar Co loading to the monometallic catalysts supported on NaY with a fixed Pt loading of 1 wt%. The bimetallic catalysts were prepared by co-impregnation method and

reduced at the same condition to that of the monometallic catalysts to observe the enhancement of the reducibility after addition of Pt. The XANES spectra of reduced xCo-1Pt/NaY are shown in Figure 6.9.

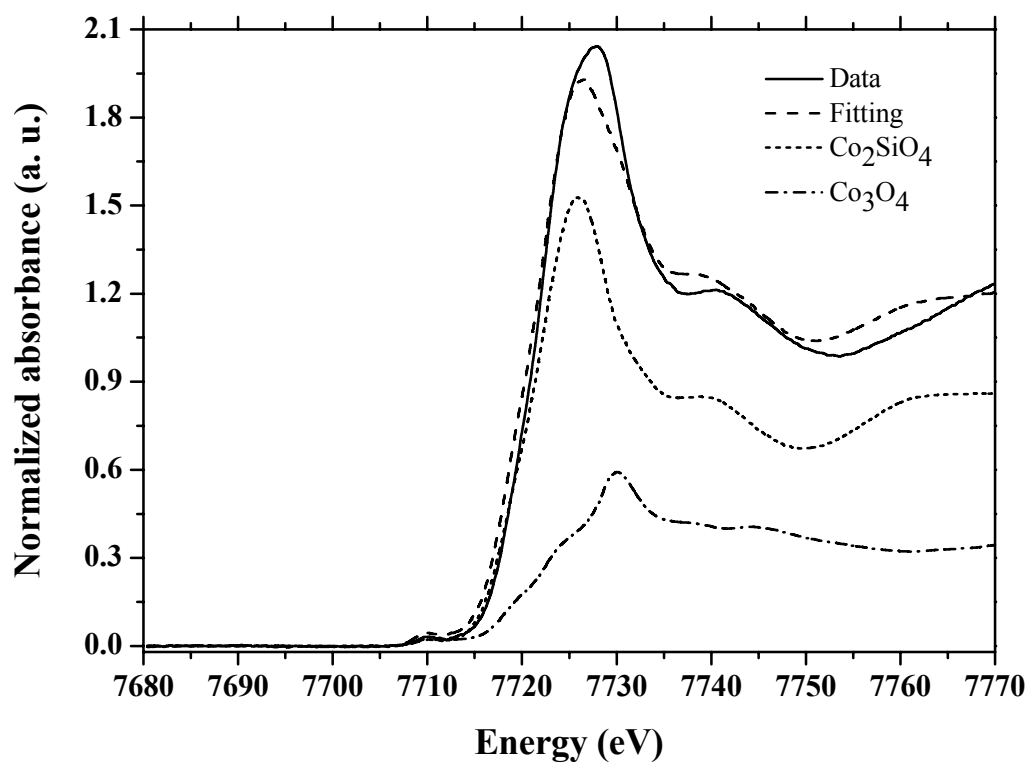


**Figure 6.9** The XANES spectrum of reduced xCo-1Pt/NaY supported on NaY (x = 10%wt, 6%wt, and 1%wt, respectively)

The spectrum of reduced 1Co-1Pt/NaY was significantly different from that of reduced 6Co-1Pt/NaY and 10Co-1Pt/NaY. The spectra of 1Co-1Pt/NaY showed a small pre-edge which is a characteristic of distorted octahedral geometry (Vrålstad et al., 2006). During calcination mixed oxides, cobalt aluminate or cobalt silicate was generated and these species could strongly interact with surface of NaY as Co-O-Al or

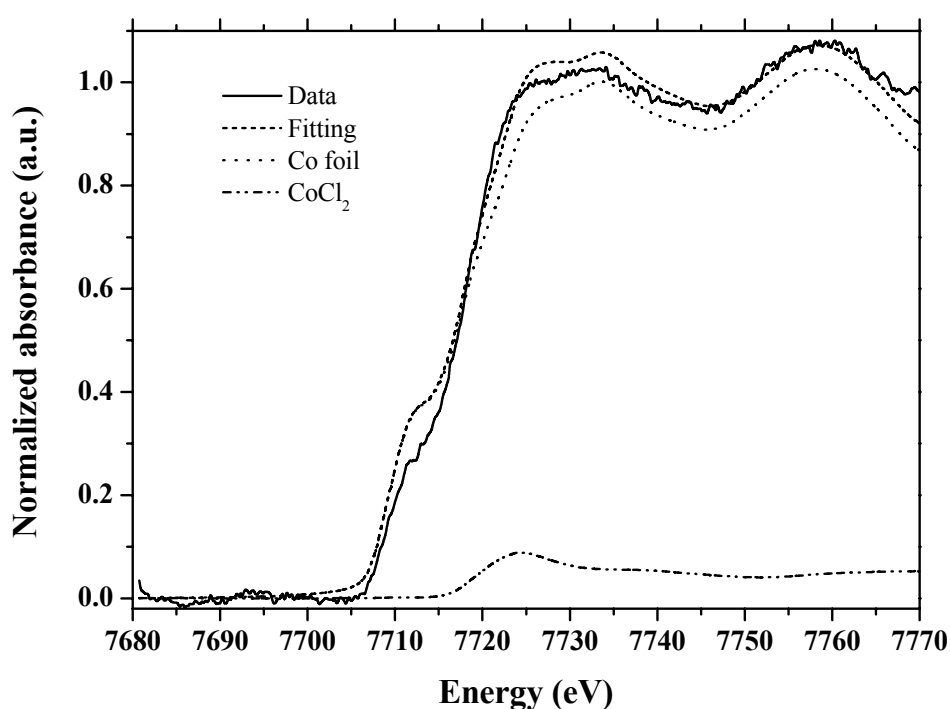


Co-O-Si, respectively. These species could not be reduced at mild condition and more reducible at high temperature (400°C – 800°C) (Jacobs et al., 2007; Wang et al., 1991). In addition, a small amount of  $\text{Co}_3\text{O}_4$  was difficult to reduce at mild conditions. The percentage of reduction of xCo-1Pt/NaY with Co loading of 1 wt%, 6 wt% and 10 wt% was determined by a linear combination fit. The fitting results are shown in Figures 6.10 – 6.12 and the calculated values and parameters are listed in Table 6.4. Figure 6.10 shows result from a linear combination fit of freshly reduced 1Co-1Pt/NaY compared with all reference materials.



**Figure 6.10** Linear combination fit of reduced 1Co-1Pt/NaY compare with standard reference material. Note that only observed components were included in the plot.

Similar result to the monometallic 1Co/NaY was observed that metallic cobalt was not observed. Only  $\text{Co}_2\text{SiO}_4$  and  $\text{Co}_3\text{O}_4$  were deduced from the fitting. The percentages of suggested components from the calculation are included in Table 6.4. The result indicated that cobalt in bimetallic catalyst with low metal loading could not be reduced by this condition.

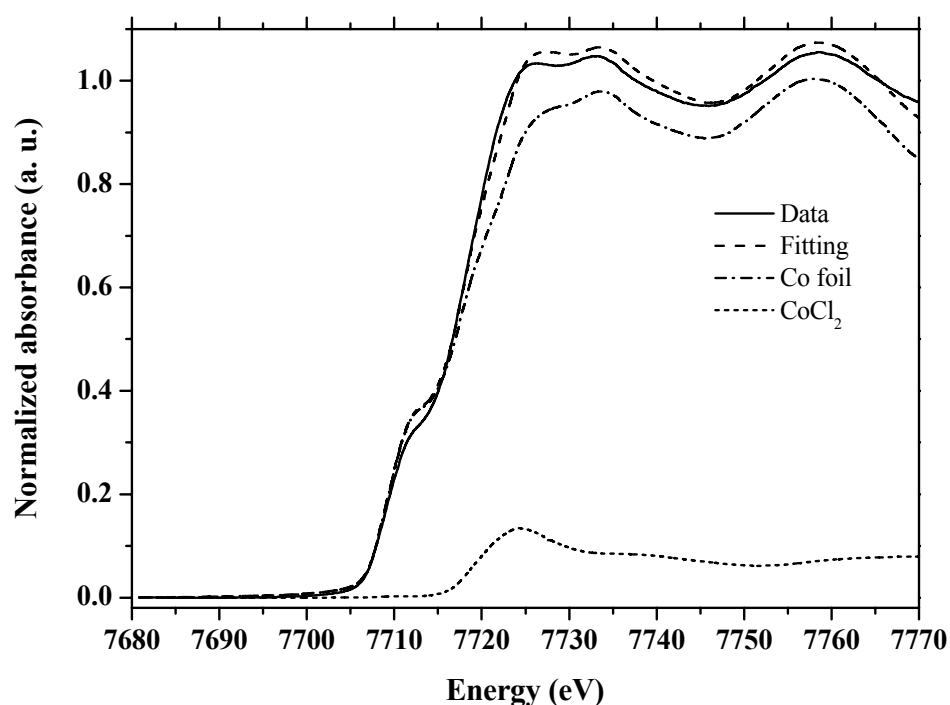


**Figure 6.11** Linear combination fit of reduced 6Co-1Pt/NaY compare with standard reference material. Note that only observed components were included in the plot.

The incorporation of Pt at this loading could not enhance the reducibility of cobalt. Other researchers reported that the reduction was strongly influenced by the

particle size of Co crystallite (Jacobs et al., 2007; Said et al., 2006) with smaller, more interacting particles (6 nm) being more difficult to reduce than larger crystallites.

The reducibility of cobalt was significantly higher in 6Co-1Pt/NaY. This phenomenon was similar to the monometallic catalyst that the reducibility increased with the metal loading. As shown in Figure 6.11, the major cobalt component was in metallic form with a trace amount of  $\text{CoCl}_2$ .



**Figure 6.12** Linear combination fit of reduced 10Co-1Pt/NaY compare with standard reference material. Note that only observed components were included in the plot.

The percentage of reduced cobalt from linear combination fit (Table 6.4) was much higher than the percentage of reduction in the monometallic catalyst with the same cobalt loading. This result suggested an enhancement of reduction by Pt. Figure

6.12 shows result from a linear combination fit of reduced 10Co-1Pt/NaY compared with all reference materials. The reduction of cobalt in this catalyst was nearly complete. Lapidus suggested that at a high Co loading (10 wt%), there was more oxidic cobalt surface phase which was not stabilized by interaction with support that could be reduced easily. An addition of Pt to this loading could also enhance the cobalt reducibility. However, the enhancement was not significant (namely, from 93.8% to 98.8%) as the reducibility was already increased by increasing cobalt loading. The result of linear combination curved fitting of bimetallic 10Co-1Pt/NaY was also summarized in Table 6.4.

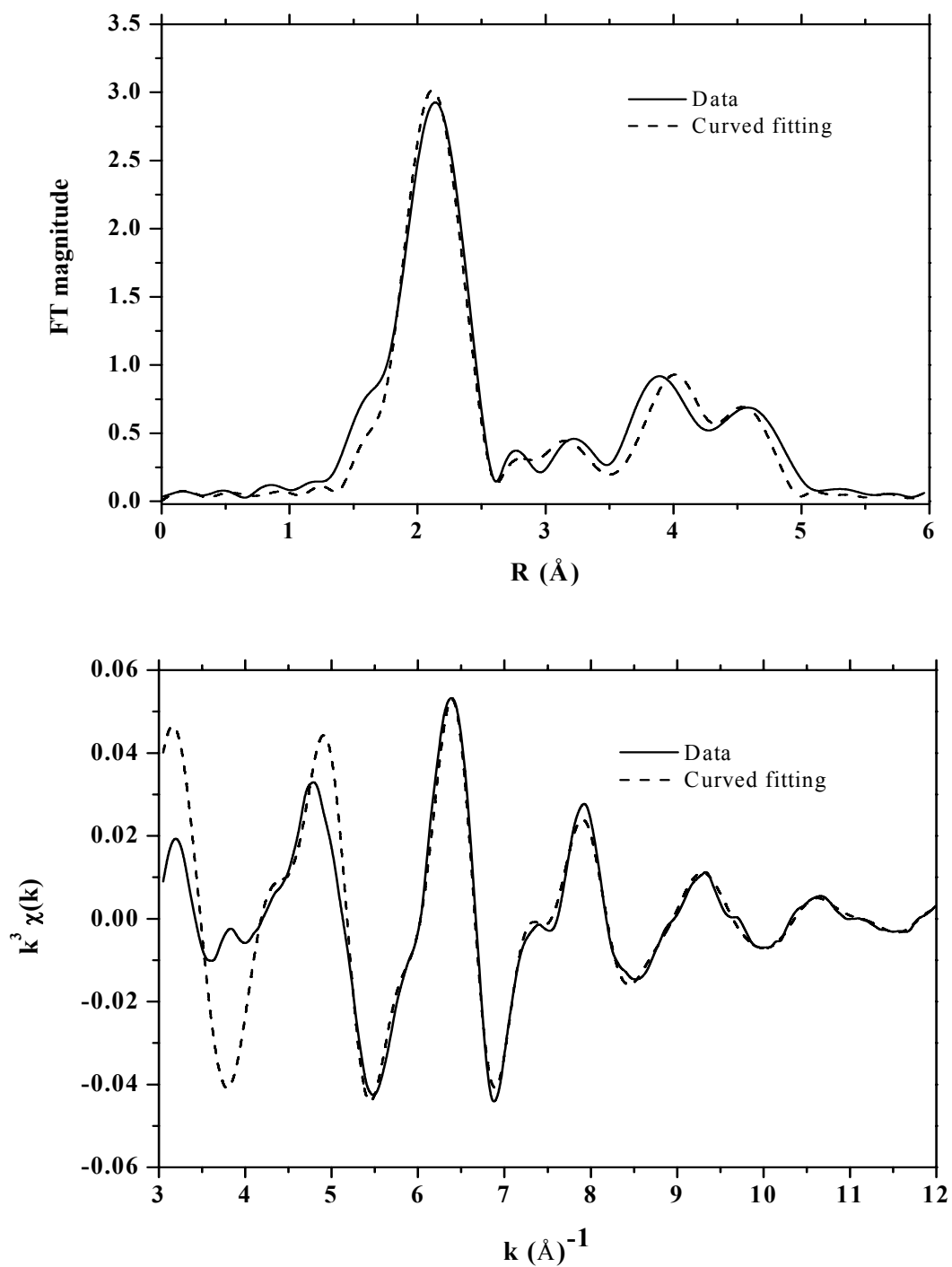
**Table 6.4** Percent reduction of cobalt in reduced xCo-1Pt/NaY catalysts from linear combination fitting of XANES spectra and fitting parameters.

Group	Weight (%)	R-factor	Chi-square	Reduced chi-square
<hr/>				
Reduced 1Co-1Pt/NaY		0.0035	1.1409	0.0046
1: Co <sub>2</sub> SiO <sub>4</sub>	67.60			
2: Co <sub>3</sub> O <sub>4</sub>	32.40			
Reduced 6Co-1Pt/NaY		0.0057	0.1587	0.0032
1: Co foil	95.90			
2: CoCl <sub>2</sub>	4.10			
Reduced 10Co-1Pt/NaY		0.000484	0.07513	0.0003
1: Co foil	98.80			
2: CoCl <sub>2</sub>	1.20			
<hr/>				

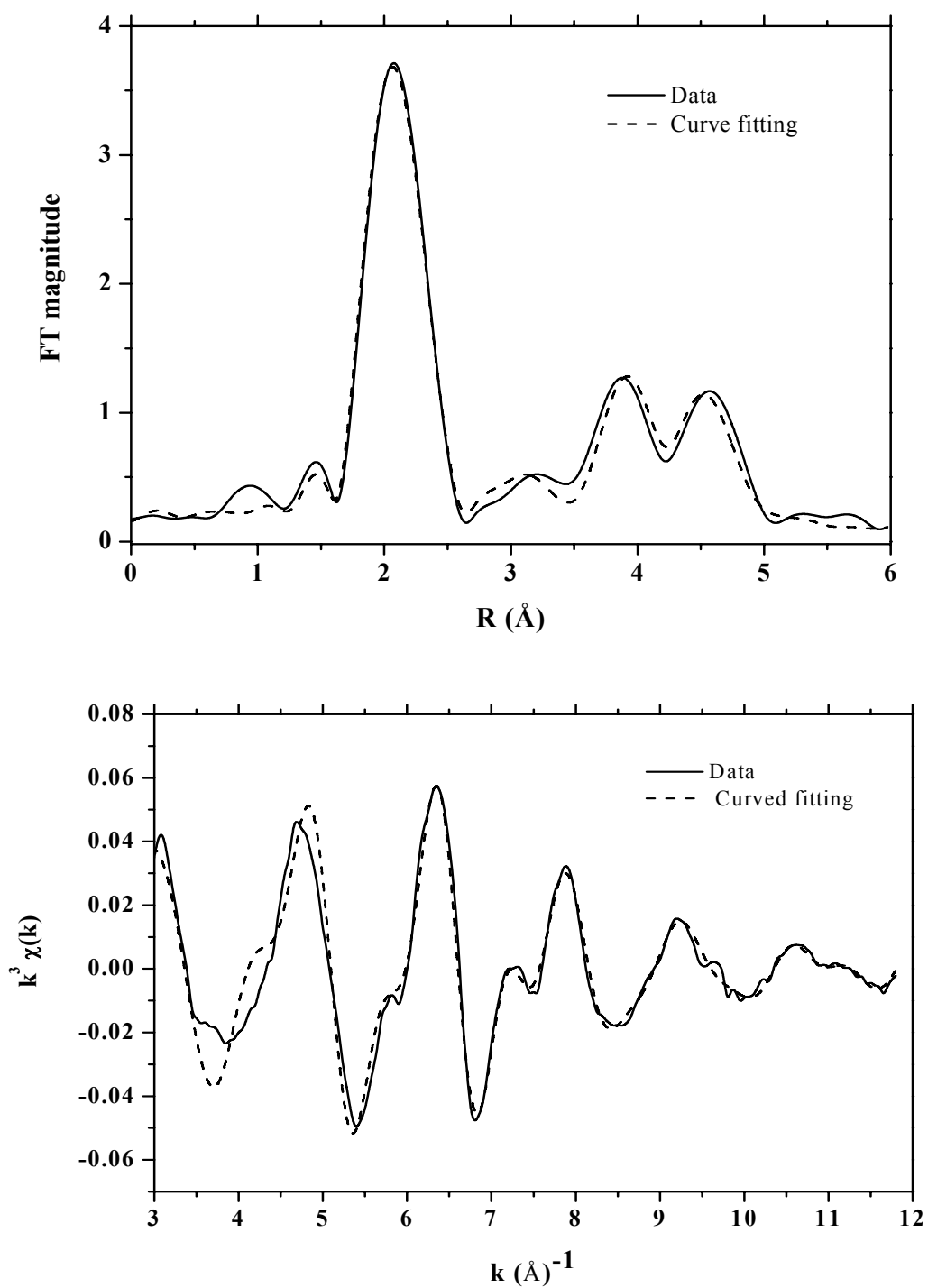
### **6.3.5 Structure of reduced mono- and bimetallic Co catalysts from EXAFS study**

EXAFS spectra of all reduced catalysts were measured and the atomic environments of cobalt including interatomic distances and co-ordination numbers were obtained by comparing the experimental data with that of model structure. The EXAFS spectrum of reduced catalysts with 1 wt% of Co would not be included here because it was not reducible. In addition, with low metal content the data quality was poor and not suitable for the analysis.

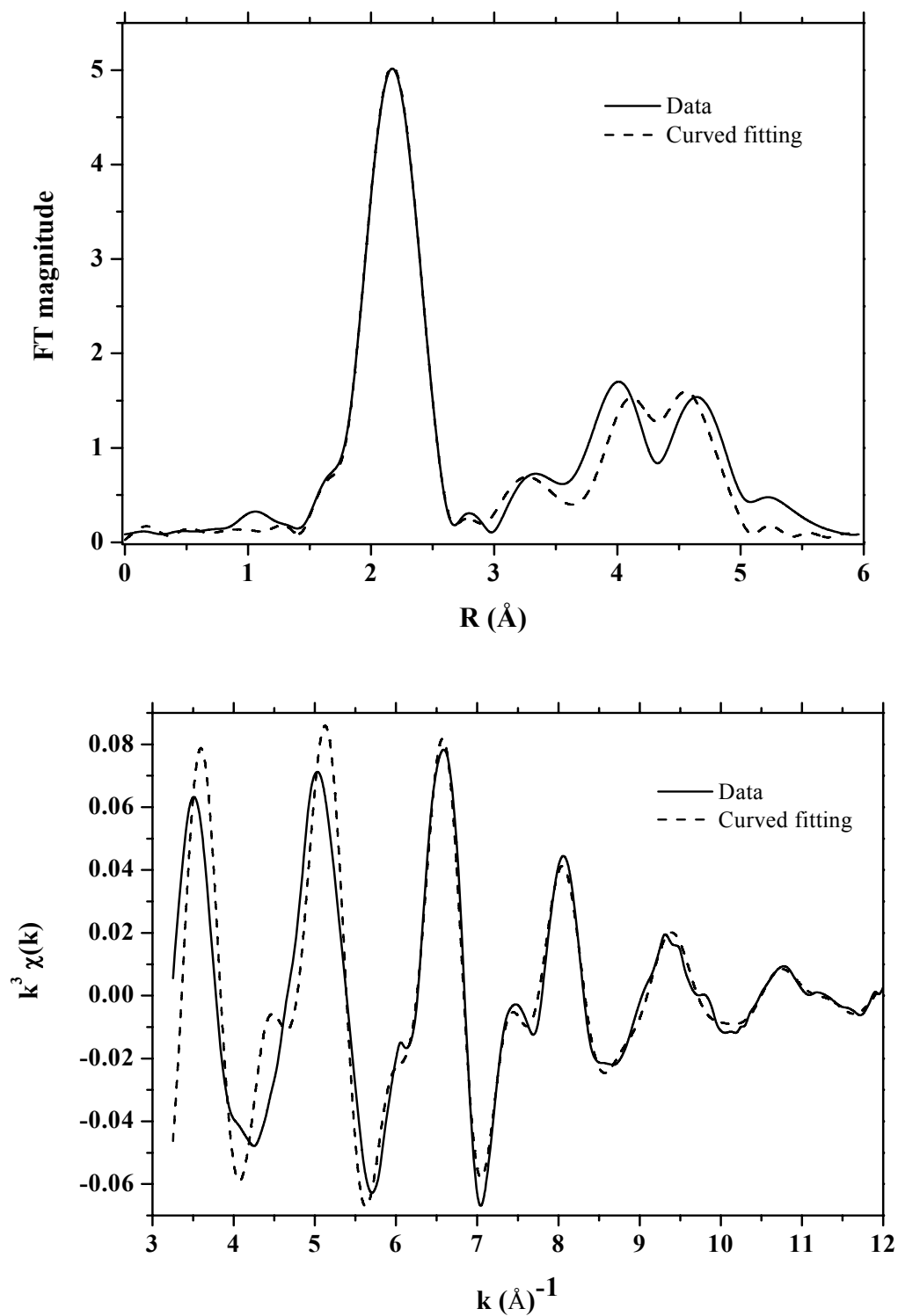
After Co catalysts were treated in pure hydrogen, the cobalt oxides in samples are reduced to the metallic state. This indicated by EXAFS spectra (see the appendix C). The curve fitting results of xCo/NaY and xCo-1Pt/NaY were plotted in Figure 6.13 – 6.14 shows the  $k^3$ -weighted EXAFS Fourier transforms magnitude spectra using the long k-range of  $3 \text{ \AA}^{-1} - 12 \text{ \AA}^{-1}$ , and the result of the fit was summarized in Table 6.5. The results of the Fourier-transformed spectra are always shorter than the real ones because of the phase shift (Schwartz et al., 2002). Based on the best fit, the first-shell coordination numbers (N) of Co-Co for 6Co/NaY and 10Co/NaY after reductions were 7.8 and 7.1, respectively. While xCo-1Pt/NaY, the first shell becomes Co-Co with  $N = 11.5$  and  $10.3$ , respectively, indicated that Co particle were agglomeration during reduction of bimetallic Co catalysts.



**Figure 6.13** Fourier transforms (top) and  $k^3$ -weighted Co K-edge EXAFS function ( $k^3 \chi(k)$ ) (bottom) of reduced 6Co/NaY: experiment (—) and curved fitting results (-----)

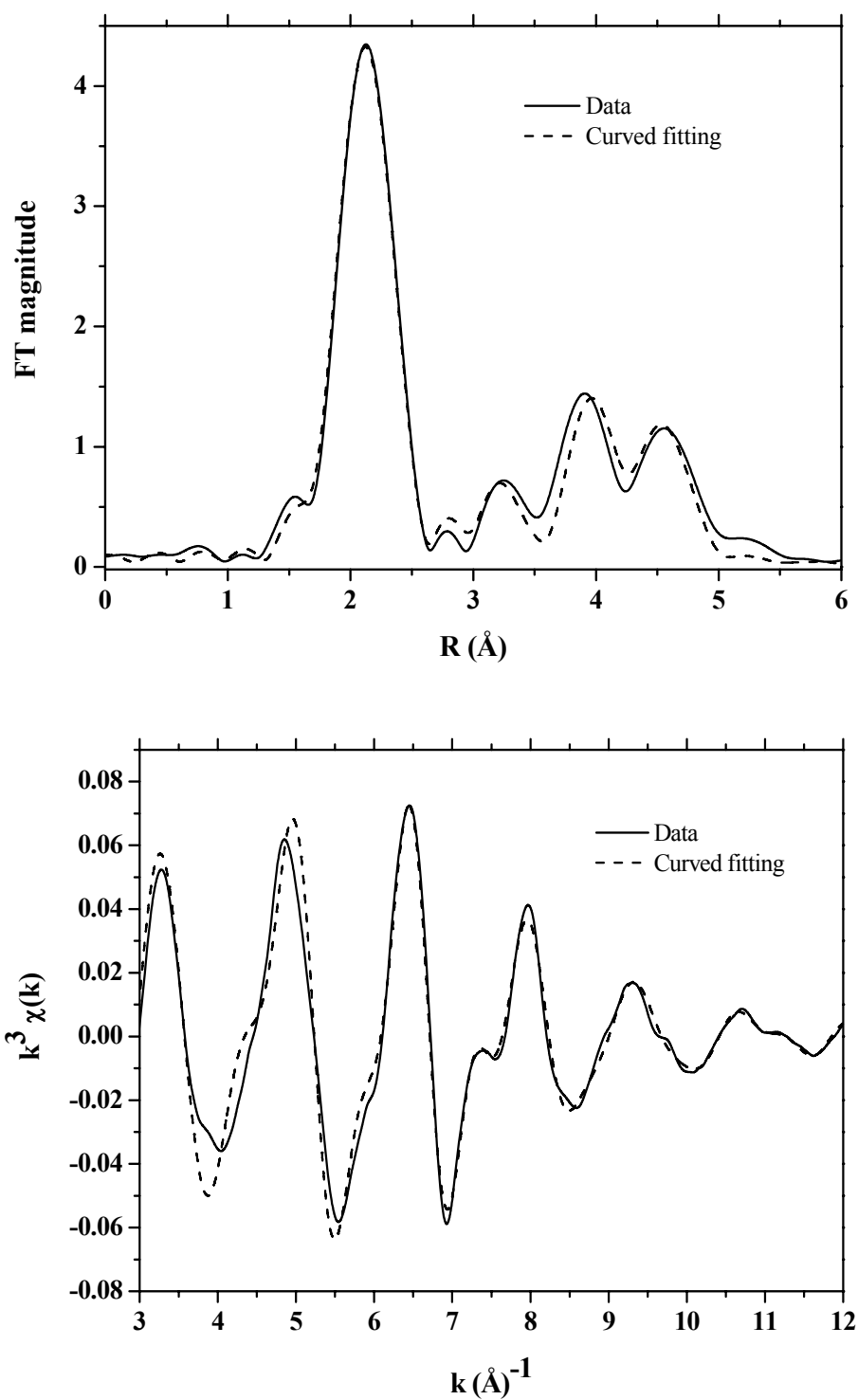


**Figure 6.14** Fourier transforms (top) and  $k^3$ -weighted Co K-edge EXAFS function ( $k^3 \chi(k)$ ) (bottom) of reduced 10Co/NaY: experiment (—) and curved fitting results (-----)



**Figure 6.15** Fourier transforms (top) and  $k^3$ -weighted Co K-edge EXAFS function ( $k^3 \chi(k)$ ) (bottom) of reduced 6Co-1Pt/NaY: experiment (—) and curved fitting results (-----)





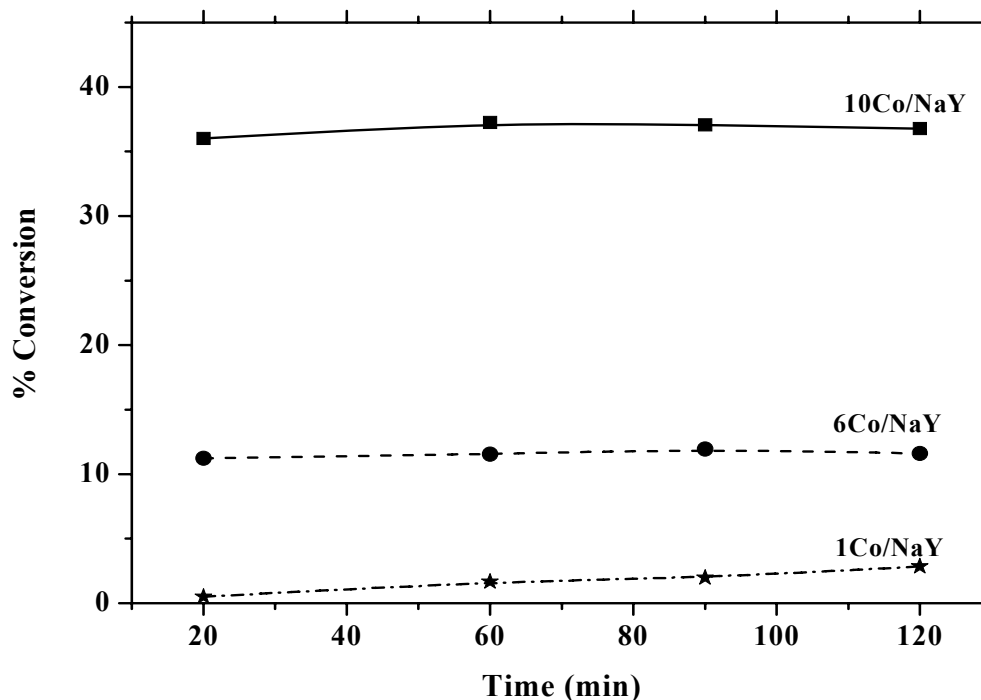
**Figure 6.16** Fourier transforms (top) and  $k^3$ -weighted Co K-edge EXAFS function ( $k^3 \chi(k)$ ) (bottom) of reduced 10Co-1Pt/NaY: experiment (—) and curved fitting results (-----)

**Table 6.5** Results from the analysis of EXAFS data of reduced xCo/NaY and xCo-1Pt/NaY

Samples	Component (1 <sup>st</sup> shell)	CN	R (Å)	E <sub>0</sub> (eV)	σ <sup>2</sup> (Å <sup>2</sup> )
6Co/NaY	Co-Co	7.82	2.47	-4.69	0.008
10Co/NaY	Co-Co	7.17	2.48	-8.64	0.007
6Co-1Pt/NaY	Co-Co	11.55	2.49	5.32	0.008
10Co-1Pt/NaY	Co-Co	10.33	2.48	-2.33	0.008

### 6.3.6 Catalytic testing of *n*-butane hydrogenolysis

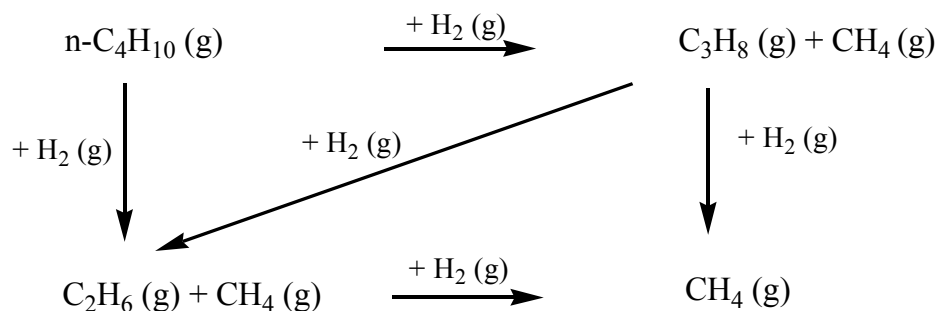
In order to reach steady state conditions the reactant gases were flowed through the catalyst samples, xCo/NaY and xCo-1Pt/NaY, for 20 minutes before the product analysis. The reaction was carried out at 300°C for 2 h to compare the influence of metal content in catalytic activity. The conversions of *n*-butane over monometallic xCo/NaY with Co loading of 1 wt%, 6 wt% and 10 wt% are shown in Figure 6.17. The only product observed over these catalysts was methane. The conversions during the two-hour test were constant on each metal loading. The conversions increased with cobalt loading on the catalysts. The increase of conversion could be related to the reduction of cobalt. The 1Co/NaY was not active for this reaction because cobalt was not reduced to the active metallic form. The 10Co/NaY was more active than 6Co/NaY because of higher metal loading and higher percentage of reduced cobalt.



**Figure 6.17** The conversion in butane hydrogenolysis of supported  $x\text{Co}/\text{NaY}$  catalysts at  $300^\circ\text{C}$

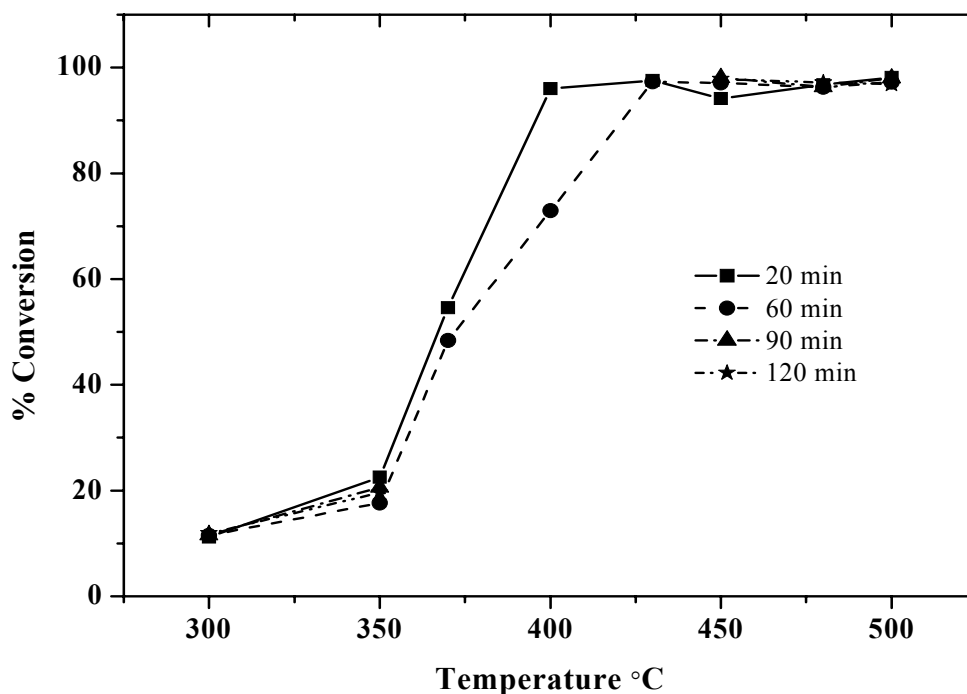
There were several reports in the literatures that the metal function of supported catalysts had influence on the hydrogenolysis characteristics (Larsson 1992, 1992; Sinfelt 1991; Jackson et al., 1998; Lomot et al., 2002). The high electronegative elements such as Co and Fe are good catalysts for multiple hydrogenolysis which involves breakages of more than one C-C bonds per a visit of hydrocarbon reactant to the catalyst surface with tendency to degrade to methane. The multiple hydrogenolysis reaction of *n*-butane can be expressed in Figure 6.18.

According to the previous report, we tested  $6\text{Co}/\text{NaY}$  for butane hydrogenolysis. The performance depended on the form of support. Because cobalt on HY was not reducible, it was not active for the reaction.



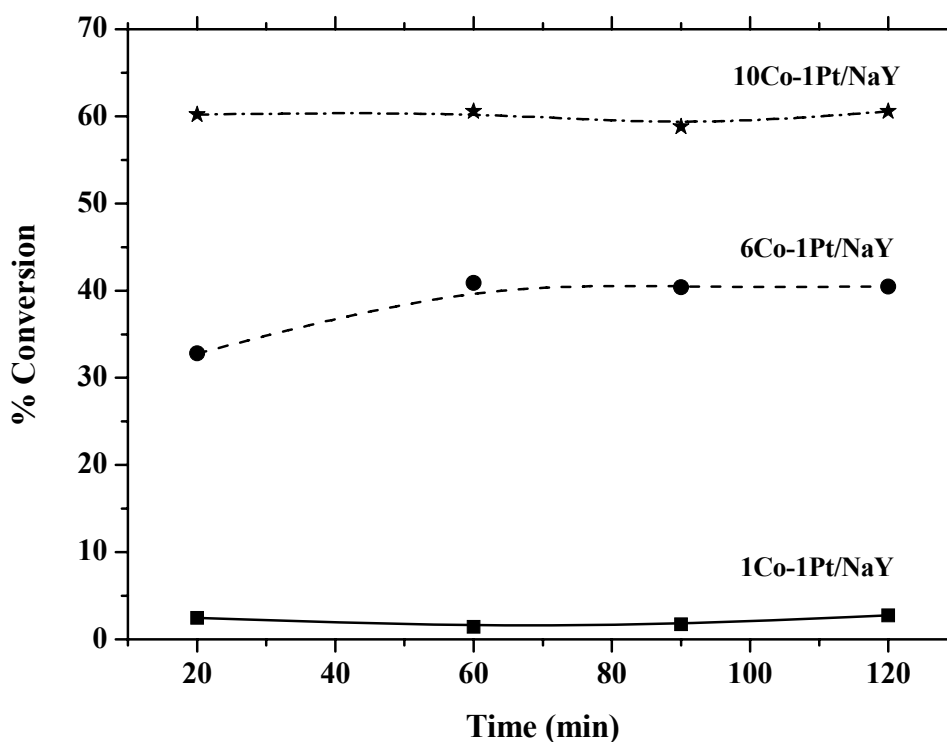
**Figure 6.18** Scheme of the multiple hydrogenolysis reaction from *n*-butane

Thus, this work would focus on the catalytic testing on 6Co/NaY to investigate the influence of temperature on activity from 300°C – 500°C. The results are shown in Figure 6.19. The conversions at each temperature were measured at 20 min, 60 min, 90 min and 120 min and averaged in the plot.



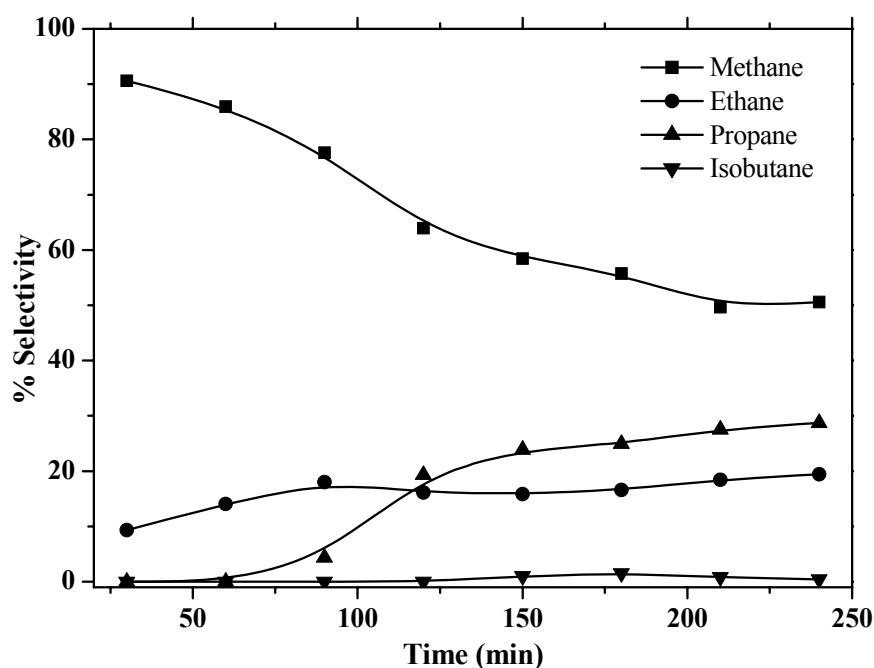
**Figure 6.19** Conversion in butane hydrogenolysis on 6Co/NaY at 300°C – 500°C

The conversions increased with temperature and reached a complete conversion at 400°C. Methane was the only product observed at all temperatures. The *n*-butane hydrogenolysis was also tested on bimetallic Co-1Pt/NaY with Co loading of 1 wt%, 6 wt% and 10 wt% at 300°C for 2 h. The results are shown in Figure 6.20. The trend of conversions was similar to that of monometallic catalysts that the conversion increased with Co loading. However, the conversions in bimetallic catalysts for the Co loading of 6 wt% and 10 wt% were higher than those of the monometallic with similar cobalt loading. This might be contributed from the percentages of reduced cobalt that were enhanced in the presence of Pt. In the next part, only the performance of 6Co-1Pt/NaY would be discussed.



**Figure 6.20** Conversion in butane hydrogenolysis on xCo-1Pt/NaY at 300°C

In contrast to monometallic 6Co/NaY cobalt that produced only methane, the bimetallic 6Co-1Pt/NaY produced methane, ethane and propane. As shown in Figure 6.21, at the early stage methane was the major product and decreased with time. At the beginning only ethane occurred along with methane. After the first hour, propane was formed and increased with time. The results indicated that the presence of platinum could minimize sequential hydrogenolysis of *n*-butane.

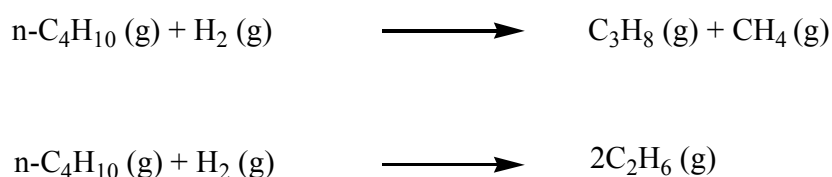


**Figure 6.21** The selectivity in butane hydrogenolysis of 6Co-1Pt/NaY at 300°C

A small amount of *iso*-butane, an isomerization product was also observed. Isomerization has been suggested to process through 1,3 di-adsorbed intermediates which were not involved in the hydrogenolysis reaction (Jackson et al., 1991). It was possible that the presence of platinum had an influence on the reaction selectivity. Jackson et al. (1991, 1998) reported that Pt has a high influence on selectivity for

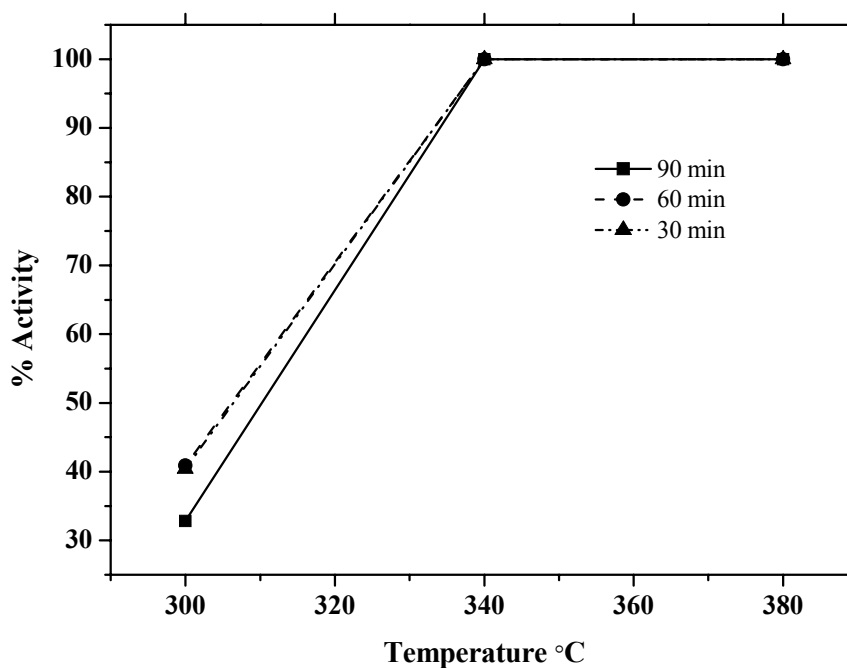
single hydrogenolysis. Single hydrogenolysis is defined as the breaking of single C-C bond per visit to the catalyst surface. This dominant in selectivity towards propane is associated in both cases with increases in ethane production.

The selectivity towards single hydrogenolysis of *n*-butane is shown in Figure 6.22 to produce propane in the first step, followed by the formation of ethane.

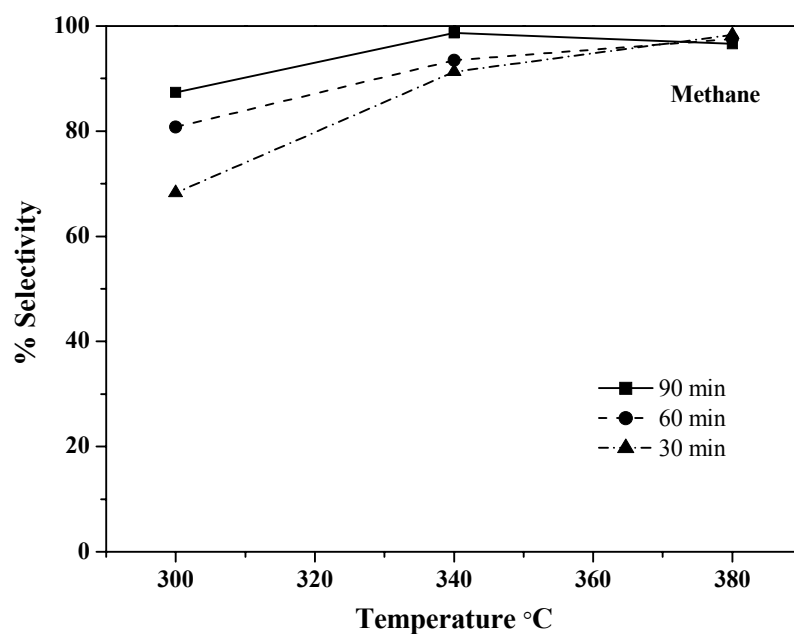


**Figure 6.22** Scheme of the single *n*-butane hydrogenolysis reaction

Figure 6.23 shows the influence of temperature in hydrogenolysis of *n*-butane on 6Co-1Pt/NaY. The conversion increased with the temperature and reached 100% at 340°C. The complete conversion on the bimetallic catalyst occurred at lower temperature than that on monometallic one which was 400°C. The selectivity for methane also increased with temperature while the selectivities for ethane and propane decreased when the temperature increased (Figure 6.24). At each temperature, the selectivity of methane increase with time indicated that the intermediate did not adsorbed strongly on the active sites. The results suggested that at high temperature the intermediates had a tendency to dissociate to methane production. In short, multiple hydrogenolysis on 6Co-1Pt/NaY occurred at high temperature.

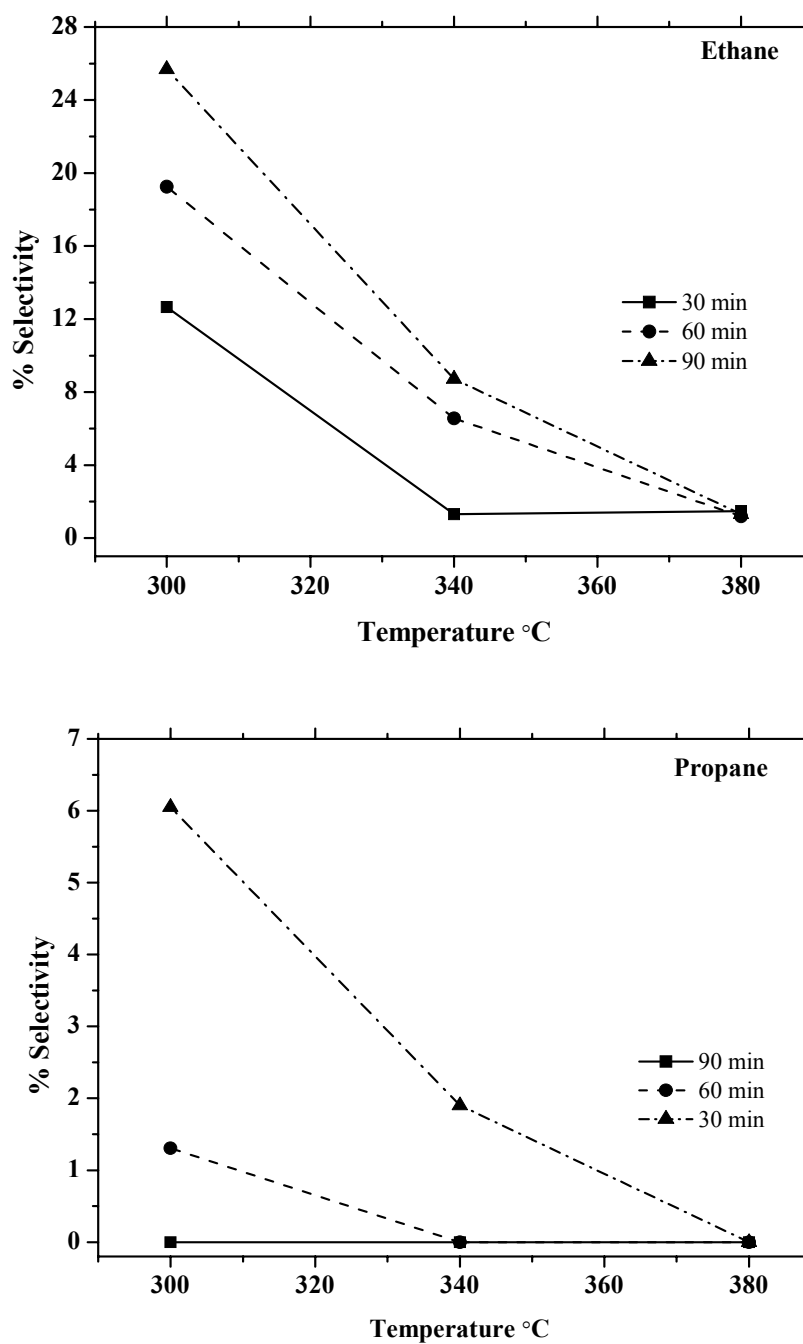


**Figure 6.23** Conversion in butane hydrogenolysis on supported 6Co-1Pt/NaY at various temperatures from 300°C – 380°C



**Figure 6.24** Selectivity in butane hydrogenolysis on supported 6Co/NaY at various temperatures from 300°C – 380°C

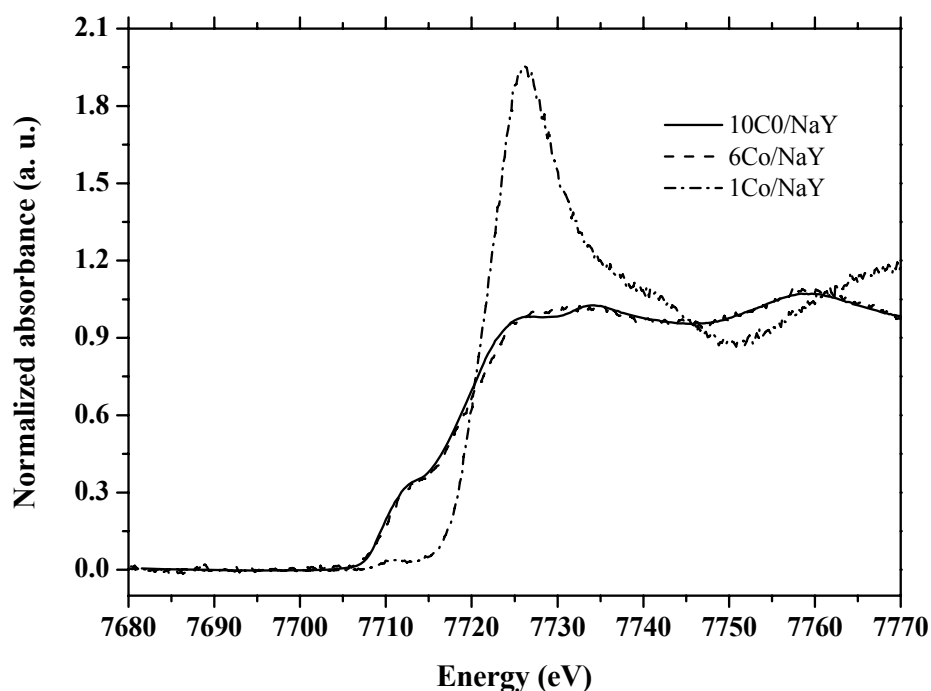




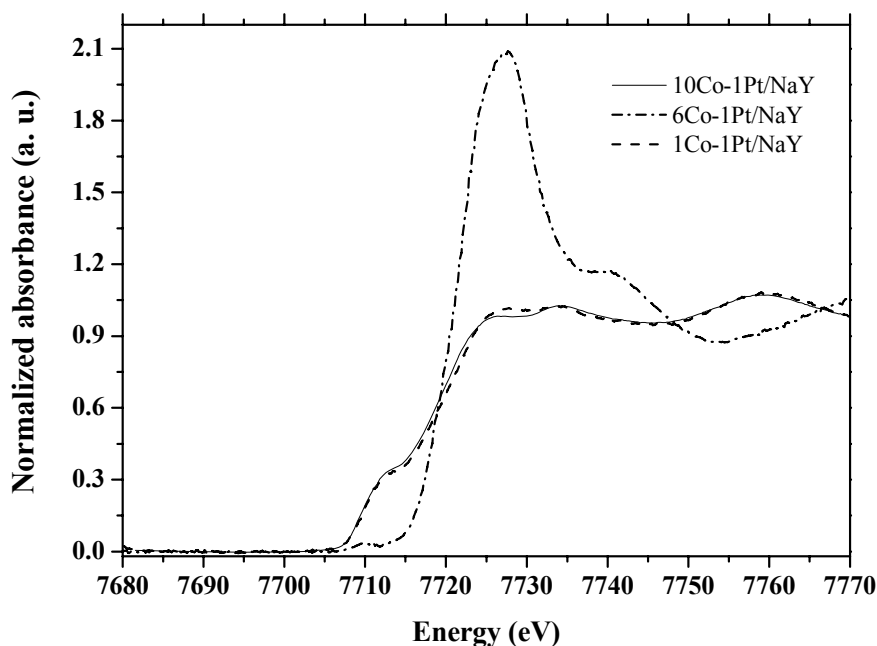
**Figure 6.24** (continued) Selectivity in butane hydrogenolysis on supported 6Co-1Pt/NaY at various temperatures from 300°C – 380°C

### 6.3.7 XANES study on reducibility of Co catalysts after spent in the reaction

After the reaction, the monometallic Co/NaY and bimetallic Co-Pt/NaY with cobalt loading of 1 wt%, 6 wt% and 10 wt% were characterized again by XANES. Their XANES spectra are shown in Figure 6.23 and 6.24. The spent 1Co/NaY and 1Co-1Pt/NaY still showed characteristic of  $\text{Co}^{2+}$  similar to the fresh catalysts. The catalysts with higher cobalt loading still showed characteristics of metallic cobalt demonstrating that they were not poisoned during the reaction. In addition, the percentage of reduction in these catalysts increased after the reaction because they were exposed to hydrogen stream during the test.



**Figure 6.25** XANES spectra of spent xCo/NaY (x = 10 wt%, 6 wt%, and 1 wt%, respectively)



**Figure 6.26** The XANES spectra of spent xCo-1Pt/NaY (x = 10 %wt, 6 %wt, and 1 %wt, respectively)

## 6.4 Conclusions

The reducibility of cobalt species supported on NaY depends on the amount of metal loading which low metal loading as 1 wt%. Generated a small particle of Co crystallites and difficult to reduce from cobalt oxide forms to Co metal form. Therefore, at high metal loading as 6 wt% and 10 wt% generated a large particle of cobalt oxides and easy to reduce at mild temperature. The addition of Pt, increased the reducibility of 6Co-1Pt/NaY and 10Co-1Pt/NaY bimetallic catalysts, especially the last one was almost fully reduce. The coordination numbers of monometallic after reduction were less than bimetallic catalysts. This form is active for butane hydrogenolysis and very selective to methane production.

## 6.5 References

- Chotisuwan, S., Wittayakun, J., and Gates, B. C. (2006). Pt<sub>3</sub>Ru<sub>6</sub> clusters supported on  $\gamma$ -Al<sub>2</sub>O<sub>3</sub>: synthesis from Pt<sub>3</sub>Ru<sub>6</sub>(CO)<sub>21</sub>( $\mu_3$ -H)( $\mu$ -H)<sub>3</sub>, structural characterization, and catalysis of ethylene hydrogenation and n-butane hydrogenolysis. **J. Phys. Chem. B.** 110: 12459-12469.
- Choy, J. H., Jung, H. and Yoon, J-B. (2001). Co K-edge XAS study on a new cobalt doped-SiO<sub>2</sub> pillared clay. **Synchrotron Rad.** 8: 599-601.
- Dominko, R., Arčon, I., Kodre, A., Hanžel D. and Gaberšček, M. (2009). In-situ XAS study on Li<sub>2</sub>MnSiO<sub>4</sub> and Li<sub>2</sub>FeSiO<sub>4</sub> cathode materials. **J. Power Sources.** 189: 51-58.
- Drozdová, L., Prins, R., Dědeček, J., Sobalík, Z. and Wichterlová, B. (2002). Bonding of Co ions in ZSM-5, ferrierite, and mordenite: An X-ray absorption, UV-Vis, and IR study. **J. Phys. Chem. B.** 106: 2240-2248.
- George, G. N. and Pickering, I. J. (2006). EXAFSPAK; A Suite of computer programs for analysis of X-ray absorption spectra [On-Line]. Available: <http://www-ssrl.slac.stanford.edu/exafspak.html>.
- Groot, F. D. (2005). Multiplet effects in X-ray spectroscopy. **Coordin. Chem. Rev.** 249:31-63.
- Haddad, G. J. and Goodwin, J. G. (1995). The impact of aqueous impregnation on the properties of prereduced vs precalcined Co/SiO<sub>2</sub>. **J. Catal.** 157: 25-34.
- Hagen, A., Schneider, E., Benter, M., Krogh, A., Kleinert, A. and Roessner, F. (2004). Modification of acid supports by solid-state redox reaction part II. Acid and catalytic properties. **J. Catal.** 226: 171–182.

- Idariss, H. (2008). The reactions of model metal oxides surface. In G. Ertl, H. Knözinger, F. Schüth, J. Weitkamp (ed.). **Handbook of Heterogeneous Catalysis** (2nd ed. vol.3 pp. 1344 – 1346) Weinheim, Germany: Wiley-VCH.
- Jackson, S. D., Kelly, G. J. and Webby, G. (1998). Supported metal catalysts; preparation, characterisation, and function part VI. Hydrogenolysis of ethane, propane, n-butane and iso-butane over supported platinum catalysts. **J. Catal.** 176: 225-234.
- Jacobs, G., Ji, Y., Davis, B. H., Cronauer, D., Kropf, A. J. and Marshall, C. L. (2007). Fischer–Tropsch synthesis: Temperature programmed EXAFS/XANES investigation of the influence of support type, cobalt loading, and noble metal promoter addition to the reduction behavior of cobalt oxide particles. **Appl. Catal. A- Gen.** 333: 177-191.
- Khemthong, P., Klysubun W. and Wittayakun J. (2009). Reducibility of cobalt catalysts supported on NaY and HY investigated by XAS and their performance on butane hydrogenolysis, submitted.
- Larsson, R. (1992). The mechanism of ethane hydrogenolysis over ruthenium catalysts and the isokinetic effect. **Catal. Lett.** 16: 273-285.
- Larsson, R. (1992). The mechanism of the ethane hydrogenolysis reconsideration of some kinetic data. **Catal. Lett.** 13: 71-86.
- Li, W., Yu, S. Y., Meitzner, G. D. and Iglesia, E. (2001). Structure and properties of cobalt-exchanged H-ZSM5 catalysts for dehydrogenation and dehydrocyclization of alkanes. **J. Phys. Chem. B.** 105: 1176-1184.

- Lomot, D., Juszczak, W., Karpinski, Z. and Larsson, R. (2002). Hydrogenolysis of ethane on silica-supported cobalt catalysts. **J. Mol. Catal. A- Chem.** 186:163-172.
- Mériaudeau, P., Thangaraj, A., Dutel, J. F., Gelin, P. and Naccache, C. (1996). Studies on Pt<sub>x</sub>In<sub>y</sub> bimetallics in NaY: II. Further characterization results and catalytic properties. **J. Catal.** 163: 338-345.
- Mhamdi, M., Khaddar-Zine, S and Ghorbel, A. (2009). Influence of the cobalt salt precursors on the cobalt speciation and catalytic properties of H-ZSM-5 modified with cobalt by solid-state ion exchange reaction. **Appl. Catal. A-Gen.** 357: 42-50.
- Profeti, L. P.R., Ticianelli, E. A. and Assaf, E. M. (2008). Production of hydrogen by ethanol steam reforming on Co/Al<sub>2</sub>O<sub>3</sub> catalysts: Effect of addition of small quantities of noble metals. **J. Power Sources.** 175: 482-489.
- Ravel, B. and Newville, M. (2005). Athena, Artemis, Hephaestus: data analysis for X-ray absorption spectroscopy using IFEFFIT. **J. Synchrotron Rad.** 12: 537-541.
- Rice, R. W. and Keptner, D. C. (2004). The effect of bimetallic catalyst preparation and treatment on behavior for propane hydrogenolysis. **Appl. Catal. A-Gen.** 262: 233-239.
- Ramallo-López, J. M., Ledesma, E. J., Requejo, F. G., Rodríguez, J. A., Kim, J.-Y., Rosas-Salas, R. and Domínguez, J. M. (2004). XANES characterization of extremely nanosized metal-carbonyl subspecies (Me= Cr, Mn, Fe, and Co) confined into the mesopores of MCM-41 materials. **J. Phys. Chem. B.** 108: 20005-20010.

- Saib, A.M., Borgna, A., Loosdrecht, J., Berge, P.J., Geus, J.W. and Niemantsverdriet, J.W. (2006). Preparation and characterisation of spherical Co/SiO<sub>2</sub> model catalysts with well-defined nano-sized cobalt crystallites and a comparison of their stability against oxidation with water. **J. Catal.** 239: 326-339.
- Schwartz, V., Prins, R., Wang, X. and Sachtler, W. M. H. (2002). Characterization by EXAFS of Co/MFI catalysts prepared by sublimation. **J. Phys. Chem. B.** 106: 7210-7217.
- Sinfelt, J.H. (1991). Catalytic hydrogenolysis on metals. *Catal. Lett.* 9: 159-172.
- Zhou, Y. Y., Yu, A. Q., Xu W. Y. and Wu P. (2006). Effect of Na addition on catalytic performance of PtSn/ZSM-5 catalyst for propane dehydrogenation. **Acta. Phys-Chim. Sin.** 22: 672-678.
- Vrålstad, T. Glomm, W. R., Rønning, M., Dathe, H., Jentys, A., Lercher, J. A. , Øye, G., Stöcker, M. and Sjöblom, J. (2006). Spectroscopic characterization of cobalt-containing mesoporous materials. **J. Phys. Chem. B.** 110: 5386-5394.
- Wang, W-J., Lin, H-Y. and Chein, Y-W. (2005). Carbon monoxide hydrogenation on cobalt/zeolite catalysts. **J. Porous Mat.** 12: 5-12.
- Wittayakun, J., Khemthong, P. and Prayoonpokarach, S. (2008). Synthesis of zeolite NaY from rice husk silica. **Korean J. Chem. Eng.** 25: 861-864.
- Wu , S.Q., Zhang , J.H., Zhu, Z.Z. and Yang, Y. (2007). Structural and electronic properties of the Li-ion battery cathode material Li<sub>x</sub>CoSiO<sub>4</sub>. **Curr. Appl. Phys.** 7: 611–616.

# CHAPTER VII

## ISOMERIZATION OF *n*-HEXANE OVER PLATINUM SUPPORTED ON ZEOLITE Y SYNTHESIZED FROM RICE HUSK SILICA

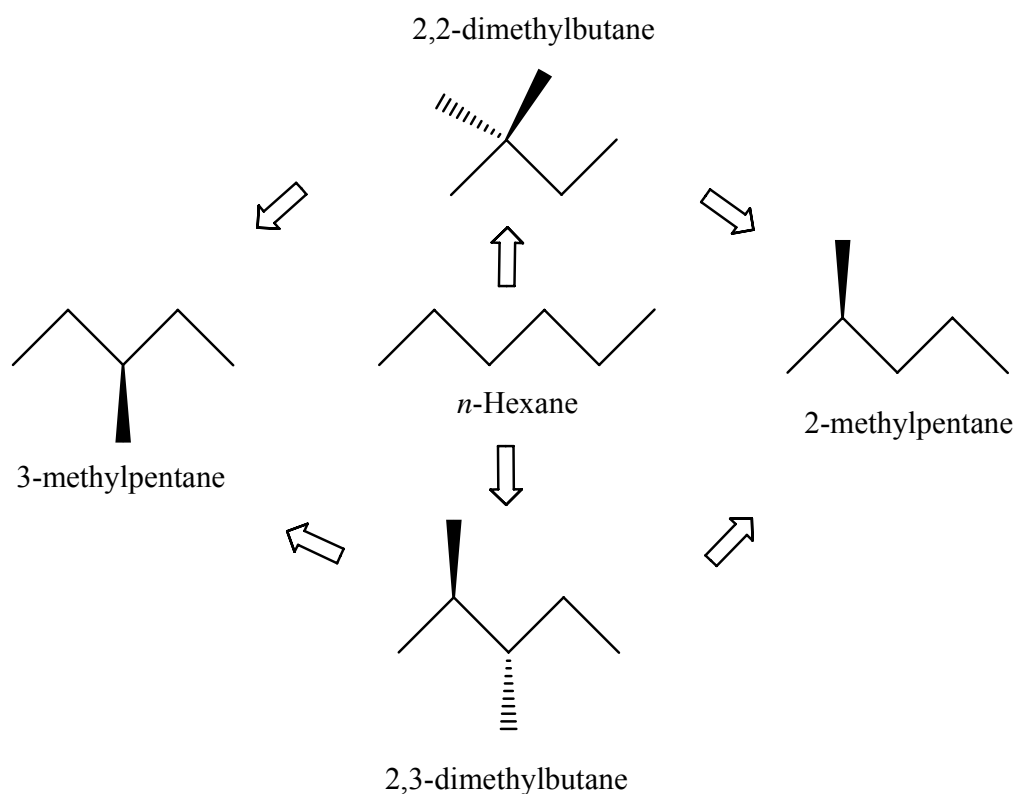
### **Abstract**

Bifunctional catalysts containing Pt supported on zeolite are interesting for isomerization of alkanes because the substrates can adsorb on both metal and zeolite acidic sites. Pt is also necessary for hydrogen active sites in the hydroisomerization reaction. This work studied isomerization of *n*-hexane in a plug flow reactor on Pt/HY and a mixture between Pt/NaY and Pt/HY (ratio 1:3) to understand the influence of zeolite acidity. Zeolite Y was synthesized with rice husk silica and the catalysts were prepared by incipient wetness impregnation and characterized by XRD, nitrogen and ammonia adsorption-desorption. The catalytic testing was conducted at 300°C and 450°C using hydrogen as a reactant and carrier. At 300°C the selectivities of isomerization were similar on both catalysts, with the methylpentanes (MP) and dimethylbutane (DMB) as main products. At 450°C, the 1Pt/HY gave higher cracking products including ethane, propane and butane. The isomerization products were similar to that at 300°C but with higher yields. The mixture Pt/NaY:Pt/HY gave a higher selectivity for *n*-hexane isomerization at high temperature than Pt/HY indicating that an addition of NaY was necessary for isomerization.



## 7.1 Introduction

Isomerization is a process that a molecule rearranges its structure and transforms to another molecule with exactly the same atoms. Isomerization of light paraffins to branched ones is a way to improve octane number of gasoline. It is an important process of petroleum industry to produce gasoline by isomerization of C<sub>4</sub> to C<sub>6</sub> paraffins. Figure 7.1 shows isomerization of *n*-hexane (C<sub>6</sub>H<sub>14</sub>) to produce various branched products including 2-methylpentane (2MP), 3-methylpentane (3MP), 2,2-dimethylbutane, 2,3-dimethylbutane.



**Figure 7.1** *n*-hexane isomerization products

The major units of isomerization are based on bifunctional catalysts which composed of noble metal dispersed on an acidic zeolite (Eswaramoorthi and Lingappan, 2003; Bobik et al., 2004; Phatanasri et al., 2000). The most effective

catalysts which are selective for isomerization composed of Pt metal (Lipidus et al., 2008; Ali et al., 2001; Kuhlmann et al., 2004). Examples of bifunctional Pt catalysts on various supports are shown in Table 7.1. These catalysts on zeolites with strong acidity are promising for isomerization of normal alkanes (Vasina et al., 2000).

**Table 7.1** Examples of supported Pt catalysts on various supports

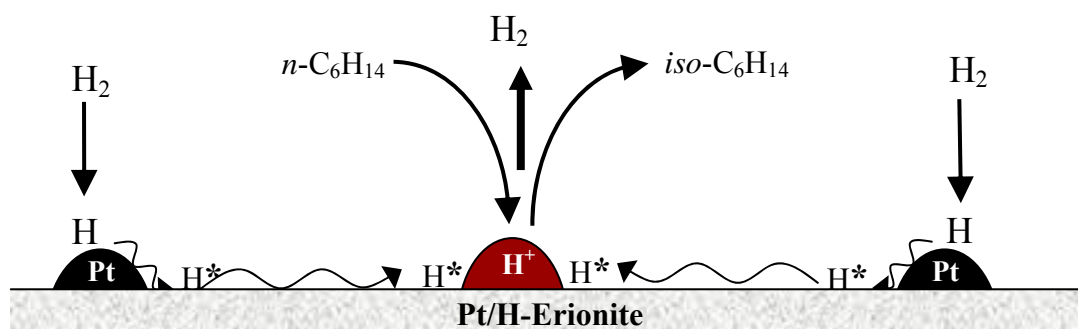
Metals/Support	Result from reaction	Reference
Ni-Pt/HUSY*	The additional small amount of Pt to Ni catalyst increased the catalytic activity for isomerization and selectivity to isomer products.	Yoshioka et al., 2005
Ni-Pt/H-BEA	Additional of Ni increased n-hexane conversion and selected to dimethyl butane.	Eswaramoorthi and Lingappan, 2003
Pt/Na(H)Y	The presence of strongly acidic site was favorable for <i>n</i> -hexane isomerization resulting in high isomer yield and high selectivity.	Boskovic et al., 2001
Pt/H-BEA	The catalysts exhibited high activity and selectivity to dimethylbutane and methylpentane with 72% of conversion and 98% of selectivity, respectively.	Phatanasri et al., 2000

**Table 7.1** (continued) Examples of supported Pt catalysts on various supports

Metals/Support	Result from reaction	Reference
Pt/H-MCM-41	The incorporation of Pt into MCM-41 for isomerization of <i>n</i> -butane promoted large extent of hydrogenolysis reaction which product methane, ethane, propane, butane, and isobutene as the main products.	Nieminen et al., 2004
Pt/NH <sub>4</sub> NaY	The catalytic activity increased linearly with increasing of degree of ammonium exchange.	Bremer et al., 1980

\*H-ultra stable Y zeolite

Although, Pt catalysts supported on zeolite exhibited high conversion but they gave low selectivity at high temperature and had a tendency to produce cracking products including methane, ethane, propane and butane. The strength of Bronsted and Lewis acid sites affected the catalytic activity and selectivity (Phatanasri et al., 2000, Bovik et al., 2004). Incorporation of small amount of Na<sup>+</sup> can increase the strength of Lewis acid site led to high selectivity to isomerization products of *n*-hexane. The mechanism of *n*-hexane isomerization over Pt/zeolites has been studied extensively and expressed by Roland et al. (1996) in term of hydrogen spillover as shown in Figure 7.2. Hydrogen molecules adsorbed dissociatively on the Pt surface. When the surface was completely covered, the spillover hydrogen atoms could migrate to react with alkanes adsorbed on the zeolite and transform to isomers.



**Figure 7.2** Schematic diagram for *n*-hexane isomerization via hydrogen spillover

This work investigated the catalytic performance of Pt supported on zeolite Y in sodium form (NaY) synthesized from rice husk silica. The effect of temperature on the catalytic activity and selectivity in the *n*-hexane isomerization was also studied. The effect of acid strength was also investigated by mixing 1Pt/NaY with 1Pt/HY.

## 7.2 Experimental

### 2.1.1 Catalyst preparation

Zeolite Y in Na<sup>+</sup> form (NaY) was synthesized by using rice husk silica as describe in chapter II. Then the synthesized NaY was converted to ammonium form (NH<sub>4</sub>Y) by exchange with a solution of NH<sub>4</sub>NO<sub>3</sub> for 5 times to ensure the maximum ion exchange. The obtained NH<sub>4</sub>Y was filtered and washed thoroughly and dried in oven overnight. Catalysts containing 1 wt% of Pt over HY and NaY were prepared by impregnation of NH<sub>4</sub>Y and NaY respectively, with a aqueous solution of H<sub>2</sub>PtCl<sub>6</sub>. Then they were dried at 100°C over night and calcined at 300°C for 3 h. After calcination the NH<sub>4</sub>Y was converted to proton form (HY). The calcined catalysts were palletized, crushed and sieved to particle size of 200 μm – 350 μm. In addition, a

physical mixture from 0.1 g of Pt/NaY and 0.3 g of Pt/HY was also prepared for each test.

### 2.1.2 Catalysts characterization

The specific surface areas (BET method) was obtained by nitrogen adsorption–desorption isotherms by using a Micromeritics 2010 instrument, and the data was collected at the liquid nitrogen temperature.

Temperature programmed desorption of ammonia (NH<sub>3</sub>-TPD) was conducted on Raczek Analysentechnik equipped with thermal conductivity detector (TCD) as described in section 6.3.3 in Chapter 6.

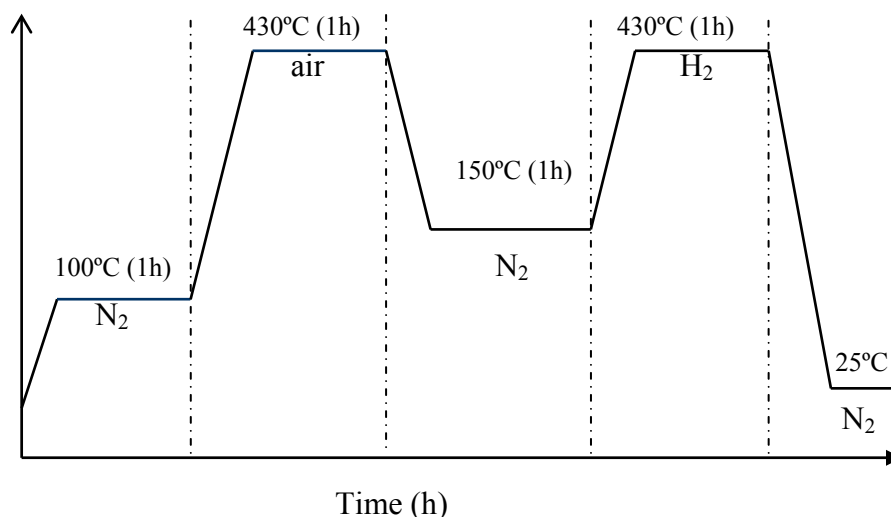
### 2.1.3 Catalytic activity testing

The conversion of *n*-hexane isomerization was conducted in a fixed-bed plug flow microreactor (Figure 7.4) with diameter 1 cm, filled with 0.4 g of catalysts (pelletized and sieved to particle sizes of 200 μm – 350 μm) and carry out the reaction at 300°C and 450°C.

Catalytic blank tests were done on HY and a mixture of HY and NaY (1:3 ratio). Prior to the test the NH<sub>4</sub>Y or a mixture of NH<sub>4</sub>Y and NaY was calcined in the reactor under N<sub>2</sub> flow at the rate of 50 mL/min at 400°C for 3 h to convert it to HY.

Diagram in Figure 7.3 shows the temperature programming and conditions for catalyst pretreatment before the catalytic testing. The 1Pt/HY catalyst in the reactor was first heated from room temperature to 100°C under nitrogen flow. Then it was heated to 430°C in flowing of dry air (50 mL/min) with heating rate of 10°C/min at and held for 3 h to remove adsorbed species on the catalyst surface. After that it was purged with N<sub>2</sub>, and cool down temperature to 150°C for 1 h. Finally, the catalyst was

reduced in a flow of  $H_2$  from  $150^\circ C$  –  $410^\circ C$  and held at the final temperature for 3 h before cooling down to room temperature.



**Figure 7.3** Diagram of temperature program and condition of catalyst treatment

Figure 7.4 shows the reactor setup. The liquid n-hexane was injected with a flow rate of 1.2 mL/h and heated at  $150^\circ C$  in evaporator which was made from stainless steel filled with aluminium scrap. The vapor of n-hexane was passed through the reactor by  $H_2$  carrier gas with a total flow rate of 50 mL/min. The reaction was done at  $300^\circ C$  and  $450^\circ C$  and the effluent was analysis by online GC-MS (HP 5890 – MSD 5973) equipped with Pona capillary column and controlled by HP CHEMSATATION software with conditions described in Table 7.2. The effluent gas was also analyzed by GC-FID (HP 6890) with Optima Wax column with conditions described in Table 7.3.

**Table 7.2** The overview of the separation conditions of GC-MS (HP 5890)

Carrier gas	He
Flow	1.3 mL/min (constant flow) 30 cm/s
Injector type	split/splitless
Injection temperature	220°C
Split	300:1
Detector	quadrupole mass spectrometer
Temperature of the transfer pipe	280°C
Temperature of the ion source	230°C
Temperature of quadrupole	150°C

**Table 7.3** The overview of the separation conditions of GC-FID (HP 6890)

Carrier gas	helium
Flow	0.6 mL/min (constant flow) 11 cm/sec
Injector type	split/splitless
Injection temperature	250°C
Split	85.8:1
Detector	FID
Temperature	150°C

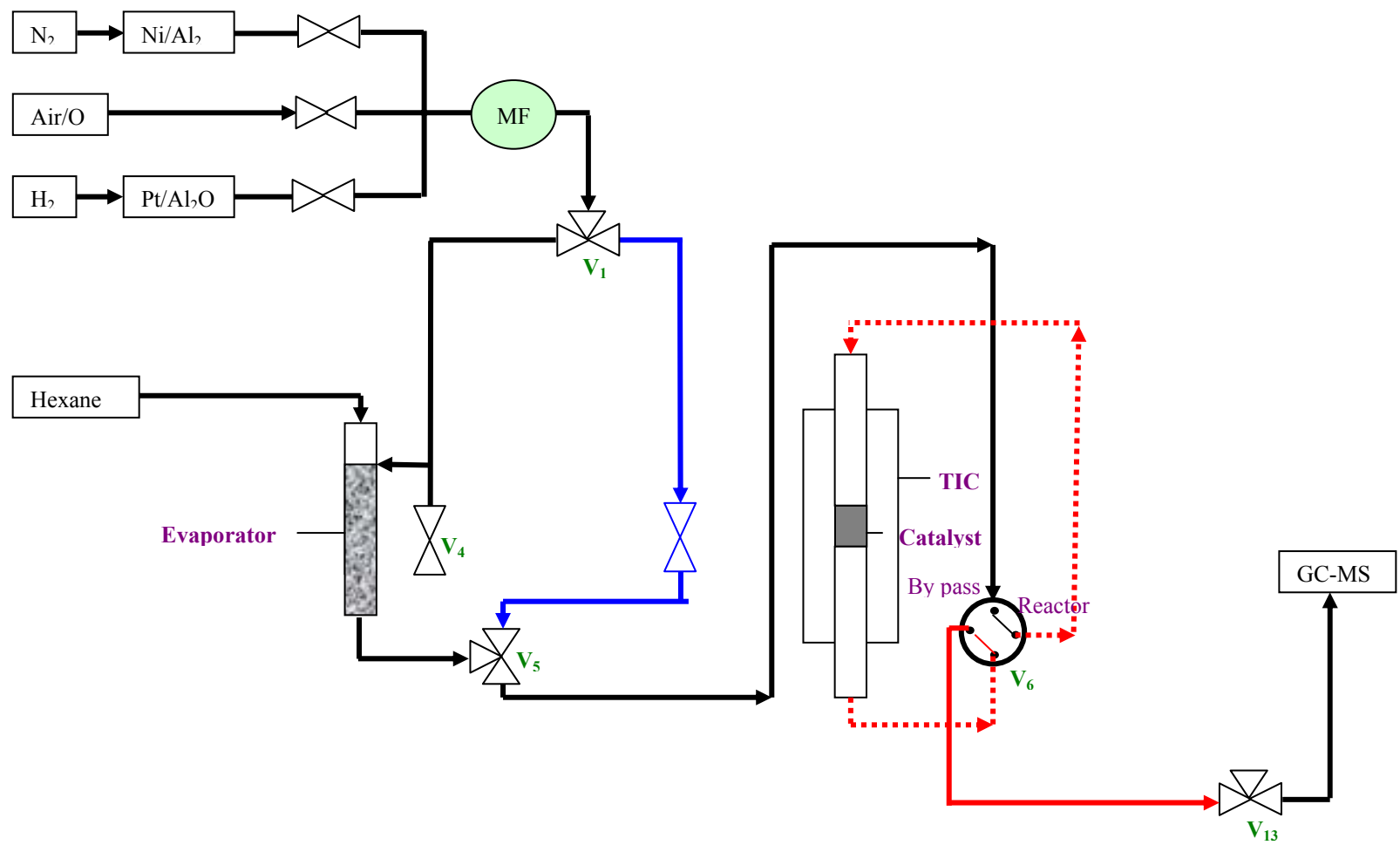


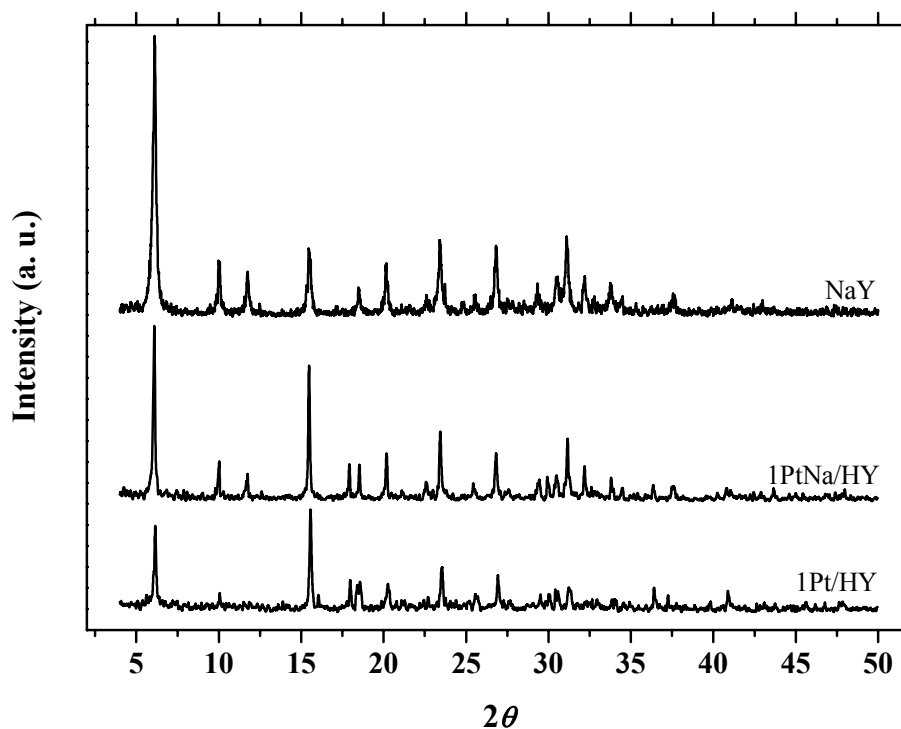
Figure 7.4 Schematic diagram of *n*-hexane isomerization reactor



## 7.3 Result and discussion

### 7.3.1 XRD result

The XRD spectra of NaY as a parent, 1Pt/NaY and 1Pt/HY are shown in Figure 7.5. The spectrum of Pt/NaY and Pt/HY showed the characteristic of NaY indicating that the zeolite structure is retained. However, the intensity of  $d_2$  peak was higher indicating that the presence of Pt could induce structural distortion. In the Pt/HY the zeolite structure was affected after the exchange with ammonium and the further exchange could occur during the catalyst preparation. The peaks of Pt were not observed because of low metal loading and good metal dispersion on each support.



**Figure 7.5** XRD spectra of calcined catalysts

### 7.3.2 NH<sub>3</sub>-TPD result

The NH<sub>3</sub>-TPD is particularly useful in study of interaction between reactants and catalyst's surface in catalytic reaction and adsorption of gases on metals and metal oxides (Gorte, 1996). The NH<sub>3</sub>-TPD technique has proved to be very useful for investigating adsorption on the solid surface, especially Bronsted-acid (Gorte, 1996). The result yielded information about the number of Bronsted as well as Lewis acid of platinumized zeolites (Pt-zeolites). The incorporated of cation as Pt and Na<sup>+</sup> into Bronsted acid site of HY zeolites increased the Lewis acid site and lead undergo ion exchange with OH group of zeolite. The total acid site was increased as increased Pt content as show as Table 7.4. Pt supported on NaY and HY which will increase as increasing of Na<sup>+</sup> content.

**Table 7.4** Experimental result on acidity of noble metal promoted Pt samples

Catalyst names	Desorption Temperature (°C)	Total acid site (mmol/g)
NaY	321	0.24
HY	263	0.07
1Pt/HY	267	0.05
1Pt/NaY	280	0.49

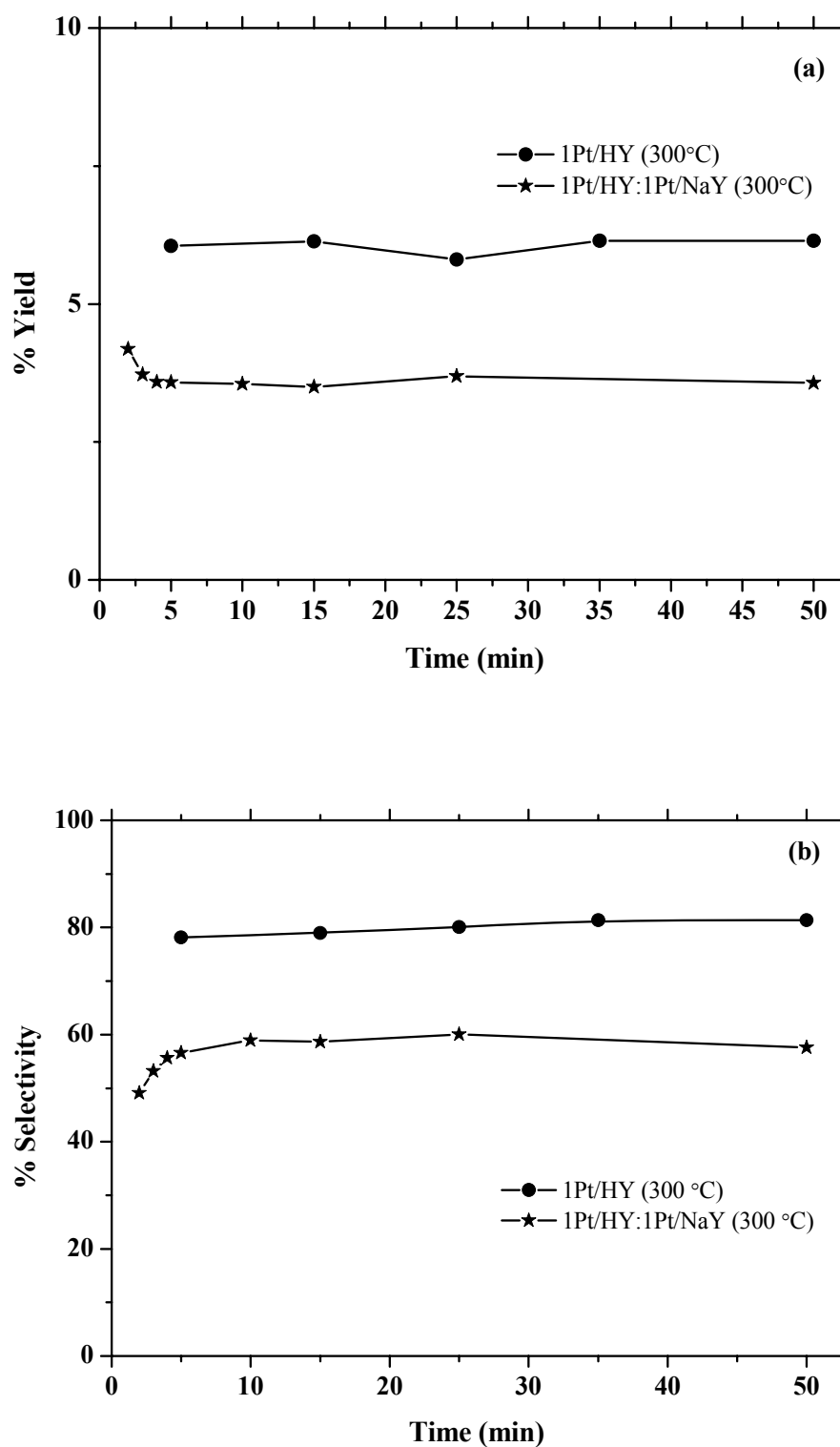
### 3.3.1 Catalytic studies

In the blank tests, isomerization of *n*-hexane was not observed and small amount of cracking products were detected (conversion less than 5%).

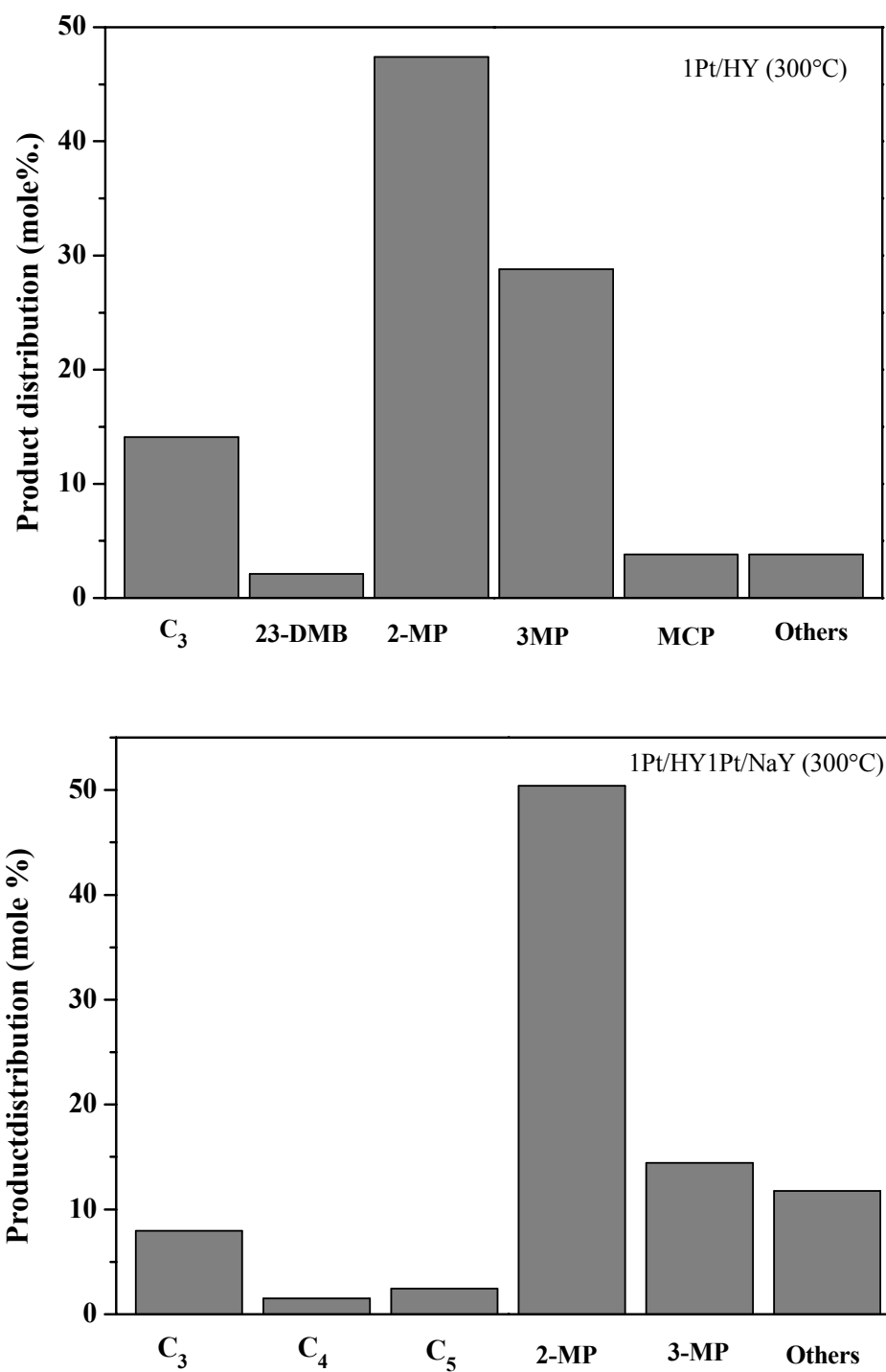
The catalytic performances for *n*-hexane isomerization of Pt/HY and the mixture of Pt/HY and Pt/NaY are presented as a function of time. The conversions and

selectivities on both catalysts at 300°C and 450°C are illustrated in Figure 7.6 to 7.9. The conversion on 1Pt/HY was higher than that of the mixture of Pt/HY and Pt/NaY at both temperatures and the conversions of both catalysts increased with temperature. The conversion of Pt/HY and the mixture of Pt/HY and Pt/NaY were about 7 and 4 respectively (Figure 7.6a) and the conversions were not changed during the testing period. Their selectivities for isomerization were about 80% and 60% respectively (Figure 7.6b). The low conversion was also observed at 300°C in another work but it showed the optimum selectivity of isomer product, regarding to the hydrogenolysis reaction on the primary C atom on metallic site is not favored to any extent with this condition (Zhan et al., 1994). Zhan et al. (1994) reported the conversions on 0.8Pt/HY and 0.8Pt/NaHY to be 5.1% and 4.2% respectively, at 330°C; the selectivities for isomerization products were 49% for methylpentane and 6% for dimethylbutane.

In this work, the distribution of products Pt/HY and the mixture of Pt/HY and Pt/NaY after 50 min are shown in Figure 7.7. The major isomerization product on Pt/HY was 2-methylpentane (2-MP, 47 mole%) followed by 3-methylpentane (3-MP, 30 mole%). The major isomerization product over a mixture of Pt/HY and Pt/NaY was 2- methylpentane (50 mole%). Phatanasri et al. (2000) reported that Bronsted and Lewis acid sites have influence on the catalytic activity and selectivity. Boskovic et al. (2001) suggested that selectivity of paraffin isomerization required strong Bronsted acid site, 1Pt/HY, and strong Lewis acid site, 1Pt/NaY. Therefore, after physical mixing with a small amount of 1Pt/NaY, the selectivity of 2-MP at was enhanced at 300°C.



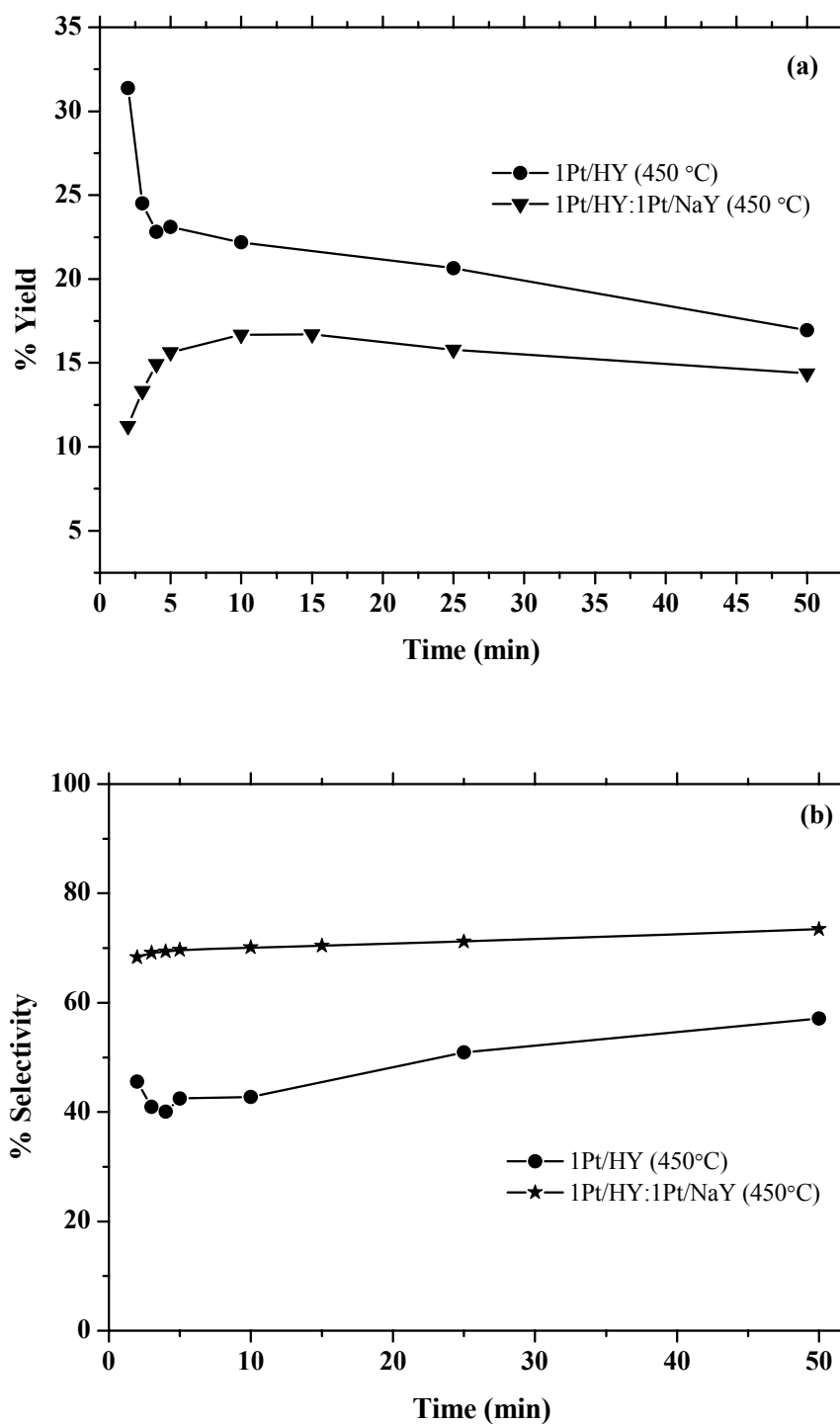
**Figure 7.6** (a) Conversions of n-hexane and (b) Selectivities for isomerization over 1Pt/HY and mixed 1Pt/HY:1Pt/NaY (1:3) at 300°C



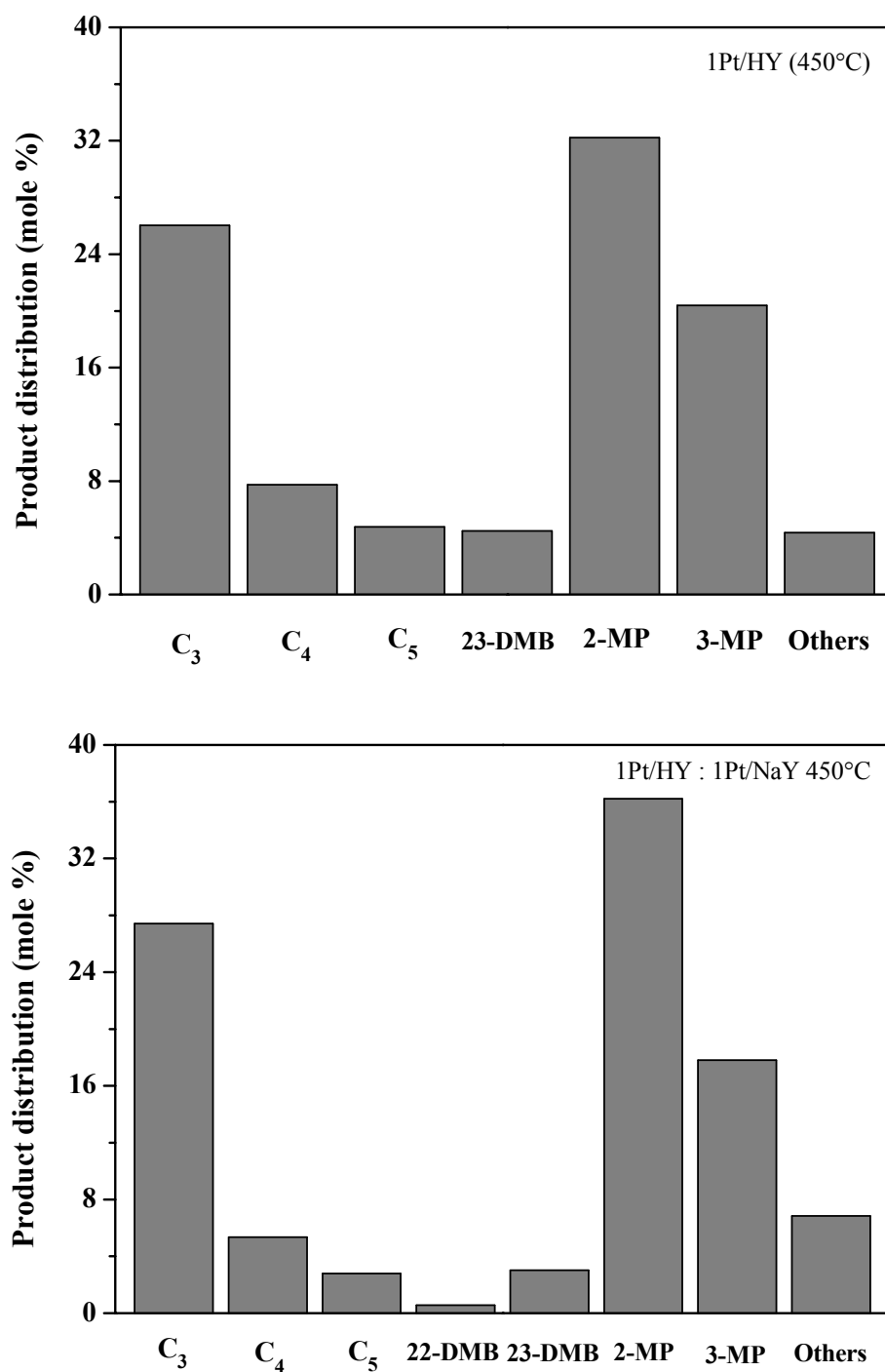
**Figure 7.7** Product distribution of *n*-hexane isomerization over 1Pt/HY and a mixture of 1Pt/HY:1Pt/NaY (1:3) at 300°C and 450°C

At 450°C the Pt/HY showed conversions about 7.5 times higher than those of the mixture of Pt/HY and Pt/NaY at 300°C indicating that the activity was enhanced by temperature. However, the conversion was decreased slowly with time possibly from benzene product from the reaction as explained by Chen et al. (1988) that benzene inhibited the rate of *n*-hexane hydroisomerization while favoring the conversion of benzene.

At 450°C the selectivities for isomerization on the mixture of Pt/HY and Pt/NaY was higher than those on Pt/HY indicating that the mixing of 1Pt/NaY enhance product selectivity. However, cracking products also appeared on both catalysts at this condition. The reaction products were produced mainly isomers, fragments of C<sub>2</sub> – C<sub>5</sub> and trace amount of benzene. In case of fragment compositions indicated that pronounced cracking occurs over Pt-catalysts, together with minor hydrogenolysis on the metallic centers. Zhan et al. (1994) reported that HY catalyst exhibited high selectivity for fragment products addition of Pt enhances the reaction. The cracking product, propane was produced in a large amount according to *n*-hexane cracked in the middle of the molecule. In case of C<sub>2</sub>, C<sub>4</sub> and C<sub>5</sub> species are formed through hydrogenolysis over metal sites or proton transfer mechanism as hydrogen spill over (Boskovic et al., 2001, Chen et al., 1988).



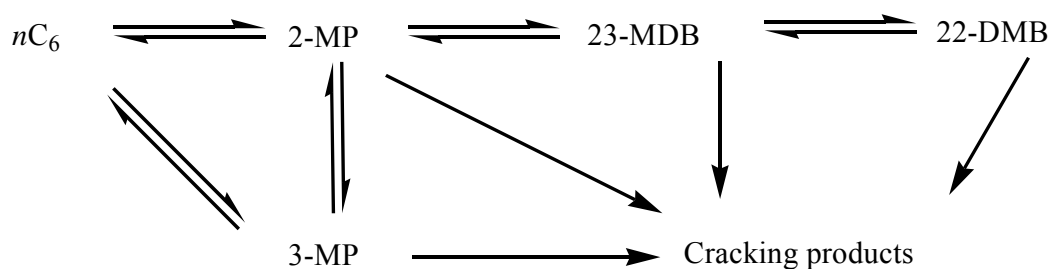
**Figure 7.8** Conversions (a) of n-hexane and Selectivities (b) for isomerization over 1Pt/HY and mixed 1Pt/HY:1Pt/NaY (1:3) at 450°C



**Figure 7.9** Product distribution of *n*-hexane isomerization over Pt/HY and a mixture of 1Pt/HY:1Pt/NaY (1:3) at 300°C and 450°C



According to those results, the selectivities for isomerization of *n*-hexane are structure sensitive. Many researchers proposed the mechanism of *n*-hexane isomerization that the transformation over metal containing catalysts and generated intermediate complex which further to produce *iso*-hexane or cracking products as illustrated in the schematic below (Bremer et al., 1980; Eswaramoorthi and Lingppan, 2003; Yang and Somorjai, 2004; Lapidus et al., 2008; Kuhmann et al., 2004, Roessner et al., 1995; Chen et al., 1988).



**Figure 7.10** Proposed mechanism pathway of *n*-hexane isomerization

The selectivity on product distribution was optimal at 450°C over 1Pt/HY:1Pt/NaY. The selectivity was more favorable to isomers of *n*-hexane. The cracking was minor because of the hydrogenolysis reaction on primary C atom on metallic site is still not favored to any extent after added 1Pt/NaY to 1Pt/HY. The dominant cracking of *n*-hexane produced propane.

## 7.4 Conclusions

Pt/HY and mixed Pt/HY:1Pt/NaY are acidic and active in *n*-hexane isomerization. Both catalysts, tested at 300°C showed the optimal selectivity to isomer products: methylcyclopentane and dimethylbutane. Propane was a minor cracking product at this temperature. At 450°C cracking was more favorable but the major products were still from isomerization.

## 7.5 References

- Roland, U., Braunschweig, T. and Roessner, F. (1996). Hydrogen spillover in bifunctional catalysis. **J. Mol. Catal. A-Chem.** 112: 401-412.
- Gorte, R.J. (1996). Temperature programmed desorption for the characterization of oxides catalyst. **Catal. Today.** 28: 405-414.
- Idariss, H. (2008). The reactions of model metal oxides surface. In G. Ertl, H. Knözinger, F. Schüth, J. Weitkamp (ed.). **Handbook of Heterogeneous Catalysis** (2nd ed. vol.3 pp. 1344 – 1346) Weinheim, Germany: Wiley-VCH.
- Zhan Z., Manninger I., Paal Z. and Barthomeuf D. (1994). Reactions of *n*-Hexane over Pt-zeolite catalysts of different acidity. **J. Catal.** 147: 333-341.
- Paal Z., Zhan Z. Q., Manninger I. and Sachtler W. M. H. (1995). Skeletal reactions of *n*-hexane over Pt-NaY, Pt/SiO<sub>2</sub>, HY, and mixed Pt/SiO<sub>2</sub> + HY catalysts. **J. Catal.** 155: 43-51.
- Bremer, H., Kornig, J., Reschetilowski, W., Vogt, F. and Wendlandt, K.-P. (1980). Isomerization of *n*-hexane over Pt/NH<sub>4</sub>NaY zeolite. **React. Kinet. Catal. Lett.** 13: 209 – 215.

- Eswaramoorthi I. and Lingappan, N. (2003). Nickel impregnated Pt/H-b and Pt/H-mordenite catalysts for hydroisomerization of n-Hexane. **Korean J. Chem. Eng.** 20: 207-216.
- Bobik, V. V., Voloshina, Y. G. and Bobonich, F. M. (2004). Effect of external acid site content in PdHZSM-5 catalyst on its activity and selectivity in hydroisomerization of *n*-hexane. **Theoretical and Experimental Chemistry.** 40: 307-311.
- Phatanasri, S., Praserttham, P., Kularbkeaw, S., and Panichsarn, S. (2000). Isomerization of n-hexane over platinum ionexchanged zeolite beta. **React. Kinet. Catal. Lett.** 71: 281 – 287.
- Kuhlmann, A., Roessner, F., Schwieger, W., Gravenhorst, O. and Selvam, T. (2004). New bifunctional catalyst based on Pt containing layered silicate Na-ilerite. **Catal. Today.** 97; 303–306.
- Lapidus, A. L., Mikhailov, M. N. Dergachev, A. A. and Mishin, I. V. (2008). Role of extraframework nanoparticles in *n*-hexane isomerization on platinum-containing high-silica zeolites, **Dokl. Phys. Chem.** 422: 240–243
- Ali, A.-G. A., Ali, L. I., Aboul-Fotouh, S. M. and Aoul-Gheit, A. K., (2001). Hydroisomerization, hydrocracking and dehydrocyclization of n-pentane and n-hexane using mono- and bi-metallic catalysts promoted with fluorine. **Appl. Catal. A:-Gen.** 215: 161 – 173.
- Vasina, T. V., Masloboishchikova, O. V., Khelkovskaya-Sergeeva, E. G., Kustov, L. M., Houzvirka, J. and Zeuthen, P. (2000). Isomerization of *n*-pentane and *n*-hexane on modified zeolites. **Rus. Chem. B+.** 49: 1838-1841.

- Yoshioka, C. M. N., Garetto, T. and Cardoso, D. (2005). *n*-Hexane isomerization on Ni-Pt catalysts/supported on HUSY zeolite: The influence from a metal content. **Catal. Today.** 107–108: 693–698.
- Boskovic, G., Micic, R., Pavlovic, P. and Putanov, P. (2001). *n*-Hexane isomerization over Pt–Na(H)Y catalysts obtained by different preparation methods. **Catal. Today.** 65: 123–128.
- Nieminen, V., Kumar, N., Salmi, T. and Murzin, D. Y. *n*-Butane isomerization over Pt–H–MCM-41. **Catal. Comm.** 5: 15–19.
- Chen, J.-K., Martin, A. M., Kim, Y. G. and John, V. T. (1988). Competitive reaction in intrazeolitic media. **Ind. Eng. Chem. Res.** 27: 401-409.
- Yang, M. and Somorjai, G. A. (2004). Adsorption and reactions of C<sub>6</sub> hydrocarbons at high pressures on Pt(111) single-crystal surfaces studied by sum frequency generation vibrational spectroscopy: mechanisms of isomerization and dehydrocyclization of *n*-hexane. **J. Am. Chem. Soc.** 126: 7698-7708.
- Roessner, F., Roland, U. and Braunschweig, T. J. (1995). Investigations on hydrogen spillover Part 2. hydrocarbon conversion on bifunctional catalysts. **J. Chem. Soc. Farad. Trans.** 91: 1539–1545.

## CHAPTER VIII

### CONCLUSIONS

Rice husk silica in amorphous phase with 98% purity was prepared by leaching rice husk with HCl acid and calcination, and used as a silica source for the synthesis of zeolite NaK-LSX and zeolite Y. The NaK-LSX crystal morphology was multi-faceted spherulite particles. The particle size distribution shows a large scale in crystal size. The BET surface area was approximately 400 m<sup>2</sup>/g. The structure was still maintained after ion exchange. However, the structure collapsed after calcination to convert to proton form. Thus, this zeolite was not used for further application.

The NaY in pure phase was obtained from two-step synthetic route in which starting gels were mixed, aged for 24 h at room temperature and crystallized for 24 h at 90°C. The NaY crystals were octahedral with twinned and overgrowth polycrystals. The diameter of single crystal was approximately 0.6 μm – 1.0 μm whereas the average diameters of zeolite particles from laser diffraction particle size analyzer were approximately 10 μm. When the crystallization time was longer than 24 h, NaY slowly transformed to zeolite NaP. The structure was still maintained after ion exchange and after calcination to convert to proton form. This zeolite was used further as support materials for catalysts containing cobalt and platinum.

The reducibility of cobalt species supported on zeolite Y depends on the zeolite form. The cobalt oxides in Co/NaY are reducible and become metallic cobalt particle with coordination number of eight after reduction. This form is active for

butane hydrogenolysis. In contrast, the cobalt oxides in Co/HY can not be reduced with similar conditions and it is remained as cobalt oxides surrounded by six oxygen atoms, inactive for butane hydrogenolysis.

The reducibility of cobalt species supported on NaY depends on the amount of metal loading which low metal loading as 1 wt% generated a small particle of Co crystallites and difficult to reduce from cobalt oxide forms to Co metal form. Therefore, at high metal loading generated a large particle of cobalt oxides and easy to reduce at mild temperature. The addition of Pt, increased the reducibility of 6Co-1Pt/NaY and 10Co-1Pt/NaY bimetallic catalysts, especially the last one was almost fully reduce. The coordination numbers of monometallic after reduction were less than bimetallic catalysts. This form is active for butane hydrogenolysis and very selective to methane production.

Pt/HY and mixed Pt/HY:1Pt/NaY are acidic and more active to *n*-hexane isomerization. Both catalysts, tested at 300°C showed the optimal selectivity to isomer products: methylcyclopentane and dimethylbutane. Propane was a minor cracking product at this temperature. The simultaneous performed at 450°C, 1Pt/HY is favorable for cracking and hydrogenolysis while the mixed catalysts exhibited high selectivity to isomerization of *n*-hexane. At 450°C cracking was more favorable but the major products were still from isomerization. From the results, it is indicated that Pt/HY and mixed Pt/HY:1Pt/NaY are acidic and active in *n*-hexane isomerization.

## **APPENDICES**

**APPENDIX A**  
**CHARACTERIZATIONS OUTPUT**



## C.1 Particle size analyzer

### Result: Histogram Table

ID: NaX(RHs)	Run No: 25	Measured: 6/3/106 12:14PM
File: TOU	Rec. No: 25	Analyzed: 6/3/106 12:14PM
Path: C:\SIZERS\DATA\		Source: Analy sed

Range: 300RF mm	Beam: 2.40 mm	Sampler: MS17	Obs': 10.1 %
Presentation: 3OHD	Analysis: Poly disperse		Residual: 0.559 %
Modifications: None			

Conc. = 0.0075 %Vol	Density = 1.000 g/cm <sup>3</sup>	S.S.A.= 1.7298 m <sup>2</sup> /g
Distribution: Volume	D[4, 3] = 13.31 um	D[3, 2] = 3.47 um
D(v, 0.1) = 1.44 um	D(v, 0.5) = 12.43 um	D(v, 0.9) = 25.18 um
Span = 1.910E+00	Uniformity = 5.625E-01	

Size (um)	Volume Under %	Size (um)	Volume Under %	Size (um)	Volume Under %	Size (um)	Volume Under %
0.055	0.00	0.635	5.24	7.31	26.10	84.15	100.00
0.061	0.00	0.700	5.80	8.06	29.16	92.79	100.00
0.067	0.00	0.772	6.36	8.89	32.84	102.3	100.00
0.074	0.00	0.851	6.91	9.80	37.15	112.8	100.00
0.082	0.00	0.938	7.45	10.81	42.07	124.4	100.00
0.090	0.00	1.03	8.01	11.91	47.52	137.2	100.00
0.099	0.00	1.14	8.57	13.14	53.37	151.3	100.00
0.109	0.00	1.26	9.15	14.49	59.60	166.8	100.00
0.121	0.00	1.39	9.76	15.97	66.07	183.9	100.00
0.133	0.00	1.53	10.38	17.62	72.30	202.8	100.00
0.147	0.01	1.69	11.02	19.42	78.01	223.6	100.00
0.162	0.02	1.86	11.65	21.42	83.13	246.6	100.00
0.178	0.06	2.05	12.29	23.62	87.53	271.9	100.00
0.196	0.11	2.26	12.93	26.04	91.18	299.8	100.00
0.217	0.20	2.49	13.56	28.72	94.08	330.6	100.00
0.239	0.36	2.75	14.17	31.66	96.30	364.6	100.00
0.263	0.61	3.03	14.78	34.92	97.89	402.0	100.00
0.290	0.95	3.34	15.39	38.50	98.95	443.3	100.00
0.320	1.38	3.69	16.04	42.45	99.62	488.8	100.00
0.353	1.86	4.07	16.77	46.81	99.97	539.0	100.00
0.389	2.38	4.48	17.62	51.62	100.00	594.3	100.00
0.429	2.92	4.94	18.66	56.92	100.00	655.4	100.00
0.473	3.49	5.45	19.95	62.76	100.00	722.7	100.00
0.522	4.07	6.01	21.56	69.21	100.00	796.9	100.00
0.576	4.67	6.63	23.58	76.32	100.00	878.7	100.00

**Table A.1-1** The percentile of particle size distribution of NaX analyzed by DPSA displayed by volume under percent.

**Result: Histogram Table**

ID: NaY (RHs)	Run No: 1	Measured: 6/3/106 10:12PM
File: TOU	Rec. No: 1	Analyzed: 6/3/106 10:12PM
Path: C:\SIZERS\DATA\		Source: Analy sed

Range: 300RF mm	Beam: 2.40 mm	Sampler: MS17	Obs': 11.2 %
Presentation: 3OHD	Analysis: Poly disperse		Residual: 0.681 %
Modifications: None			

Conc. = 0.0052 %Vol	Density = 1.000 g/cm <sup>3</sup>	S.S.A.= 3.4956 m <sup>2</sup> /g
Distribution: Volume	D[4, 3] = 15.67 um	D[3, 2] = 1.72 um
D(v, 0.1) = 0.66 um	D(v, 0.5) = 6.18 um	D(v, 0.9) = 25.93 um
Span = 4.090E+00	Unif ormity = 2.124E+00	

Size (um)	Volume Under %	Size (um)	Volume Under %	Size (um)	Volume Under %	Size (um)	Volume Under %
0.055	0.00	0.635	9.75	7.31	55.21	84.15	95.37
0.061	0.01	0.700	10.29	8.06	58.40	92.79	95.85
0.067	0.02	0.772	10.83	8.89	61.68	102.3	96.33
0.074	0.03	0.851	11.45	9.80	65.04	112.8	96.80
0.082	0.06	0.938	12.15	10.81	68.49	124.4	97.26
0.090	0.09	1.03	12.94	11.91	71.99	137.2	97.71
0.099	0.15	1.14	13.84	13.14	75.35	151.3	98.15
0.109	0.22	1.26	14.88	14.49	78.48	166.8	98.56
0.121	0.34	1.39	16.07	15.97	81.31	183.9	98.94
0.133	0.49	1.53	17.43	17.62	83.80	202.8	99.27
0.147	0.70	1.69	18.96	19.42	85.91	223.6	99.55
0.162	0.97	1.86	20.66	21.42	87.64	246.6	99.77
0.178	1.31	2.05	22.51	23.62	89.00	271.9	99.91
0.196	1.74	2.26	24.52	26.04	90.04	299.8	100.00
0.217	2.26	2.49	26.64	28.72	90.81	330.6	100.00
0.239	2.86	2.75	28.87	31.66	91.38	364.6	100.00
0.263	3.54	3.03	31.16	34.92	91.81	402.0	100.00
0.290	4.28	3.34	33.53	38.50	92.15	443.3	100.00
0.320	5.05	3.69	35.95	42.45	92.47	488.8	100.00
0.353	5.82	4.07	38.43	46.81	92.79	539.0	100.00
0.389	6.56	4.48	40.98	51.62	93.14	594.3	100.00
0.429	7.27	4.94	43.61	56.92	93.53	655.4	100.00
0.473	7.95	5.45	46.34	62.76	93.96	722.7	100.00
0.522	8.59	6.01	49.18	69.21	94.41	796.9	100.00
0.576	9.19	6.63	52.14	76.32	94.88	878.7	100.00

**Table A.1-2** The percentile of particle size distribution of NaY analyzed by DPSA displayed by volume under percent.

### C.1 Morphology of synthesized NaY by SEM

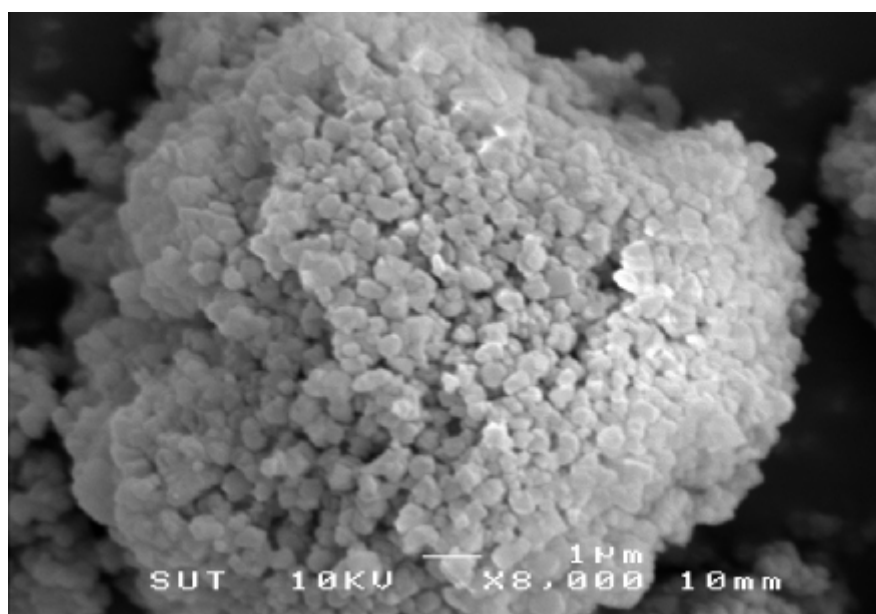


Figure A.2-1 SEM images of NaY from two-step synthesis with crystallized at 22 h

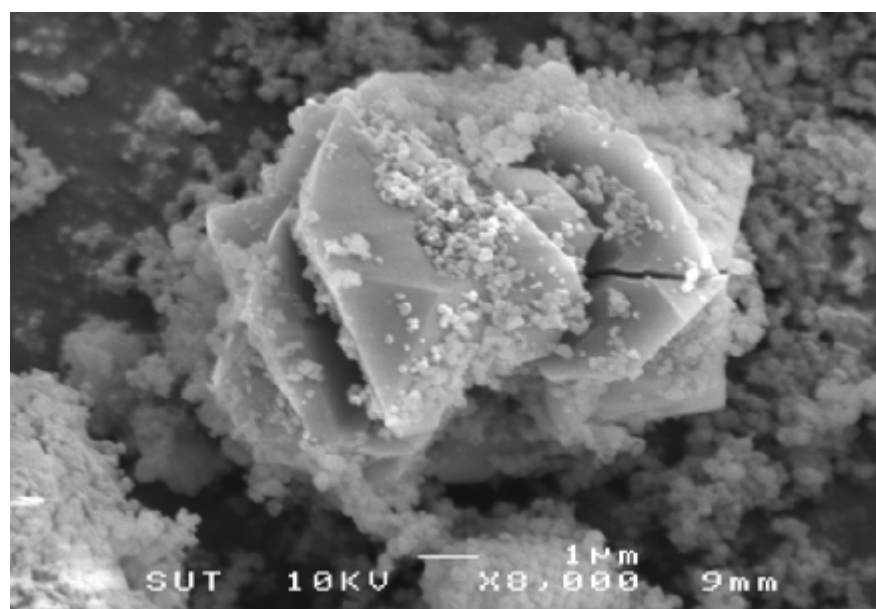
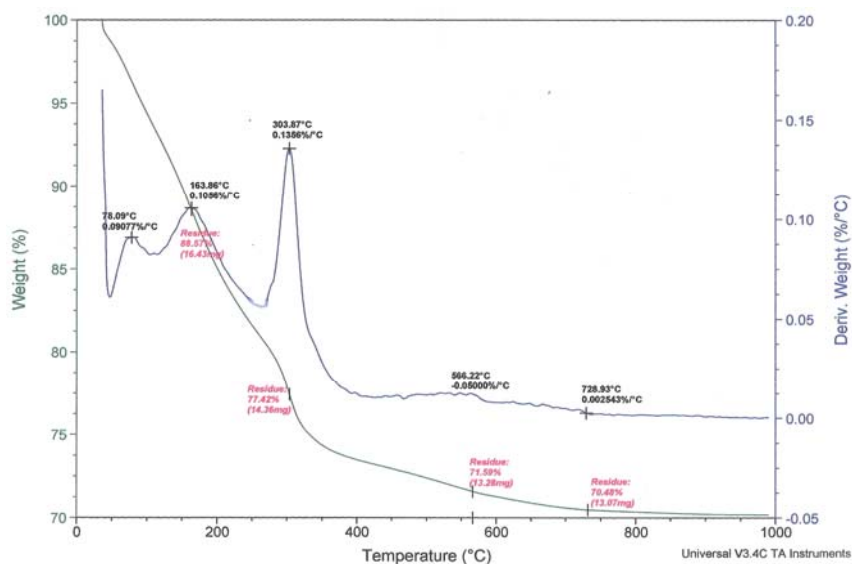
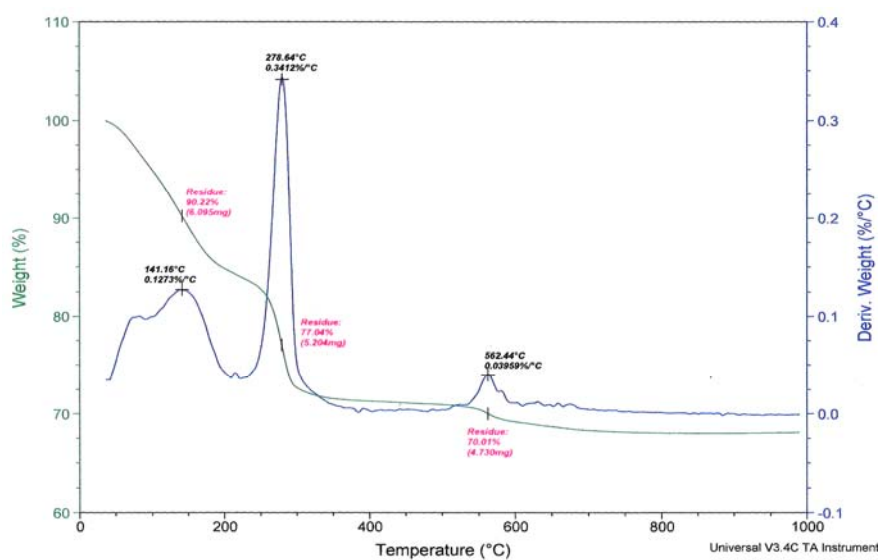


Figure A.2-2 SEM images of NaY from two-step synthesis with crystallized at 48 h

## C.1 Thermogravimetric-Differential Analysis (TGA-DTA) result

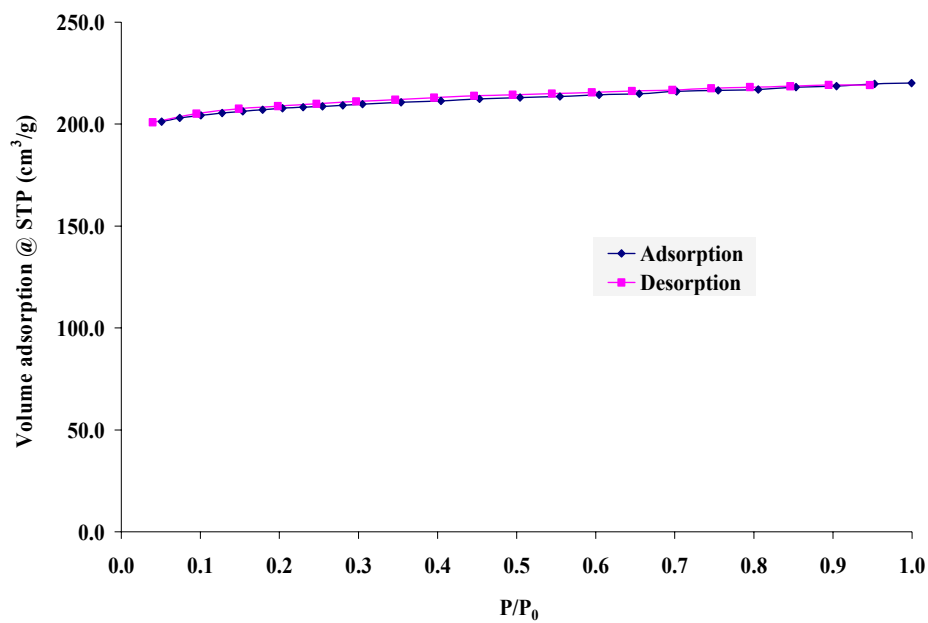


**Figure A.3-1** Thermogram of zeolite NH<sub>4</sub>LSX (solid line is weight and dash line is first derivative of weight with respect to temperature)

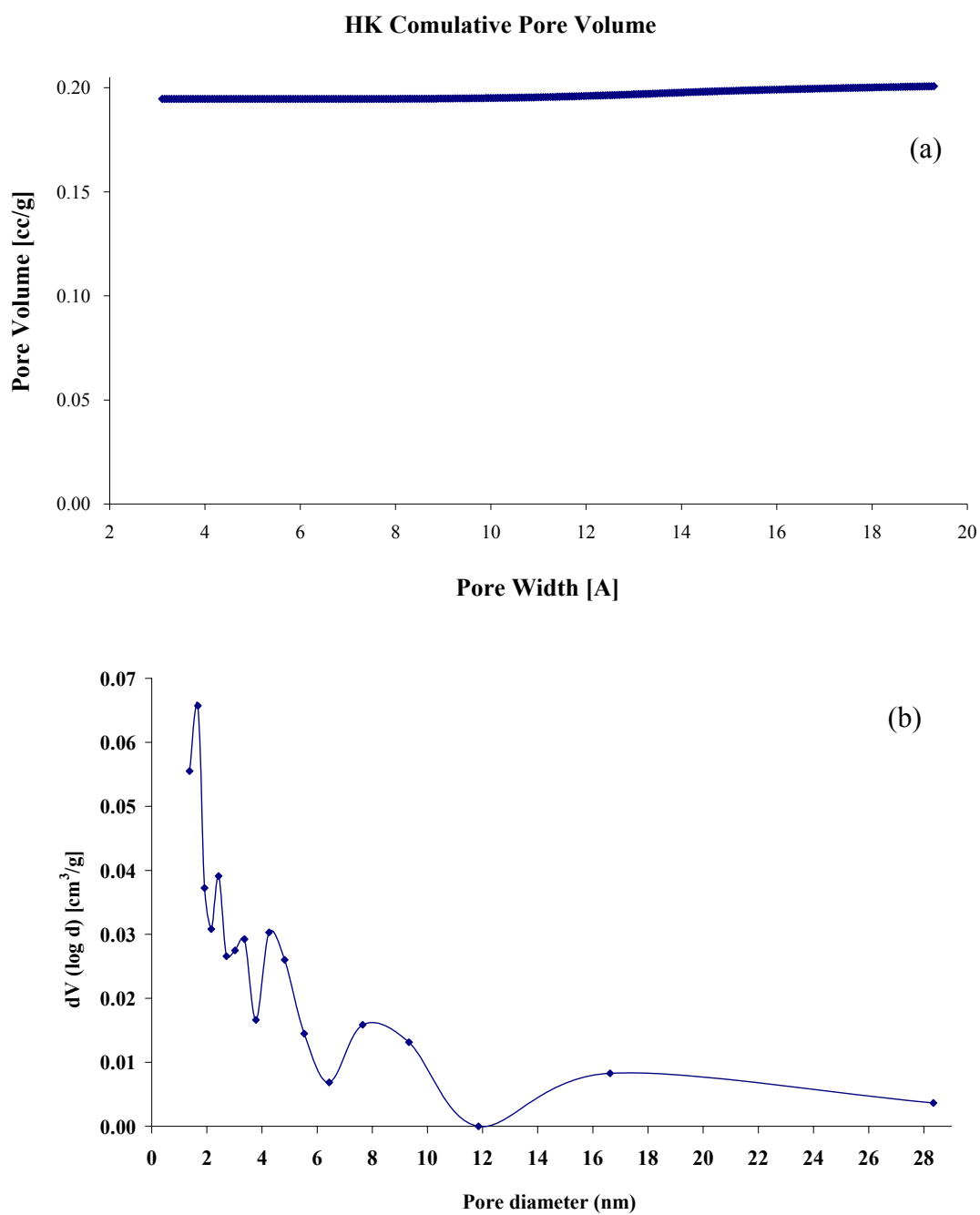


**Figure A.3-2** Thermogram of zeolite NH<sub>4</sub>Y (solid line is weight and dash line is first derivative of weight with respect to temperature)

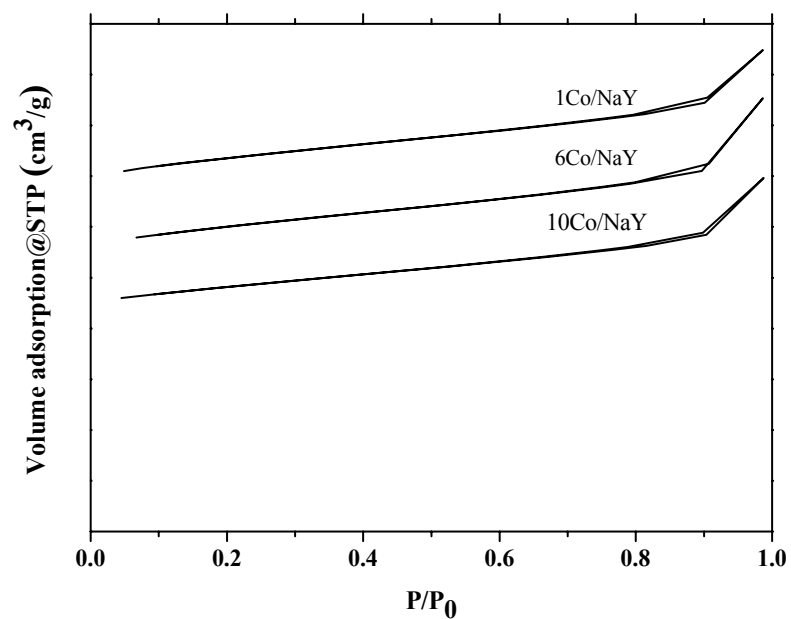
### C.1 N<sub>2</sub> adsorption-desorption isotherm of samples



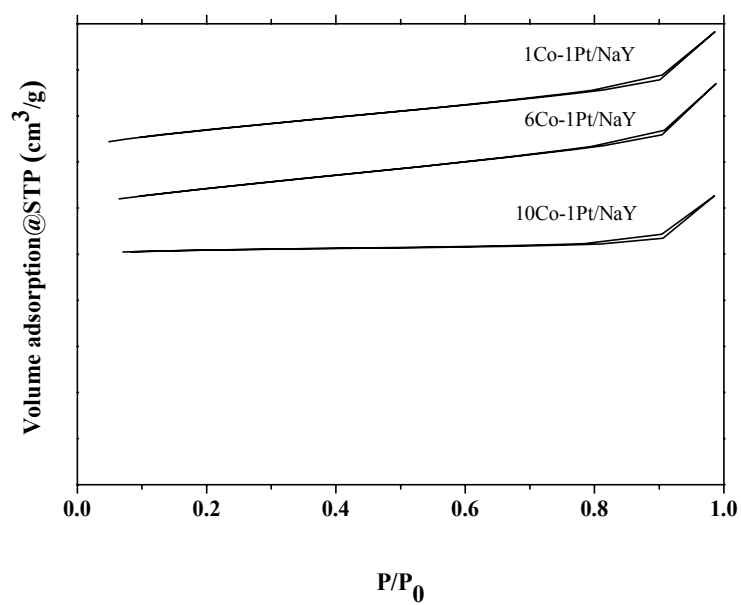
**Figure A.4-1** N<sub>2</sub> adsorption-desorption isotherm at N<sub>2</sub> temperature of synthesized NaY zeolite



**Figure A.4-2** HK cumulative pore volume (a) and BJH pore size distribution (b) of synthesized NaY zeolite



**Figure A.4-3** N<sub>2</sub> adsorption-desorption isotherm at liquid nitrogen temperature on xCo/NaY catalysts



**Figure A.4-4** N<sub>2</sub> adsorption-desorption isotherm at liquid nitrogen temperature on xCo-1Pt/NaY catalysts

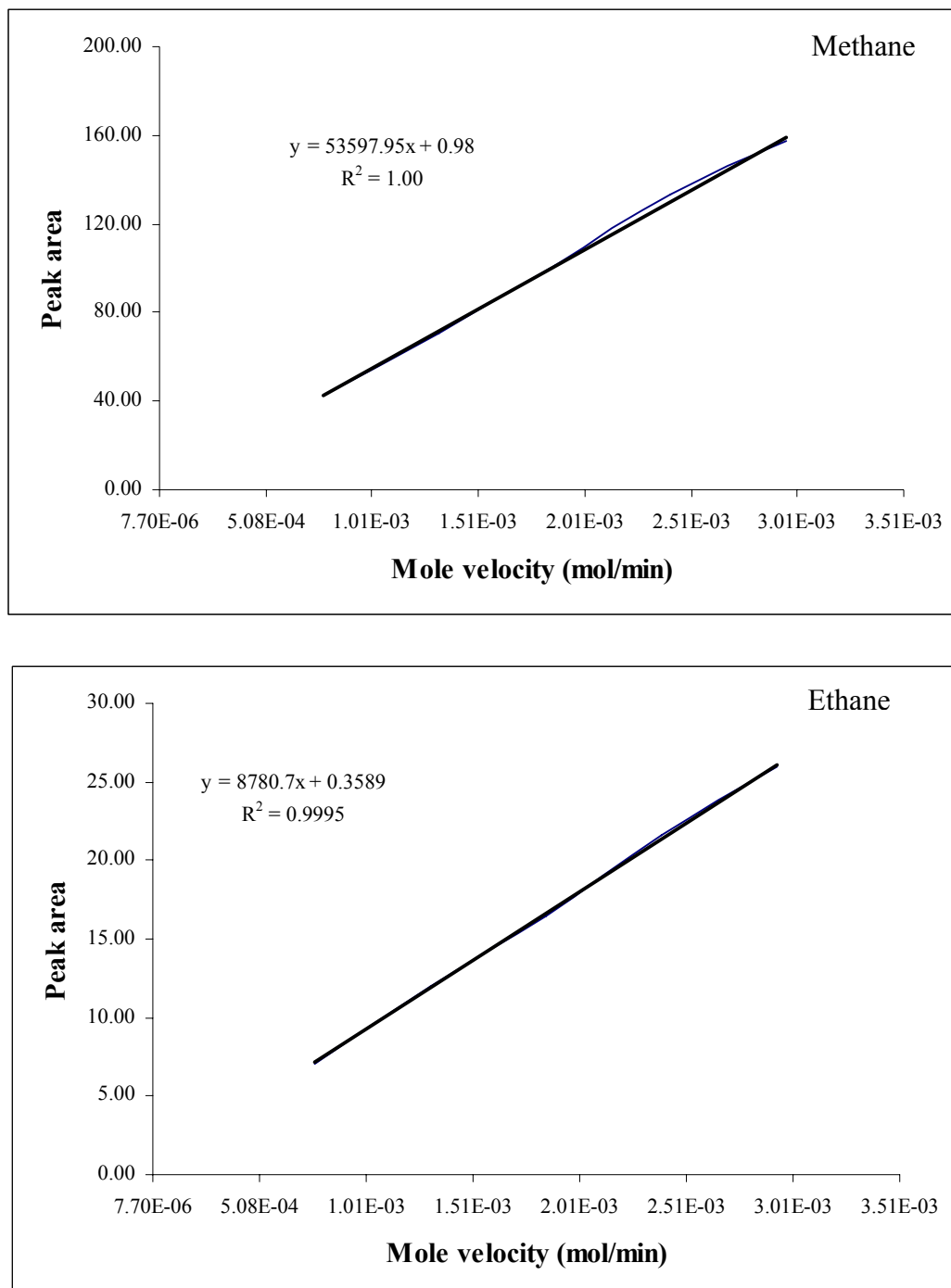
**APPENDIX B**

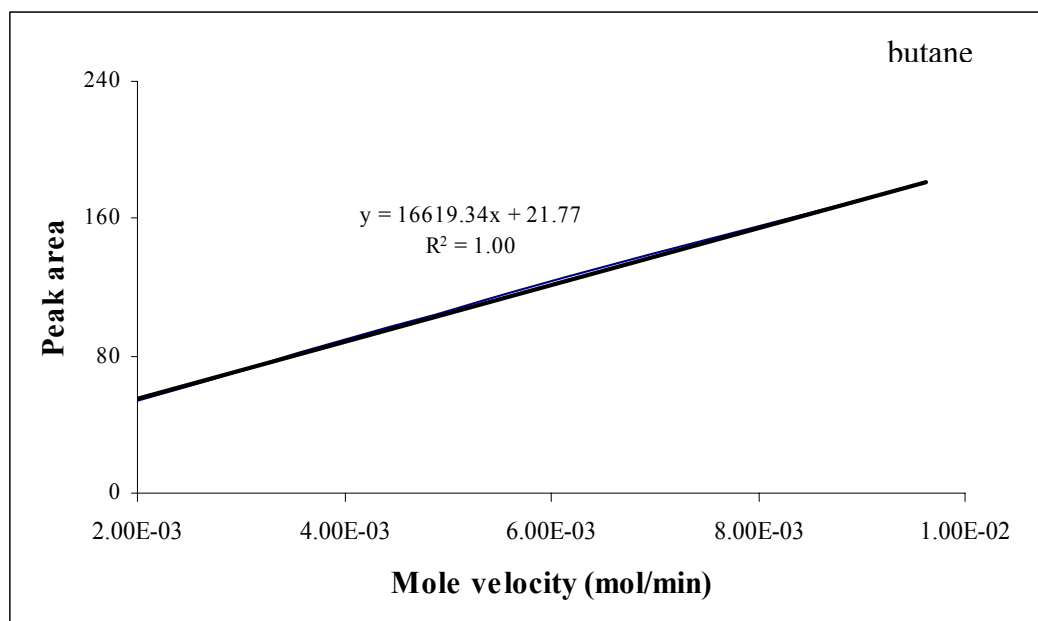
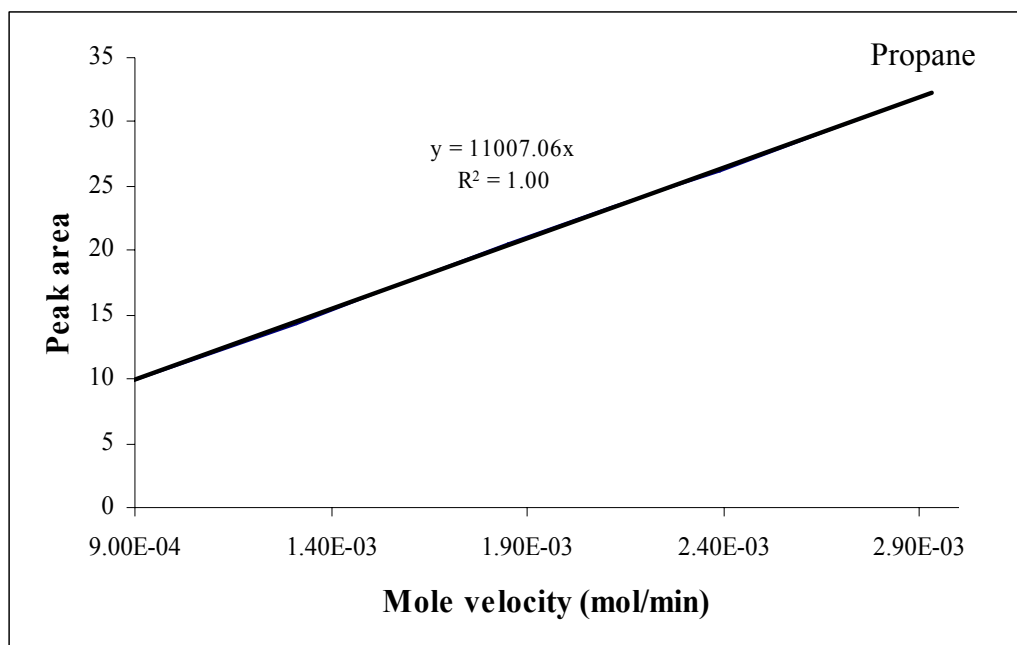
**REACTION OUTPUT OF BUTANE HYDROGENOLYSIS**

**AND**

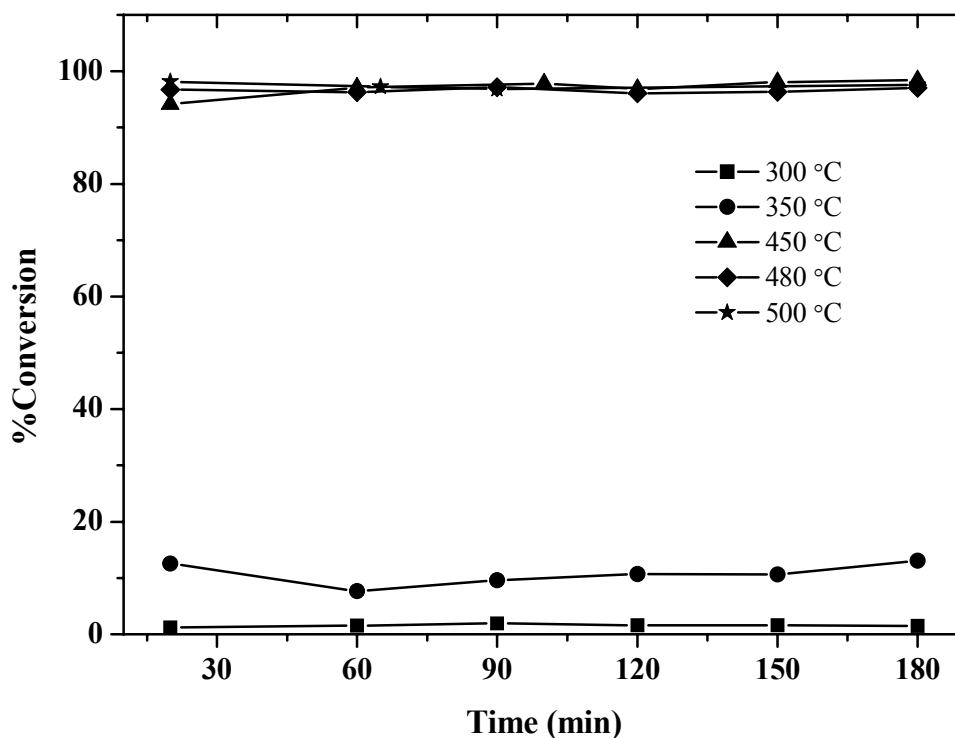
***n*-HEXANE ISOMERIZATION**



**B.1 *n*-Butane hydrogenolysis reaction****Figure B.1-1** Standard calibration curve of methane, ethane, propane and butane

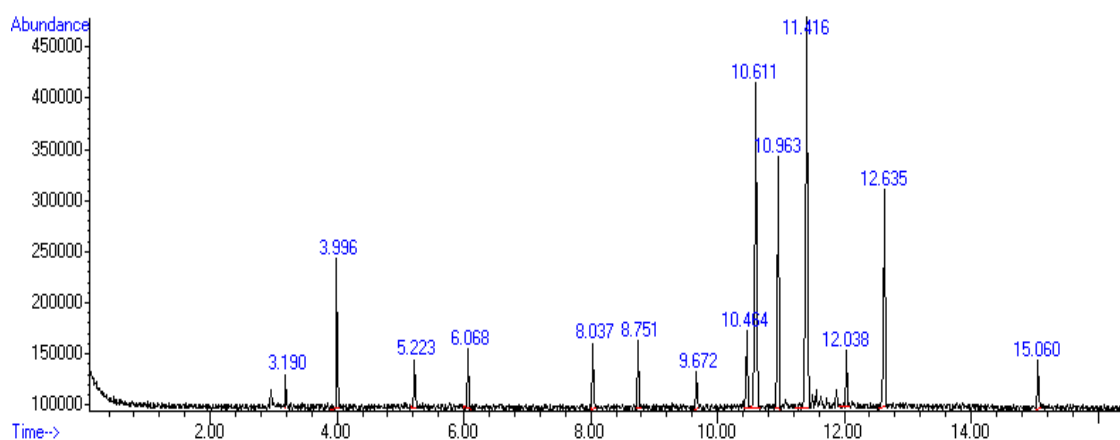


**Figure B.1-1** (continued) Standard calibration curve of methane, ethane, propane and butane



**Figure B.1-2** Conversion in butane hydrogenolysis on 6Co/NaY (various time and temperature)

## B.2 *n*-Hexane isomerization reaction



**Figure B.2-1** Chromatogram of products distribution at 450°C with time on stream (TOS) 25 minutes of 1Pt/HY catalyst

**Table B.2-1** Products distribution of 1Pt/HY on n-hexane isomerization at 450°C with TOS 25 min.

Peak	Compounds name	Retention time (min)	Amount (μg)
1	Ethane	3.191	0.010
2	Propane	3.996	0.017
3	Isobutane	5.222	0.005
4	Butane	6.067	0.006
5	2-methylbutane	8.036	0.004
6	Pentane	8.750	0.003
7	2,2-dimethylbutane	9.671	0.001
8	2,3-dimethylbutane	10.464	0.003
9	2-methylpentane	10.612	0.016
10	3-methylpentane	10.964	0.011
11	Hexane	11.417	0.016
12	Methylcyclopentane	12.037	0.002
13	Benzene	12.636	0.003
14	Toluene	15.061	

## **APPENDIX C**

### **X-RAY ABSORPTION SPECTROSCOPY OUTPUT**

## C.1 Analysis of XAS data

Analysis of EXAFS data is separated into three parts. First that simply seeks to fingerprint, the spectrum of sample being studied and to compare it with the reference compounds. The second seek more information of disordered systems that have an isolated first shell to identify the bonding configuration or valence state of the absorbing atom. The third type of experiment attempts to extract the maximum information possible from the EXAFS data.

The procedure is divided into two parts. First the data processing that includes those steps used to change the raw data into normalized EXAFS data that can be interpreted according to the usual theoretical formulations which perform by Athena program. Some of these steps include energy calibration, alignment of the energy scale, deglitching of the reflection from the crystal monochromator, EXAFS background removal, pre-edge subtraction, normalization, and transformation to  $k$  space. Second steps are operated by EXAFSPAK program; the data are analyzed to extract the parameters of interest. The procedures are Fourier transform of data, including effect of weighting and windows, filtering in R space, single and multiple-shell fitting, and direct  $k$  space analysis (ratio method) including recent generalizations.

### Data reduction step for reducing measured data to $\mu(E)$ and then to $\chi(k)$

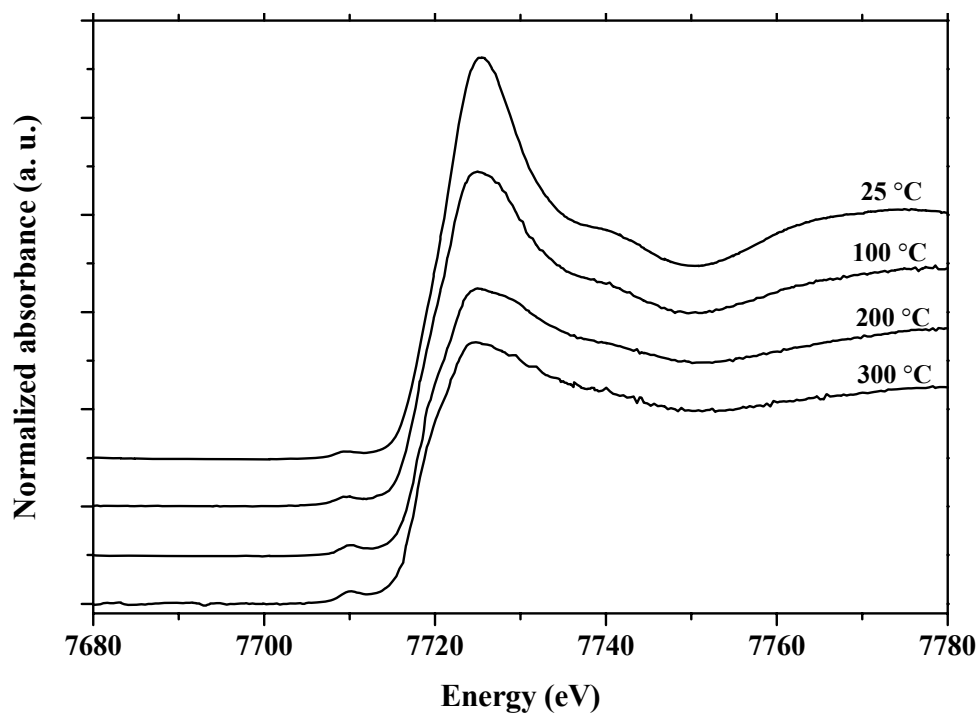
1. Convert measured intensities to  $\mu(E)$
2. Subtract a smooth pre-edge function, to get rid of any instrumental background, and absorption from other edges.
3. Normalize  $\mu(E)$  to go from 0 to 1, so that it represents the absorption of 1 x-ray.

4. Remove a smooth post-edge background function to approximate  $\mu_0(E)$  to isolate the XAFS  $\chi$ .
5. identify the threshold energy  $E_0$ , and convert from E to k space:

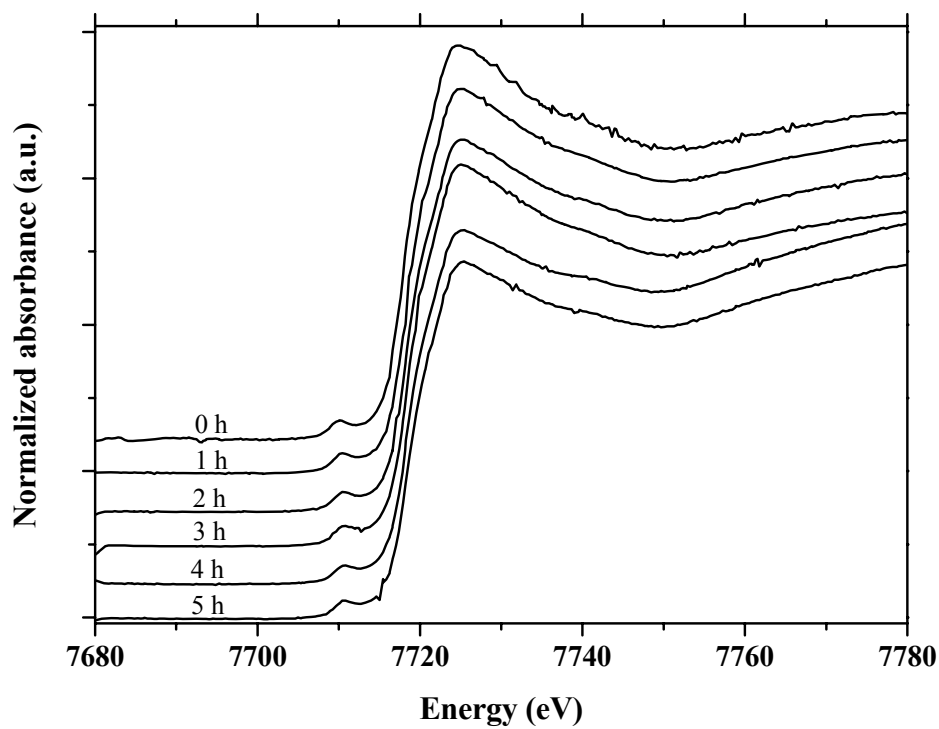
$$k = \sqrt{\frac{2m(E - E_0)}{\hbar^2}}$$

6. Weight the XAFS  $\chi(k)$  and Fourier transform from k to R space.
7. Isolate the  $\chi(k)$  for an individual “shell” by Fourier filtering.
8. After we get this far, we’ll model  $f(k)$  and  $\chi(k)$  and analyze  $\chi(k)$  to get distance R, coordination number N.

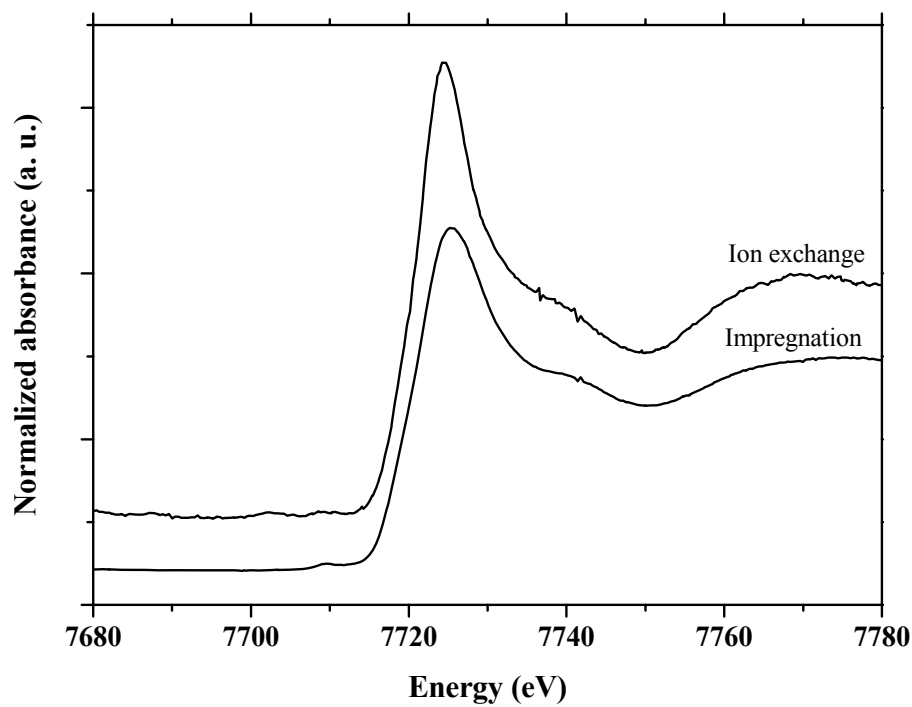
## C.2 XANES measurement



**Figure C.2-1** The plot of Co K-edge XANES spectra during reduction of 6Co/HY from room temperature to 300°C under H<sub>2</sub> atmosphere



**Figure C.2-2** The plot of Co K-edge XANES spectra during reduction of 6Co/HY at 300°C for 5 h under H<sub>2</sub> atmosphere



**Figure C.2-3** The XANES spectra of calcined Co/HY prepared different method



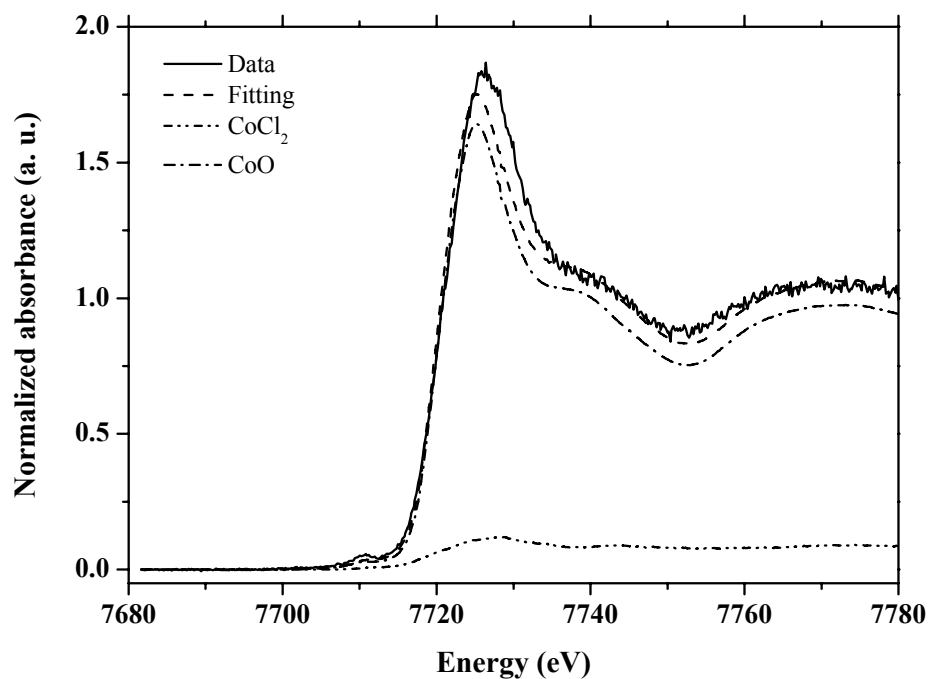


Figure C.2-4 Linear combination fit of calcined 6Co/HY compare with standard of CoO and CoCl<sub>2</sub>

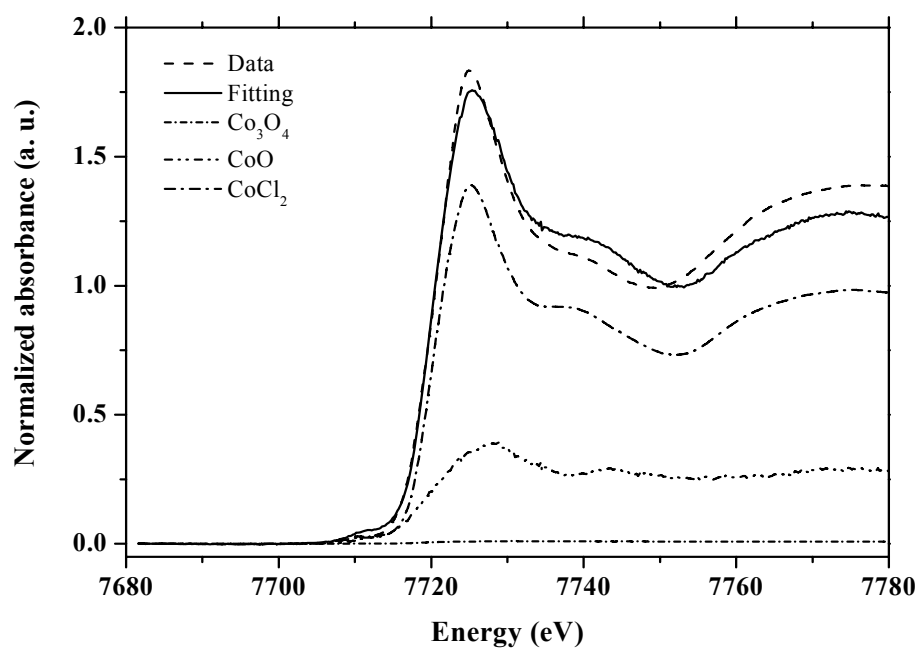
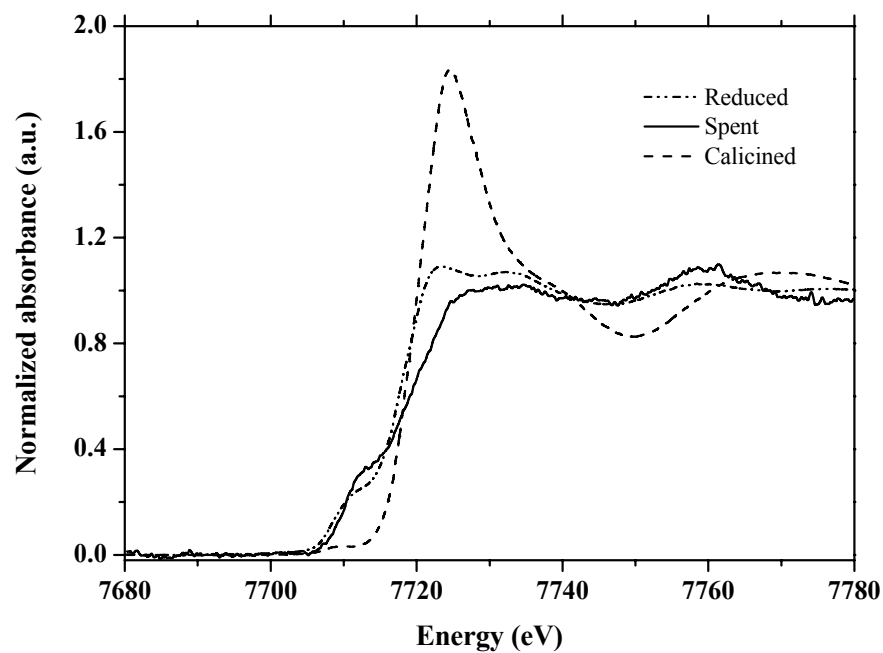
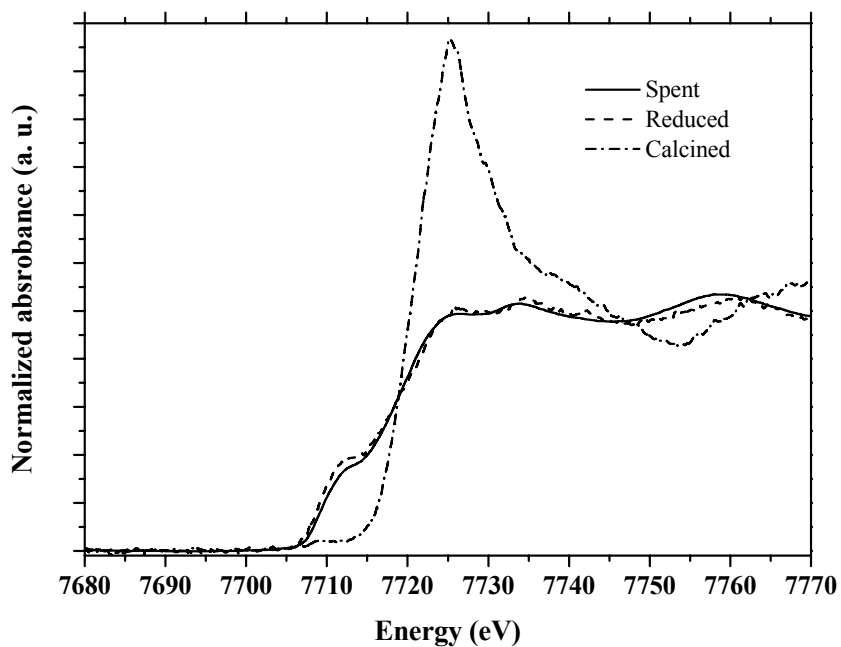


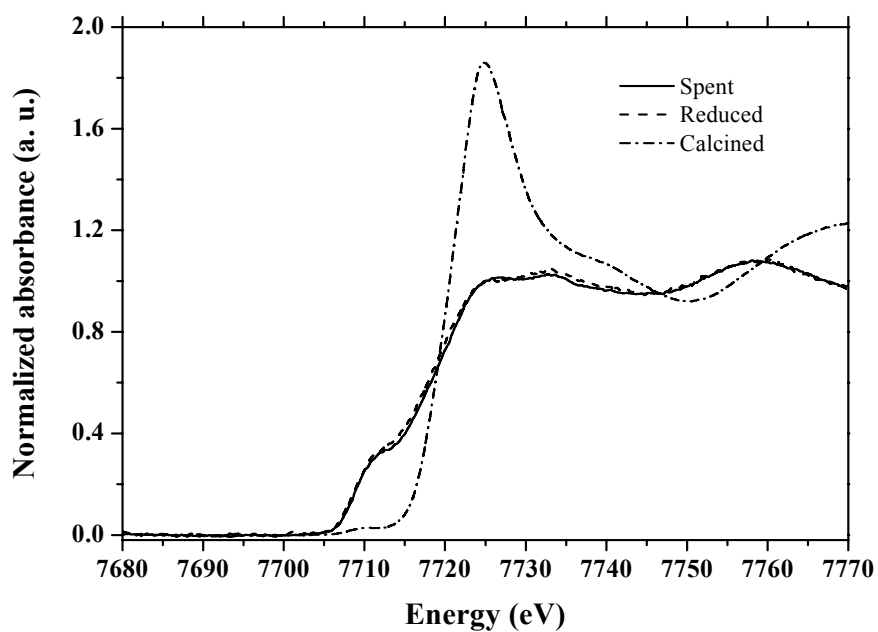
Figure C.2-5 Linear combination fit of calcined 6Co/NaY compare with standard of Co<sub>3</sub>O<sub>4</sub>, CoO and CoCl<sub>2</sub>



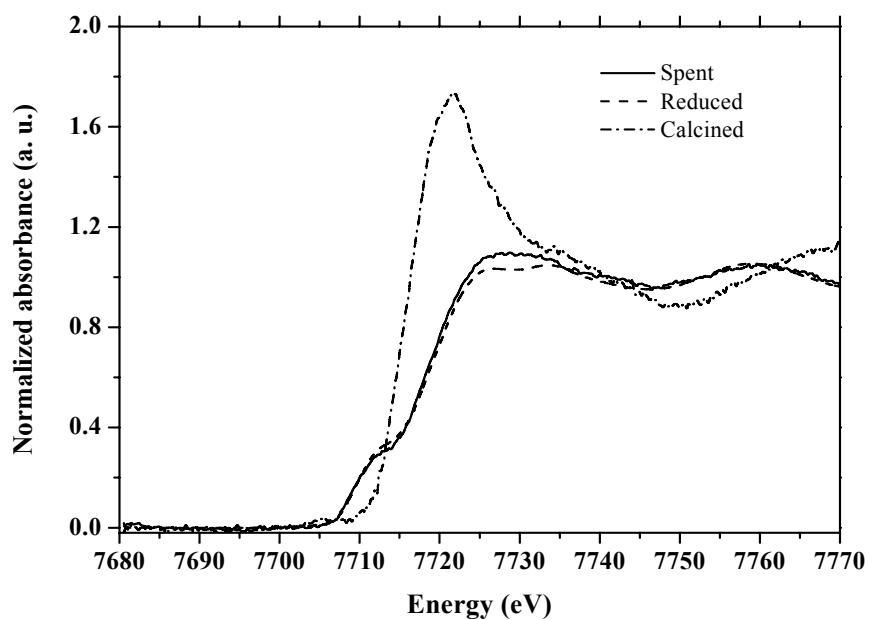
**Figure C.2-6** The XANES spectra of 6Co/NaY after being calcined (•••••), reduced (---), and tested on butane hydrogenolysis (—)



**Figure C.2-7** The XANES spectra of 10Co/NaY after being calcined (•••••), reduced (---), and tested on butane hydrogenolysis (—)

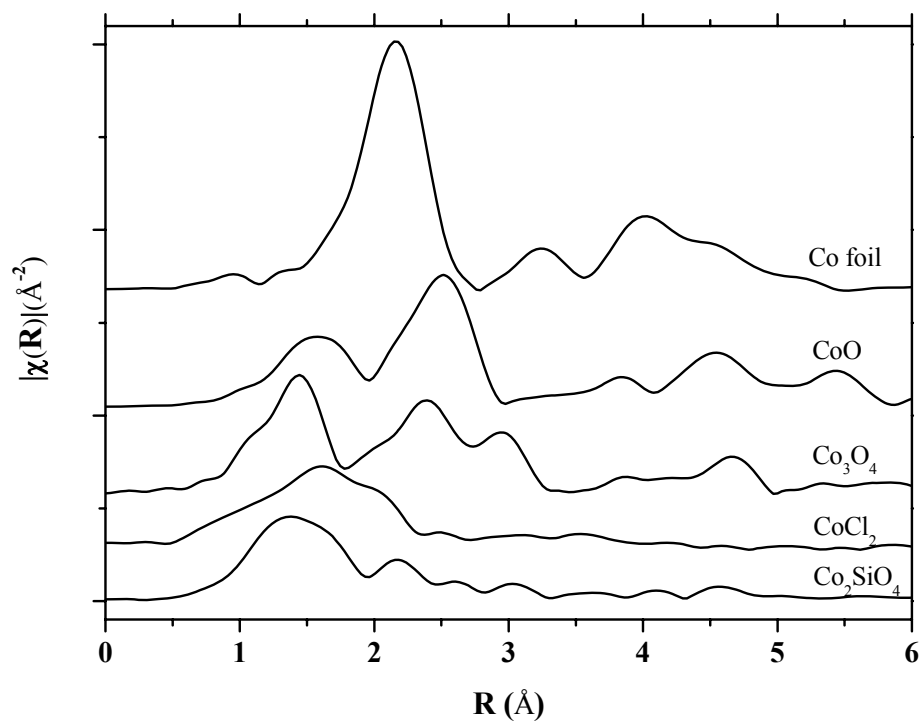


**Figure C.2-8** The XANES spectra of 6Co-1Pt/NaY after being calcined (•••••), reduced (---), and tested on butane hydrogenolysis (—)



**Figure C.2-9** The XANES spectra of 10Co-1Pt/NaY after being calcined (•••••), reduced (---), and tested on butane hydrogenolysis (—)

### C.3 EXAFS measurement



**Figure C.3-1** Modules of Fourier transform of standard materials Co foil, CoO,  $\text{Co}_3\text{O}_4$ ,  $\text{CoCl}_2$  and  $\text{Co}_2\text{SiO}_4$

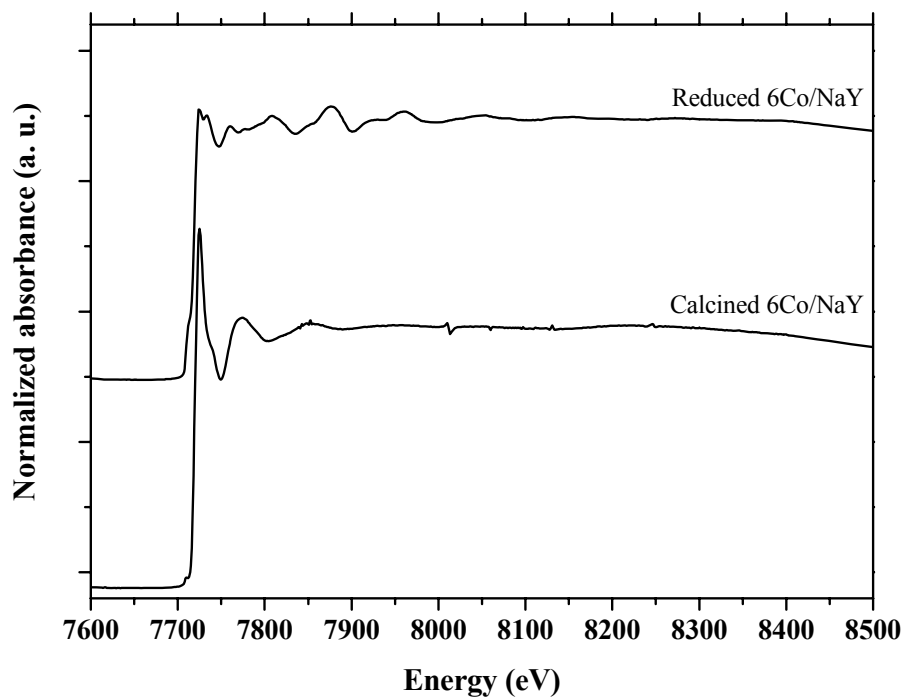


Figure C.3-2 EXAFS spectrum of 6Co/NaY after being calcined and reduced

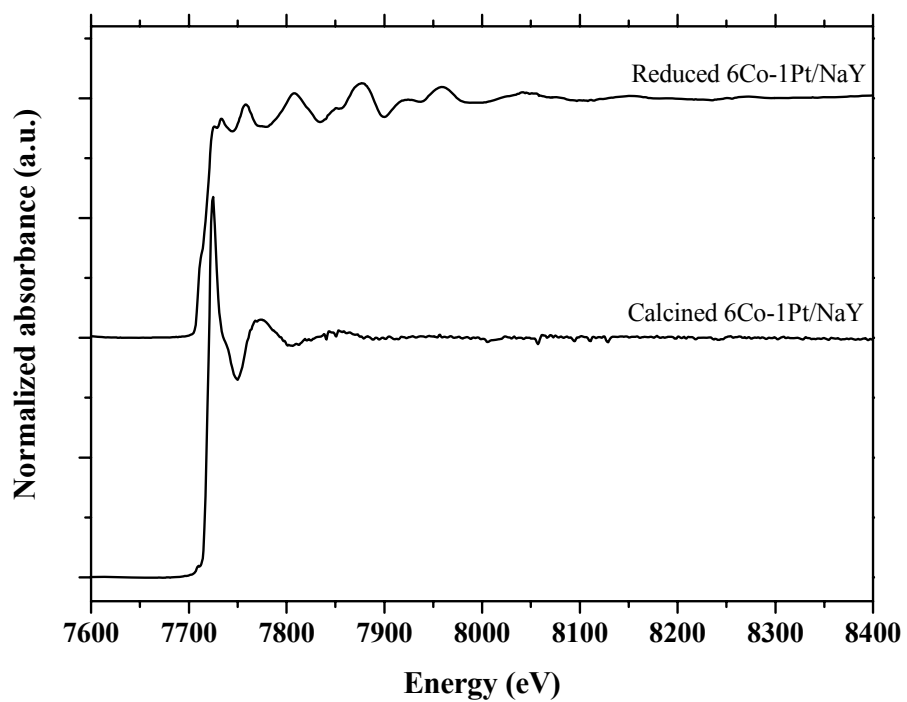
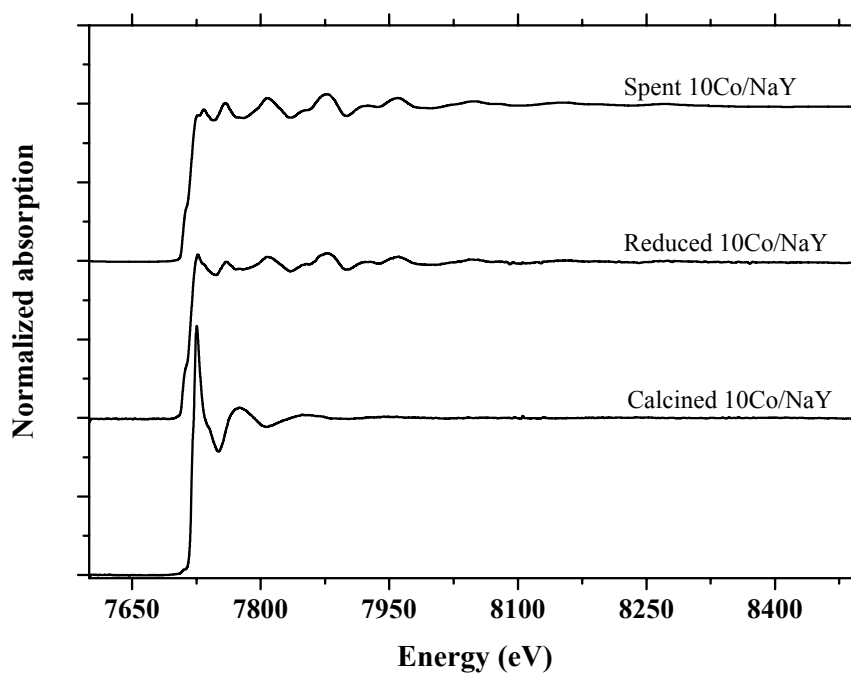
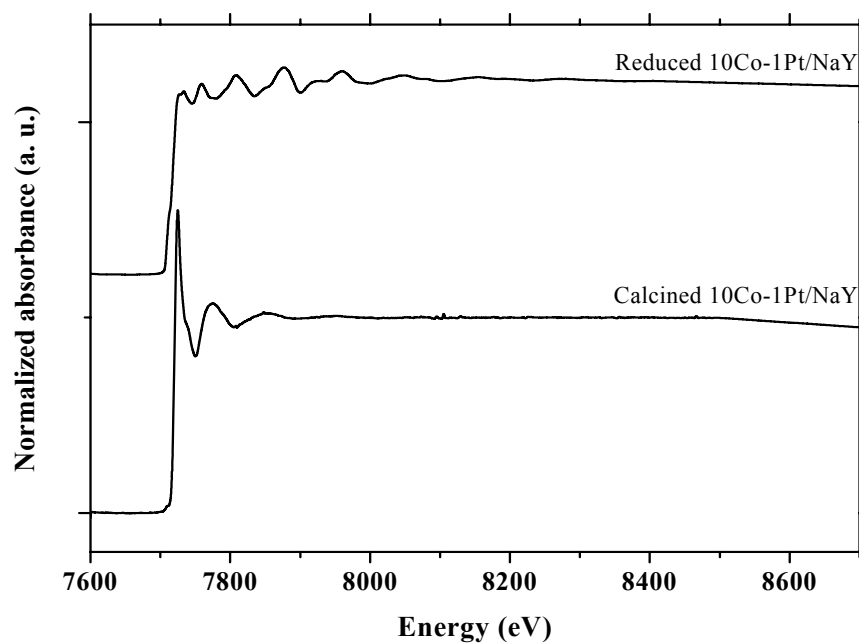


Figure C.3-3 EXAFS spectrum of 6Co-1Pt/NaY after being calcined and reduced



**Figure C.3-4** EXAFS spectrum of 10Co/NaY after being calcined, reduced and tested on butane hydrogenolysis



**Figure C.3-5** EXAFS spectrum of 10Co-1Pt/NaY after being calcined and reduced

# CURRICULUM VITAE

## Mr. PONGTANAWAT KHEMTHONG

**Date of Birth** March 26<sup>th</sup>, 1979

### Education

2008 Research at Carl von Ossietzky University Oldenburg, Germany for 6 months (February - June)

2003 - 2009 Ph. D. (Chemistry) Suranaree University of Technology. Thailand

1999 - 2001 B.Sc. Ubon Ratchathani University, Thailand

### National publications

1. Khemthong, P., Prayoonpokarach, S. and Wittayakun, J. (2007). Suranaree Journal of Science and Technology, 14 (4), 367 – 379.
2. Khabuanchalad, S., Khemthong, P., Prayoonpokarach, S. and Wittayakun, J. (2008). Suranaree Journal of Science and Technology, 15(3):233-239

### International publications

1. Wittayakun, J., Khemthong, P. and Prayoonpokarach, S. (2008). Korean Journal of Chemical Engineering, 25 (4), 861 – 864.

### Manuscript preparation

1. Comparative reducibility of Co catalyst supported on NaY and HY by XAS and performance on butane hydrogenolysis, submitted.
2. Reducibility of cobalt and cobalt-platinum supported on zeolite NaY investigated by X-ray absorption and the catalytic performance for butane hydrogenolysis, submitted.
3. *n*-Hexane Isomerization over HY and 1Pt/HY, manuscript in preparation.